

University of Warwick institutional repository: <http://go.warwick.ac.uk/wrap>

**A Thesis Submitted for the Degree of PhD at the University of Warwick**

<http://go.warwick.ac.uk/wrap/50241>

This thesis is made available online and is protected by original copyright.

Please scroll down to view the document itself.

Please refer to the repository record for this item for information to help you to cite it. Our policy information is available from the repository home page.

AUTHOR: Gregory Jon Rees      DEGREE: Ph.D.

TITLE: Development of Solid State NMR to Understand Materials Involved  
in Catalytic Technology used in Fuel Cells

DATE OF DEPOSIT: .....

I agree that this thesis shall be available in accordance with the regulations governing the University of Warwick theses.

I agree that the summary of this thesis may be submitted for publication.

I **agree** that the thesis may be photocopied (single copies for study purposes only).

Theses with no restriction on photocopying will also be made available to the British Library for microfilming. The British Library may supply copies to individuals or libraries, subject to a statement from them that the copy is supplied for non-publishing purposes. All copies supplied by the British Library will carry the following statement:

“Attention is drawn to the fact that the copyright of this thesis rests with its author. This copy of the thesis has been supplied on the condition that anyone who consults it is understood to recognise that its copyright rests with its author and that no quotation from the thesis and no information derived from it may be published without the author’s written consent.”

AUTHOR’S SIGNATURE: .....

---

USER’S DECLARATION

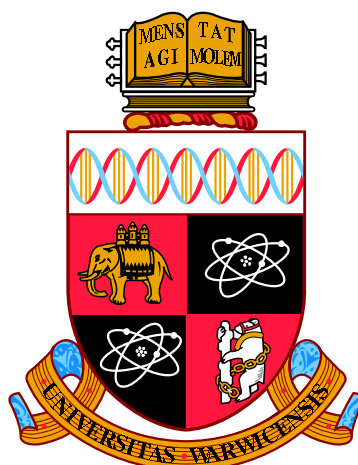
1. I undertake not to quote or make use of any information from this thesis without making acknowledgement to the author.
2. I further undertake to allow no-one else to use this thesis while it is in my care.

DATE

SIGNATURE

ADDRESS

.....  
.....  
.....  
.....  
.....



**Development of Solid State NMR to Understand  
Materials Involved in Catalytic Technology used in  
Fuel Cells**

by

**Gregory Jon Rees**

**Thesis**

Submitted to the University of Warwick

for the degree of

**Doctor of Philosophy**

**Department of Physics**

July 2012

THE UNIVERSITY OF  
**WARWICK**

# Contents

<b>List of Tables</b>	<b>vi</b>
<b>List of Figures</b>	<b>vii</b>
<b>Acknowledgments</b>	<b>ix</b>
<b>Declarations</b>	<b>xi</b>
<b>Abstract</b>	<b>xii</b>
<b>Abbreviations</b>	<b>xv</b>
<b>Chapter 1 Historical Context &amp; Motivation</b>	<b>1</b>
1.1 The History of NMR . . . . .	1
1.1.1 In the Beginning, 1920s - 1960s . . . . .	1
1.1.2 Modern Day NMR, 1960s - Present Day . . . . .	4
1.2 Motivation . . . . .	5
1.2.1 Why NMR Of Catalysts . . . . .	6
1.2.2 Why NMR on Tight Hydrogen Bonds . . . . .	7
<b>Chapter 2 Introduction to Solid State Nuclear Magnetic Resonance</b>	<b>8</b>
2.1 Background . . . . .	8
2.2 Angular Momentum . . . . .	8
2.3 Interactions . . . . .	9
2.3.1 Hamiltonians, The Principal Axis System and Frame Rotations	9
2.3.2 Zeeman Interaction . . . . .	14
2.3.3 Indirect Dipole - Dipole Coupling . . . . .	15
2.3.4 Dipolar Coupling . . . . .	16
2.3.5 Chemical Shift . . . . .	17
2.3.6 Quadrupole Interaction . . . . .	21



2.3.7	The Knight Shift . . . . .	29
2.3.8	The Korringa Relation . . . . .	31
2.3.9	Paramagnetic Shift . . . . .	32
2.4	Magic Angle Spinning . . . . .	32
2.4.1	Theory . . . . .	33
2.4.2	NMR Interactions under MAS . . . . .	35
2.4.3	Chemical Shift Anisotropy under MAS . . . . .	35
2.4.4	Quadrupole Interaction under MAS . . . . .	37

### **Chapter 3 Pulsed Fourier Transform Solid State Nuclear Magnetic Resonance**

		<b>40</b>
3.1	Solid State NMR Instrumentation . . . . .	40
3.1.1	The Magnet . . . . .	41
3.1.2	The Probes . . . . .	42
3.1.3	The Consoles . . . . .	43
3.1.4	Signal Detection . . . . .	44
3.2	Relaxation . . . . .	45
3.2.1	Longitudinal Relaxation . . . . .	46
3.2.2	Transverse Relaxation . . . . .	48
3.3	Fourier Transform . . . . .	49
3.4	The NMR Experiment . . . . .	50
3.4.1	Radio Frequency Pulses . . . . .	50
3.4.2	Coherence and Phasing . . . . .	53
3.4.3	One Pulse . . . . .	54
3.4.4	Echo Experiments . . . . .	55
3.4.5	Cross Polarisation . . . . .	56
3.4.6	Wide Line Acquisition for Nonquadrupolar and Quadrupolar Nuclei . . . . .	57
3.4.7	Pulsed Fourier Transform Field Sweep Nuclear Magnetic Resonance . . . . .	63
3.4.8	Multiple Quantum Magic Angle Spinning . . . . .	64
3.4.9	Shearing . . . . .	66
3.4.10	Double Orientation Rotation . . . . .	68
3.5	Density Functional Theory Calculations; The CASTEP Code . . . . .	70

### **Chapter 4 Characterisation of Platinum-based Fuel Cell Catalyst Materials using Wideline Solid State NMR**

		<b>75</b>
4.1	Introduction . . . . .	75

4.1.1	Background . . . . .	75
4.1.2	Platinum Nanoparticles . . . . .	76
4.1.3	NMR of Clusters . . . . .	78
4.1.4	Wideline Solid State NMR Techniques . . . . .	79
4.2	Experimental . . . . .	79
4.2.1	Synthesis . . . . .	79
4.2.2	XRD Measurements . . . . .	79
4.2.3	Solid State NMR . . . . .	79
4.3	Results and Discussion . . . . .	81
4.3.1	Theory Versus Field Sweep Fourier Transform NMR . . . . .	81
4.3.2	Comparison of Commonly used Wideline Reconstruction Techniques . . . . .	83
4.3.3	Field Sweep Fourier Transform (FSFT) NMR comparison Versus Spin Echo Height Spectroscopy (SEHS) NMR . . . . .	85
4.3.4	Platinum Clusters . . . . .	89
4.3.5	Platinum-Tin Intermetallic Nanoparticles . . . . .	90
4.3.6	Platinum Alloy Nanoparticles . . . . .	92
4.4	Conclusions . . . . .	97
<b>Chapter 5 Apatite Oxide Ion Conductors</b>		<b>99</b>
5.1	Introduction to Solid Oxide Fuel Cells and Apatite Oxide Ion Conductors . . . . .	99
5.2	Experimental and Synthesis . . . . .	103
5.2.1	Synthesis and Sample Preparation . . . . .	103
5.2.2	Density Functional Theory . . . . .	103
5.2.3	Solid State NMR . . . . .	103
5.3	Results and Discussion . . . . .	105
5.3.1	Modelling and DFT of Rare Earth Apatite Conduction . . . . .	105
5.3.2	Rare Earth Apatite Silicates . . . . .	106
5.3.3	Rare Earth Apatite Germanates . . . . .	109
5.3.4	$P_Q$ Calculations . . . . .	112
5.3.5	The 3QMAS spectra of highly labelled Apatite Ion Conductors	116
5.3.6	The Double Rotation spectra of of highly labelled Apatite Ion Conductors . . . . .	116
5.3.7	Proton Motion Studies . . . . .	119
5.4	Conclusions . . . . .	120

<b>Chapter 6</b>	<b>A Multinuclear Solid State NMR, DFT and Diffraction study of Tight Hydrogen Bonds in Group IA Hemibenzoate</b>	<b>122</b>
6.1	Introduction to Solid State NMR and the Measurement of Hydrogen Bonding . . . . .	122
6.2	Experimental . . . . .	126
6.2.1	Sample Preparation . . . . .	126
6.2.2	Crystallography . . . . .	127
6.2.3	Solid State NMR . . . . .	127
6.2.4	Computational Aspects . . . . .	129
6.3	Results and Discussion . . . . .	130
6.3.1	Crystallography . . . . .	130
6.3.2	Proton One Dimensional NMR . . . . .	134
6.3.3	Carbon Chemical Shift Anisotropy Determination . . . . .	138
6.3.4	<sup>17</sup> Oxygen Spectra, Simulations and MQMAS . . . . .	138
6.3.5	Double Rotation . . . . .	143
6.3.6	NMR of the Group IA Metal Hemibenzoates . . . . .	146
6.4	Conclusions and Trends . . . . .	149
<b>Chapter 7</b>	<b>Summary</b>	<b>152</b>
7.1	Characterisation of Platinum-based Fuel Cell Catalyst Materials using Wideline Solid State NMR . . . . .	152
7.2	Apatite Oxide Ion Conductors . . . . .	153
7.3	A Multi-Nuclear Solid State NMR, DFT and Diffraction study of Tight Hydrogen Bonds in Group IA Hemibenzoates . . . . .	153
<b>Appendix A</b>	<b>Appendix</b>	<b>177</b>
A.1	History . . . . .	177
A.1.1	Endnotes . . . . .	177
A.2	Characterisation of Platinum-based Fuel Cell Catalyst Materials using Wideline Solid State NMR . . . . .	177
A.3	Apatite Oxide Ion Conductors . . . . .	178
A.3.1	DFT Simulation Input Files . . . . .	178
A.4	A Multi-Nuclear Solid State NMR, DFT and Diffraction study of Tight Hydrogen Bonds in Group IA Hemibenzoates . . . . .	178
A.4.1	Experimental . . . . .	178
A.4.2	Synthesis and Characterisation . . . . .	179
A.4.3	<sup>17</sup> O-Enriched benzoic acid . . . . .	179
A.4.4	Lithium hemibenzoate . . . . .	180

A.4.5	Sodium benzoate . . . . .	180
A.4.6	Potassium hemibenzoate . . . . .	180
A.4.7	Rubidium hemibenzoate . . . . .	181
A.4.8	Caesium hemibenzoate - monoclinic polymorph . . . . .	181
A.4.9	Caesium hemibenzoate - orthorhombic polymorph . . . . .	181
A.4.10	X-ray Crystallography . . . . .	182
A.4.11	Crystal data . . . . .	182
A.4.12	CASTEP Output of Hemibenzoate CIFs by different Opti- sation Methods . . . . .	183

# List of Tables

4.1	Experimental Pulsed NMR Parameters used for the Various Nuclei .	81
4.2	Theoretical and experimental values for the relative intensities of the different regions based on a total atom number five layered nanoparticle.	83
4.3	A comparison of the theoretical model against the deconvolution of the platinum sweeps for various platinum nanoparticle sizes. . . . .	88
4.4	Experimentally measured $^{195}\text{Pt}$ and $^{119}\text{Sn}$ NMR interaction parameters for PtYSnX bimetallics systems. . . . .	91
4.5	Relaxation Times of Platinum-X Alloys and Intermetallics . . . . .	96
5.1	Experimentally measured and NMR-CASTEP DFT calculated $^{17}\text{O}$ NMR interaction parameters for various apatite systems. . . . .	115
6.1	Experimentally measured and NMR-CASTEP DFT calculated $^1\text{H}$ Isotropic shifts and $^{13}\text{C}$ CSA parameters . . . . .	137
6.2	Experimentally measured and NMR-CASTEP DFT calculated $^{17}\text{O}$ Isotropic shifts and Quadrupolar parameters . . . . .	142
6.3	A comparison of the solid state NMR data achieved for the group IA metals with their corresponding DFT-CASTEP data . . . . .	148
6.4	A Comparison of Techniques used to Define Hydrogen Bonding Character . . . . .	150
A.1	The Lattice Paramters for the Platinum Intermetallics and Alloys . .	178
A.2	The CASTEP Results from the Experimentally Determined CIFs . .	184
A.3	The CASTEP Results from the Proton Optimised CIFs . . . . .	184

# List of Figures

2.1	Euler angle rotations . . . . .	10
2.2	The Legendre polynomials . . . . .	12
2.3	Zeeman Splitting of Common Nuclei . . . . .	15
2.4	Chemical Shift Anisotropy . . . . .	20
2.5	Quadrupole Coupling Constant ( $C_Q$ ) and Asymmetry parameter ( $\eta$ )	22
2.6	Euler Angles . . . . .	28
2.7	Magic Angle Spinning . . . . .	33
3.1	Longitudinal Relaxation . . . . .	47
3.2	Free induction decay during static and MAS experiments . . . . .	48
3.3	Nutation rates in yttrium aluminium garnet . . . . .	52
3.4	A one pulse NMR experiment . . . . .	54
3.5	Spin echo . . . . .	55
3.6	Chemical shift ranges of some the spin- $\frac{1}{2}$ nuclei . . . . .	58
3.7	QCPMG pulse sequence . . . . .	62
3.8	Coherence pathway of a Z-Filter MQMAS . . . . .	65
3.9	DOuble rotation . . . . .	69
4.1	Field Sweep Fourier Transform of a Platinum Nanoparticle . . . . .	82
4.2	Comparison of Wideline NMR Techniques on a Platinum Nanoparticle	84
4.3	Comparison of Spin Echo Height Spectroscopy and Field Sweep Fourier Transform NMR on varying sizes of Platinum Nanoparticles . . . . .	86
4.4	Platinum $^{13}\text{C}$ Clusters . . . . .	90
4.5	NMR and X-ray Crystallography of Platinum - Tin Intermetallics . .	92
4.6	Alloys and their corresponding Metals . . . . .	93
4.7	Platinum NMR and X-ray Crsytallography of Alloys . . . . .	95
5.1	The structure of a Rare Earth Apatite and the proposed Oxide Ion Conduction Pathway . . . . .	101

5.2	The Density Functional Theory CASTEP determined spectra for sample lanthanum-yttrium germanate . . . . .	105
5.3	The silicon MAS and oxygen MAS NMR Spectra of Rare Earth Silicate Oxide Ion Conductors . . . . .	107
5.4	The oxygen MAS NMR of Rare Earth Germanate Oxide Ion Conductors	110
5.5	The Quadrupole Coupling Parameters, MQMAS and Calculated Parameters for the Silicates and Germanates . . . . .	113
5.6	3QMAS Spectra of highly labelled Apatite Ion Conductors . . . . .	117
5.7	DOR Spectra of highly labelled Apatite Ion Conductors . . . . .	118
5.8	Proton Mobility Spectra for Determination of the Water and Hydroxyl Environment in Apatites . . . . .	119
6.1	Chemical Shift Anisotropy Tensors of Carboxylic Group . . . . .	125
6.2	Crystal Structures of the Hemibenzoates . . . . .	131
6.3	The Packing Structures of the Hemibenzoates . . . . .	133
6.4	The Fast MAS Proton Solid State NMR of the Hemibenzoate Series	135
6.5	Chemical Shift Anisotropy of the Carboxy Group in the Hemibenzoate Series . . . . .	139
6.6	17-Oxygen MAS NMR of the Hemibenzoate Series . . . . .	141
6.7	17-Oxygen DOR NMR of the Hemibenzoate Series . . . . .	144
6.8	The Calculated Isotropic Shift and Quadrupole Parameter for the Hemibenzoate Series . . . . .	146
6.9	NMR of the Group IA Metals . . . . .	147
A.1	An Example of a pNMRsim Input File . . . . .	179

# Acknowledgments

Without the help, guidance and instruction of the following people none of the work presented here in this thesis would be possible. I would like to express my gratitude to my supervisors Dr John Hanna and Prof. Mark Smith, whose support, expertise, knowledge and understanding added considerably towards my research experience.

Beside my supervisors, I would like to express thanks to Dr Andrew Howes for his technical expertise and his immense patience when it came to the double rotation experiments present in this thesis. I am indebted to my many of my colleagues who have offered me guidance and generally useful discussions throughout my research and thesis writing, these include Scott King, Dr Thomas Partridge, Stephen Day, Andrew Tatton, Prof. Ray Dupree, Dr Simon Orr, Dr Lindsay Cahill, Dr Nathan Barrow, Dr Jonathan Bradley, Prof. Steven Brown, Dr Dinu Iuga, Dr Kevin Pike and Dr Thomas Kemp.

I am grateful for all the help supplied by my collaborators. At Johnson Matthey the advice supplied from Dr David Thompsett, Dr Jennifer Houghton, Dr Janet Fischer and Dr Geoffrey Spikes was appreciated greatly. Prof. John Wallis and Dr Alberth Lari (Nottingham Trent University) gave me a massive amount of assistance and advice when it came to the organic sections of my thesis; discussions with them both were greatly valued. I am grateful for the high quality labeled apatite samples and knowledge offered by Dr Peter Slater and Dr Alodia Orera from the University of Birmingham.

I would also like to thank my parents, brother, sister and grandparents (past and present) for the support they provided throughout my academic studies. I also express my sincere thanks to Anna whose understanding and zeal for knowledge has



given me a huge amount of lift during rocky times.

Finally, I recognise that this research would not have been possible without the financial backing from the Engineering and Physical Science Research Council (EPSRC), Johnson Matthey and the University of Warwick.

A handwritten signature in black ink, appearing to be 'G. Rees', with a large, sweeping loop at the end.

Gregory J. Rees

# Declarations

I hereby declare that this dissertation entitled **Development of solid state NMR to understand materials involved in catalytic technology used in fuel cells** is an original work and has not been submitted for a degree or diploma or other qualification at any other University.

Results from other authors are referenced in the usual manner throughout the text. All collaborative results are indicated in the text along with the nature and extent of my individual contribution, a brief summary is given here:

In the chapter 4 all the samples were supplied and synthesised by partners at Johnson Matthey Technology Centre, UK. Johnson Matthey's in house analysis facilities supplied the X-ray diffraction results.

In the chapter 5 the samples were synthesised by Dr. Alodia Orera and Dr. Peter Slater at the University of Birmingham, the published density functional theory calculations in reference [1] by Dr. Pooja Panchmatia were duplicated in our laboratory to give greater accuracy and were simulated by myself.

All samples and X-ray diffraction present in chapter 6 were supplied by collaborators Dr. Alberth Lari and Prof. John Wallis from Nottingham Trent University.

# Abstract

The utility of the little used Field Sweep Fourier transform (FSFT) method is demonstrated for recording wideline nuclear magnetic resonance (NMR) of  $^{195}\text{Pt}$  resonances for various sized platinum nanoparticles, as well as platinum-tin bimetallics used in fuel cell catalysts, and various other related platinum ( $\text{Pt}_3\text{X}$ ;  $\text{X} = \text{Al}, \text{Sc}, \text{Nb}, \text{Ti}, \text{Hf}$  and  $\text{Zr}$ ) alloys. The lineshapes observed from  $\text{PtSn}$  for both  $^{195}\text{Pt}$  and  $^{119}\text{Sn}$  suggest that it is more ordered than other closely related intermetallics, which might be expected from other measurements (e.g. XRD linewidths). From these reconstructed spectra the mean number of platinum atoms in the nanoparticle can be accurately determined along with detailed information regarding the number of atoms present effectively in each layer from the surface. This can be compared with theoretical predictions of the number of platinum atoms in these various layers for cubo-octahedral nanoparticles, thereby providing an estimate of the particle size. A comparison of the common NMR techniques used to acquire wideline spectra from spin  $I = \frac{1}{2}$  nuclei shows the advantages of the automated FSFT technique over the spin echo height/integration approach that dominates the literature. A study of small 13 atom platinum clusters, with variable particle size dispersion for which there is no experimental characterisation in the literature, provides evidence for an isotropic chemical shift of these platinum nanoparticles and provides a better basis for determining the Knight shift when compared to referencing against the primary IUPAC standard which has a different local structure.

Rare earth apatite oxide ion conductors are novel candidates for electrolytes in solid oxide fuel cells. It has been shown that  $\text{La}_8\text{Y}_2\text{Ge}_6\text{O}_{27}$  is an excellent oxide

conductor at lower temperatures when compared to the market leader yttrium stabilised zirconia (YSZ). To understand the mechanism of its conduction  $^{17}\text{O}$ -labelled water was allowed to conduct through the sample and  $^{17}\text{O}$  solid state NMR was employed to comment on this pathway in a series of germanium and silicon substituted apatites. The linear channels running through the centre of the structure were believed to contain vacancies and as with perovskites it was commonly believed these allowed hopping of the oxygen to enable the apatite to conduct. It was shown that a limited amount of the  $^{17}\text{O}$ -oxygens made it to the channel and almost all of the label was located in the tetrahedra. This suggested that the mechanism of conduction was via the tetrahedral backbone. Molecular dynamics studies on these systems confirmed this  $S_N2$  mechanism of conduction as the excess oxygen hopped onto the tetrahedral site to form a five coordinate bridging oxygen which then forced a neighbouring oxygen to hop onto another tetrahedra.

A comparison of analytical techniques used to characterise hydrogen bonding in benzoic acid and its corresponding group IA hemibenzoates indicates the need to draw upon multiple methods to fully understand the nature of the bond. The X-ray diffraction (XRD) data cannot confirm precisely the position of the hydrogen in the complex and hence cannot comment on the nature of the bond. Traditionally the angle at the central bonded proton and the oxygen-oxygen bond distance are used to comment on the strength of the hydrogen bonding, the results present here show the limitations of these analysis methods. Due to the oxygen-proton-oxygen bond angle variations commenting on the oxygen-oxygen length and correlating it to the hydrogen bonding is not feasible. There is heavy literature present on correlating the  $^1\text{H}$  isotropic shifts to the hydrogen bond strength, here we show a step wise change in hydrogen bonding from benzoic acid and lithium hemibenzoate down the periodic table to potassium, rubidium and cesium hemibenzoate. We show that the anisotropic tensor,  $\delta_{22}$ , is pointed along the carbonyl bond and changes with the hydrogen bonding strength. However this method of characterising the bonding interaction gives a linear correlation from benzoic acid to cesium hemibenzoate. The  $^{17}\text{O}$  MAS of the carbonyl groups show an inflated quadrupole coupling constant

when compared to the hydroxyls. There is a correlation between the anisotropic  $^{13}\text{C}$   $\delta_{22}$  parameter and the quadrupole coupling ( $C_Q$ ), as the  $\delta_{22}$  decreases the  $C_Q$  seems to give an overall increase. These oxygen results have been confirmed by multiple field double rotation results. All the crystallographic and solid state NMR data present is tied together by density functional theory calculations which show varying degrees of agreement with the achieved results.

# Abbreviations

<b>3Q</b>	Triple Quantum
<b>BZA</b>	Benzoic Acid
<b>CG</b>	Centre of Gravity
<b>CIF</b>	Crystallographic Information File
<b>CP</b>	Cross Polarisation
<b>CPMG</b>	Carr Purcell Meiboom Gill
<b>CS</b>	Chemical Shift
<b>CSA</b>	Chemical Shift Anisotropy
<b>CT</b>	Central Transition
<b>DAS</b>	Dynamic Angle Spinning
<b>DFT</b>	Density Functional Theory
<b>DOR</b>	Double Rotation
<b>DQ</b>	Double Quantum
<b>EFG</b>	Electric Field Gradient
<b>EM</b>	Electromagnetic
<b>EMF</b>	Electromotive Force
<b>FAM</b>	Fast Amplitude Modulation
<b>FID</b>	Free Induction Decay
<b>FSFT</b>	Field Sweep Fourier Transform
<b>FT</b>	Fourier Transform
<b>GC</b>	Gas Chromatography
<b>HB</b>	Hemibenzoate
<b>Hz</b>	Hertz

<b>IR</b>	Infra-Red Spectroscopy
<b>Iso</b>	Isotropic Shift
<b>IUPAC</b>	International Union of Pure and Applied Chemistry
<b>MAS</b>	Magic Angle Spinning
<b>MQ</b>	Multiple Quantum
<b>MQMAS</b>	Multiple Quantum Magic Angle Spinning
<b>MS</b>	Mass Spectrometry
<b>NMR</b>	Nuclear Magnetic Resonance
<b>NPD</b>	Neutron Powder Diffraction
<b>PAS</b>	Principal Axis System
<b>PEM</b>	Proton Exchange Membrane Fuel Cell
<b>ppm</b>	Parts Per Million
<b>QCPMG</b>	Quadrupolar Carr Purcell Meiboom Gill
<b>QIS</b>	Quadrupolar Induced Shift
<b>RAPT</b>	Rotor-Assisted Population Transfer
<b>RF</b>	Radio Frequency
<b>S/N</b>	Signal-to-Noise
<b>SEHS</b>	Spin Echo Height Spectroscopy
<b>SEIS</b>	Spin Echo Integration Spectroscopy
<b>SEM</b>	Scanning Electron Microscopy
<b>SOFC</b>	Solid Oxide Fuel Cell
<b>SQ</b>	Single Quantum
<b>SSNMR</b>	Solid State Nuclear Magnetic Resonance
<b>STMAS</b>	Satellite Transition Magic Angle Spinning
<b>TEM</b>	Transmission Electron Microscopy
<b>VAS</b>	Variable Angle Spinning
<b>VOCS</b>	Variable Offset Cumulative Spectroscopy
<b>WURST</b>	Wideband, Uniform Rate, and Smooth Truncation
<b>XRD</b>	X-Ray Diffraction
<b>YSZ</b>	Yttrium Stabilised Zirconia

# Chapter 1

## Historical Context & Motivation

### 1.1 The History of NMR

As with all history the beginning of nuclear magnetic resonance (NMR) cannot be traced to a single point in time. Every development, every discovery and every experiment can be traced back to some fundamental piece of physics that was discovered years, decades or even centuries before. A major discovery which aided the discovery of NMR was the concept of spin as a quantum mechanical entity. Below is a discussion of many of the key discoveries and ideas which have been utilised in this thesis for understanding NMR in its application to a range of molecules to provide an insight into their structure.

#### 1.1.1 In the Beginning, 1920s - 1960s

In the 1920s a phenomena which could not be explained by classical Newtonian physics suddenly had reasoning with the development of Bohr <sup>1</sup> quantum mechanics. [2–4] The experiment which heralded the acceptance of quantum mechanics was the existence of discrete lines in the absorption and emission spectra of atoms, the spacings of these lines could not be explained quantitatively. As the spectral resolution of the instrumentation increased however there were some observations made which cast doubt on Bohr quantum mechanics. The observation was that these spectral lines formed doublets which were packed tightly together.

In 1925, Uhlenbeck and Goudsmit <sup>2</sup> introduced the concept of the electrons in an atom spinning, with angular momentum given as  $\frac{1}{2}\hbar$  and arising from this a magnetic dipole moment was determined. [5] A year later, the Schrödinger -



Heisenberg <sup>3</sup> interpretation of quantum mechanics replaced the Bohr theory as a more satisfactory explanation for many of the observed phenomena. [6, 7] Pauli and Darwin, <sup>4</sup> in 1927 developed a framework for grafting the electrons spin onto this formulation of new quantum mechanics. [8] The following year, Dirac <sup>5</sup> gave a relativistic view of quantum mechanics, which showed a fourth quantum number is required, this was the electron spin. [9] The final discovery of interest from the 1920s was made by Dennison, <sup>6</sup> he proposed that the protons would also have spin. He used an example of hydrogen ( $H_2$ ) which would have two proton spins orientated parallel and anti-parallel towards each other. [10, 11] It was commonly believed at the time that protons and electrons made up the atoms nucleus, the discovery of neutrons in 1932 changed this. Work in the 20s by Stern and Gerlach <sup>7</sup> and later in the 30s by Rabi <sup>8</sup> to measure the magnetic moment of hydrogen using magnets to deflect molecular beams confirmed quantum theory and showed that nuclear and electron spins contributed towards the magnetic moments. [8] This work continued with resonance methods until the beginning of the Second World War and is largely considered the first nuclear magnetic resonance experiments using molecular beams. [12, 13]

NMR in bulk materials was first attempted by Gorter in 1936 <sup>9</sup>, he used a sweepable 1.4 T magnet with a large  $B_1$  field of 1 mT to observe temperature changes in LiF, he expected a 0.3 degree Celsius change in temperature at 20 K, he observed nothing. [14] After the Second World War in MIT, Edward Purcell (who was not aware of Gorter's experiments) took up the challenge of observing NMR in bulk materials. Across Cambridge (Boston, MA) in Harvard, Felix Bloch was thinking about how to use NMR on bulk materials to measure magnetic fields and make precise measurements of the magnetic moments on neutrons. Purcell posed the question of whether it was possible to detect transitions between nuclear magnetic energy levels to his then supervisor Henry Torrey; Torrey calculated the energies required and decide it was feasible as a side project. The only stable magnet capable for this work was across Cambridge in Harvard, hence the first NMR experiment was completed by three MIT employed staff at Harvard university. Early theoretical work proceeded on spin-lattice relaxation times along with magnetic dipole interactions, this was completed to give an idea of the repetition rate of the experiment. On Thursday 13th December 1945 they filled the Harvard magnet with paraffin wax and attempted to observe a resonance, they failed. On the following Saturday, they raised the magnetic field to its maximum value (100 A) and found the resonance they were looking for. [15, 16] The work was published in *Physical Review* in January 1946.[17]

Bloch moved to Stanford in 1945 and began their NMR experiments around the time Purcell's work was being published. Bloch presumed, just like Purcell, that spin-lattice relaxation time could be days, whilst the dipole-dipole relaxation time due to motion was rapid. The experience at Stanford was almost a repeat of that in Harvard as magnet strength used was not accurate. Only when Bloch decided to increase the field a weak signal was observed. Although Bloch's work was second to that of Purcell, Bloch was able to explain everything he saw, his work was published in the same journal a month later. The Nobel prize committee noted that the two discoveries were independent and awarded them both the Nobel prize in 1952 'for their development of new methods for nuclear magnetic precision measurements and discoveries in connection therewith'. [18, 19]

Bloch was the first to exploit this method, in July of the same year he submitted two long papers to the same journal, one discussing the theory and the second discussing the experimental arrangement. These papers popularized the technique amongst the physics community and led Russel Varian to create Varian Associates. This was quite a gamble by Varian as he had only the work of Bloch to go by. [18, 19]

The first University outside of MIT/Harvard and Stanford to attempt NMR was the University of Illinois, here Herbert Gutowsky, Erwin Hahn and Charles Slichter had gathered. Each of these three made a considerable investment into NMR; Gutowsky's pioneering work on chemical shift effects and was the first person to apply NMR to structural problems from chemistry, Hahn was to discover the spin echo experiment and be the first to use radio-frequency pulses and Slichter is considered by many the first person to explain  $J$ -coupling. [20–22] In 1948 Raymond Andrew moved to Purcell's group to undertake a post-doc position. Moving back to the University of Wales (Bangor) he created his own permanent NMR magnet and become the first person to implement magic angle spinning (MAS). [23, 24] Anatole Abragam began a career in NMR in 1950s (Saclay, Paris), he would later publish '*The Principles of Nuclear Magnetism*;' amongst the French scientific community it became irreverently known as 'the bible.' [25] Before the discovery of the chemical shift, Walter Knight had discovered that many metals appeared shifted from similar non conducting samples, arguably he had discovered both the Knight shift and the chemical shift at the time. However, as this shift was deemed an effect of the conduction electrons he only gained credit for the shift which is named after him. [26] A year later Pound became the first person to propose the nuclear quadrupole moment at the nucleus. [27] Finally in 1952, Varian finally produced its first commercially available spectrometer which was purchased by the Humble Oil Company.

All these rapid developments across USA, UK and France had sowed the seeds for further NMR research over the next fifty years. [28]

### 1.1.2 Modern Day NMR, 1960s - Present Day

By 1960 NMR had proven its worth in chemical analysis and structural characterisation, it was key that NMR gave data which could be more readily interpreted than other spectroscopic techniques. Yet, NMR remained a tool only used by specialists who could master idiosyncrasies of large complicated instrumentation.

A key development for solid state NMR in 1960 which was deduced by Sven Hartmann and Erwin Hahn was a way of transferring polarization from one nuclear species to another, even though their precession frequencies are quite different. [29] The coupled spins in rotating fields obey a relation called the Hartmann-Hahn coefficient, even though their precession inside a static field are wide apart. This produced cross polarization pulse sequences and heralded an opportunity for solid state NMR spectroscopists to study nuclei with low natural abundance as with  $^{13}\text{C}$  (1.1 % abundant).

Alex Pines group at Berkeley became particularly prominent at line narrowing methods for quadrupolar nuclei. His group utilised high speed MAS along with sampling in synchronisation with this spinning. They managed to dramatically decrease line widths in deuterium samples by this method. He also advanced double angle spinning techniques namely dynamic angle spinning (DAS) and double rotation (DOR), invented by Lipmaa and Samoson, which would narrow the second order quadrupolar effects. [30] This work came from the original theory by Llor and Virlet and from experiments conducted by Eric Oldfield, who would spin quadrupolar nuclei off angle. [31]

Multinuclear NMR now came into focus with the range of solid state line narrowing techniques. Natural abundance  $^{17}\text{O}$  was first observed by Alder and Yu in 1951, however it took a few years before chemical shifts were truly investigated. [32] Its significant shift range of over 1200 ppm has proved popular for many studies on hydrogen bonding,  $\pi$  stacking and correlations to metal atoms. Eric Oldfield was once again prominent in this area producing a large amount of work on oxygen studies of aluminosilicates including zeolites, proteins and super conductors.

The  $^{195}\text{Pt}$  nucleus is one of the easiest heavy metals to observe in NMR and was initially detected by Proto and Yu; they measured the magnetic moment of the now accepted reference  $\text{H}_2\text{PtCl}_6$ . [33] Little else was done until the 1960s when Pidcock and co workers studied several platinum compounds and related the chemical shift to its bonding characteristics. The invention of Fourier transform

NMR in the 1970s meant platinum studies became more favourable and Pregosin managed to show that platinum has massive coupling constants of up to 30 kHz. [34, 35]

Another significant leap forward in NMR resolution was the advent of 2D NMR which was credited to Ernst and Jeener. Richard Robert Ernst won the Nobel Prize Chemistry 1991 for his work on 2D NMR and Fourier Transform techniques in NMR during 1974. Ernst's earliest NMR spectroscopy paper explained all the various phase, coherence pathways and lineshape considerations required to complete a 2D experiment. The possibility of exciting and detecting multiple quantum transitions was also addressed. [36–38] With many 2D experiments now conceived for spin- $\frac{1}{2}$  nuclei and application to quadrupolar nuclei was finally invented by Frydman and Harwood, it was called multiple quantum magic angle spinning (MQMAS). Instead of trying to remove the second-order effects, as with DOR, they instead refocused it into the second dimension. Upon shearing this spectra an isotropic 1D dataset was observed without any 2nd order broadening. [39]

Present day solid state NMR is generally split into two groups which have a certain degree of overlap. The first major group relies on the development of pulse programs usually on model systems, whilst the second group is dominated by solving the structures of complicated samples ranging from proteins to metals. The purpose of this thesis is to apply already developed techniques towards commercial catalysts which have structural ambiguity with the aim to understand their structure and hence improve their overall properties.

## 1.2 Motivation

Heterogeneous catalysts are vital in various production processes such as the Fischer-Tropsch, energy processing in catalytic convertors and petro-chemical cracking processes. The word catalyst comes from the Greek to 'annul' or 'to unite'. Fuel cells use these catalysts to lower the activation energy of REDOX reactions which in turn produced energy in the form of electrical current. The aim of this thesis is to complete a study on two types of these fuel cells; high temperature solid oxide fuel cells (SOFC) which are being utilised for industrial and housing power needs and catalysts used in proton exchange membranes (PEM) or direct ethanol fuel cells (DEFC). The overall aim is to understand these catalyst structures which will help in understanding their function and hopefully improve their efficiencies, cost and operating temperatures.

### 1.2.1 Why NMR Of Catalysts

Many of the catalysts featured in this thesis have unfavourable NMR properties and hence studies on them present in the literature are few and far between. Another reason for them being so under analysed is the commercial significance of these samples means companies are reluctant to publish work that may give their competitors an edge.

The motivation behind the PEM/DEFC project is to address the issue of expense; one of the central components in many fuel cells is the precious metal electrodes which are very expensive, such that their longevity and high expense often limit fuel cell economics. These precious metal catalysts are found dispersed in nanoparticle form along membrane layers, the structure and size of these particles have implications on the cost and activity of the cell. Due to synthetic constraints they are usually found in a highly disordered form meaning probing them by commonly implemented analysis techniques (XRD, TEM, etc) can be difficult.

Platinum based catalysts have been used for these low temperature fuel cells and alloying these with other *d*-block metals has given increased stability, activity and decreased precious metal content (expense). These have been utilised for various catalytic processes from fuel cells to increasing the half-life of banana shipments. This has led to the advancement of core-shell materials in which the cheaper metal is used to effectively create a nanoparticle which is then coated in the active more costly precious metal. Structural characterisation of these formulations has been left behind by the synthesis due to difficulties with disorder and limitations of many analysis techniques. The overall aim of this work is to test the suitability of solid state NMR to these alloys and to harvest structural information that can be achieved from spectra obtained.

Tubular solid oxide fuel cells (SOFC) are a major candidate for green household and industrial power, however they suffer from some serious disadvantages which need to be addressed before large scale commercialisation takes place. They have high efficiencies (80 %) but to get these benefits they have operating temperatures greater than 700+ K; this means they have very long start up times. The high operating temperatures offers opportunities for internal water heating, however the long start up times (hours although thermal expansion processes can turn this into minutes) are not desirable. To understand these processes it is often beneficial to have an appreciation of the conduction mechanism used in the electrolyte. The motivation of this project was to use labelled oxygen to follow the conduction in the SOFC. If this conduction process is fully understood then increasing it can be modelled and lead to lower temperature SOFCs.

### 1.2.2 Why NMR on Tight Hydrogen Bonds

Hydrogen bonds exist in two forms, very general, weak hydrogens bonds are known and understood from biological samples. Much work has taken place to develop methods to study these systems and to understand protein folding.

The second type of hydrogen bond are not normally found in nature, these are tight bonds in which the hydrogen is effectively disowned and rehomed by both neighbours simultaneously. To locate the exact position of these protons is difficult as they generally do not form well defined crystals and XRD fails to give exact proton coordinates. In this section of the thesis we aim to use multinuclear NMR to study these bond formations in benzoic acid species which are cojoined to group one alkali earth metals.

The motivation is to understand these interactions in small systems; as these will become scaled giving many different aromatic rings (possible catalytic and photolytic properties) then using common carbon and proton NMR becomes very difficult in the solid state. However, as the sample is a salt and contains alkali earth metals and oxygen these tend to have larger chemical shift ranges and are hence more desirable to study in the solid state. For these reasons it is important to study all the nuclei (including the carbon and proton) in these model systems to understand these tight hydrogen bonds and draw conclusions which can be applied to the oxygen and metal sites.

# Chapter 2

## Introduction to Solid State Nuclear Magnetic Resonance

### 2.1 Background

Nuclear magnetic resonance (NMR) is a spectroscopic technique concerned with the transition between energy levels which is governed by the Planck equation ( $\Delta U = U_1 - U_2 = hv$ ). When the difference in energy levels is equal to the incoming photon, a transition between the energy levels can occur. The transition can then be effectively observed in the form of a spectrum.

The focus of this chapter is to explain the underlying theory behind many of the observations made in the Result Sections and to give an overview of all the major interactions present in NMR spectra encountered in this thesis.

### 2.2 Angular Momentum

At a fundamental level all NMR active nuclei are known to possess two intrinsic properties charge and spin ( $I$ ). A nuclear magnetic resonance relies on  $I$ , which possess angular momentum, being present. The spin arises from a nucleus having an inequality of protons and neutrons at its nucleus and can be quantified by:

$$\hat{\mu} = \gamma \hat{I} \tag{2.1}$$

The gyromagnetic ratio,  $\gamma$ , is the characteristic frequency of the nucleus. In both classical and quantum equations angular momentum is conserved, where in the quantum state it is present as  $\hbar$ . This means nuclei with the given spin  $I$  can have  $2I + 1$  differing orientations, with the smallest possible  $I = \frac{1}{2}$  as the difference

between the spin up and down states is proportional to  $\hbar$ . In the absence of a magnetic field the energy levels are degenerate. [40]<sup>1</sup>

## 2.3 Interactions

In a NMR experiment an observation is made of how the spins behave under a radio frequency (*rf*) pulse and periods of free evolution. The evolution of the state vector with time depends on the Hamiltonian of the structure. The appearance of the operator details the interactions present in the sample. These Hamiltonians consist of individual components, shown below:

$$\hat{\mathcal{H}}_{total} = \hat{\mathcal{H}}_Z + \hat{\mathcal{H}}_{RF} + \hat{\mathcal{H}}_{CS} + \hat{\mathcal{H}}_D + \hat{\mathcal{H}}_{scalar} + \hat{\mathcal{H}}_{quad}^{(1)(2)} + \hat{\mathcal{H}}_P + \hat{\mathcal{H}}_{KS} \quad (2.2)$$

Where  $\hat{\mathcal{H}}_D$  corresponds to a through space spin-spin interaction, this is an axially symmetric traceless tensor which subjugate spin spectra.  $\hat{\mathcal{H}}_{scalar}$  indicates the through bond interactions of spins via the bonding electrons, this is also controlled by the spin-spin contact.  $\hat{\mathcal{H}}_{quad}^{(1)(2)}$  is a communication of the electric field gradient with the nucleus quadrupole moment. The effect on the magnetic field in compounds from the surrounding electrons is determined by  $\hat{\mathcal{H}}_{CS}$ . The Knight shift is due to the conduction electrons in metals. They introduce an effective field at the nuclear centre, due to the orientations of the spins and the conduction electrons in the presence of  $B_0$  (the external magnetic field). The shift comes from two sources, one is the Pauli paramagnetic spin susceptibility, and the other is the *s*-component wave functions at the nucleus; this is depicted with the  $\hat{\mathcal{H}}_{KS}$  shielding in the summarised internal Hamiltonian. The final two Hamiltonians are the interaction known as the Zeeman interaction and the radio frequency pulse which are intrinsic to any nucleus with a spin and angular momentum in the presence of  $B_0$  and  $B_1$  (the applied RF pulse). All of these interactions are discussed in the following paragraphs.

### 2.3.1 Hamiltonians, The Principal Axis System and Frame Rotations

To completely describe a NMR experiment an understanding of rotations between various co-ordinate frames is required. If you evaluate the Hamiltonian of various

---

<sup>1</sup>The Earth's field and internal magnetic fields can also be used remove this degeneracy, these techniques are called zero field NMR or nuclear quadrupole resonance (NQR) respectively



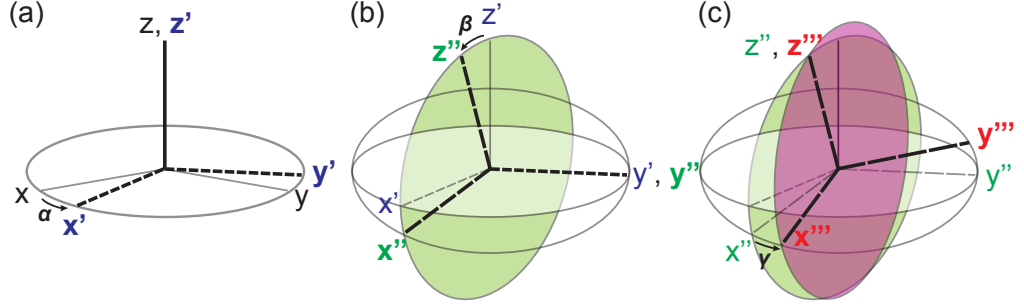


Figure 2.1: The Euler angles ( $\alpha, \beta$  and  $\gamma$ ) describe the rotations about the  $z, y'$  and  $z''$  axis to liberate the final  $x''', y'''$ , and  $z'''$  coordinates.

interactions, explained later, you can thoroughly describe the spin system and hence the resultant NMR spectra. Rotations between various frames are best described using a Hamiltonian which is expressed as a spherical tensor: [41]

$$\hat{\mathcal{H}} = C \sum_l \sum_{m=-l}^{+l} (-1)^{l-m} A_{l,m} \hat{T}_{l,-m} \quad (2.3)$$

The  $A$  and  $T$  tensors here are irreducible spherical tensors representing the spatial and spin components respectively. The limit  $l$  gives the rank of the tensor whilst  $m$  gives its order. Here  $m$  can take  $2m+1$  states with the extremes being  $+m$  and  $-m$ . Many of the discussed interactions have various constants and these have all been bundled together in the term  $C$ . The spin part of the equation is described separately as only the spatial component is directly affected by rotation.

All the Hamiltonians discussed in 2.2 can be specified in a spatial tensor format. For simplicity it is possible to envisage each interaction in a frame where only the diagonal components are observed, this is known as the principal axis system (PAS). It is now desirable to rotate the spatial part of the Hamiltonian tensor  $A^{PAS}$  to the static magnetic fields frame known as the laboratory frame,  $A^{LAB}$ .

Rotations of frames require the specification of the  $\alpha, \beta$  and  $\gamma$  Euler angles. The description below is used by Rose and coworkers and proceeds as follows: [40]

1. Rotation of  $x, y$ , and  $z$ , about the  $z$ -axis through an angle described as  $\alpha$  creates the new coordinates axes named  $x', y'$ , and  $z'$ .
2. The next rotation is made about the  $y'$ -axis through an angle labeled  $\beta$ , this forms the second set of coordinates called  $x'', y''$ , and  $z''$ .

3. The final rotation is made again along the  $z$ -axis through the final angle  $\gamma$ , which liberates the final set of coordinates termed  $x'''$ ,  $y'''$ , and  $z'''$ .

This is illustrated diagrammatically in 2.1. The rotation ( $R$ ) operator  $\hat{R}_z(\alpha)\hat{R}_y(\beta)\hat{R}_y(\gamma)$  is then produced as the product of the three operators, where the  $\hat{R}_z(\alpha)$  term acts first to give:

$$R(\alpha, \beta, \gamma) = \hat{R}_z(\alpha)\hat{R}_y(\beta)\hat{R}_y(\gamma) \quad (2.4)$$

This is equal to:

$$\begin{pmatrix} c_\alpha c_\beta c_\gamma - s_\alpha s_\gamma & -c_\alpha c_\beta c_\gamma - s_\alpha s_\gamma & c_\alpha s_\beta \\ s_\alpha c_\beta c_\gamma + c_\alpha s_\gamma & -s_\alpha c_\beta c_\gamma + c_\alpha s_\gamma & s_\alpha s_\beta \\ -s_\beta c_\gamma & s_\beta s_\gamma & c_\beta \end{pmatrix} \quad (2.5)$$

Where  $c_\theta = \cos \theta$  and  $s_\theta = \sin \theta$ . The  $\hat{R}_z(\alpha)\hat{R}_y(\beta)\hat{R}_y(\gamma)$  represent rotations about the  $z$ ,  $y'$  and  $z''$  axes respectively. The above operator ( $R(\alpha, \beta, \gamma)$ ) can be shown to have a unitary properties such that the operator  $\hat{\Omega}$  would become  $\hat{U}\hat{\Omega}\hat{U}^{-1}$ . As a result of this property you can express  $\hat{R}_\beta$  in the coordinate system of  $\hat{R}_\alpha$ :

$$\hat{R}_\beta = \exp^{-i\beta\hat{I}_{y'}} = \exp^{-i\alpha\hat{I}_z} \exp^{-i\beta\hat{I}_y} \exp^{i\alpha\hat{I}_z} \quad (2.6)$$

This can be combined with similar terms for  $\exp^{-i\beta\hat{I}_{z'}}$  and  $\exp^{-i\beta\hat{I}_{z''}}$  to be expressed as:

$$R(\alpha, \beta, \gamma) = \exp^{-i\alpha\hat{I}_z} \exp^{-i\alpha\hat{I}_y} \exp^{-i\alpha\hat{I}_z} \quad (2.7)$$

We can show that we have three successive Euler rotations each with its own coordinate systems. However, it is also observed that this transformation can be achieved in the same coordinate system, when the order of the rotations are reversed. By keeping the coordinate system constant the rotation can be simplified and expressed with a single matrix, this is known as the Wigner  $D$ -matrix. This can acts on a spherical tensor as follows: [42, 43]

$$\hat{R}(A_{l,m'}) = \sum_{m=-l}^l A_{l,m} D_{m'm}^l \quad (2.8)$$

Here the  $D$ -matrix ( $D_{m'm}^l$ ) is given by:

$$D_{m'm}^l(\alpha, \beta, \gamma) = \exp^{-i\alpha} d_{m'm}^l(\beta) \exp^{-i\gamma} \quad (2.9)$$

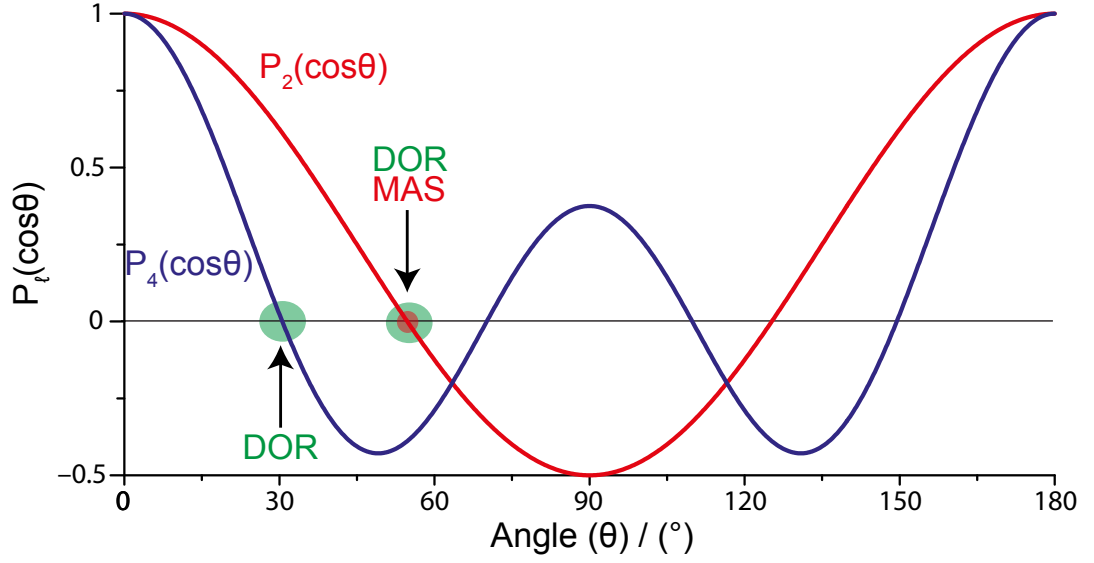


Figure 2.2: The Legendre polynomials for  $l = 2$  and  $4$ . The roots from the magic angle is labeled in red ( $\approx 54.74^\circ$ ) whilst the roots used in double rotation are labeled in green ( $\approx 54.74^\circ$  and  $\approx 30.56^\circ$ ). This diagram is adapted from Nathan Barrows thesis. [44]

Here  $d_{m'm}^l$  is the reduced rotation matrix which is solely dependent on  $\beta$  and its products are usually referenced from previous calculations. In a typical NMR experiment  $m = m' = 0$ , meaning the reduced Wigner matrix is proportional to the Legendre polynomials by: [45]

$$D_{00}^l(\beta) = P_l[\cos(\beta)] \quad (2.10)$$

The angle  $\beta$  (described from here on as  $(\theta)$ ) describes the angle between the frames after transformations. The terms of interest are the relationship between the LAB frame (static magnetic field,  $B_0$ ) and the PAS frame. The terms of  $l$ , of interest during an NMR experiment, are given below:

$$P_0 \cos(\theta) = 1 \quad (2.11)$$

$$P_2 \cos(\theta) = \frac{1}{2}(3 \cos^2(\theta) - 1) \quad (2.12)$$

$$P_4 \cos(\theta) = \frac{1}{8}(35 \cos^4(\theta) - 30 \cos^2(\theta) - 1) \quad (2.13)$$

The significance of the final two equations will be made apparent in the magic angle spinning and double rotation sections of this thesis. The roots of these

equations are shown in figure 2.2.

The coupling Hamiltonians between a nuclear spin and a magnetic field or other spins can be expressed as a contraction of two second rank Cartesian tensors:

$$\hat{\mathcal{H}} = \sum_{k,l=1,2,3} U_{kl} V_{kl} \quad (2.14)$$

Where  $U$  and  $V$  are the second rank Cartesian tensors. From the above equations it has been observed that  $\hat{\mathcal{H}}$  is a rank 0 tensor.

$$V_{kl} = V^0 \delta_{kl} + V_{kl}^a + V_{kl}^s \quad (2.15)$$

which when substituted into equation 2.14 gives:

$$\hat{\mathcal{H}} = 3U^0 V^0 + \sum_{k,l=1,2,3} U_{kl}^a V_{kl}^a + U_{kl}^s V_{kl}^s \quad (2.16)$$

The above equation is decomposed in terms of isotropic, symmetric and antisymmetric rank 2 Cartesian tensors. The process of summing over the indices effectively averages out and eliminates the cross terms between the symmetry types. This can be done by inverting the zero, first and second rank spherical tensors and substituting them back into the above equation.

The determined rank tensors are given, from zero to second order, as: [41]

$$T_{00} = V^0 \quad (2.17)$$

$$T_{10} = V_{12}^a, \quad T_{1\pm 1} = \pm \frac{1}{\sqrt{2}} (V_{23}^a \pm i V_{13}^a) \quad (2.18)$$

$$T_{20} = \sqrt{\frac{3}{2}} V_{33}^s, \quad T_{2\pm 1} = \pm (T_{13}^s \pm i T_{23}^s) \quad (2.19)$$

$$T_{2\pm 2} = \frac{1}{2} (V_1 1 - V_2 2 \pm i 2 V_{12}^s) \quad (2.20)$$

Which when substituted into the previous equation becomes:

$$\hat{\mathcal{H}} = \sum_{l=0}^2 (3-l) \sum_{m=l, l-1, \dots, l} (-)^m T_{l-m}(U) T_{lm}(V) \quad (2.21)$$

Here  $T_{l-m}(U)$  and  $T_{lm}(V)$  represent the irreducible tensors derived from the Cartesian roots  $U$  and  $V$  respectively. It is desirable to re-write this equation to become interaction ( $\gamma$ ) specific and to take into consideration the respected interactions strength ( $\omega_\lambda$ ).

$$\hat{\mathcal{H}}^\lambda = \gamma \sum_{l=0}^2 (3-l) \sum_{m=l, l-1 \dots l} (-)^m T_{l-m}(U) T_{lm}(V) \quad (2.22)$$

The corresponding expressions from the chemical shift, dipolar coupling and the quadrupolar interactions are given in the future sections.

### 2.3.2 Zeeman Interaction

NMR is conducted at a strong magnetic field which has traditionally been defined as the z-axis giving  $B = (0, 0, B_0)$ . The Zeeman interaction is shown to quantize these spins along this vector,  $I_Z = m$ . With the energy of this interaction defined as the Zeeman Hamiltonian: [46]

$$\hat{\mathcal{H}}_Z = -\gamma B_0 I_Z \quad (2.23)$$

where  $\gamma$  is the previously noted gyromagnetic ratio between the magnetic moment,  $\mu$ , and the spin angular momentum defined as  $I$ .

$$\mu = \gamma I \quad (2.24)$$

The strength of this interaction is defined by the precession frequency of the nucleus in the static strong magnetic field  $B_0$ , which is typically five orders of magnitude higher than the Earth's magnetic field:

$$\omega_0 = -\gamma B_0 \quad (2.25)$$

Where  $\omega_0$  is the Larmor frequency given in terms of  $rad s^{-1}$  and the gyromagnetic ratio is measured in  $rad s^{-1} T^{-1}$  and the static magnetic field is usually expressed in Tesla ( $T$ ). Without this strong magnetic field then the spin-up and spin-down states would be degenerate, hence the magnetic field is required to break this degeneracy by a difference of  $\omega_0$ .

Each NMR active isotope's nucleus has a different Larmor frequency since each magnetic moments differ, this allows an NMR experiment to view differing isotopes, which makes the technique a valuable tool in the analysis of materials. However, each isotope's receptivity ( $\Gamma$ ) is proportional to its gyromagnetic ratio, its nuclear spin ( $I$ ) and its natural abundance ( $NA$ ).

$$\Gamma = \gamma^3 \times NA \times I(I+1) \quad (2.26)$$

The receptivity of the isotope governs its responsiveness to NMR and is

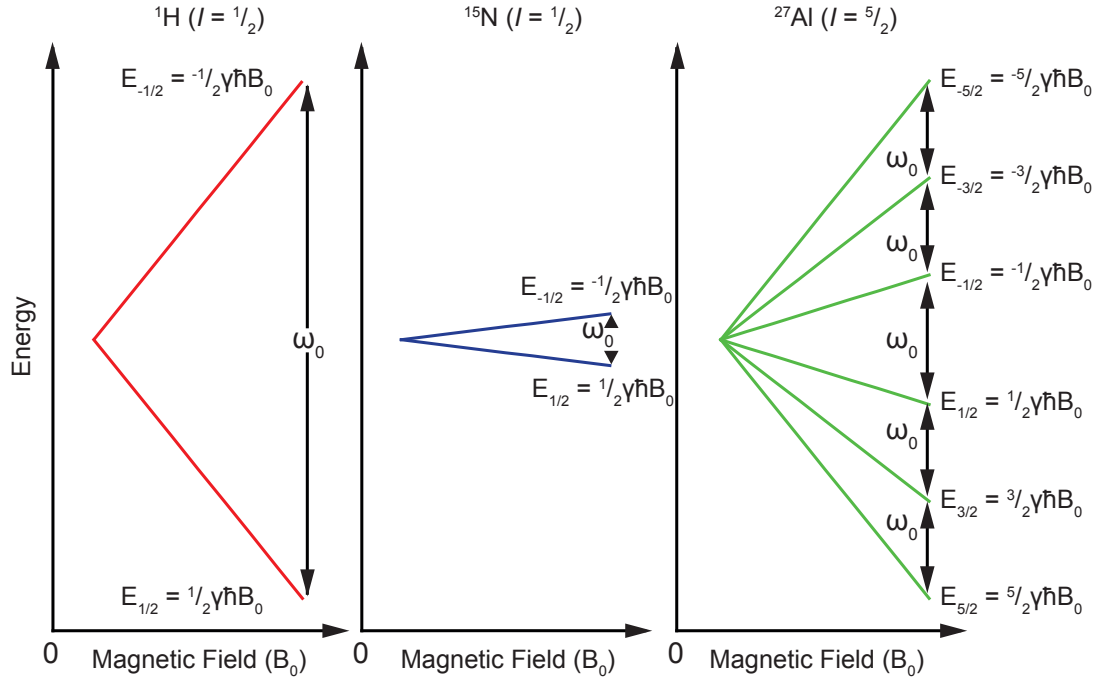


Figure 2.3: The proportional Zeeman splitting for the nuclei  $^1\text{H}$ ,  $^{15}\text{N}$  and  $^{27}\text{Al}$  in an arbitrary incremented magnetic field. Adapted from reference [46]

typically referenced to proton or the significantly less receptive  $^{13}\text{C}$  nucleus (0.00017 with respect to 1.00 for the proton nucleus).

### 2.3.3 Indirect Dipole - Dipole Coupling

The indirect dipole - dipole coupling is often referred to as the  $J$ -coupling, scalar coupling or spin-spin coupling.  $J$ -coupling is the indirect through bond coupling of two nuclear spins caused by the influence on the system's electrons inside a magnetic field. Nuclear spins can interact via their neighbouring electrons to perturb the Hamiltonian of a local through space nuclear spin. [47]

The full Hamiltonian for the  $J$ -coupling term between two spins labeled  $I$  and  $S$  is given as:

$$\hat{\mathcal{H}}_J = 2\pi \hat{I} \cdot J_{IS} \cdot \hat{S} \quad (2.27)$$

Where  $J_{IS}$  is the second rank tensor and the only nuclear spin interaction given generally in the unit of Hz; this can be larger for some samples such as tin and platinum (in the order of kHz). Another point to note is that the  $J$ -coupling does not scale with field as there is no dependence on induced currents. In a liquid

the  $J_{IS}$  term is averaged to its isotropic form making the  $J$ -coupling a scalar which is equal to its average diagonal elements: [46, 48]

$$J_{IS} = \frac{1}{3}(J_{xx} + J_{yy} + J_{zz}) \quad (2.28)$$

The anisotropic part of the  $J$ -coupling tensor has the same form as the dipolar coupling interaction, however it is usually smaller making deconvolution of the interactions very difficult. For the purpose of this thesis the  $J$ -coupling interactions (isotropic and anisotropic) tend to be so small they are ignored.

### 2.3.4 Dipolar Coupling

The dipolar coupling is heavily used in NMR as it can be used to give distance information between spins. This has been universally explained by the analogue of two bar magnets near each other, when you move one the other tries to correct itself to minimise the energy. It is possible to describe this in a classical expression which can be combined with the quantum mechanical magnetic moment ( $\mu$ ) to produce the dipolar Hamiltonian displayed below: [49]

$$\hat{\mathcal{H}}_D = -\frac{\mu_0}{4\pi} \frac{\hbar\gamma_I\gamma_S}{r^3} \left( \hat{I} \cdot \hat{S} - \frac{3(\hat{I} \cdot r)(\hat{S} \cdot r)}{r^2} \right) \quad (2.29)$$

Here the gyromagnetic ratios of the two spin system  $I$  and  $S$  are represented by  $\gamma_I$  and  $\gamma_S$  respectively. The 'strength' of this interaction is dependent on the distance between the two spins, hence it is possible to determine the distance between two spins if the dipolar coupling terms can be isolated. To complete this a dipole-dipole coupling ( $b_{jk}$ ) constant, between two spins  $j$  and  $k$ , is required to be defined.

$$b_{jk} = -\frac{\mu_0}{4\pi} \frac{\hbar\gamma_I\gamma_S}{r^3} \quad (2.30)$$

When converted into the PAS frame, the spatial term does not commute to zero, leaving the following Hamiltonian:

$$\hat{\mathcal{H}}_D^{PAS} = A_{20}^{PAS} \hat{T}_{20}^{PAS} \quad (2.31)$$

Here the spatial term is proportional to:

$$A_{20}^{PAS} = \sqrt{6}b_{jk} \quad (2.32)$$

With the corresponding spherical tensor giving:

$$\hat{T}_{20}^{PAS} = \frac{1}{\sqrt{6}}(3\hat{I}_Z\hat{S}_Z - \hat{I}_Z \cdot \hat{S}_Z) \quad (2.33)$$

When rotated into the LAB frame using a single rotation matrix ( $D_{00}^2$ ), which creates the Legendre polynomial, the final dipolar Hamiltonian becomes:

$$\hat{\mathcal{H}}_D^{LAB} = b_{jk} \frac{1}{2}(3\cos^2\theta - 1)(3\hat{I}_Z\hat{S}_Z - \hat{I}_Z \cdot \hat{S}_Z) \quad (2.34)$$

In the above equation  $\theta$  (see figure 2.7) is the angle between the two spins which may vary between 0 and  $\pi$ . Early experiments on well isolated spins showed that the angular dependence would produce a *Pake doublet*. [50] However, systems with large numbers of interacting spins the end result is usually broadened into a Gaussian/Lorentzian peak. Due to the size of this interaction being comparatively small when observed next the discussed quadrupole and chemical shift components this interaction is not present in any results in this thesis.

### 2.3.5 Chemical Shift

NMR is a widely used technique today due to the ability to detect differing nuclear environments. This was named the chemical shielding and indicates that the exact resonance frequency is sensitive to the chemical environment around a studied nucleus. Chemical shielding is down to a change in the local magnetic field around the nuclei studied, as electrons around these centres produce local magnetic fields. The chemical shift Hamiltonian is best described by: [51]

$$\hat{\mathcal{H}}_{CS} = -\gamma\hbar I \cdot \delta B_0 \quad (2.35)$$

where  $\delta$  is the chemical shift tensor. The chemical shielding tensor is given as  $\sigma$  ( $\delta = -\sigma$ ). It should be noted that the magnetic shielding ( $\sigma$ ) is a tensor property as it depends on the orientation of the molecule with respect to the magnetic field. This becomes apparent during the rotation of a single crystal during a NMR experiment. The magnetic shielding tensor describes the change in magnetic field due to the interaction of the neighbouring electrons with  $B_0$ . This change can produce shielding or deshielding at the nuclear site as the local magnetic field is increased and decreased respectively. This means that the shielding tensor is referenced to the bare nucleus of atom.

This thesis will use the chemical shift,  $\delta_i$ , rather than the shielding tensor,  $\sigma$ , as this is the experimental measurement of the shift against a given standard resonance ( $\sigma_{ref}$ ). However, only the shielding can be measured quantum mechanically



and calculated directly and hence all calculations of shifts are taken by converting the shielding to the shift via a known standard (see Density Functional Theory section for more on this). From the International Union of Pure and Applied Chemistry (IUPAC) guidelines the relationship between the chemical shift and the magnetic shielding is given as: [52]

$$\delta_i = \frac{(\sigma_{ref} - \sigma_i)}{(1 - \sigma_{ref})} \quad (2.36)$$

The references selected in the IUPAC guidelines take into consideration the paramagnetic contribution to the magnetic shielding as well as the molecules centre of mass.

The chemical shift is a second-rank tensor quantity which experimentally is given as a real symmetric 3 x 3 matrix.

$$\begin{pmatrix} \delta_{xx} & \delta_{xy} & \delta_{xz} \\ \delta_{xy} & \delta_{yy} & \delta_{yz} \\ \delta_{xz} & \delta_{yz} & \delta_{zz} \end{pmatrix} \quad (2.37)$$

The observable part of the shift tensor is symmetric with  $\delta_{ij} = \delta_{ji}$ , the six parameters can be measured per observed nucleus. It is experimentally difficult to achieve this due to lack of resolution and the only recorded data of this type in the literature takes place on very large single crystals with established diffraction data. Hence, the emphasis is usually put on the diagonalized form of the tensor equation and the three values that can be measured in powder line shapes are as follows: [53]

$$\begin{pmatrix} \delta_{11} & 0 & 0 \\ 0 & \delta_{22} & 0 \\ 0 & 0 & \delta_{33} \end{pmatrix} \quad (2.38)$$

The three non-zero components of the matrix (the principal components) are defined in a Haeberlen-Mehring-Speiss convention such that  $\delta_{11} \geq \delta_{22} \geq \delta_{33}$ . These components represent the shielding in three orthogonal directions of a Cartesian coordinate system. The orientations of the shielding components with respect to the molecule are lost in the diagonalisation process, therefore the values are ordered serially. In a NMR experiment the  $\delta_{11}$  component of the line represents the least shielded resonances, whilst the  $\delta_{33}$  parameter is the most shielded. The isotropic shift ( $\delta_{iso}$ ) is the average of the three components. The data in this thesis will be

discussed in this format (IUPAC,  $\delta_{11}, \delta_{22}, \delta_{33}$ ) and will be presented in the results as the IUPAC, Haeberlen and Hertzfeld-Berger methods derived below.

In the Hertzfeld-Berger notation, a tensor is described by three parameters, which are combinations of the principal components in the standard notation. The first is the isotropic value, which is as previously discussed, the centre of gravity of the resonance. The span ( $\Omega$ ) describes the maximum width of the powder pattern and finally the skew ( $\kappa$ ) of the tensor is a measure of the degree of the asymmetry of the tensor. Depending on the position of  $\delta_{22}$  with respect to  $\delta_{iso}$ , the sign is either positive or negative. If  $\delta_{22}$  equals  $\delta_{iso}$ , the skew is zero. In the case of an axially symmetric tensor,  $\delta_{22}$  equals either  $\delta_{11}$  or  $\delta_{33}$ . Hence, the skew falls within the range  $\pm 1$ . This method is commonly used by simulation programs (i.e. Quadfit) as it only requires two shifts being known. [54]

$$\delta_{iso} = \frac{(\delta_{11} + \delta_{22} + \delta_{33})}{3} \quad (2.39)$$

$$\Omega = \delta_{11} - \delta_{33}, \quad \Omega > 0, \quad \text{formally} = \frac{\delta_{11} - \delta_{33}}{1 - \sigma_{ref}} \quad (2.40)$$

$$\kappa = \frac{3(\delta_{22} - \delta_{iso})}{\Omega}, \quad 1 \leq \kappa \leq -1 \quad (2.41)$$

The Haeberlen convention uses different combinations of the principal components to describe the line shape. This convention requires that the principal components are ordered according to their separation from the isotropic value. The centre of gravity of the line shape as previously described by the isotropic value, which is the average value of the principal components. The anisotropy and reduced anisotropy describe the largest separation from the centre of gravity. The sign of the anisotropy indicates on which side of the isotropic value one can find the largest separation. The asymmetry parameter indicates by how much the line shape deviates from that of an axially symmetric tensor. In the case of an axially symmetric tensor,  $\Delta\delta = (\delta_{YY} - \delta_{XX})$  will be zero and hence  $\eta = 0$ . [55]

$$\text{Principal Components} = |\delta_{ZZ} - \delta_{iso}| \geq |\delta_{XX} - \delta_{iso}| \geq |\delta_{YY} - \delta_{iso}| \quad (2.42)$$

$$\text{Isotropic Shift, } \delta_{iso} = \frac{(\delta_{11} + \delta_{22} + \delta_{33})}{3} \quad (2.43)$$

$$\text{Reduced Anisotropy, } \delta = \delta_{ZZ} - \delta_{iso} \quad (2.44)$$

$$\text{Anisotropy, } \Delta\delta = \frac{\delta_{ZZ} - (\delta_{XX} + \delta_{YY})}{2}, = \frac{3\delta}{2} \quad (2.45)$$

$$\text{Asymmetry, } \eta = \frac{\delta_{YY} - \delta_{XX}}{\delta}, \quad 1 \leq \eta \leq -1 \quad (2.46)$$

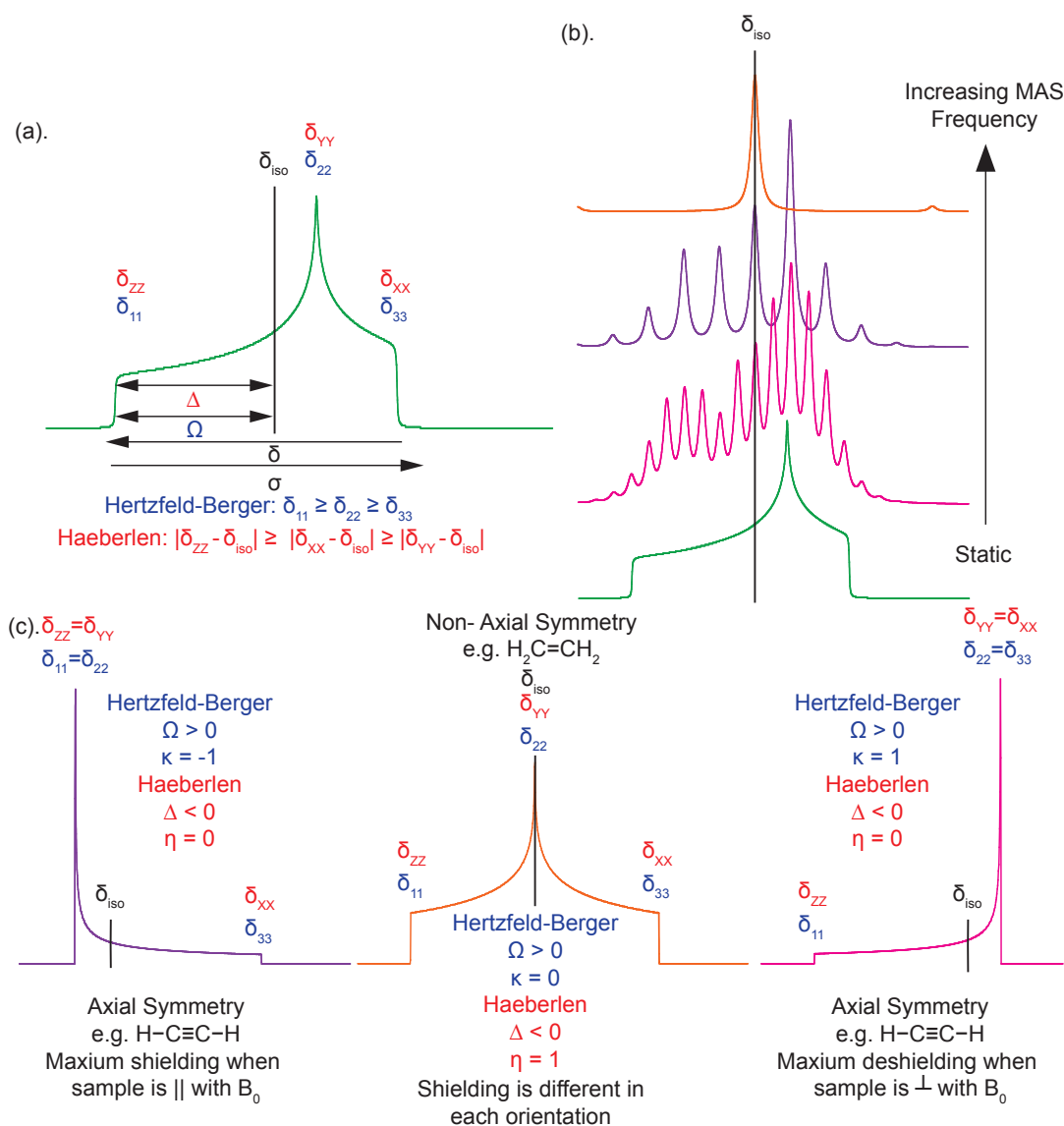


Figure 2.4: Chemical shift anisotropy shielding parameters. (a) shows a typical CSA resonance which is labeled with the shielding parameters. (b) shows the evolution of the line shape at increasing MAS frequencies and (c) shows the line shape product for various symmetries with respect to  $B_0$ .

The previous conventions have been summarised in diagrammatic format in figure 2.4.

### 2.3.6 Quadrupole Interaction

Over two-thirds of the nuclei present in the Periodic Table are quadrupole, meaning they contain a non-spherical nucleus which produces electric quadrupole moment. The coupling of this quadrupole moment to its surrounding electric field gradient is known as the quadrupole interaction.

If a quadrupole nucleus is considered in free space, where  $x$ ,  $y$  and  $z$  axis are equivalent then the Hamiltonian is as follows: [43]

$$\hbar\hat{\mathcal{H}}_Q = \frac{eQ}{6I(2I-1)} \sum_{j,k=x,y,z} V_{jk} \left\{ \frac{3}{2}(I_j I_k + I_k I_j) - \delta_{jk} I(I+1) \right\} \quad (2.47)$$

Here  $V_{jk}$  are the Cartesian components of EFG ( $\mathbf{V}$ ) at the nuclear site, which is given as a second-rank symmetrical tensor.  $I_j$  is operator of the  $J$ -component of the spin,  $I$  is the spin quantum number,  $\delta_{jk}$  is the Kronecker delta. [56]<sup>2</sup>

$$\mathbf{V} = \begin{pmatrix} V_{XX} & 0 & 0 \\ 0 & V_{YY} & 0 \\ 0 & 0 & V_{ZZ} \end{pmatrix} \quad (2.48)$$

where

$$|V_{ZZ}| \geq |V_{YY}| \geq |V_{XX}| \quad (2.49)$$

The Laplace equation ( $\nabla^2\varphi = 0$ ) still holds true for  $\mathbf{V}$  such that  $V_{XX} + V_{YY} + V_{ZZ} = 0$  as the electric field gradient produced by the nucleus is generated by external nuclear charges. This means only two independent parameters remain the  $eq$  and the  $\eta$ , which are given as: [57]

$$eq = V_{ZZ} \quad (2.50)$$

---

<sup>2</sup>Kronecker delta is a function of two variables, usually integers, which is 1 if they are equal and 0 otherwise.

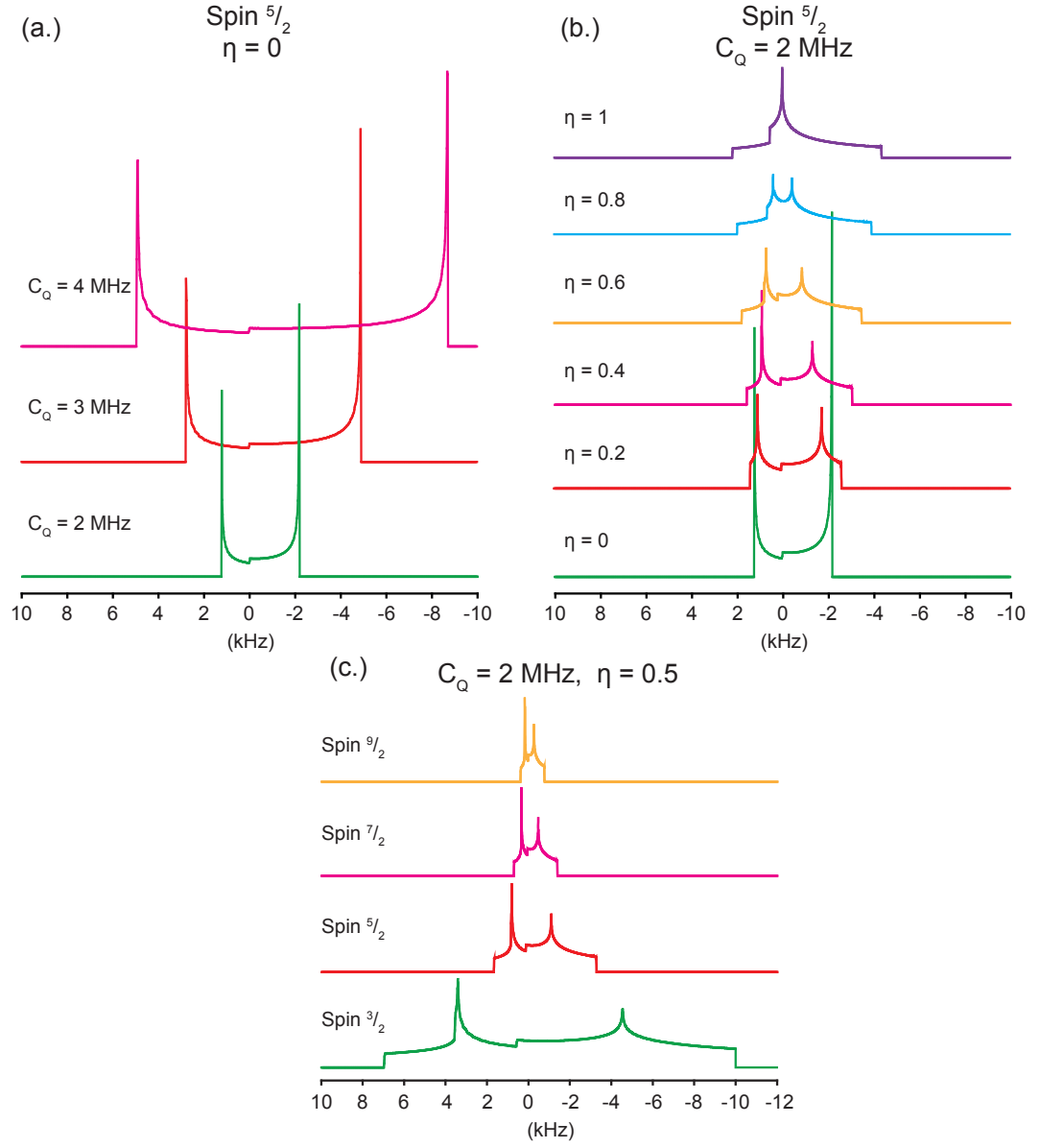


Figure 2.5:  $C_Q$  and  $\eta$ . (a) Shows the evolution of the resonance as the  $C_Q$  increases linearly, (b) shows the how line shape changes for varying  $\eta$  and (c) shows how the scale of the resonance decreases with increasing spin  $I$ .

$$\eta_Q = \frac{V_{XX} - V_{YY}}{V_{ZZ}}, \quad -1 \leq \eta \leq 1 \quad (2.51)$$

As  $V_{ZZ}$  is the largest component of  $\mathbf{V}$  then this only needs to be considered when addressing  $eq$ . In static powder lineshapes obtained during the NMR experiment,  $eq$  describes the width of the line in MHz and  $\eta$  gives the characteristic quadrupolar line shape produced. From this the quadrupolar coupling constant can be arrived at by dividing by Planck's constant, as shown below:

$$Cq = \frac{e^2 q Q}{h} \quad (2.52)$$

When moving from the principal axis system (PAS), with respect to  $\mathbf{V}$  the quadrupole interaction takes the form: [58]

$$\hbar \hat{\mathcal{H}}_Q = \frac{e^2 q Q}{4I(2I-1)} \{3I_Z^2 - I(I+1) + \eta(I_X^2 - I_Y^2)\} \quad (2.53)$$

If the quadrupole interaction of the above proposed free nucleus is now transferred from Cartesian tensor space into a second-rank irreducible spherical tensor then a simplified representation is observed.

$$\hat{\mathcal{H}}_Q = \frac{eQ}{2I(2I-1)\hbar} \sum_{q=-2}^2 (-1)^q V_{(2,-q)} T^{(2,q)} \quad (2.54)$$

also used in the literature is:

$$\hat{\mathcal{H}}_Q = \sqrt{\frac{3}{2}} \frac{eQ}{2I(2I-1)\hbar} \sum_{q=-2}^2 (-1)^q A_{(2,-q)} T^{(2,q)} \quad (2.55)$$

Here  $V(A)_{(2,-q)}$  and  $T^{(2,q)}$  are the spherical tensor representations of  $\mathbf{V}$  and  $\mathbf{T}$ . The relationship between Cartesian coordinates of  $\mathbf{V}$  and  $\mathbf{T}$  and their corresponding spherical coordinates (presuming  $I_+ = I_X + iI_Y$  and  $I_- = I_X - iI_Y$ ) are given by: [59]

$$\mathbf{V}_{(2,0)} = \frac{\sqrt{6}}{2} V_{ZZ} \quad (2.56)$$

$$\mathbf{V}_{(2,1)} = -V_{XZ} - iV_{YZ} \quad (2.57)$$

$$\mathbf{V}_{(2,-1)} = V_{XZ} - iV_{YZ} \quad (2.58)$$

$$\mathbf{V}_{(2,2)} = \frac{1}{2}(V_{XX} - V_{YY}) + iV_{XY} \quad (2.59)$$

$$\mathbf{V}_{(2,-2)} = \frac{1}{2}(V_{XX} - V_{YY}) + iV_{XY} \quad (2.60)$$

$$\mathbf{T}^{(2,0)} = \frac{\sqrt{6}}{6} \{3I_Z^2 - I(I+1)\} \quad (2.61)$$

$$\mathbf{T}^{(2,1)} = -\frac{1}{2}(I_Z I_+ + I_+ I_Z) = -\frac{1}{2} I_+ (2I_Z + 1) \quad (2.62)$$

$$\mathbf{T}^{(2,-1)} = \frac{1}{2}(I_Z I_- + I_- I_Z) = \frac{1}{2} I_- (2I_Z - 1) \quad (2.63)$$

$$\mathbf{T}^{(2,2)} = \frac{1}{2} I_+^2 \quad (2.64)$$

$$\mathbf{T}^{(2,-2)} = \frac{1}{2} I_-^2 \quad (2.65)$$

With these considerations the spherical tensor representation of the quadrupole interaction equation becomes:

$$\begin{aligned} \hat{\mathcal{H}}_Q = \frac{eQ}{2I(2I-1)\hbar} \frac{\sqrt{6}}{6} [3I_Z^2 - I(I+1)] V_{(2,0)} + \frac{1}{2} I_+ (2I_Z + 1) V_{(2,1)} \\ - \frac{1}{2} I_- (2I_Z - 1) V_{(2,-1)} + \frac{1}{2} I_+^2 V_{(2,-2)} + \frac{1}{2} I_-^2 V_{(2,2)} \end{aligned} \quad (2.66)$$

If this result is expressed in terms of the PAS Hamiltonian of the EFG tensor along with equations determined for  $\mathbf{V}$  and  $\mathbf{T}$ , then the following spherical tensor components can be revealed. [58]

$$V_{(2,0)}^{PAS} = \sqrt{\frac{3}{2}} eq \quad (2.67)$$

$$V_{(2,\pm 1)}^{PAS} = 0 \quad (2.68)$$

$$V_{(2,\pm 2)}^{PAS} = \frac{1}{2} eq\eta \quad (2.69)$$

In a high magnetic field the quadrupole interaction effects the Zeeman states, the terms of the above Hamiltonian which commute with  $I_Z$  lead to perturbation of the first order quadrupole coupling.

As previously commented, a nuclear spin possesses a magnetic moment  $\mu$  and an angular momentum  $\hbar I$ . These fundamental parameters are related by the gyro-magnetic ratio  $\gamma$ . In the LAB frame the coupling of this magnetic moment with  $B_0$  is known and previously stated as the Zeeman interaction. The quadrupole Hamiltonian ( $\hat{\mathcal{H}}_Q$ ) can be treated as a weak perturbation on this Zeeman interaction ( $\hat{\mathcal{H}}_Z$ ). For this process to take place it is convenient to make the subject time-dependent which requires converting from the LAB frame to the rotating (OBS) frame.

$$\hbar \hat{\mathcal{H}}_Q(t) = \exp(i\hat{\mathcal{H}}_Z t) \hbar \hat{\mathcal{H}}_Q \exp(-i\hat{\mathcal{H}}_Z t) \quad (2.70)$$

$$\begin{aligned} = & \frac{eQ}{4I(2I-1)} \left\{ \frac{1}{3} \sqrt{6} [3\hat{I}_Z^2 - I(I+1)] V_0 \right. \\ & + \hat{I}_+(2\hat{I}_Z + 1) V_{-1} \exp(-i\omega_0 t) - \hat{I}_-(2\hat{I}_Z - 1) V_1 \exp(i\omega_0 t) \\ & \left. + \hat{I}_+^2 V_{-2} \exp(-i2\omega_0 t) + \hat{I}_-^2 V_2 \exp(i2\omega_0 t) \right\} \quad (2.71) \end{aligned}$$

The secular term remains time-independent and in order to make the equation completely time-independent,  $\hat{\mathcal{H}}_Q(t)$  is averaged over one Larmor period ( $\frac{2\pi}{\omega_0}$ ) up to the first order.

$$\langle \hat{\mathcal{H}}_Q(t) \rangle = \frac{\omega_0}{2\pi} \int_0^{\frac{2\pi}{\omega_0}} dt \hat{\mathcal{H}}_Q(t) - \frac{i\omega_0}{4\pi} \int_0^{\frac{2\pi}{\omega_0}} dt \int_0^t dt' [\hat{\mathcal{H}}_Q(t), \hat{\mathcal{H}}_Q(t')] \quad (2.72)$$

$$= \hat{\mathcal{H}}_Q^{(0)} + H_Q^{(1)} \quad (2.73)$$

As only the secular terms commute with  $I_Z$  and with some simplification  $\hat{\mathcal{H}}_Q^{(0)}$  and  $\hat{\mathcal{H}}_Q^{(1)}$  can be considered as the first ( $\hat{\mathcal{H}}_Q^{[1]}$ ) and the second ( $\hat{\mathcal{H}}_Q^{[2]}$ ) order quadrupole terms.

$$\hat{\mathcal{H}}_Q^{[1]} = \hat{\mathcal{H}}_Q^{(0)} = \frac{eQ}{4I(2I-1)\hbar} \frac{\sqrt{6}}{3} [3\hat{I}_Z^2 - I(I+1)] V_0 \quad (2.74)$$

$$\begin{aligned} \hat{\mathcal{H}}_Q^{[2]} = \hat{\mathcal{H}}_Q^{(1)} = & -\frac{1}{\omega_0} \left[ \frac{eQ}{4I(2I-1)\hbar} \right]^2 \\ & \times (2V_{-1}V_1 I_Z [4I(I+1) - 8\hat{I}_Z^2 - 1] \\ & + 2V_{-2}V_2 I_Z [2I(I+1) - 2\hat{I}_Z^2 - 1]) \quad (2.75) \end{aligned}$$

There are no changes to the above equations when converted from the rotat-



ing frame to the laboratory frame, as they both commute with  $I_Z$ . A more obvious point to note is that  $\hat{\mathcal{H}}_Q^{[1]}$  is independent of  $\omega_0$ , whilst  $\hat{\mathcal{H}}_Q^{[2]}$  is inversely proportional to  $\omega_0$ , therefore at higher magnetic fields there is a reduction in the second order quadrupole term.

The energy levels  $(2I+1)$  of a free spin  $I$  when introduced to a static magnetic field, creating the Zeeman interaction, are defined as  $\langle m | \hat{\mathcal{H}}_Z | m \rangle = -m\omega_0$  with the difference between two neighbouring energy levels  $(m-1, m)$  given with respect to angular velocity as:

$$\omega_{m-1,m}^{(Z)} = \langle m-1 | \hat{\mathcal{H}}_Z | m-1 \rangle - \langle m | \hat{\mathcal{H}}_Z | m \rangle = \omega_0 \quad (2.76)$$

From this basis the first order quadrupole interaction shifts the energy levels by an amount proportional to

$$\langle m | \hat{\mathcal{H}}_Z^{[1]} | m \rangle = \frac{eQ}{4I(2I-1)\hbar} \frac{\sqrt{6}}{3} [3m^2 - 1(I+1)] V_0 \quad (2.77)$$

With the contribution of the line position associated with the transition of  $m-1, m$  being equal to

$$\omega_{m-1,m}^{(1)} = \langle m-1 | \hat{\mathcal{H}}_Z^{[1]} | m-1 \rangle - \langle m | \hat{\mathcal{H}}_Z^{[1]} | m \rangle \quad (2.78)$$

$$= \frac{3eQ}{4I(2I-1)\hbar} \frac{\sqrt{6}}{3} (1-2m) V_0 \quad (2.79)$$

The spectrum conceived from this equation gives  $2I$  lines, a central transition which is represented by the  $-\frac{1}{2}, \frac{1}{2}$  transitions which is located at  $\omega_0$ , with the other  $2I-1$  representing the satellite resonances.

The following line is shifted further when you take into consideration the second order quadrupole interaction: [60]

$$\begin{aligned} \hat{\mathcal{H}}_Q^{[2]} = \hat{\mathcal{H}}_Q^{(1)} = & -\frac{1}{\omega_0} \left[ \frac{eQ}{4I(2I-1)\hbar} \right]^2 \\ & \times (2V_{-1}V_1m[4I(I+1) - 8m^2 - 1] \\ & + 2V_{-2}V_2m[2I(I+1) - 2m^2 - 1]) \end{aligned} \quad (2.80)$$

when expressed in  $\omega_{m-1,m}^{(2)}$  resonance position; the second order quadrupole shift is given as:

$$\omega_{m-1,m}^{(2)} = \langle m-1 | \hat{\mathcal{H}}_Z^{[2]} | m-1 \rangle - \langle m | \hat{\mathcal{H}}_Z^{[2]} | m \rangle \quad (2.81)$$

$$= -\frac{2}{\omega_0} \left[ \frac{eQ}{4I(2I-1)\hbar} \right]^2 \times (V_{-1}V_1[24m(m-1) - 4I(I+1) + 9] + \frac{1}{2}V_{-2}V_2[12m(m-1) - 4I(I+1) + 6]) \quad (2.82)$$

Thus the associated contribution of the first and second order quadrupole interaction is given as:

$$\omega_{m-1,m} = \omega_0 + \omega_{m-1,m}^{(1)} + \omega_{m-1,m}^{(2)} \quad (2.83)$$

In order to produce an equation representative of a static NMR resonance it is required to express the  $V_0$  terms of the above  $\omega_{m-1,m}^{(1)}$  equation and the  $V_1, V_{-1}, V_2$  and  $V_{-2}$  terms of the  $\omega_{m-1,m}^{(2)}$  derivation in the terms of  $\mathbf{V}$  in the principal axis system. Thus, it is required to define the Euler angles in a strong static magnetic field.

$$V_i = \sum_{j=-2}^2 D_{j,i}^{(2)}(\alpha, \beta, \gamma) V_j^{PAS} \quad (2.84)$$

Here the Euler angles ( $\alpha, \beta$  and  $\gamma$ ) describe the direction in the magnetic field ( $\sum^{PAS}$ ).  $D_{j,i}$  is the Wigner rotation matrix defined in the following diagram (see figure 2.6). [61]

Therefore,  $V_0$  is given as:

$$V_0 = \sqrt{\frac{3}{2}}eq \left[ \frac{1}{2}(3 \cos^2 \beta - 1) + \frac{1}{2}\eta \sin^2 \beta \cos 2\alpha \right] \quad (2.85)$$

When this equation is substituted into equation 2.74 yields:

$$\hat{\mathcal{H}}_Q^{[1]} = \frac{1}{3}\omega_Q[3I_Z^2 - I(I+1)] \quad (2.86)$$

with:

$$\omega_Q = \frac{3\chi}{4I(2I-1)} \left[ \frac{1}{2}(3 \cos^2 \beta - 1) + \frac{1}{2}\eta \sin^2 \beta \cos 2\alpha \right] \quad (2.87)$$

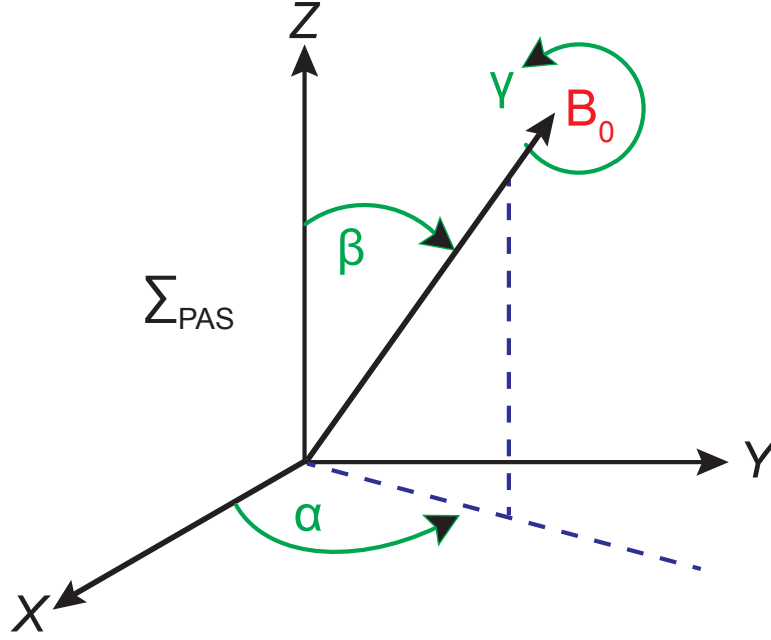


Figure 2.6: The Euler angles defining the direction of  $B_0$  in the PAS of the EFG during a static NMR experiment

Depending on the Euler angle convention used a negative sign can be substituted in front of the  $\eta$  parameter. When reproduced to take into consideration the first order quadrupolar shift of the line as in equation 2.78. [25]

$$\omega_{m-1,m}^{(1)Static} = (1 - 2m)\omega_Q \quad (2.88)$$

The lines in the spectrum will become shifted by the same quantity ( $2\omega_Q$ ) with the central line not being shifted.

The other two factors deduced from equation 2.82 are:

$$\begin{aligned} 2V_1V_{-2} = & -\frac{3}{2}e^2q^2\left[\left(-\frac{1}{3}\eta^2\cos^2 2\alpha + 2\eta\cos 2\alpha - 3\right)\cos^4 \beta \right. \\ & + \left(\frac{2}{3}\eta^2\cos^2 2\alpha - 2\eta\cos 2\alpha - \frac{1}{3}\eta^2 + 3\right)\cos^2 \beta \\ & \left. + \frac{1}{3}\eta^2(1 - \cos^2 2\alpha)\right] \quad (2.89) \end{aligned}$$

$$\begin{aligned}
V_2 V_{-2} = & -\frac{3}{2} e^2 q^2 \left[ \left( \frac{1}{24} \eta^2 \cos^2 2\alpha - \frac{1}{4} \eta \cos 2\alpha + \frac{3}{8} \right) \cos^4 \beta \right. \\
& + \left( -\frac{1}{12} \eta^2 \cos^2 2\alpha + \frac{1}{6} \eta - \frac{3}{8} \eta^2 + 3 \right) \cos^2 \beta \\
& \left. + \frac{1}{24} \cos^2 2\alpha + \frac{1}{4} \eta \cos 2\alpha + \frac{3}{8} \right] \quad (2.90)
\end{aligned}$$

The second order quadrupole shift of the central line is derived from equation 2.82 giving:

$$\begin{aligned}
\omega_{-1/2,1/2}^{(2)Static} = & -\frac{1}{6\omega_0} \left[ \frac{3\chi}{2I(2I-1)} \right]^2 \left[ I(I+1) - \frac{3}{4} \right] \\
& \times [A(\alpha, \eta) \cos^4 \beta + B(\alpha, \eta) \cos^2 \beta + C(\alpha, \eta)] \quad (2.91)
\end{aligned}$$

Here:

$$A(\alpha, \eta) = -\frac{27}{8} + \frac{9}{4} \eta \cos 2\alpha - \frac{3}{8} (\eta \cos 2\alpha)^2 \quad (2.92)$$

$$B(\alpha, \eta) = \frac{30}{8} - \frac{1}{2} \eta^2 - 2\eta \cos 2\alpha + \frac{3}{4} (\eta \cos 2\alpha)^2 \quad (2.93)$$

$$C(\alpha, \eta) = -\frac{3}{8} + \frac{1}{3} \eta^2 - \frac{1}{4} \eta \cos 2\alpha - \frac{3}{8} (\eta \cos 2\alpha)^2 \quad (2.94)$$

When the EFG has axial symmetry at  $\eta = 0$  then the equation simply reduces to:

$$\begin{aligned}
\omega_{-1/2,1/2}^{(2)Static} = & -\frac{1}{16\omega_0} \left[ \frac{3\chi}{2I(2I-1)} \right]^2 \left[ I(I+1) - \frac{3}{4} \right] \\
& \times (1 - \cos^2 \beta)(9 \cos^2 \beta - 1) \quad (2.95)
\end{aligned}$$

It is worth noting that the Euler angle  $\gamma$  is not present in any of the above equations, this is because  $B_0$  is the symmetry axis for the spins. Wolf and co-workers have shown that the third order term is proportional to  $\frac{2m-1}{\omega_0^2}$ , hence the line is not shifted further by the addition of this perturbation. [62]

### 2.3.7 The Knight Shift

The Knight shift, named after its discoverer Walter David Knight, is the relative shift  $K$  in metallic complexes when compared to an equivalent non-metallic surrounding. [26] The Knight shift scales linearly with field,  $B_0$ , and is inversely proportional

to the absolute temperature. In superconductors (at operational temperatures) the shift decreases dramatically as the electron spins pair up to form spin-pair bosons. This is a primary characteristic of a superconducting state. [22]<sup>3</sup>

As conduction electrons in a metal are not uniquely associated with any particular nucleus more than another then they all exist within eigenstates known as a band. The highest occupied state of this band is known as the Fermi energy,  $E_f$  at  $T = 0\text{K}$ . Close to  $E_f$  the electron wavefunctions tend to be dominated by mixtures of  $p$  and  $d$  orbitals whilst at lower energies the  $s$  states are more prevalent. The  $s$ -electrons at the nuclear site have a high probability density ( $R = 0$ ), as each electron contains spin and charge this in turn causes an interaction which produces a local magnetic field. Hence, the Knight shift is caused by the non-localised conduction electrons effectively producing additional shielding at the nuclear site. The conduction electron states occupy a Fermi distribution and due to the Pauli exclusion principle they become occupied pairwise: meaning every energy level will contain a spin up and spin down electron. When a magnetic field is applied, there is an imbalance in this spin up and down distribution causing the Pauli susceptibility and a net magnetization giving a shift in the resonance. The observed shielding term is the sum of the chemical shift and the induced Knight shift ( $K$ ) and as they both scale with field it becomes difficult to separate the components. The total shift of the line is hence described as a percentage of the field: [48]

$$Total\ Shift = Ks + Kd + Kcp + \sigma = K + \sigma \quad (2.96)$$

Where  $Ks$  represents the  $s$ -electron contribution to the shift and  $Kd$  gives the  $d$ -electron involvement, these both give a positive shift as seen in tin metal. If the hyperfine fields of the conduction  $s$ -electrons induce a polarisation in the inner core  $s$ -electrons then a subsequent shift can be produced, this is termed the core polarisation  $Kcp$ . This gives a negative shift as seen in platinum metal. In a two band model of a simple spherical platinum nanoparticle, the contribution from the platinum  $5d$  band is shown to be negative whilst those from the  $6s$  band is positive, the relaxation is proportional to a sum of the squares (i.e.  $Ki^2$ ) and is therefore always positive. The  $d$ -electron contribution is shown to decay exponentially from bulk metal as you move upfield towards the platinum 001 surface. This is discussed at far greater length in the platinum PEM catalyst chapter. [63]

The Knight shift is typically expressed as a percentage with respect to the primary IUPAC reference used for the chemical shift ranges. The limitations of this

---

<sup>3</sup>Charles Slitcher's work in this area is regarded as the first which helped prove BCS theory of superconductivity

method are discussed in the platinum alloys and bimetallics sections of this thesis.

$$K(\%) = \frac{v_{metal} - v_{ref}}{v_{ref}} \times 100 \quad (2.97)$$

If the symmetry of the material is lower than cubic then the full electron-nucleus interaction needs to be considered, hence an anisotropic term is applied to the Knight shift term. The orientation of the principal axes of the shift tensor ( $\Theta, \Phi$ ) with respect to the magnetic field are determined by the following equation: [64]

$$K(\Theta, \Phi) = K_{iso} + K_{ax}(3\cos^2\Theta - 1) + K_{asym} \sin^2\Theta \cos 2\Theta \quad (2.98)$$

Where  $K_{iso}$  is the isotropic component of the Knight shift,  $K_{ax}$  represents the axially symmetrical component and the asymmetric component is determined by the  $K_{asym}$  term. These can be converted into a chemical shift tensor IUPAC conventions highlighted in the previous anisotropic sections.

$$K_{iso} = \frac{1}{3}(K_1 + K_2 + K_3) \quad (2.99)$$

$$K_{ax} = \frac{1}{3}(K_1 - \frac{1}{2}K_2 - \frac{1}{2}K_3) \quad (2.100)$$

$$K_{asym} = \frac{1}{2}(K_2 - K_1) \quad (2.101)$$

As most metals have axial symmetry then  $K_{\parallel} = K_3$  and  $K_{\perp} = K_1 = K_2$  meaning the above equations can be re-written as follows:

$$K_{iso} = \frac{1}{3}(2K_{\perp} + K_{\parallel}) \quad (2.102)$$

$$K_{ax} = \frac{1}{3}(K_{\perp} - K_{\parallel}) \quad (2.103)$$

$$K_{asym} = 0 \quad (2.104)$$

These  $K_{1-3}$  terms can be determined by the deconvolution of peaks and shoulders achieved in the spectra, as explained previously in the anisotropic shift section (2.3.5).

### 2.3.8 The Korringa Relation

The spin-lattice relaxation ( $T_1$ ) in metals proceeds via the Fermi contact interaction with polarised conduction electron spins. This is the same interaction that causes

the above discussed Knight shift. The relationship between the two has been derived by Korringa; where  $T_1$  is directly determined by the electrons above the Fermi level. [65]

$$T_1 K^2 = \frac{\hbar}{4\pi k_B T} \left( \frac{\gamma_e}{\gamma_n} \right)^2 B \quad (2.105)$$

Where  $k_B$  is the Boltzmann constant,  $T$  is the temperature,  $\gamma_e$  and  $\gamma_n$  are the respective gyromagnetic ratios of the electron and nucleus and  $B$  is a constant which is equal to the unity for a metal in which many body effects are neglected. If you consider many body effects than  $B$  is proportional to: [48]

$$B = \left( \frac{\chi^s \rho_0 E_f}{\chi_0^2 \rho E_f} \right)^2 \quad (2.106)$$

Carter *et al.* has shown for platinum that  $B = 6$ , with  $\chi_0^2$  being the electron spin susceptibility,  $\rho_0 E_f$  is the density of state at the Fermi energy,  $\chi^s$  and  $\rho E_f$  are the same except they include many-body effects. [66]

### 2.3.9 Paramagnetic Shift

NMR studies on paramagnetic materials have recently become far more common in the literature with the advent of ultra-fast ( $\geq 40$  kHz) MAS on low field magnets ( $\leq 2.35T$ ). A paramagnetic material is defined by the presence of a localised unpaired electron, which interacts proportionally with an applied magnetic field. [67]

$$\hat{\mathcal{H}}_P = \gamma_1 \hbar I \cdot P \cdot S \quad (2.107)$$

The above equation shows a hyperfine coupling between nucleus  $I$  and electron  $S$ . Paramagnetic coupling can be very strong resulting in the signal being broadened to a level where it is not observable. If the range is manageable a lot of information can be extracted from paramagnetic coupling. The coupling tensor above is dependent on the average component of the electron spin along the magnetic field. There is a  $\frac{1}{T}$  relationship meaning thermal flipping can be utilised to minimize paramagnetic effects, hence variable temperature experiments can confirm whether paramagnetic effects are causing the generally large observed shift.

## 2.4 Magic Angle Spinning

Mechanical sample spinning on the time-scale of the experiment is regularly used in solid state NMR to improve resolution as it supplies a modulation on the anisotropic

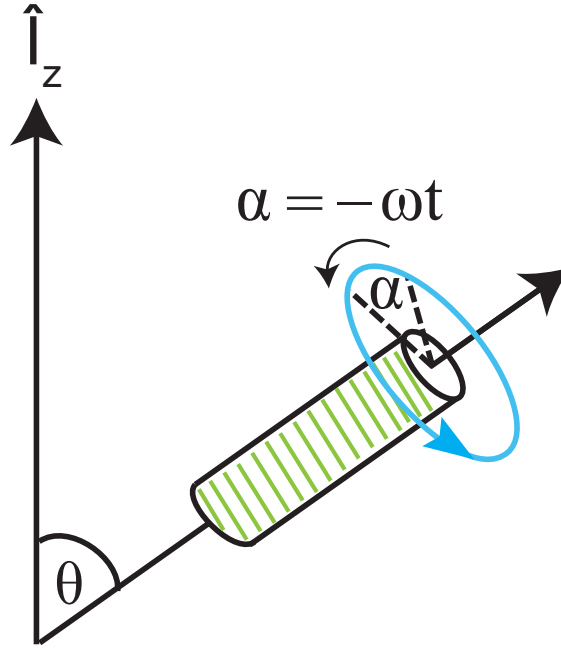


Figure 2.7: A schematic of magic angle spinning experiment showing the rotor inclined and rotated rapidly at angle  $\theta$  with respect to the static magnetic field  $B_0$ .

broadening factors. In most solids there is not enough motion present to narrow the lines sufficiently to gain a resolution enhancement, so MAS was developed by Raymond Andrew and independently by Lowe, to mimic nature and impose motion on the solid sample. [23, 24]

If sufficiently fast spinning rates are achieved, only the isotropic parts of the lineshape should be present as  $P_0 \cos(\beta) = 1$  (figure 2.2). MAS functions by imposing a time dependence on the interactions present in solids.

### 2.4.1 Theory

To describe this technique it is necessary to perform a double frame transformation using the previously discussed Wigner matrices. The first rotation transforms the PAS into the rotating frame and the second transforms this into the LAB frame. This double frame rotation is described by: [68]



$$A(l, n)^L AB = \sum_{m'=-l}^l \sum_{m=-l}^l D_{m'n}^l(\alpha_{RL}, \beta_{RL}, \gamma_{RL}) D_{mm'}^l(\alpha_{PR}, \beta_{PR}, \gamma_{PR}) A_{lm}^{PAS} \quad (2.108)$$

Due to the invariance of the Hamiltonian during rotations about  $B_0$  it is desirable to set one of the Euler angles to zero, giving angles of  $(0, \theta, -\omega t)$ ; this is highlighted in figure 2.7. Expanding the above equation into a second rank tensor would leave twenty five terms, if we only consider the time dependence added to the equation we find:

$$\hat{\mathcal{H}} = \sum \hat{\mathcal{H}}_0 \exp(i n \omega t) \quad (2.109)$$

Here  $\hat{\mathcal{H}}_0$  is a time dependent Hamiltonian. If you consider one complete rotor period such that  $T_r = \frac{2\pi}{\omega}$ , hence averaging the time dependence it is possible to significantly reduce the number of terms describing the rotation above to:

$$\frac{1}{T_r} \int_0^{\frac{2\pi}{\omega}} \exp(i n \omega t) dt = \begin{cases} \frac{2\pi}{\omega} T_r = 1 & \text{if } n \text{ is } 0 \\ \frac{\cos(n2\pi) + i \sin(n2\pi) - 1}{i n \omega} = 0 & \text{if } n \text{ is } \pm 1, \pm 2 \text{ etc} \end{cases} \quad (2.110)$$

Therefore if we rotate the sample and take an average over a rotor period all  $D_{\neq 0, m'}^l$  are removed so that the rotation becomes:

$$A(l, n)^L AB = \sum_{m'=-l}^l D_{00}^l(0, \theta, -\omega t) D_{0m'}^l(\alpha_{PR}, \beta_{PR}, \gamma_{PR}) A_{lm}^{PAS} \quad (2.111)$$

In a powder sample all the angles of this interaction should be equally represented, however as a result of the frame transformation each term has acquired a modulation factor. The modulation factor is seen to be dependent on the angle  $\theta$ ; this is the angle between the rotor and the static magnetic field illustrated in figure 2.7. This is shown to follow the Legendre polynomial ( $l = 2$ ) expressed in figure 2.2. Hence rapidly rotating the sample about this axis will remove the final five terms of the previous equation and will average any second rank tensor to zero over a complete rotor cycle.

For magic angle spinning to remove the entire interaction the spinning frequency must exceed the static linewidth, with a spinning speed of up to 130 kHz currently available this means only nuclei with quite narrow lines are possible. The

other downside of this is the sheer size of the rotor and number of nuclei present in the rotor being significantly decreased. A further complication is that this time dependence means that some of the interactions act like fourth rank tensors, this will be addressed in the MQMAS and DOR sections of this thesis.

### 2.4.2 NMR Interactions under MAS

The anisotropic interactions which are required to be reduced are direct dipolar interactions from homonuclear and heteronuclear neighbours, indirect electron coupled interactions from homonuclear and heteronuclear neighbours, electric quadrupolar interactions and electronic shielding interactions as in the chemical shielding and Knight shift.

The main and initial use for MAS was to reduce the dipolar coupling in spin- $\frac{1}{2}$  nuclei to give increased resolution. The previously derived truncated dipolar interaction for all the nuclear parts of  $j$  and  $k$  was previously given as:

$$\hat{\mathcal{H}}_D^{LAB} = b_{jk} \frac{1}{2} (3 \cos^2 \theta - 1) (3 \hat{I}_Z \hat{S}_Z - \hat{I}_Z \cdot \hat{S}_Z) \quad (2.112)$$

Reduction of this interaction can be achieved by rapidly rotating the sample at the root of  $3 \cos^2 \theta - 1$ , here it can be seen that  $\theta = \cos^{-1}(\frac{1}{\sqrt{3}}) = 54^\circ 44'$ . When Raymond Andrew first presented these results at the Ampere conference in Pisa (1960), it was noted by Gorter <sup>4</sup> that rotating the sample had magic properties and hence magic angle spinning (MAS) was coined. The first experiment completed was on NaCl cubic crystal salt with no line broadening defects and a static linewidth of less than 2 kHz. The line was narrowed and spinning sidebands (1.6 kHz) were observed at multiples of  $\omega_r$ .

### 2.4.3 Chemical Shift Anisotropy under MAS

The electron shielding or chemical shift interaction of a nucleus in a nonmetallic solid maybe written as: [51]

$$\hat{\mathcal{H}}_{CS} = -\gamma \hbar I \cdot \delta B_0 \quad (2.113)$$

Where  $\delta$  is the chemical shielding tensor of the nucleus; this can be changed to  $K$  for the shift given by the Knight shift. The metallic systems will not be discussed here as all metals present in this thesis have been obtained using a static experiment. Metals build up eddy currents inside magnetic fields which tend to

---

<sup>4</sup>the aforementioned Gorter in the history section of this thesis

slow the samples velocity; this combined with high densities make spinning metals difficult.

It is noted that  $\delta$  is a second rank tensor which is not traceless and can be asymmetric. Since the components of the shift tensor are in practice small compared with their unity, we need only to retain  $\sigma_{zz}$  and give the above equation as:

$$\hat{\mathcal{H}}_{CS} = \gamma \hbar I \sigma_{zz} \delta B_0 \quad (2.114)$$

Here:

$$\sigma_{zz} = \sum_p \lambda_p^2 \sigma_p \quad (2.115)$$

$\sigma$  is  $\sigma_p$  ( $p = 1, 2, 3$ ) and the direction cosines of its principal axes with respect to the static magnetic field are given as  $\lambda_p$ . Since the isotropic average of each  $\lambda_p^2$  is  $\frac{1}{3}$ , the average value of  $\sigma_{zz}$  in an ordinary isotropic fluid is:

$$\sigma_{zz} = \frac{1}{3} \text{tr} \sigma = \sigma \quad (2.116)$$

where  $\sigma$  is the scalar chemical shift encountered in the high resolution NMR spectra of solutions. When a rigid solid is rotated with angular rotation rate  $\omega_r$  about an axis labeled  $\theta$  to the stationary static magnetic field and at angles  $\chi_p$  to the principal axes of  $\sigma$ , you obtain:

$$\lambda_p = \cos \theta \cos \chi_p + \sin \theta \sin \chi_p \cos(\omega_r t + \psi_p) \quad (2.117)$$

If the above equation is then substituted into equation 2.115, for each nucleus we find:

$$\sigma_{zz} = \frac{3}{2} \sigma \sin^2 \theta + \frac{1}{2} (3 \cos^2 \theta - 1) \sum_p \sigma_p \cos^2 \chi_p \quad (2.118)$$

Consequently when  $\theta$  is at the magic angle, we see that the  $\sigma_{zz}$  reduces to the scalar isotropic value and the shift anisotropy is removed. This is shown in the simulated spectra shown in figure 2.4. If the term is expressed with respect to the anisotropy parameters such that  $\delta = \sigma_{33} - \sigma_{iso}$  and the asymmetry parameter is given as  $\eta = \frac{\sigma_{22} - \sigma_{11}}{\delta}$ , you get:  $\eta$

$$\sigma_{zz} = \sigma + \frac{1}{2} (3 \cos^2 \theta - 1) \delta \left[ \frac{1}{2} (3 \cos^2 \theta' - 1) + \frac{1}{2} \eta \sin^2 \theta' \cos 2\phi' \right] \quad (2.119)$$

Where the polar angles  $\theta'$  and  $\phi'$  coordinating the specimen rotation axis to the principal axis of the shift tensor. Expressed in this manner you can observe the Legendre factor of  $\frac{1}{2}(3\cos^2\theta' - 1)$  controls the shift anisotropy in the time averaged chemical shift Hamiltonian for every nucleus in the sample.

If the rotational frequency ( $\omega_{rot}$ ) is not faster than the static linewidth then spinning sidebands are observed. These spinning sidebands are present  $\pm n \omega_{rot}$  away from the central isotropic line over the entire static linewidth. As the chemical shielding commutes with itself at different times then the sideband lines are also narrow and simulation programs can be used to analyze the sideband manifold to achieve anisotropic information.

#### 2.4.4 Quadrupole Interaction under MAS

For all the previous expressions of  $V_0$ ,  $V_1$ ,  $V_{-1}$ ,  $V_2$  and  $V_{-2}$  that have been derived in the previous quadrupolar sections (equations 2.65) must be expressed in terms of the coordinate frame  $\sum^{MAS}$  of the rotor. To complete this, the Wigner rotation matrix is once again applied: [58, 59]

$$V_i = \sum_{j=-2}^2 D_{j,i}^{(2)}(\omega_r t, \theta, 0) V_j^{MAS} \quad (2.120)$$

where  $\omega_r$  is the angular velocity of the rotor and as always  $\theta$  is the magic angle, then transforming this equation into the PAS gives:

$$V_j^{MAS} = \sum_{k=-2}^2 D_{k,j}^{(2)}(\alpha, \beta, \gamma) V_k^{PAS} \quad (2.121)$$

The Euler angles  $\alpha, \beta$  and  $\gamma$  give the direction of the rotor with respect to the PAS. Transferring this to take into consideration the perturbation caused by the first order quadrupole coupling gives:

$$\omega_{m-1,m}^{(1)MAS} = \frac{1}{2}(1 - 2m)\omega_Q(3\cos^2\theta - 1) \quad (2.122)$$

As with all the previous equations the  $3\cos^2\theta - 1$  term is present and if you rotate fast enough at the magic angle the first order shift becomes zero. This means the energy levels become equally spaced and a single line appears in the spectrum at  $\omega_0$ .

The second order quadrupole effect is more complicated with the result of substituting the static equation into the Wigner matrix giving:

$$\begin{aligned}
\omega_{m-1,m}^{(2)MAS} = & -\frac{3}{32\omega_0} \left[ \frac{\chi}{I(2I-1)} \right]^2 \left( 1 + \frac{1}{3}\eta^2 \right) \\
& \times [2I(I+1) - 14m(m-1) - 5] \\
& + \frac{3}{128\omega_0} \left[ \frac{\chi}{I(2I-1)} \right]^2 \\
& \times [6I(I+1) - 34m(m-1) - 13]g(\alpha, \beta, \eta) \quad (2.123)
\end{aligned}$$

where:

$$\begin{aligned}
g(\alpha, \beta, \eta) = & \frac{1}{2}(1 + 6\cos^2\beta - 7\cos^4\beta) \\
& + \frac{1}{3}\eta(1 - 8\cos^2\beta + 7\cos^4\beta)\cos 2\alpha \\
& + \frac{1}{18}[-7(1 - \cos^2\beta)^2\cos^2 2\alpha + 8 - 4\cos^2\beta] \quad (2.124)
\end{aligned}$$

There is no  $3\cos^2\theta - 1$  term present in the second order equation meaning the interaction cannot be reduced to zero during MAS. To cope with this interaction many techniques have been created to give improved resolution. These include multiple field NMR, DObble rotation (DOR) and multiple quantum MAS (MQMAS), these will all be discussed and implemented at length throughout this thesis. The overall aim of many of the quadrupolar spectrum acquired throughout this thesis is to gain resolution despite the broadening caused by the second order quadrupole moment.

These equations hold true for a MAS experiment on perfect crystal, however a powder lineshape is just presumed to be a series of crystallites randomly orientated with respect to the magnetic field within the rotor. When spinning a quadrupolar powder sample at the magic angle the effect is similar to the case seen with spinning a CSA interaction. If the quadrupolar interaction is dominant and linewidth is smaller than the spinning frequency then a comb of sidebands is once again observed. It is possible to complete sideband analysis to achieve data on the size and asymmetry of the quadrupole tensor or its distribution. As the interaction is typically very strong the sideband manifold is very sensitive to any deviations from the magic angle, therefore extracting this data is very difficult and requires accurate set up of the angle.

If the CSA term is dominant over the  $C_Q$ , then the sidebands which fall

within the size of the span have regular amplitude, whereas the outer ones which are dominated by the quadrupolar moment lose amplitude. In very favourable cases this method can be used to determine the CSA parameters.

## Chapter 3

# Pulsed Fourier Transform Solid State Nuclear Magnetic Resonance

Now that the nuclear interactions have been addressed, it is possible to understand how the resultant NMR resonances in this thesis form. However, to complete a solid state NMR experiment an understanding of the instrumentation is required to achieve the best possible resolution of the resonance, from this it is then possible to determine the interactions present and to finally comment on the structure of the material. It is also desirable to utilise the required  $B_1$  pulse to enhance favourable interactions and remove undesired interactions to get a better understanding of the parameters used to make up the lineshape. The following chapter discusses the main equipment and pulse sequences used throughout this thesis to achieve the results in future sections.

### 3.1 Solid State NMR Instrumentation

Advancements in electronics, superconductivity and engineering have led to more highly resolved experiments, higher fields and faster MAS over the past thirty years. An NMR experiment is only as good as the equipment used to take the measurement. In a general sense, any instrument used for recording a magnetic resonance signal can be regarded as a spectrometer. As such this statement includes devices such as magnetometers for measuring magnetic fields, magnetic resonance imaging spectrometers, relaxometers and instruments used to measure nuclear spin responses. As NMR spectroscopy developed many specific requirements for the above applications

required differing specialised spectrometers. In recent years however, a number of these instruments with many of these requirements began to converge. The purpose of this section is to provide an overview of the components and operation of a SS-NMR spectrometer with a heavy emphasis on spectrometers used throughout the results section of this thesis.

### 3.1.1 The Magnet

Permanent and electromagnets typically produce magnetic fields between two parallel pole faces, these are usually mounted on a cylindrical pole piece which are in turn connected by an iron yoke to complete a magnetic circuit. A typical magnetic field for a permanent magnet is about 1.4 T corresponding to a proton frequency of 60 MHz. An electromagnet with an iron yoke core can typically produce a magnetic field around 2.3 T; yielding a proton frequency of 100 MHz. The limit of the attainable field is the saturation of the pole piece and the pole cap. A typical 2.3 T electromagnet for NMR purposes has an electric power consumption of several kilowatts per hour and water cooling is required for the magnet coils. [69]

Because of the high power consumption and limited magnetic field capability, the use of electromagnets, for most applications, has been superseded by superconducting magnets. Their configuration is in the form of a multilayer wound solenoid with superconducting wire, which is then bathed in liquid helium. This has a bore running through its centre so various probes can be inserted into the magnet (see section 3.1.2). Surrounding this chamber is a liquid nitrogen reservoir and thermal shields to provide cooling to minimise the loss of the liquid helium.

The type of superconducting wire used in these applications varies depending on the field strength. For fields up to 9.4 T, niobium-titanium alloys are used. This alloy is arranged as filaments along the copper sheath. The wire is favourable as it can be wound and shaped into the solenoid. For higher magnetic fields niobium-tin alloys are used. [70] These can produce fields in excess of 20 T. The use of high-temperature superconductors has not been utilised in NMR, however by cooling them to liquid helium it is possible to produce even higher magnetic fields. [71–73]

For high resolution applications the magnetic field developed at the sample may not be stable enough to give high enough resolution; this can be due to field drift or environmental fluctuations. Magnet uniformity can be improved by *shimming*<sup>1</sup>. In modern NMR magnets electric shims are used to produce a desired field gradient. Gradients which are inherent in the magnet may be cancelled out by the operator

---

<sup>1</sup>This term is derived from the use of metallic shims placed between the pole pieces and the yoke of a magnet to adjust the alignment of the pole faces



varying the currents in these shim coils; hence giving increased field homogeneity. [74, 75]

### 3.1.2 The Probes

Due to the lack of molecular tumbling in solids, solid state NMR probes require a large bandwidth to excite the larger line widths. A wideline NMR probe is usually required to produce a sub-  $3\ \mu s$  pulse length which represents a 80 kHz bandwidth; giving peak to peak voltages of  $\approx 3\ kV$  (although this figure varies with coil sizes). The most common commercial solid state NMR probe is the double resonance MAS probe, this offers the ability to undertake cross polarisation (see section 3.4.5) and to average the interactions previously discussed. [76]

There are a series of requirements for capacitors present in a solids probe. They must have very low magnetic susceptibility, high  $Q$ ,<sup>2</sup> high current, high voltage, very low piezoelectric effects and the dielectrics must be low of unwanted NMR background signals. Ceramic oxide glass (COG) rf capacitors usually fit these requirements. [77, 78] However, the magnetic properties of ceramics are quite unpredictable, they are usually doped with bismuth which is strongly diamagnetic; over the years manufacturers have become acquainted with the requirements of NMR capacitors and produce a nonmagnetic chip capacitor. These are always tested for magnetic properties using the crude method of suspending a magnet on a piece of string above the capacitor.

The work horse of the NMR experiment is the coil which effectively acts in transmitting the selected frequency and receiving the signal; much the way an aerial on a mobile phone works. Almost all solid probes use solenoidal rf coils for higher filling factors and  $Q$ : when compared to the rival saddle coils. [79] Oxygen free, high conductivity electronic wire with low iron impurities is the common choice for most coils. The enamel coating on these wires is usually removed as it contains a carbon background and may be observed during an NMR experiment where carbon is in trace amounts. The length of the coil is typically the same as the diameter for static probes, with it being as much as three times as long for MAS ones. However, longer coils give decreased excitation bandwidths so most manufacturers use smaller coils at the sacrifice of signal to noise. [80, 81]

For high resolution experiments, MAS is required to remove or partially remove some of the interactions present in solid samples. [82] Rotation rates ranging from 1 kHz to 90 kHz are now possible for varying rotor sizes from 14 mm down

---

<sup>2</sup>Electric charge is a physical property of matter that causes it to experience a force when near other electrically charged matter

to 1 mm respectively. To achieve such speeds (usually with an accuracy of  $\pm 10$  Hz) double bearing cylindrical rotors are used. [83] High strength ceramics ( $\text{Si}_3\text{N}_4$ ) have the highest strength to mass ratio, however as  $^{29}\text{Si}$  is a commonly studied nuclei and silicon nitride rotors contain large amount of defects, partially stabilised zirconia (PSZ) rotors are preferred. The consequence of these desirable properties means that rotors are usually very expensive. For ease of use, press fit VESPEL caps are used; these however have poor wear resistance and require replacing quite often. [84]

The rapid development of MAS solids probes, since Raymond Andrews pioneering attempts in 1958, has led to many advances in structural characterisation in solid state NMR and has made the technique feasible for large disordered materials such as proteins, glasses and oxide conductors. [23, 24] Probe development has single handedly given the greatest enhancement to the technique over its short life span and as it reaches its limits (speed of sound for MAS, material development etc.) then other techniques (multiple pulses, improved analysis, polarisation techniques etc.) may be required to move the field further forward.

### 3.1.3 The Consoles

The console contains the electronic portion of the spectrometer which includes, frequency selection, signal detection, signal amplifiers, control systems and digital data electronics. The elements of just the rf system are the frequency synthesis, transmitter system, power amplification, coupling to the probe, receiver system and signal detection (see section 3.1.4).

The transmitter provides the rf signals to excite all the spins, if only a single frequency is required then a fixed frequency source can be used. A modern pulse spectrometer is designed to satisfy a wide range of applications and to observe a wide range of nuclear spins, this requires a more complex frequency generation scheme. It was common to use a crystal oscillator (digitally reproduced in modern spectrometers) operating at a standard frequency to provide a stable frequency from which all other frequencies can be derived. A frequency synthesizer is used to give this variable frequency output. Finally to generate the output frequency it is advantageous to mix many frequencies. This has the advantage of allowing gating before the end frequency is produced and one of the frequencies can remain constant and hence become a control. The major disadvantage is that each mixing stage introduces multiple frequency components that require filtering and suppression to give only the desired frequency. [85]

The rf signals produced in the transmitter are amplified to the appropriate

level before being sent to the probe. Once again the output varies depending on magnet strength, coil size and nuclei being studied; between very low watts for high  $\gamma$  nuclei in small coils at high field to kilowatts for low  $\gamma$  nuclei in large coils at very low magnetic fields. In a modern spectrometer a linear amplifier is currently used which gives variable amplitude drive. The disadvantage of these is that they are a lot more expensive and generate a noise output even when they are not pulsing. To overcome this, most modern spectrometers, actively blank off by switching the bias of the output stage until an output pulse is required.

The amplified transmitter pulse must now be coupled to the probe and the received signal must be coupled out of the probe. In a pulse spectrometer these sequences occur sequentially and a switching circuit is used to direct the signal correctly. Some of the older spectrometers used in this thesis employ the use of cross diodes and quarter wavelength lines to effectively give the switching by the application of rf itself. High voltages during the rf pulse cause the diodes to conduct and effectively short the circuit. Those ground in front of the pre-amplifier protect the amplifier from overload and also reflect energy so that all the transmitter power is delivered to the probe. During the receive cycle, voltages are so low that the diodes effectively act as an open circuit, isolating the transmitter and all the signal is then sent to the pre-amplifier. The above discussed cross diode circuit is non linear and a threshold pulse is required to activate the circuit.

### 3.1.4 Signal Detection

The receiver system works by amplifying a very weak NMR signal with the minimum distortion and degradation. The total gain required in the NMR system is typically between 60-100 dB. In a few applications this might all be provided at the NMR frequency. More commonly the signal is amplified by around half the figures suggested above and transferred into a fixed intermediate frequency by mixing with a local oscillator frequency derived from the transmitter. This provides a more stable receiver and allows most of the amplification to be done at a fixed frequency. Phase detection at the final intermediate frequency provides the output signal of the spectrometer. During pulse NMR applications this is required to decouple the receiver during the initial transmitter pulses to prevent overload and subsequent slow recovery to optimum performance. [86, 87]

The output of a mixer contains both the sum and the difference frequencies of the two inputs, hence the unwanted frequencies are removed by limiting the bandwidth with filters. Unfortunately the signal still contains the image frequency; for example in the first mixer of the receiver the two signals are converted to inter-

mediate frequencies given as:

$$\omega_1 = \omega_{LO} - \omega_{IF} \quad (3.1)$$

$$\omega_1 = \omega_{LO} + \omega_{IF} \quad (3.2)$$

While only one of these frequencies corresponds to the NMR signal ( $\omega_0$ ) any noise present in the intermediate frequency will be to the detriment of the signal to noise. The image frequency must therefore be rejected either by a filter or the use of a single sideband mixer. In a spectrometer used to function at broadband frequencies a single sideband mixer is used.

The output of the final mixers is the frequency ( $\omega_s$ ) which is equal to the difference between the NMR frequency and the transmitter frequency. As such it is equal to the precession frequency in a reference rotating frame (at the frequency of the spectrometers transmitter). By using a two phase detector driven by reference signals in quadrature the two outputs are providing the projections onto two orthogonal axes in the rotating frame. The sense of rotation of the signals can distinguished by the phase relationship, hence NMR signals at frequencies above and below the transmitter frequency can be distinguished.

Noise above and below the transmitter frequency can also be distinguished with only a single detector. The noise components from either side of the transmitter frequency both contribute to the noise output and the signal to noise ratio decreases by  $\sqrt{2}$ .

In most modern spectrometers, the analogue signal following detection is converted to a digital signal for time averaging and other processing. The analogue-to-digital (ADC) converter must have sufficient resolution and accuracy to make a representation of the signal in a digital domain. Linearity can be maintained by adjusting the receiver gain to limit the strength of the signal intensity to less than that of the full scale response of the 16-bit ADC. If all of the above is satisfied the free induction decay (FID) will be free from errors and artifacts leaving it available for further processing from the time domain into the frequency domain.

## 3.2 Relaxation

Consider a basic NMR experiment of an isolated spin system which is not coupled to any other nuclei. Then on inserting this system into a large static magnetic field ( $B_0$ ) the net magnetization of the system ( $M_{eq}$ ) is found along the  $B_0$  axis. On

adding a radio frequency (rf) pulse to the system, two observations can be made. Firstly a rather large signal will be obtained instantly, but the intensity of this free induction decay will gradually decrease over time. Secondly if enough time is then left after the pulse the experiment can be re-run giving exactly the same results. From these basic observations a few conclusions can be drawn.

The signal is induced in a receiver coil that is wound along the  $y$ -axis, the pulse must tip  $M_0$  away from  $B_0$  and into the  $x, y$  transverse plane. Secondly as the signal observed is seen along the transverse plane then the decay of the signal must be from the resultant decay of the signal away from this plane. Finally, as the experiment can be repeated with the same results, the component along the  $B_0$   $z$ -axis must be returning after the rf pulse. The decay of the signal and recovery of the signal back to the  $B_0$  axis (to give  $M_Z$ ) are both known as relaxation processes. The growth along the  $z$ -axis is known as  $T_1$  (longitudinal) relaxation and the decay of the signal is known as the  $T_2$  (transverse) relaxation.

### 3.2.1 Longitudinal Relaxation

For an NMR experiment to be repeated it is required that a large percentage of the spins to return to equilibrium after each rf pulse in a reasonable time frame. If the relaxation is too fast then (generally) as  $T_1 \geq T_2$  then the signal will appear very broad, conversely if the relaxation is too slow then the rate of repetition becomes a limiting factor. Typical spin lattice relaxation times are in the order of seconds, however the metals discussed in this thesis have very rapid relaxation times ( $\mu s$ ). The mechanisms of relaxation depend on the state of the matter, the nuclear spin ( $I$ ), sample temperature, paramagnetic impurities, magnetic impurities, electronic environments and whether or not external fields such as radio waves are applied. [46]

The major materials studied in this thesis suffer from three major types of relaxation; the first is motion caused by neighbouring hydrogen atoms, the second is quadrupolar relaxation and the final is electronic relaxation in metals. A mechanism for quadrupolar relaxation has been proposed by Van Kranendonk. [88] Briefly this method involves an incident phonon being destroyed at the nuclear site, the nuclear spin is flipped and an energy conserving phonon is created. The mechanism has been shown to be temperature dependent. [89] In amorphous materials this Van Kranendonk two-phonon quadrupolar relaxation Raman process has been shown to be limited. Another mechanism is described as being due to the abundant existence of two level defects. An example of this is shown in bridging oxygens tunneling between two potential wells causing a modulation of the EFG at the nuclear site.

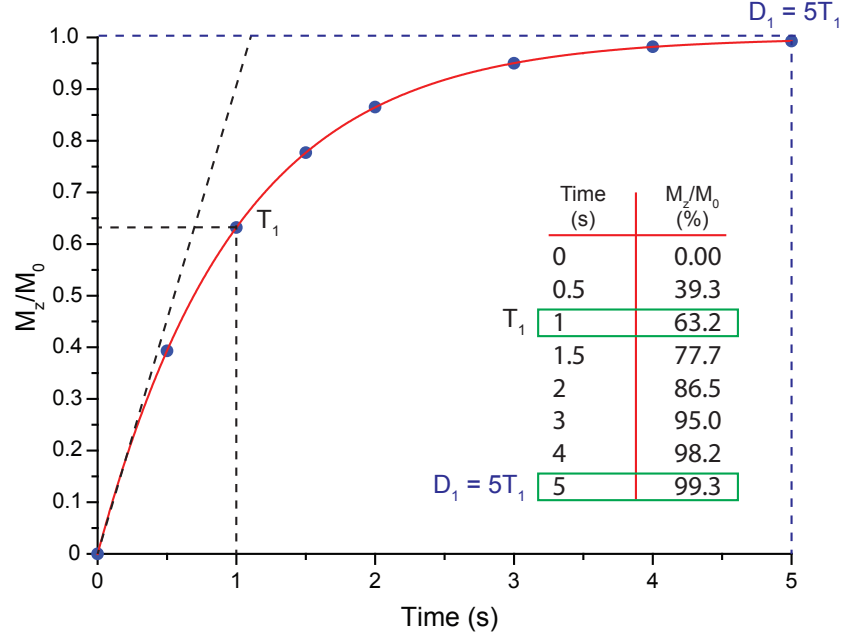


Figure 3.1: A plot of the initial rate of growth of a magnetization vector with  $T_1$  equal to 1 second. The dashed line intersects the  $M_0$  line at a time equal to  $T_1$ , which is the time that the relaxation would be complete if it continued at its initial rate. At this time however only 63.2 % of the maximum value is shown. The  $D_1$  is the actual relaxation time used in the experiment which is proportional to  $5T_1$  and this is when 99 % of the signal has formed. The inserted table shows the percentage recovery of  $M_z$  as a function of time, in units of  $T_1$ .

[90] This changing field is a more efficient process at relaxing the nuclear spins. [91] The electronic relaxation method for metals has been previously discussed in the Korringa relation section of this thesis.

If a NMR active nuclei is exposed to a large static magnetic field ( $B_0$ ), the bulk magnetization is given as:

$$M_z(t) = M_{eq}(1 - \exp^{-t/T_1}) \quad (3.3)$$

where  $M_z$  is the bulk magnetization across the  $z$ -axis at a given time ( $t$ ) and  $M_{eq}$  is the bulk magnetization at equilibrium, hence fully relaxed. The key parameter here is the  $T_1$  relaxation time; as shown in figure 3.1 when  $t = T_1$  the magnetization will only be 63.2% relaxed and during the experiment the time delay used between pulses will be  $5T_1$ ; known as  $D_1$ . [92]

An experiment to measure the  $T_1$  relaxation is called a saturation recovery experiment. [48] This involves using a pulse comb to saturate the signal. The pulse

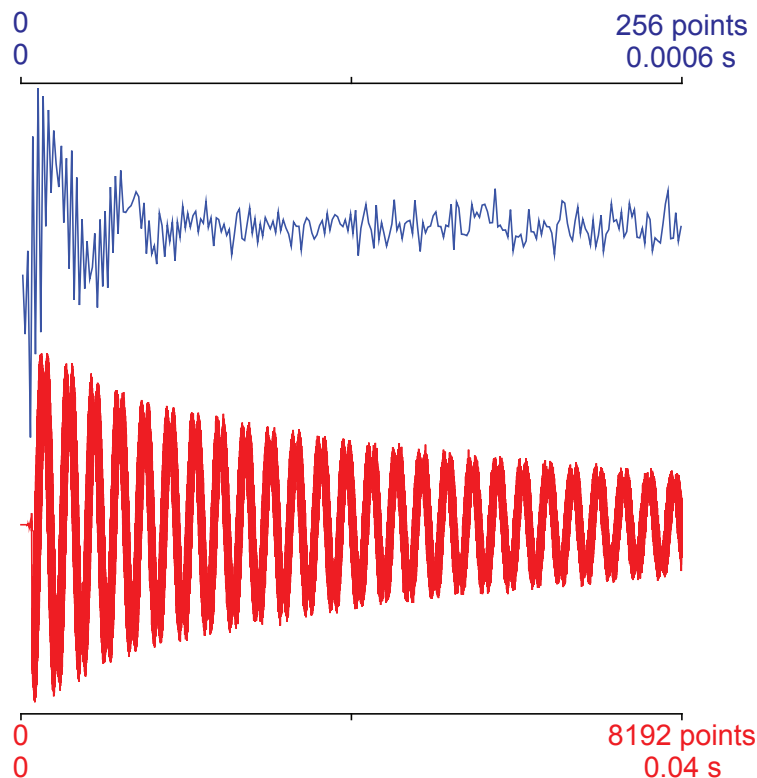


Figure 3.2: A  $T_2^*$  relaxation time of a  $^7\text{Li}$  (11.7 T) sample showing the blue static FID which gives a broad single resonance spectrum and the red fast (32.5 kHz) MAS spectrum which gives a single narrow line shape.

comb usually exists of a series (100 pulses) with a delay proportional to  $T_2$  between each pulse. Then a time delay is left followed by a  $90^\circ$  pulse which will excite all the spins which are aligned all the  $z$ -axis. If the time delay is sufficient then all the spins could be excited and a larger signal maybe observed. Saturation recovery data is fitted to equation 3.3.

### 3.2.2 Transverse Relaxation

The coherence dephasing time ( $T_2$ ) can be imagined as the individual precessing magnetic moments falling out of synchronisation with each other in the  $x, y$  plane. The longer the  $T_2$  relaxation the narrower the line and as the relaxation is dependent on the interactions present in the nuclei then they can be reduced using methods such has MAS as shown in figure 3.2.

During the  $rf$  pulse the magnetic moments are flipped along the  $x, y$  axis and can be imagined to initially be pointing along a single direction in the  $x, y$  plane.

As time progresses these vectors spread out evenly along this plane to give zero net transverse magnetisation. Ideally, the bulk magnetization of fully relaxed nuclei after a  $90^\circ$  pulse with no interactions present in the LAB frame is given as:

$$M_x(t) = M_{eq} \sin(\omega_0 t) (\exp^{-t/T_2}) \quad (3.4)$$

$$M_y(t) = -M_{eq} \cos(\omega_0 t) (\exp^{-t/T_2}) \quad (3.5)$$

The above equation describes an exponentially bulk magnetic moment precessing with an angular frequency ( $\omega_0$ ) in the  $x, y$  plane. [25] In reality there will be a spread of precession frequencies which will give a broadening effect to the spectrum. This obviously effects the resolution and masks informative interactions present in solid state NMR.

The experimentally measured peak width in a spectrum will be proportional to  $\frac{1}{T_2^*}$ .  $T_2^*$  is summation of the intrinsic transverse relaxation ( $T_2$ ) and the equipment specific dephasing ( $T_2'$ ) so:

$$\frac{1}{T_2^*} = \frac{1}{T_2} + \frac{1}{T_2'} \quad (3.6)$$

The  $T_2'$  term takes into consideration instrument imperfections and the nuclear spin interactions not being fully reduced.

To measure the  $T_2$  term and to remove the  $T_2'$  term a spin echo is usually utilised, see spin echo section below. Only factors that incoherently dephase the transverse magnetization remain and from this the true  $T_2$  can be observed.

### 3.3 Fourier Transform

The result of a NMR experiment is the production of a free induction decay (FID) with respect to time. [93, 94] The frequency spectrum used in most modern results is transferred from the time domain into the frequency domain by a Fourier transform (FT). Fourier transform NMR allows you to visualise the data in the frequency domain which generally has better spatial resolution as they are inversely proportional, the disadvantages are that you can get pseudo-baselines and artifacts in your spectra. These are all caused by the fact that information is conserved during a FT. [36, 37]

The signal is a digitised list of complex numbers,  $s[n]$  where  $n$  goes from zero to the number of acquired points (TD). The discrete time FT is then used:



$$S(\omega) = \sum_{n=0}^{TD-1} s[n]e^{-i\omega n} \quad (3.7)$$

As an ideal case we can use a signal, at the frequency of  $\omega$ , with a transverse relaxation rate  $R = \frac{1}{T_2}$ . Thus the signal can be described as:

$$S(t) = e^{-i\phi} e^{i\Omega t} e^{-tR} \quad (3.8)$$

where  $e^{-i\phi}$  is given as an arbitrary phase factor.

Now if we keep  $\phi = 0$  then the FT yields a complex spectrum which comprises of two parts. The absorptive and dispersive parts are given as:

$$S(\omega) = A(\omega) + iD(\omega) \quad (3.9)$$

The absorptive part is given as:

$$A(\omega) = \frac{R}{R^2 + (\Omega - \omega)^2} \quad (3.10)$$

and the dispersive part given as:

$$D(\omega) = \frac{\Omega - \omega}{R^2 + (\Omega - \omega)^2} \quad (3.11)$$

This result would give a Lorentzian line shape centre at a frequency of  $\Omega$ . Instrumental factors mix the absorptive and dispersive terms and hence the  $e^{-i\phi}$  term is used to correct this and hence achieve a purely absorptive line shape in a process known as phasing.

## 3.4 The NMR Experiment

The previously discussed interactions and hardware can only be utilised by applying a *rf* pulse to the sample inside the static magnetic field. These pulses can be tuned and added to delays to select different interactions and differing chemical sites. These interactions can be probed by creating an internal magnetic field  $90^\circ$  in addition to the static magnetic field using radio frequency pulses.

### 3.4.1 Radio Frequency Pulses

NMR relies on resonant techniques to detect the population difference in the spin system. The part of the spectrum corresponding to typical Larmor frequencies on

the nuclei in Periodic Table range from 1.7 MHz ( $^{197}\text{Au}$  at 2.34 T) to 1 GHz ( $^1\text{H}$  at 23.5 T), placing them in the radio end of the spectrum. A *rf* pulse on resonance can interact with the nuclei to create a resonant effect; this process is not entirely known as a typical NMR coil may only be capable of producing a magnetic field of about 1 mT range.

Hoult suggests that *rf* waves have no contribution to the NMR signal. Instead a quantum electrodynamical near field effect created by virtual photons is applied. [86, 87] This is beyond the scope of this thesis and instead a classical *rf* wave Hamiltonian theory will be discussed. The *rf* pulse produces a time dependent oscillating field ( $B_1$ ) adding this time dependence to the spin system. The Hamiltonian describing the system is now the combination of the Zeeman interaction and the *rf* Hamiltonian giving:

$$\hat{\mathcal{H}}(t) = \hat{\mathcal{H}}_Z + \hat{\mathcal{H}}_{rf} \quad (3.12)$$

$$= -\gamma\hbar I_Z B_0 - \gamma\hbar \hat{I} B_1(t) \quad (3.13)$$

$$= \hbar\omega_0 \hat{I}_Z + \omega_1 \hat{I}_X \cos(\omega_{rf}t + \phi) \quad (3.14)$$

Here  $B_1$  is the applied oscillating field along the  $x$ -axis with a carrier frequency of  $\omega_{rf}$ , which has an amplitude of  $\omega_1 = -\gamma B_1$ . The angle  $\phi$  represents the phase of the *rf* pulse.

To simplify the above equation we transform it into the rotating frame. We choose one rotating around  $B_0$  at a frequency of  $\omega_{rf}$ . In this frame the Hamiltonian becomes:

$$\hat{\mathcal{H}}^{ROT} = -\hbar((\omega_0 - \omega_{rf})\hat{I}_Z + \omega_1 \hat{I}_X) \quad (3.15)$$

The term  $-\hbar(\omega_0 - \omega_{rf})$  represents the  $z$  direction of the magnetic field. It is often referred to as the reduced field ( $\Delta B$ ), owing to the fact that as  $\omega_{rf}$  approaches  $\omega_0$  the term diminishes, thus the equation now becomes:

$$\hat{\mathcal{H}}^{ROT} = -\hbar\omega_1 \hat{I}_X \quad (3.16)$$

Before any *rf* pulse has been implemented, the spins precess about the static field,  $\hat{I}_Z$ . The consequences of the *rf* pulse is that the spin precession cones now start to tip toward  $-\hat{I}_Y$ . This is known as nutation and some of the magnetisation is now said to lie in the transverse plane.

The amount of tipping depends on the duration of the *rf* pulse,  $\tau_1$ . The

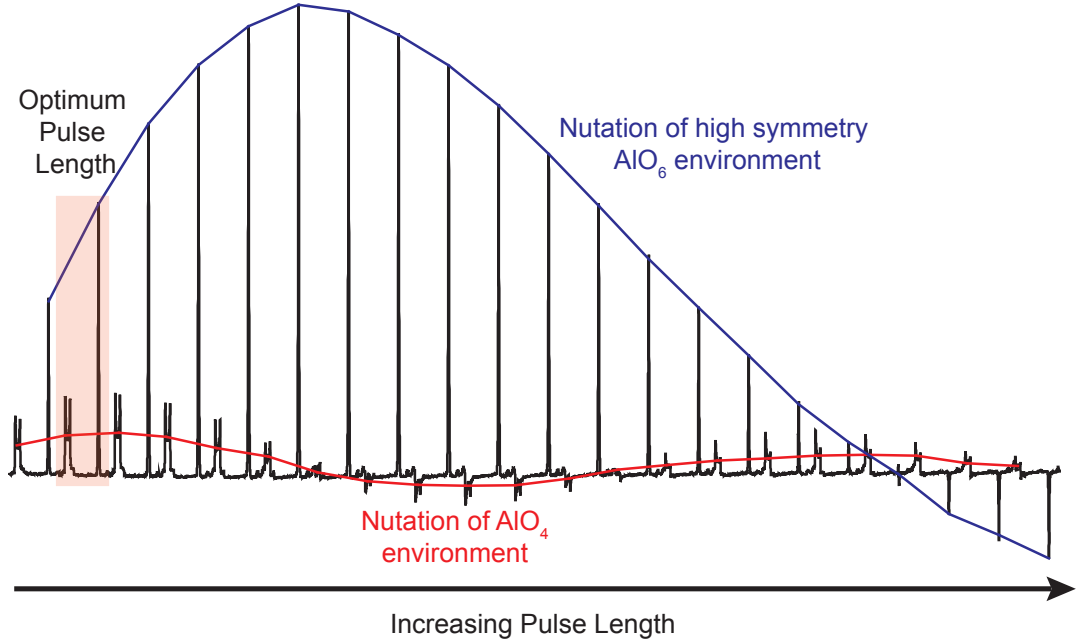


Figure 3.3: The nutation is faster for sites with a larger  $C_Q$ , this is an array of pulse times for yttrium aluminium garnet (YAG), at 14.1 T with an MAS rate of 20 kHz, which shows the lineshape and intensity as the pulse length is increased. The site with the smallest  $C_Q$  nutates slowest and a  $90^\circ$  pulse length for this site would give a  $180^\circ$  zero crossing for the high  $C_Q$   $\text{AlO}_4$  site. The optimum highlighted pulse length gives a 1:1 ratio between the  $\text{AlO}_4$  and  $\text{AlO}_6$  sites. For solid state NMR the x-axis is usually displayed in  $\mu\text{s}$  and it is desirable that the optimum pulse length be approximately 1 to 3  $\mu\text{s}$ .

nutation tipping angle can be defined as:

$$\theta_{\text{nut}} = \omega_1 \tau_1 \quad (3.17)$$

When a  $90^\circ$  pulse has been applied ( $\frac{\pi}{2} = \omega_1 \tau_1$ ) and the respective density matrix lies entirely in the  $-\hat{I}_Y$  direction. In this case where  $I = \frac{1}{2}$ , there is a selection rule imposed such that  $\Delta m = \pm 1$ . In quadrupolar nuclei there is the possibility that other transitions could occur such that  $\Delta m = \pm 2, \pm 3$  etc etc.. These double quantum (DQ) or triple quantum (TQ) transitions appear to be forbidden by the requirement of  $\omega_{rf} \approx \omega_0$ . Upon expanding to higher order terms it has been shown that for a central transition pulse can be excited these forbidden transition terms.

The excitation of single and multiple transitions is governed by the characteristic of the pulse. A complex spectrum can have many resonances so it is difficult to be on resonance for all these (see wide line NMR section). However by applying

a short sharp pulse a large enough  $B_1$  can be excited to effectively fulfill this characteristic. For this to take place the magnitude of the rf field in the rotating frame,  $B_1$  must be greater than that of  $\Delta B$ . Since these short sharp hard pulses excite the entire frequency range equally they are termed *non-selective pulses*. Low power pulses are consequently known as *selective pulses*, these can be used to excite single resonances or transitions without the accompanying multiple quantum excitation.

### 3.4.2 Coherence and Phasing

It can be observed how coherence relates to the bulk transverse magnetisation caused by the synchronisation of the nuclear magnetic moments precessing. Transverse magnetization (e.g.  $I_X$ ) and zero quantum coherence (e.g.  $\hat{I}^+\hat{S}^-$ ) have a coherence order of zero. During free precession the coherence order cannot change as only rf pulses can transfer magnetization. A  $\frac{\pi}{2}$  pulse will excite all the spin states in a system to coherence ( $p$ ) whilst a  $\pi$  pulse will convert them to  $-p$ . [95]

If we consider a quadrupolar system with multiple coherence orders and possible population states, then these can no longer be considered in a vector model. However using the irreducible spherical tensor model developed in section 2.3.1, the density matrix can be viewed as spherical harmonics. At a very basic level it can be observed that by applying  $\frac{\pi}{2}$  and  $\pi$  pulses it is possible to control the nuclear spins. However this has been observed as an all or nothing response, you either excite all the coherences or none of them. Hence why phase cycling is utilised to select for the required coherence pathway.

The phase is given as  $\phi$ . It has been previously noted in the signal detection (section 3.1.4) that the mixer produces rf pulses with differing phases and can also receive these differing phases. Hence if the coherence pathway is changing by  $\Delta p$  then a phase shift of  $-\Delta p \Delta \phi$  will be present. If you match the receiver phase with the shift then you are effectively selecting that coherence and over the course of an entire phase cycle the undesired coherences should average to zero.

Different pulse sequences which rely on exciting the multiple quantum coherences are a source for many new experiments with quadrupolar nuclei. These each select a specific interaction and attempt to use the coherences to enhance or remove its features and give a desired signal and require phase cycling to remove unwanted artifacts. [96]

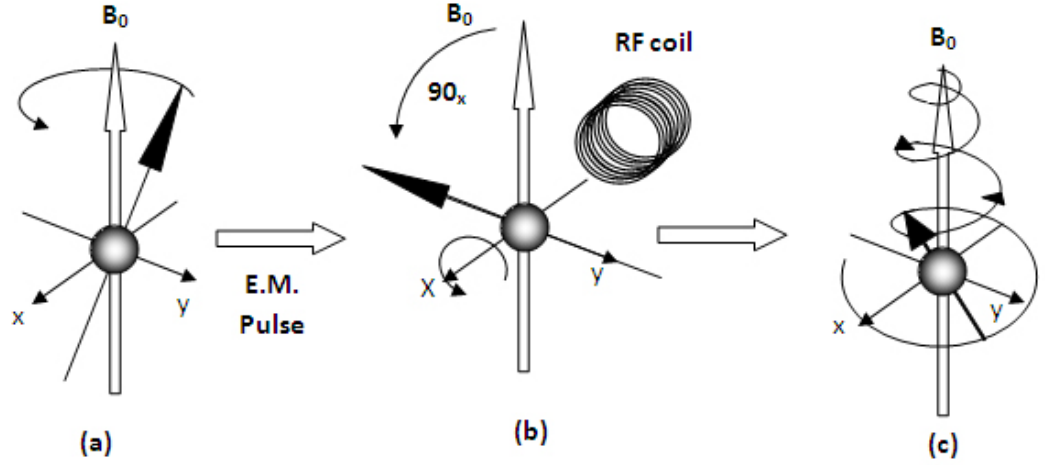


Figure 3.4: An NMR one pulse experiment showing (a) a spin aligning with the magnetic field  $B_0$ , (b) a radio frequency pulse  $B_1$  is applied to tip the spins to  $90^\circ$  and finally (c) the spin-spin relaxation is measured to give your NMR spectra. This diagram is adapted from *Spin Dynamics* [46].

### 3.4.3 One Pulse

The most regularly used and simplest NMR pulse sequence is a known as a one pulse experiment. It begins with the preparation of a transverse magnetization of spins  $S$ . This is done with a  $\frac{\pi}{2}$  pulse that rotates the longitudinal equilibrium magnetization (spins aligned along the static magnetic field,  $B_0$ ) into the transverse plane which is  $90^\circ$  to  $B_0$  as shown in figure 3.4. [48]

This is then followed by the precession of the transverse magnetization of  $S$  in the transverse plane, at a frequency of  $\omega = \omega_0 + \omega_{int}$ , close to its Larmor frequency ( $\omega_0$ ). This precession magnetization induces signal, which is acquired and Fourier transformed.

During the precession time, the interactions are made time dependent in order to average out their anisotropic part, which in powders causes the line broadening effects. When the spins are observed evolving independently, the observed signal is given as:

$$\begin{aligned}
 S(t) &= S(0) \exp \left[ -i \left( \omega_0 + \int_0^t \omega_{int}(\tau) d\tau \right) t \right] \\
 &= S(0) \exp[-i(\omega_0 + \varphi_{int}(t))t] \quad (3.18)
 \end{aligned}$$

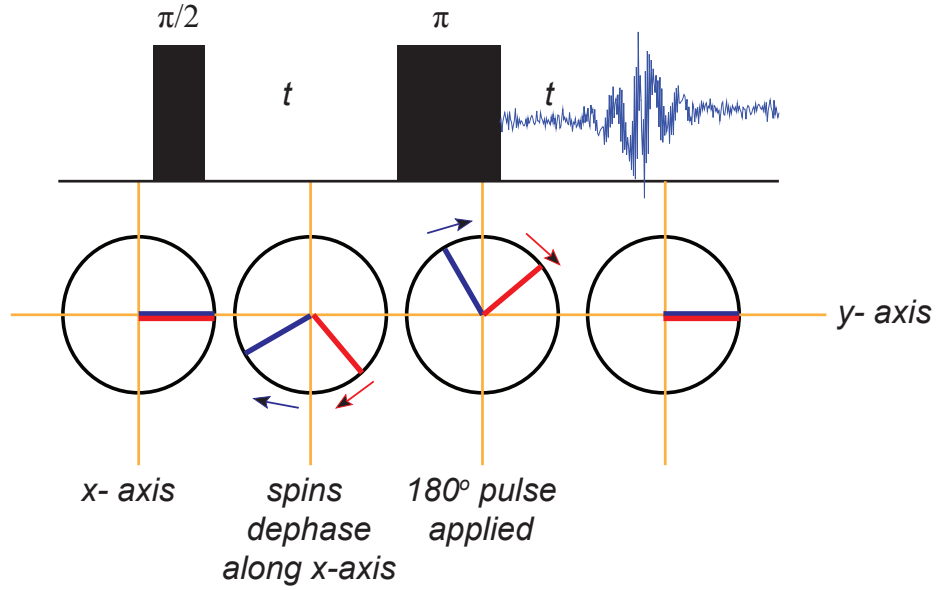


Figure 3.5: Classical picture of the spin echo: the left two circles show the polarisation and  $90^\circ$  pulse followed by the dephasing of the resonance in the x-y plane. The  $180^\circ$  (can also use another  $90^\circ$ ) refocusing pulse in the right two circles, this is followed by rephasing and signal detection.

Where  $\omega_{int}(t)$  is the time dependent frequency shift due to the interactions. This assumption of an independent evolution of each  $S$  is exact only when the interactions present are the ones previously discussed in the theory chapter. If there is a strong dipolar coupling between the like spins, then generally, you must study the evolution as a whole coupled (homogeneous) spin system.

### 3.4.4 Echo Experiments

A sound or series of sounds caused by the reflection of sound waves from a surface back to the listener.

- *Oxford English Dictionary, 2010.* [97]

If you consider the above statement from a NMR perspective, then the sound is a sharp signal which is being broadcast, something is present to reflect this signal and the returning attenuated and distorted response is known as the echo. A spin echo NMR experiment is quite analogous to the dictionary definition of an echo. A transient transverse magnetization is created, which is then reflected backwards and at a later time this magnetization is detected.

The standard  $\frac{\pi}{2} - \tau - \pi$  pulse sequence involves the excitation of spins to

the single quantum coherence, before a  $\tau$  delay which is inversely proportional to one rotor cycle. During this  $\tau$  delay the magnetisation relaxes according to the Bloch equations. During this period the magnetic moments of the spins will begin to dephase and give a spread of frequencies about  $\omega_0$ . This is caused by some spins having an increased precession velocity. [21]

A  $\pi$  pulse is now applied to flip the spins and invert the population about the rf field. Now the magnetic moments which were rotating quicker are now behind the slower populations by the same amount. These spins effectively undo their dephasing during the first  $\tau$  period and after a given time catch up in a mechanism called rephasing. This takes place under a second  $\tau$  period. The opposite is true for the slower spins and after the time of  $2\tau$  the phase coherence is restored for the spin-echo seen in the diagram 3.5. [38]

A modification of this pulse sequence is the  $\frac{\pi}{2} - \tau - \frac{\pi}{2}$ , this can help with the refocusing of the quadrupolar interaction in  $I \geq \frac{1}{2}$  nuclei. This can also be used when larger excitation bandwidths are required and can even be cut down to a  $\frac{\pi}{4} - \tau - \frac{\pi}{4}$  sequence for construction of widelines or when long  $T_1$  relaxation times are present. [46]

There are many advantages of using echo experiment the main advantage is that if a full echo is achieved and processed a signal to noise as twice the signal is achieved.

### 3.4.5 Cross Polarisation

In order to resolve spectra of low sensitivity nuclei such as  $^{13}\text{C}$  at natural abundance, in strongly protonated solids, you can utilise MAS to reduce the anisotropic part of the linewidth and heteronuclear decoupling in order to remove the dipolar coupling between the neighbouring protons. Decoupling involves applying a strong continuous rf pulse during the acquisition of the required nucleus. [98]

To enhance the poor sensitivity a technique called cross polarisation (CP) is utilised, this takes advantages of low- $\gamma$  rare spins  $S$ , which are coupled with abundant high- $\gamma$  spins  $I$  such as protons. [29] CP is a recoupling sequence. In a doubly rotating tilted frame, where the  $X$  axis is aligned along the magnetic field  $B_0$ , the  $\hat{I}_X \hat{S}_X$  part of the  $I - S$  dipolar interaction is made time dependent by two simultaneous irradiations, at the Larmor frequencies of both the  $I$  and  $S$  spins. Each irradiation makes the term periodically time dependent with frequency  $\omega_{1I} = \gamma_I B_{1I}$  or  $\omega_{1S} = \gamma_S B_{1S}$ . If the respective amplitudes of  $\omega_{1I}$  and  $\omega_{1S}$  of the irradiations are equal (discovered and named after Hartmann-Hahn), the  $\hat{I}_X \hat{S}_X$  term becomes time independent and can induce a very fast 'flip-flop' exchange of polarisation between  $I$

and  $S$ . [99] Complications come when the sample is spun, the dipolar coupling  $I-S$  becomes modulated by the rotation of the sample giving a third time dependence. [100]

The signal intensity under CP is increased by a maximum factor of  $\frac{\gamma_I}{\gamma_S}$ . As a consequence the relaxation time of spin  $I$  before applying a second transient, as  $^1\text{H}$  generally has a faster relaxation time due to motion than its neighbours. The repetition rate can be further increased by flip back pulses that returns the remaining spin locked proton magnetization back along the magnetic field  $B_0$ .

### 3.4.6 Wide Line Acquisition for Nonquadrupolar and Quadrupolar Nuclei

Many nuclei have properties which generate large line widths during Fourier transform of their signal. Heavy spin- $\frac{1}{2}$  nuclei tend to have the opposite magnetic response properties to those of the lighter favorable nuclei such as proton and  $^{13}\text{C}$ . A key feature is that as the element gets heavier there tends to be a large increase in its chemical shift range. Elements with more electrons are seen to react more sensitively to their chemical environment than those with fewer electrons. It can also be argued that this causes their chemical shift anisotropies to expand dramatically. The resulting spectra seen in non cubic environments will show poor signal-to-noise and present problems with uniformly exciting the line. This situation is not helped by the abundance of low magnetogyric ratio spin- $\frac{1}{2}$  nuclei. Added to these complications is the observation that many of these nuclei have very long  $T_1$  relaxation times, meaning multiple transients are difficult to complete without a large amount of spectrometer time. This inherently difficult detection problem means studies on these nuclei are few and far between in the NMR literature.

A general method for recreating wide line NMR data is to use the continuous wave (CW) method. This predecessor to the now more commonly used Fourier transform method involves scanning through the signal with a continuous pulse which excites everything in the sample. The sensitivity is low for narrow signals, hence why it has been superseded by FT techniques. However, for broader spectra the disadvantages are minimized as swept detection always operates on resonance with constant-RF amplitude, this avoids offset effects and artifacts due to pulse imperfections.

There are two methods for CW, the first is called the slow passage experiment (this was the main method for completing a NMR experiment in the 1960-70s). [101] The result of the experiment from non infinitely slow scanning was that the signal shape ( $g(\omega)$ ) is dependent on the RF field ( $B_1$ ). For a typical Lorentzian peak with



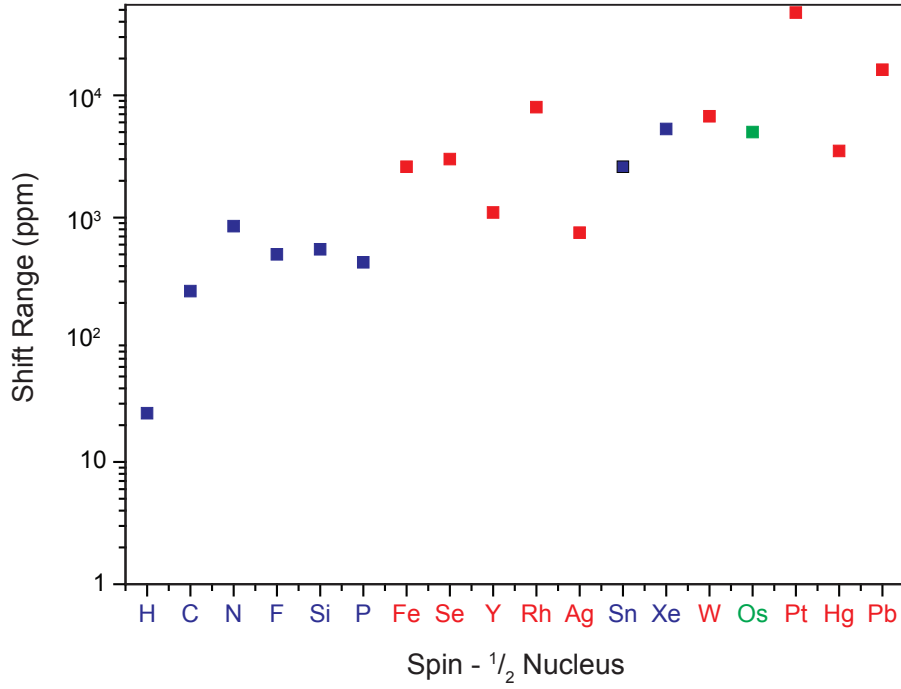


Figure 3.6: Shift ranges of some spin- $\frac{1}{2}$  nuclei ordered by increasing atomic number. The blue nuclei represent the commonly studied nuclei, with the red being far more difficult and the green of Osmium being the most difficult. The tendency of heavier nuclei to show larger shift ranges is clearly visible. For the d-block elements the chemical shift range is usually dominated by the Knight shifted metal, which will usually sit at an extreme of the range.

a line width described by  $T_2$  you get:

$$g(\omega) \propto \gamma B_1 \frac{1/T_2}{(1 + S)/T_2^2 + \omega^2} \quad (3.19)$$

where

$$S = (\gamma B_1)^2 T_1 T_2 \quad (3.20)$$

This is known as the saturation parameter, which is dependent on both the spin-spin relaxation and the spin-lattice relaxation. This shows that to maximize the signal the  $B_1$  has to be as large as possible, however to keep the distortions low the  $B_1$  has to be as small as possible. For solids with long  $T_1$  values this causes a substantial problem.

The second method for completing CW experiments is known as the adiabatic

fast passage. [102] This method uses the basis that the nuclear magnetism remains aligned with the effective field ( $B_e = (B_1, 0, B_0 - \frac{\omega}{\gamma})$ ) in the rotating frame. In solids, a signal can be observed if the  $B_1$  strength and the scanning rate ( $\frac{d|B_0|}{dt}$ ) fulfill the following condition:

$$\frac{1}{T_1} \ll \frac{1}{B_1} \frac{d|B_0|}{dt} \ll |\gamma B_1| \approx \frac{1}{T_2} \quad (3.21)$$

Since the final relationship means that the nutation frequency  $\omega_1 = \gamma B_1$  must be comparable to the line width, one has a restriction similar to that for pulse methods. The above CW methods are becoming increasingly difficult to complete as spectrometers which operate by these methods have been discarded.

To compensate for the lack of CW spectrometers, a series of pulses are used across the entire shift range. This is known as point wise detection by spin echoes, dot-to-dot detection, spin echo height spectroscopy (SEHS) and spin echo integration spectroscopy (SEIS) <sup>3</sup>. They are unable to resolve spectral features lower than the sampling resolution on the frequency axis and SEHS will not reproduce a lineshape faithfully if the acquired spectrum contains components with different relaxation times as it will under represent the intensity from slow relaxing nuclei. The advantage of point-by-point spectra is that the sampling resolution is not prescribed as for summed FT techniques and therefore fewer acquisitions can be made and the full spectrum reproduced in a shorter timescale.

The disadvantage of this technique is it provides a lineshape estimate due to difficulties with the number of points to sample on the line, normalising probe tuning and the duration of the experiment. This method usually contains large errors upon deconvolution as narrow details of the line are usually not recorded. By using the principle of CW spectroscopy, sequential detection in different parts of the spectrum will trace the lineshape, as the height/integration of the spectrum is a direct measurement of the intensity of at that irradiation frequency. There are two options for achieving this goal, either the field or the frequency can be swept through the frequency range. The disadvantage of sweeping the frequency is that the probe is required to be re-tuned for each frequency. These methods are currently heavily used for wide line NMR results of both quadrupolar and spin- $\frac{1}{2}$  nuclei.

Another method for improving excitation over a wider frequency is to use composite pulses, the basic outline of this approach is to use a series of pulses which mimic a single broad band pulse. [103] The extra degrees of freedom observed in a

---

<sup>3</sup>These methods will be compared to our Field-Sweep Fourier transform method for gathering wide line Platinum data. [63] It is worth noting that the majority of solid state <sup>195</sup>Pt NMR is completed by the SEHS technique.

series of pulses are used to improve the overall pulses properties as it strives towards an ideal delta function. In the context of wide line excitation the key is to minimize the phase dispersion as a function of the offset frequency. The most common method for doing this is to employ a 'spin knotting' sequence:

$$(\phi_1)_{+x} - \tau_1 - (\phi_2)_{-x} - \tau_2 - (\phi_3)_{+x} \quad (3.22)$$

with the  $\phi_i$  angles fulfilling the condition:

$$\phi_1 - \phi_2 + \phi_3 = 90^\circ \quad (3.23)$$

A trial and error method is then employed on the remaining four degrees of freedom to optimize the performance of the sequence for varying  $B_1$  strengths.

A more direct and general approach to the construction of sequences that approximate ideal pulses predicts that the following composite pulses is equivalent to an ideal  $(\frac{1}{2}\pi)_{+x}$  with minimum phase dispersion:

$$(385^\circ)_{+x}(320^\circ)_{-x}(25^\circ)_{+x} \quad (3.24)$$

This method uses a series expansion meaning more and more pulses can be joined together to give a wider line excitation frequency with the phases of the excitation remaining almost constant.

Composite pulses do however have limitations, the power theorem of Fourier transforms:

$$\int_{-\infty}^{\infty} |p(t)|^2 dt = \frac{1}{4\pi} \int_{-\infty}^{\infty} |p(w)|^2 dw \quad (3.25)$$

This relates the power in the pulse train as a function of time ( $p(t)$ ) to the power available in the spectrum as a function of amplitude ( $p(w)$ ). These are both complex functions as they both contain phases. If you assume a constant amplitude  $|A|$  for the pulses and a flat spectrum of pulses with a constant amplitude  $|B|$  you can obtain:

$$|A|^2 \Delta t = \frac{1}{4\pi} |B|^2 \Delta w \quad (3.26)$$

Here  $\Delta t$  is total time which the transmitter is on and  $\Delta w$  is the excitation bandwidth. It is obvious that a larger frequency range can only be obtained by increasing the total length of the pulses. It must be noted that typical pulse lengths used for these complicated wide line nuclei are usually around the 5  $\mu s$  length,

meaning simple composite pulse lengths may last the entire length of the acquisition time ( $T_2 \approx 20 \mu s$  maximum), hence it is usually not possible to use more complicated pulse sequences than those discussed above.

The obvious way to achieve wide line reconstruction is by varying the frequency offset and summing the Fourier transformed products. This is known as frequency step and sum (FSS) or variable offset cumulative frequency sweeping (VOCS). [104] It consists of recording the transient signal at a series of magnetic fields and summing the corresponding FT signals. This method favours very defined quadrupolar line shapes as errors can then be derived from theoretical simulations and corrected from the final result. The sensitivity of the experiment is dependent on the size of the  $B_1$  field. A key assumption is that the signal detection collects the entire transient signal of the precessing nuclei. This can become problematic for very wide lines due to the probe dead time and usually echoes are used to improve this. Therefore it must be presumed that the echo does not favourably excite different sites or parts of the resonance as it would for narrow purely magnetic spin packets. Finally, the response of the probe and spectrometer is required to be linear across the entire stepped range, this is completed by tuning and matching the probe uniformly across the range. A way around these limitations is to use variable offset cumulative frequency stepping (VOCS) NMR. If done for a sufficient number of frequency steps, VOCS will give an accurate reproduction of the resonance. However, in order to avoid distortions of the lineshape (distortions are less than 4% of the signal strength) due to an insufficient frequent sampling the acquisitions must be no further apart than 75% of the full width at half height of the signal acquired at each frequency. So it is advantageous to maximise the excitation width and thus minimise the pulse lengths so that fewer acquisitions are required over a given frequency range. The downside of VOCS is the difficulties in normalising probe tuning and the requirement that an operator is on hand at the end of each slice. This method is the most commonly used Fourier transform method for achieving spectra of wide lines.<sup>4</sup>

Focus on wide line quadrupolar NMR has led to many techniques being developed to aid excitation bandwidths and increase signal intensity, hence achieve accurate quadrupolar line shapes. Signal enhancement followed by VOCS has been commonly used to improve signal to noise and improve the summation process of VOCS. Methods including quadrupolar Carr-Purcell-Meiboom-Gill (QCPMG), Wideband, Uniform Rate, and Smooth Truncation (WURST), direct frequency sweeping (DFS)

---

<sup>4</sup>This method is also compared against SEHS and Field sweep FT method (FSFT) in future chapters

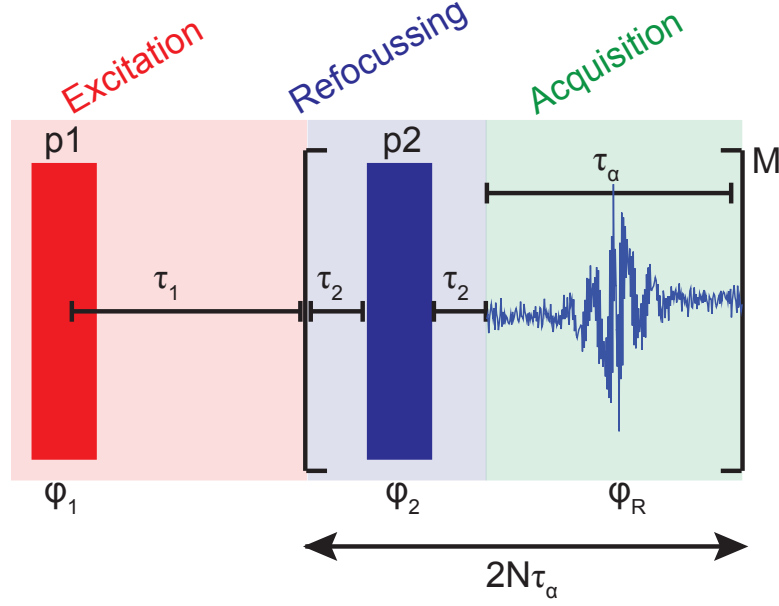


Figure 3.7: The general pulse sequence used for static CPMG, a QCPMG sequence has the addition of an initial  $90^\circ$  pulse with acquisition before this sequence is applied.  $P_1$  is the excitation pulse with  $P_2$  being the refocusing pulse.  $\tau_\alpha$  is the acquisition time for each echo which determines the spikelet separation  $\frac{1}{\tau_\alpha}$  after Fourier transformation. For the WURST-QCPMG the initial pulses  $P_1$  and  $P_2$  are changed into WURST-80 pulses.

and adiabatic pulse sequences. [105–114]

Using the QCPMG sequence, the magnetization is refocused repetitively giving rise to a train of echoes, which upon Fourier transformation gives a set of spikelets with a manifold resembling the conventional powder pattern. Since all the intensity is allocated into sharp spikelets, a large gain in signal-to-noise ratio (S/N) is obtained at the expense of resolution, which is dictated by the spikelet separation. The QCPMG sequence is capable of enhancing signal to noise by an order of magnitude.

The CPMG pulse sequence is a straightforward robust method for signal enhancement for both non quadrupolar and quadrupolar nuclei. Hung and co workers have demonstrated a set of guidelines for the practical implementation of any CPMG experiment, here is the summary: [115, 116]

1. A two step phase cycled minimise inaccurate parameters settings and also gives implicitly to the experiment.
2. A  $p_2$  flip angle at  $120 - 150^\circ$  can be used to give an increased bandwidth

excitation.

3. The number of points per echo and CPMG cycles should result in  $2n$  of the total data points.
4. When phasing the spectra a purely absorptive first order phase correction should be used
5. If acquisition using a two step phase cycle fails due to destructive interference between the coherence transfer pathway, then a four step cycle can be utilised to ensure these modulations do not give a S/N decrease.

WURST-QCPMG uses a spin echo sequence with frequency swept chirp pulses with WURST-80 pulses. Frequency sweeps provide a method of frequency independent broadband excitation and refocusing which is not limited by the time  $\times$  bandwidth  $\approx 1$  relation of monochromatic pulses. The pulse sequence has generally found application in wide line NMR and is combined with CPMG to dramatically reduce experiment time.

For a WURST-QCPMG the following rules should be attempted to be obeyed:

1. The rates of the WURST pulses should be set so  $p1 = p2$  to avoid spectral distortions.
2. The spectra may require second order phase corrections
3.  $V_1 = 0.26\sqrt{R_1}(I + \frac{1}{2})^{-1}$  can be used as a starting optimisation point for both WURST pulses
4. P2's rf field strength can be optimised around  $V_1(P_2) \approx 2V_1(P_1)$ .

These pulses sequences are represented diagrammatically in figure 3.7.

### 3.4.7 Pulsed Fourier Transform Field Sweep Nuclear Magnetic Resonance

The preferred method for wide line acquisition in this thesis is by a method called field sweep FT (FSFT) nuclear magnetic resonance. This involves maintaining the probe at a set tuned frequency and varying the magnetic field at set intervals. The results are then FT processed and offset by the respective interval size before being summed. Although in principle the technique can be used to generate line shapes in an SEHS/SEIS manner the advantage of the FT approach is the line is not limited by the sampling ratio and hence accurate deconvolution of the resonance can take

place. The probe is tuned at a single frequency throughout all acquisitions but the applied field ( $B_0$ ) is varied between each acquisitions.

$$\omega_{0\beta} = \omega_{0\alpha} \frac{B_{0\beta}}{B_{0\alpha}} \quad (3.27)$$

The above equation calculates the Larmor frequency ( $\omega_{0\alpha}$ ) at the initial field,  $B_{0\alpha}$ , for spins for which  $\omega_{0\beta} = \omega_{REF}$  at the swept field strength,  $B_{0\beta}$ . [117] By converting the different field steps into frequencies, in the initial field, the spectra can be referenced with respect to one another and summed as seen before in VOCS. As well as retaining all the benefits of summed FT frequency stepped NMR, field sweeping eliminates the errors and labour associated with retuning of the probe between acquisitions. The major disadvantage is that most of the interactions (i.e. CSA and quadrupolar) vary with field, so there can be errors when simulating the spectra if large sweeps are needed; these however are presumed to be minor. [118]

### 3.4.8 Multiple Quantum Magic Angle Spinning

The ability to distinguish between local environments in solid state NMR depends largely on the resolution of the achieved spectra. If multiple quadrupolar lines are present in the result then it may become difficult to deconvolute the spectra to its corresponding environments. The quadrupolar broadening is increasingly more difficult to remove than the corresponding CSA and dipolar interactions as it contains higher order orientational terms in significant magnitude. In the past two decades multiple quantum (MQ) pulse sequences have become more common in the literature and combining this with MAS was a natural progression to form MQMAS. [39] The most prominent nuclei readily studied by MQMAS are  $^{11}\text{B}$ ,  $^{17}\text{O}$ ,  $^{23}\text{Na}$ ,  $^{27}\text{Al}$  and  $^{87}\text{Rb}$ ; however MQMAS results have also been recorded for samples containing the low  $\gamma$   $^{43}\text{Ca}$  nuclei as well. [119]

The basic MQMAS experiment consists of four steps, the first is an RF excitation of the MQ coherences, next is the evolution of these coherences under the internal Hamiltonian during time  $t_1$ . Another RF pulse is added to convert the MQ coherences into the observable single quantum state and finally the signal is detected as a function of the time,  $t_2$ . [120–122]

If we look at the theory behind this technique we can see that under MAS conditions the Hamiltonian can be taken as the Zeeman interaction with the addition of the second-order quadrupole interaction. As previously mentioned the multiple quantum coherence (for the purpose of this thesis only triple quantum states were utilised, hence from now on a MQMAS will be named as a 3QMAS) evolves only

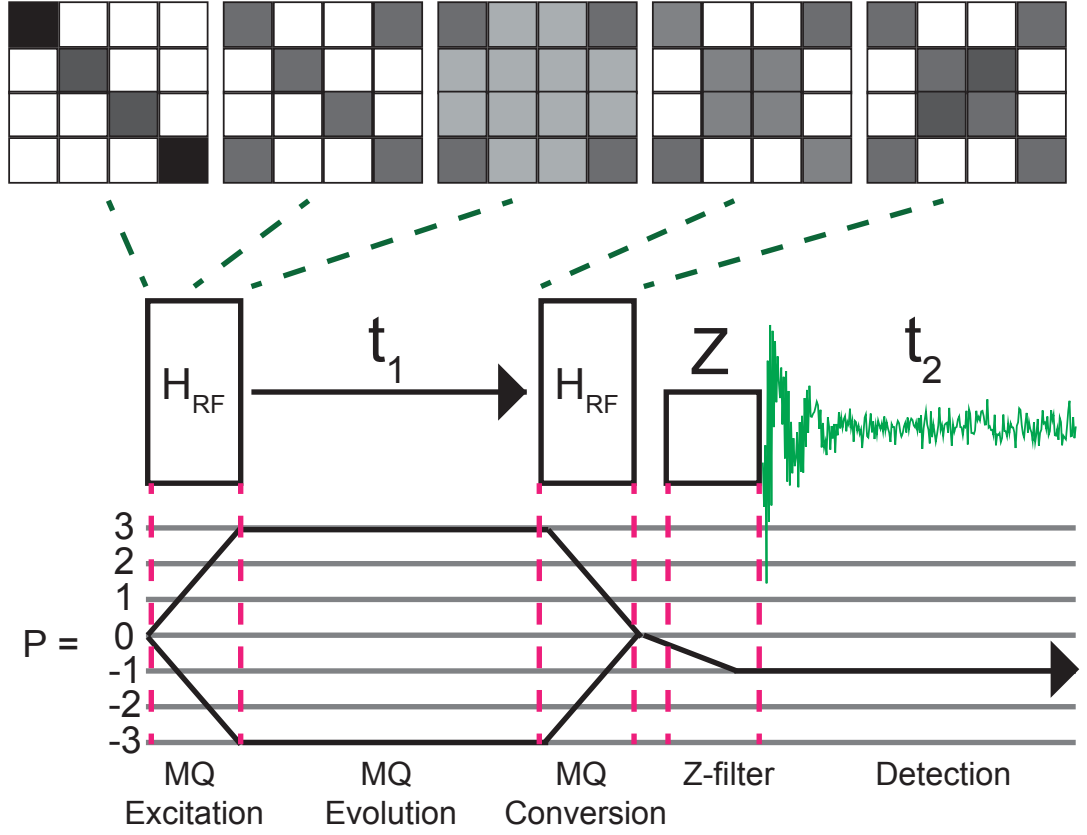


Figure 3.8: Schematic of a typical z-filter 3QMAS experiment, the time evolution of the reduced density matrix of a spin  $\frac{3}{2}$  nuclei is shown at the top with the darker the square representing the increased amount of coherence present

during the time period  $t_1$  and the single quantum only under  $t_2$ . As such, the signal can split into these two components for all half integer quadrupole nuclei: [123, 123, 124]

$$s(t_1, t_2) \propto \exp(i\omega_{\frac{3}{2}}^{(2)} t_1) + \exp(i\omega_{\frac{1}{2}}^{(2)} t_2) \quad (3.28)$$

The frequency shift is a consequence of the second-order quadrupolar Hamiltonian, with the second-rank tensor reduced as the experiment is completed under MAS with rotor synchronisation. Therefore, under fast MAS rotation ( $\Delta_m = 54.74^\circ$ ) the simplified evolution phase can be written as:



$$\begin{aligned}\phi^{MAS}[\frac{m}{2}, -\frac{m}{2}] &= p[v_0\Delta\delta + m_I J] + A_0^Q(\eta_Q)C_0(S, p) \\ &+ A_4^Q[(\alpha_R, \beta_R, \eta_Q)C_4(S, p)P_4(\cos\chi_m)]t\end{aligned}\quad (3.29)$$

Here  $p$  is being utilized to represent the multiplicity states  $m - m'$ .

The remaining anisotropic broadening originates from the final term in the above equation, which is scaled with respect to the one-dimensional static spectra and cannot be fully removed by MAS. The unconventional method of allowing the second-order quadrupolar broadening to be modulated outside the allowed central transitions and then transferred back to the observable state to be freely evolved  $t_2$ . The evolution of  $t_1$  and  $t_2$  are then correlated in a 2D experiment. The isotropic echo is observed as shown below, where  $R(S, p)$  is:

$$t_{2e} = - \left[ \frac{C_4(I, p)}{C_4(I, -1)} \right] t_1 = R(I, p)t_1 \quad (3.30)$$

where  $R$  is proportional to:

$$R(I, p) = \frac{p[36I(I+1) - 17p^2 - 10]}{36I(I+1) - 27} \quad (3.31)$$

As the sign of  $C_4(I, p)$  is reversed when changing that of  $p$ , it is always possible to obtain a positive ratio for  $R(I, p)$  which leads to a detectable echo each time ( $t_{2e}$ ). Therefore, the observed echo experiment for all of the 3QMAS experiments in the following thesis is  $0 \rightarrow p = -3 \rightarrow 1$  with the antiecho going from  $0 \rightarrow p = 3 \rightarrow -1$ .

The product of this is a two-dimensional Fourier transform of the time-domain signal which provides a correlation spectrum consisting of narrow resonances sites with ridges extended along the direction by:

$$F_1 = R(I, p)F_2 \quad (3.32)$$

where  $F_1$  and  $F_2$  represent the frequencies in the MQ and SQ dimensions respectively. The results are usually displayed in a sheared format as discussed below.

### 3.4.9 Shearing

The 3QMAS spectra can be easily analyzed by providing a shearing transformation to the raw two dimensional data. [125, 126] This places the A axis parallel to the F2

axis and creates a new dimension labeled the Fiso (or  $\delta_{iso}$ ). The direct advantage of this transformation is that the newly created Fiso axis no longer contains any of the anisotropic quadrupolar and chemical shift contributions. The distortions obtained on the F2 axis mean it is difficult to simulate this as a one dimensional spectrum, as small errors can have large effects of the  $C_Q$  and  $\eta_Q$  parameters of the lineshape.

In the sheared spectrum the frequency Fiso can be conveniently expressed as a linear combination of the sum of the F1 and F2:

$$F_{iso} = F1 + R \cdot F2 \quad (3.33)$$

This convention allows the direct determination of the sample rotation rate from the sheared spectrum when plotted in the Hz scale. In order to reference the sample (ppm), an appreciation of the quadrupolar shift to the overall line position is required. The quadrupole interaction shifts the resonance away from the chemical shift in both dimensions. Thus, after shearing the quadrupolar induced shift in the Fiso dimension becomes positive and independent of  $p$ .

$$\delta_{QIS,iso} = \frac{v_{QIS,iso}(I,p)}{(R-p)v_0} 10^6 = -\frac{10}{17} \delta_{QIS}(I, -1) = -\frac{10}{17} k_1 P_Q^2 \quad (3.34)$$

The gradient,  $-\frac{10}{17}$ , is independent of the spin and coherence states. Hence for any given spin system the chemical shift axis is independent. This method of referencing is also directly applicable to satellite transition MAS.

Some of the 3QMAS spectra produced in this thesis do not have sharp quadrupolar discontinuities and instead contain a distribution of the parameters. Here we have employed a common numerical analysis of the results to give the quantification of the quadrupolar parameter ( $P_Q$ ) and the chemical shift dispersion. This can be used to access the degree of disorder in the system. [127]

The sheared MQMAS spectrum is described by the integral of the individual lineshape two dimensional 3QMAS spectra over all possible combinations of the chemical shift and  $P_Q$ .

$$S_c(\delta_2, \delta_{iso}) = \int_{-\infty}^{+\infty} d\delta_{CS} \int_0^{+\infty} dC_Q \int_0^1 S_c(\delta_2, \delta_{iso}; \delta_{CS}, C_Q, \eta_Q) \times \Pi(\delta_{CS}, C_Q, \eta_Q) d\eta_Q \quad (3.35)$$

Where  $S_c$  is the calculated sheared 3QMAS corresponding to a single set of lineshape parameters like the chemical shift ( $\delta_{iso}$ ), quadrupole coupling constant

( $C_Q$ ) and the asymmetry parameter ( $\eta$ ).

Here we complete both techniques and present the data by the inversion method. [128] The inversion method assumes that there are only two unknown values namely the  $P_Q$  and  $\delta_{iso}$ . An approximation is used for  $\eta_Q$  in order to calculate the sheared spectrum for a given value of  $P_Q$ . In the two dimensional sheared spectrum there is a slice which contains a superposition of all the one-dimensional 3QMAS filtered spectra. The two-dimensional integral of the above equation becomes:

$$S_c(\delta_2)_{\delta_{iso}} = \int_0^\infty S_c(\delta_2; \delta_{CS}(P_Q), P_Q) \Pi(\delta_{CS}(P_Q), P_Q) dP_Q \quad (3.36)$$

Solving this equation to obtain  $\Pi(\delta_{CS}(P_Q), P_Q)$  leads to the the inversion of the spectrum. Each slice of the spectrum the distribution of  $\Pi$  is evaluated against the  $P_Q$  and for each given  $P_Q$  the  $\delta_{iso}$  is determined. This gives a calculated curve which represent the two-dimensional parameter space. The superposition of the curves obtained for all these slices give the two dimensional distribution function  $\Pi(\delta_{CS}, C_Q)$ . Solving this integral is technically difficult and a series of regularization techniques have been developed. However, the results achieved do give information about the disorder and variations of the two-dimensional line shapes.

### 3.4.10 Double Orientation Rotation

Double Orientation Rotation (DOuble Rotation, DOR) is a process of fast sample rotation at two angles, which applies a modulation on the second order quadrupole coupling causing an overall reduction in line width. [30, 129] MAS is shown to be very effective in reducing the CSA and dipole-dipole interactions in spin  $\frac{1}{2}$  nuclei, however it is far less efficient at remove the broadening caused by the quadrupole interaction. Typically the line broadening generated by the angular dependence of the 2nd order quadrupole interactions in a strong static magnetic field is large when compared with the shielding anisotropies. Generally, only the  $\frac{1}{2} \leftrightarrow -\frac{1}{2}$  can be readily observed (although overtone NMR is having some success reducing this) because the central transition is broadened only by the second-order quadrupole perturbation on the Zeeman interaction.

During a DOR experiment the sample is spun at two angles, the inner rotor rotates at  $\beta_1 = 30.56^\circ$  with a frequency between 5 - 12 kHz. The much larger outer rotor spins between 0.8 - 2 kHz at the magic angle of  $\beta_2 = 54.74^\circ$  with respect to  $B_0$ . This reduces the respective first and second order Legendre polynomials  $P_2(\cos^2 \theta)$  and  $P_4(\cos \theta)$  where (previously shown in figure 2.2):

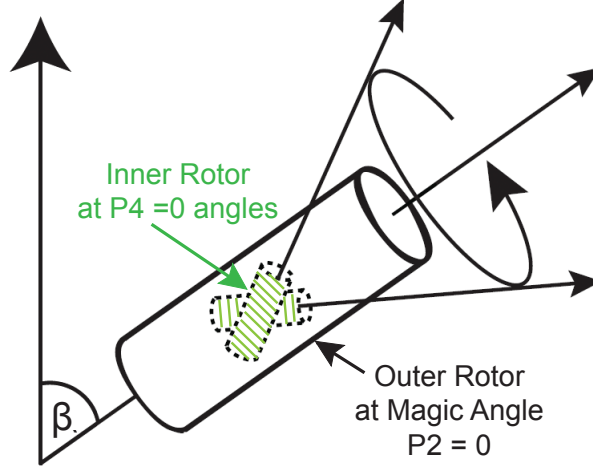


Figure 3.9: Schematic of a DOR rotor and the angles at which the inner and outer rotor spin. The outer larger rotor spins at the magic angle of  $54.74^\circ$ , with the smaller inner rotor spinning to narrow the  $P_4$  terms of the Legendre polynomials at  $30.56^\circ$  or  $72.19^\circ$ .

$$P_2(\cos \theta) = \frac{1}{2}(1 - 3 \cos^2 \theta) \quad (3.37)$$

$$P_4(\cos \theta) = \frac{1}{8}(35 \cos^4 \theta - 30 \cos^2 \theta + 3) \quad (3.38)$$

It can be observed that there is no common root to the above equations, hence when  $P_2(\cos^2 \theta) = 0$  then the  $P_4$  term is equal to  $-\frac{7}{18}$ . This is only applicable to lines in which the quadrupolar broadening is the dominant feature. The sample motion under DOR renders the Hamiltonian time-dependent through the changes in the polar angles  $(\beta, \alpha)$  with respect of the PAS. [130, 131] As the adjacent non-degenerate levels are presumed to be separated by  $h\nu_L$  the time dependence of the Hamiltonian under DOR is considered to be adiabatic<sup>5</sup> given the spinning rates of the outer rotor are much smaller than  $\nu_L$ . This spinning at these two angles reduces both the  $P_2$  and  $P_4$  terms of the polynomials and hence gives increased spectral resolution of quadrupolar broadened results.

The ability of one rotor to spin inside another depends upon the torque exerted by the inner rotor upon its outer host rotor. For successful spinning it requires the inner rotor to be small with respect to the outer rotor. The torque is zero if the following equation is satisfied:

<sup>5</sup>the quadrupole interaction is presumed to only add a small correction

$$\frac{\omega_{IR}}{\omega_{OR}} = \cos \beta_{IR} \left( \frac{I_{tr} - I_{ax}}{I_{ax}} \right) \quad (3.39)$$

Here  $\omega_{IR}$  and  $\omega_{OR}$  are the angular frequencies of the inner and outer rotors respectively,  $\beta_{IR}$  is  $30.56^\circ$  for DOR; which represents of the angular separation between the inner and outer rotors. The transverse and axial moments of inertia on the inner rotor is represented by the  $I$  terms in the above equation.

As with MAS the formation of spinning sidebands is seen with a separation governed by the outer rotor spinning speed. [132] As the sample is effectively axially orientated when compared to the outer rotor, if the start of the acquisition is alternatively synchronized at the outer rotor positions where  $\gamma_{IROR} = 0^\circ$  and  $180^\circ$ , while each phase cycle is kept fixed for two acquisitions rather than one, then all the odd numbered sidebands should be canceled. This will give increased spectral resolution when multiple peaks are present in the spectra. [130]

The resultant DOR peak ( $\delta_{DOR}$ ) occurs at the centre of gravity of the MAS spectrum as it is displaced from the  $\delta_{iso}$  by the quadrupole shift ( $\delta_{QIS}$ ).

$$\delta_{DOR} = \delta_{iso} - \delta_{QIS} = \delta_{iso} - \frac{3}{40} f(I) \frac{P_Q^2}{v_0^2} \quad (3.40)$$

where

$$P_Q = C_Q \sqrt{\left(1 + \frac{\eta_Q^2}{3}\right)} \quad (3.41)$$

and

$$f(I) = \frac{[I(I+1) - \frac{3}{4}]}{I^2(2I-1)^2} \quad (3.42)$$

for  $I = \frac{3}{2}$  then the product becomes  $\frac{1}{3}$  and for  $I = \frac{5}{2}$  it becomes  $\frac{2}{25}$ . [133] Thus to achieve isotropic shift data from DOR measurements it is necessary to achieve data at multiple fields and plot magnetic field against the observed centre gravity.

### 3.5 Density Functional Theory Calculations; The CASTEP Code

The advancement of computational calculations and NMR experiments has led to a symbiotic relationship between experimental spectra and calculated parameters in

recent years. There is a clear need for quantitative theoretical support to all major experiments. First principle quantum mechanical calculations methods have the potential to provide information regarding the expected parameters you will see during the NMR experiment. This gives an insight into what experiments maybe needed to characterise a sample or whether NMR is the correct tool for characterisation.

Density functional theory was developed by Kohn<sup>10</sup> in the 1960s. [134, 135] The main discovery was that the total electronic energy of a system in an external potential is a unique function proportional to the ground state density. Hence, if the density is known then one should be able to calculate the energy of the system. Unfortunately this ground state density is unknown, but with relatively educated guesses you can obtain excellent results. The particular external potential we are interested in is that generated by nuclei, but this is not necessary for density functional theory itself. The ground state density of the system can be estimated by generating a suitable many-body wavefunction, in principle this is a function of time which takes into consideration the coordinates of the nucleus and electrons. [49]

As the number of nuclear and electronic variables can be large a Born-Oppenheimer approximation is used to decouple the electrons from the nucleus. Hence it is presumed that the electron wavefunction is independent of the nuclear wavefunction. As the electronic wavefunction only depends on the instantaneous nuclear orientation and not its time then the wavefunction of the electronic component can be described using the time-independent Schrodinger equation. The added advantage of this is the nucleus is massive enough to be treated semi-classically and can be presumed to respond to the electrons in a Newtonian approach.<sup>6</sup>

It is important to take into consideration the crystal like arrangement of the sample when applying a wavefunction to it. In a periodic system any wavefunction must be the product of a cell part and a phase factor, this is known as Bloch's theorem. This is required in order to maintain the translational symmetry of the ground state density. The phase factor takes the form of a plane wave, whose wavevector is a linear combination of reciprocal lattice vectors. From this a plane-wave basis is used to express the wavefunction; both the phase and the cell part. This means that the basis functions are orthogonal and it is possible to Fourier transform between real and reciprocal space.

The Bloch states are labeled by their crystal momentum given the symbol  $\kappa$ . The problem of solving for an infinite number of electrons has become one of

---

<sup>6</sup>This approximation can fall short with small nuclei such as proton and lithium, with the zero point of motion can have substantial effects on the ground state

calculating for a finite number of bands at an infinite number of  $\kappa$ -points. This is surpassed as the physical properties of the studied system are expected to smoothly vary with  $\kappa$  and hence many integrals can be well approximated by finite sampling of  $\kappa$ .

If the system studied is not periodic (i.e. contains Frenkel type defects, impurities or disordered) then a supercell is required to be constructed. This is a larger unit cell with a space region to separate the region of interest from the periodic images. The space is usually just supplied as a vacuum. By using these supercells to represent the disorder in the system it still gives the advantages of Bloch's theorem and limit the size of the calculation. However, they still tend to be enormous calculations which require large national supercomputers.

As the electrons in the system are orthogonal to every other state (due to their Fermi-ionic nature) then as the higher energy states become filled the orthogonal nature forces the wavefunctions of these states to have increasing numbers of nodes. From this the width of the Fourier spectrum increases and the number of plane-waves needed to represent our wavefunction increase. To limit this, many of the nodes are presumed to be in the core region (near the nucleus). The core region is presumed to contain relatively constant (even with changing chemical environment). Hence the lower energy states in these regions are removed and replaced with an effective potential. This is combined with the nuclear Coulomb potential to create a pseudopotential. The remaining higher states are described by the wavefunctions of the remaining orthogonal electrons, this reduces the number of nodes and the size of the calculation. The use of pseudopotentials dramatically reduces the number of plane waves required to represent the wavefunctions, whilst still giving accurate results.

The major advantages of DFT is that it offers very good scaling with computational cost making it an ideal choice for large periodic systems. Also, given the large number of calculations the likely accuracy of property prediction for many properties of differing systems is already known. The obvious disadvantages is that it only applies to ground-state, with many approximations made and from this it is difficult to improve the accuracy and predict the errors of the calculations.

CASTEP (CAMbridge Serial Total Energy Package) is a code developed to complete first principle calculations to predict the properties (for the purpose of this thesis only the magnetic response is desired) in various materials with periodic order. [136] This utilizes a gauge including projector augmented waves (GIPAW) basis, which maintains the core properties with all-electron accuracy.

To calculate the chemical shielding it is required to calculate the induced

orbital current around a nuclear site and to obtain a chemical shielding by Biot-Savart Law. [137] For quadrupolar nuclei only the electric field gradient (EFG) calculation is required and hence a far easier calculation. A minor concern is that the chemical shielding is given with respect to the bare nucleus. Hence, to obtain an isotropic shift an external reference is required to be run for a known isotropic shift, this can prove difficult as most quadrupolar nuclei are shifted by  $\delta_{QIS}$ . If multiple peaks are present then internal referencing can be used or an external reference with a known  $\delta_{iso}$  and is not shifted by 2nd order  $C_Q$  can also be used. [138, 139] CASTEP calculates the EFG by summing the three discrete terms, first there is a contribution arising from the ionic charge (which is the sum of the nuclear and core electron charge, this appears as an infinite lattice of point charges whose EFG can be obtained by an Ewald summation. [140] <sup>7</sup> Secondly there is a contribution of the valence charge density and finally PAW contribution to account for differences between then pseudo and all electron density charges.

In metallic systems the shielding arises from the previously explained shielding and Knight shift. It is possible to use a planewave-pseudopotential approach to compute these shieldings in metals. This is done by GIPAW to calculate the orbital response and PAW to calculate the Knight shift. These calculations are far more demanding than for insulators as you require fine  $\kappa$ -point sampling. For heavy nuclei relativistic effects dominate and the picture become slightly more difficult. [141] The Schrodinger equation ( $\hat{H}\Psi = E\Psi$ ) is nonrelativistic meaning it is validated for particles whose velocity is much slower than the speed of light. This approximation fails as you move to heavier elements which contain relativistic effects; these give significant influences on the bonding and hence the structural properties of the materials. This in turn has a significant influence on their magnetic response. To attempt to treat these heavier materials it is more insightful to base a description on the Dirac equation ( $[i\gamma_\mu \cdot \partial^\mu - m]\Psi = 0$ ). This is able to add the special relativity onto the quantum states, the main method for employing this is to use the pseudopotential to simply add these effects. In the construction of a pseudopotential the free atom is treated relativistically to give the correct eigenvalues, in insulators pseudopotentials the spin-orbit split states are usually averaged however maintain these splits in the potential hence creating a relativistic pseudopotential. The heavy metal Knight shifted samples present in this thesis have so far proven too difficult to

---

<sup>7</sup>An Ewald summation is a special case of the Poisson summation formula (Fourier series coefficients of the periodic summation of a function to values of the function's continuous Fourier transform), replacing the summation of interaction energies in real space with an equivalent summation in Fourier space. The advantage of this approach is the rapid convergence of the Fourier-space summation compared to its real-space equivalent when the real-space interactions are long-range.



produce a working relativistic pseudopotential for, hence no CASTEP calculations are present for that work.

# Chapter 4

## Characterisation of Platinum-based Fuel Cell Catalyst Materials using Wideline Solid State NMR

### 4.1 Introduction

#### 4.1.1 Background

Platinum catalysts have been utilised in a number of highly important roles in industry such as autocatalysis and in fuel cell technologies. [142–144] Heterogeneous platinum catalysis is dominated by surface and near surface catalysis as all significant reactions are known to take place away from the bulk metallic centre. [145] Due to the expense and scarcity of this metal, accurate structural determination of these compounds is very much needed to help minimise the amount of bulk precious metal used, keeping the surface area as large as possible. Local analysis of these compounds is difficult by NMR due to the unfavourably large range of environments, hence platinum NMR studies of such metallic catalysts are relatively scarce due to their very broad lineshapes ( $\geq 3$  MHz) caused by this dispersion in the NMR interaction parameters. [146–152]

$^{195}\text{Pt}$  is a 33.8 % naturally abundant spin- $\frac{1}{2}$  nucleus with a magnetogyric ratio of  $5.83 \times 10^7 \text{ rad T}^{-1} \text{ S}^{-1}$ . [52] Solution state  $^{195}\text{Pt}$  NMR measurements are much more commonly reported due to the motional averaging of the very large anisotropies that can exist in the solid state. Hence, solid state  $^{195}\text{Pt}$  NMR stud-

ies are still not common as these measurements are hampered by the very large shift range and concomitantly large anisotropies, combined with the moderate sensitivity of the  $^{195}\text{Pt}$  nucleus. [153, 154] The considerable significance of catalytic platinum means that much of the reported  $^{195}\text{Pt}$  solid state NMR literature relates to materials in such applications. [63, 155–159] Previous work has shown that the characteristics of the  $^{195}\text{Pt}$  NMR spectra are independent of support material, but are significantly altered by chemisorption of gases. [160–162] Bimetallic systems such as PtSn are active for the lower temperature oxidation of both methanol and CO, with Sn being an excellent modifier of platinum’s properties to prevent a surface ‘over-potential’ during catalysis. [163–165] In contrast, Pt alloyed with first row transition metals such as Fe, Co, and Ni exhibit superior activity for oxygen reduction than Pt alone. Tin has three stable NMR active isotopes ( $^{115}\text{Sn}$ ,  $^{117}\text{Sn}$ ,  $^{119}\text{Sn}$ ) each are spin- $\frac{1}{2}$  with similar magnetogyric ratios of  $-8.8$ ,  $-9.6$  and  $-10.0 \times 10^7 \text{ rad T}^{-1} \text{ s}^{-1}$  respectively. [52] Like  $^{195}\text{Pt}$  NMR, Tin has a large chemical shift range with most  $^{119}\text{Sn}$  observations from solid organometallic compounds exhibit large chemical shift anisotropies (CSA). [166] Previous  $^{119}\text{Sn}$  NMR work on tin alloys and bimetallics has been reported showing large chemical shift anisotropies. [167]

#### 4.1.2 Platinum Nanoparticles

Catalytic platinum is usually deposited as nanoparticles onto carbon, alumina or possibly zeolitic supports to maximise the surface to volume ratio. NMR lineshapes from platinum nanoparticles can be best described by a layer model. This description developed by Bucher and co-workers gives a relationship between the diameter of a particle and the number of atoms in each layer of the particle. [168, 169] Here a brief description of this theory is provided, based on a presumed spherical particle with diameter  $d$  indicated by transmission electron microscope (TEM) micrographs. To convert this diameter into the number of atoms present  $N$  then:

$$N_{tot} = \frac{2\pi}{3} \left(\frac{d}{a}\right)^3 = \frac{\pi\sqrt{2}}{6} \left(\frac{d}{2r}\right)^3 \quad (4.1)$$

Where  $a$  is bulk lattice parameter ( $a = 0.392 \text{ nm}$  for platinum) and  $2r$  is the hard sphere diameter of the atom ( $r = 0.139 \text{ nm}$  for platinum). Some errors within the TEM representation of the nanoparticles are due to small particle with diameters ( $d \leq 5 \text{ nm}$ ) deviating from the accepted cubo-octahedral shape and reassembling the data achieved from the TEM experiment. [170] For the purpose of the work here is the larger particle sized samples mean any complexities arising from this

effect can be ignored. To transfer this to an NMR model, it is presumed that the atoms in the nanoparticle are arranged in cubo-octahedral layers ( $m$ ), with each layer representing a resonance in the NMR spectrum. The total number of atoms present in the  $m$ th layer is proportional to:

$$N_L = \frac{10}{3}m^3 - 5m^2 + \frac{11}{3}m - 1 \quad (4.2)$$

For such a particle the number of Pt atoms in the surface layer,  $N_S$ , is given as:

$$N_S = 10m^2 - 20m + 12 \quad (4.3)$$

The number of atoms in any sub-surface layer is given by 4.3 by substituting  $m$  by  $m - x$ , where  $x$  is the number of layers away from the surface but does not include the central atom. The total atoms ( $N_{tot}$ ) is the sum of  $N_L$  and  $N_S$ ; these equations are not applicable to a single atom of platinum.

A 2.98 nm diameter platinum black nanoparticle has approximately  $N_{tot} = 940$  (equation 4.1), giving 7 – 8 layers when equation 4.2 is considered. However, it is presumed that at some point the inner core layers are sufficiently similar (i.e. bulk-like) that these environments amalgamate into a single spectral region, this helps with the deconvolution of the spectra when simulated.

Bulk  $^{195}\text{Pt}$  metal has a Knight shift of  $-3.5\%$  referenced to the primary IUPAC chemical shift reference and not against the typical reference usually reported for metals in the literature (which represents a  $\approx 3$  MHz downfield shift at 7.05 T) with PtO resonances located on the other up field extreme of the platinum chemical shift range. Hence, a platinum nanoparticle resonance following the layer model can span over a Knight shift distribution of 3.2 MHz (at 7.05 T) if bulk metal and the oxide surface are observed.<sup>1</sup>

The Knight shift is the relative shift  $K$  in metals when compared to an equivalent non-metallic surrounding. [26, 66] The total shift of the line is a product of many differing electron-nuclei hyperfine interactions as well as a chemical shift contribution. These have all been previously discussed in the theory section of this thesis; see 2.3.7.

A negative shift as seen in platinum metal is characteristic of an  $d$ -electrons. In a simplistic two band model, the contribution from the platinum  $5d$  band is

---

<sup>1</sup>The Knight shift of platinum varies throughout the literature depending on the primary ( $\delta_{iso} = 0$  ppm) reference sample utilised. The relative isotropic shifts of commonly used solution platinum references for solid state NMR experiments can be found in the Pregosin's review on platinum NMR. [171]

shown to be negative whilst those from the 6s band is positive, the relaxation is proportional to a sum of the squares (as  $Ki^2$ ) and is therefore always positive. [48] With the  $d$ -electron contribution shown to decay exponentially from bulk metal as you move to higher frequency and towards the platinum 001 surface. [156] If the symmetry of the material is lower than cubic then the full electron-nucleus interaction needs to be considered, hence an anisotropic contribution to the Knight shift occurs, this is also previously discussed in 2.3.7. [64]

### 4.1.3 NMR of Clusters

Metal clusters are made up of a core of metallic atoms stabilized by a surrounding layer of organic or inorganic ligands; in this case a core of  $\approx 13$  platinum atoms with alumina ligands preventing oxidation. In metallic systems when commenting on the Knight shift a comparison to the reference structure,  $K_2PtCl_6$ , is required. As previously mentioned, the total shift is the result of the Knight shift and the chemical shift contributions. [172] However, platinum in the bulk metal is generally surrounded by 12 platinum neighbours rather than the six coordinated chlorine atoms in the primary reference compound. This would give a different chemical shift component of the metal centre when compared to the primary reference, meaning the overall total shift term contains the chemical shift component for the specific local environment encountered (i.e. a central platinum atom surrounded by 12 other platinum atoms). It is known from Messmer *et al.* and Bucher *et al.* that  $Pt_{13}$  cubo-octahedral clusters (which contain a central platinum atom surrounded by 12 surface platinum atoms) have a highest occupied molecular orbital (HOMO) that is full and there is  $\approx 6000$  K difference between itself and the lowest unoccupied molecular orbital (LUMO), this essentially means no conduction (electrically neutral) can take place in a realistic NMR environments. [168, 173] Although there are expected quantum size effects associated with the size of small clusters, no obvious evidence is present in the NMR literature. Thus,  $Pt_{13}$  is shown practically to be an insulator; which is also practically observed by the increased tuning capacity of the NMR probe. If there is no apparent conduction then the resonance will only represent a chemical shift due to this structure, and unless motion is present then relaxation times should increase considerably, as the electron-spin relaxation mechanism in bare metals is no longer present. It has been shown by Pronk *et al.* that the Korringa relation ( $T_{1n} \propto \frac{1}{T}$ ) is not present in small carbonyl stabilised metal clusters of 26 and 38 platinum atoms. [174] These presumptions can only be made for a perfectly cubo-octahedral stabilised  $Pt_{13}$  cluster, difficulties in this synthesis led to a dispersion of platinum cluster sizes.

#### 4.1.4 Wideline Solid State NMR Techniques

The significant linewidth that results from the large shifts experienced by platinum means that it is not often possible to excite the entire line width simultaneously with any degree of uniformity using conventional approaches. Due to the linewidth in the  $^{195}\text{Pt}$  covering several MHz, standard Fourier transform (FT) techniques are inappropriate and a point-by-point soft pulsing reconstruction of the spectrum is the norm throughout the literature of such samples. These techniques have been covered previously in this thesis in section 3.4.6 and are named Spin Echo Height Spectroscopy (SEHS) or Spin Echo Integration Spectroscopy (SEIS), Variable Offset Cumulative Spectroscopy (VOCS) and Field Sweep Fourier Transform (FSFT) NMR this is addressed individually in 3.4.7.

## 4.2 Experimental

### 4.2.1 Synthesis

The platinum nanoparticles, platinum-tin complexes and alloys were synthesised using methods previously described by Buchanan et al. [175] The platinum clusters were prepared by the synthesis method previously described by Wen and co-workers. [176]

### 4.2.2 XRD Measurements

XRD patterns were measured on a Bruker AXS D-8 diffractometer using CuK (Ni filtered) radiation at ambient temperature. Scans were typically between  $10$  and  $130^\circ 2\theta$  with  $0.02^\circ$  step sizes. Lattice parameters and crystallite sizes were calculated using the LVol-IB method, a Rietveld complete powder diffraction pattern fitting method. Reference patterns were obtained from the Powder Diffraction File; Pt (PDF No. 00 – 004 – 802, cubic  $a = b = c = 3.92310\text{\AA}$ ),  $\text{Pt}_3\text{Sn}$  (PDF No. 00 – 03501360, cubic  $a = b = c = 4.00150\text{\AA}$ ), and  $\text{PtSn}$  (PDF No. 00 – 0250614, hexagonal  $a = 4.10000$   $b = 4.1000$   $c = 5.43200$ ). The lattice parameters for the platinum alloy and intermetallic systems are shown in the table A.1.

### 4.2.3 Solid State NMR

The  $^{195}\text{Pt}$  NMR experiment was conducted on a Chemagnetics CMX-300 spectrometer (Larmor frequency of 64.1 MHz) equipped with 7.05 T Magnex magnet with a 0.5 T sweep coil within the main dewar whose operation has been described previously. [117] Due to full width a half maximum height of the line being in the order of

MHz two references were utilised; a primary reference of 1.1 M  $\text{Na}_2\text{PtCl}_6(\text{aq})$  (Alfa Aesar) was located at  $\delta_{iso} = 0$  ppm and Pt metal reference (solid, Alfa Aesar) was measured at  $\delta_{iso} = -35,350$  ppm. [52] A 10 mm Bruker static (single channel) probe was used with  $\approx 0.5$  g of sample used for each measurement. Platinum has a skin depth of  $20.85 \mu\text{m}$  at 62.2 MHz and thus all nanoparticles studied were  $\leq 41.7 \mu\text{m}$  in diameter; these specific diameters were selected by fine mesh filtration. [177, 178] For each field sweep study a  $\frac{\pi}{2} - \tau - \pi - \tau$  spin echo was adopted which employed  $5 \mu\text{s}$  ( $\frac{\pi}{2}$ ) -  $10 \mu\text{s}$  ( $\pi$ ) pulses and  $\tau$  echo delays of  $20 \mu\text{s}$ . Each measurement consisted of 65 50 kHz effective-width slices spanning 61.1 to 64.3 MHz, thus giving a full sweep width of 3.2 MHz. A total of 240,000 transients per slice were taken with a relaxation delay of 40 ms (298 K) yielding a total experiment time of  $\approx 7.25$  days. The platinum clusters had a longer delay of 0.9 s and therefore only 8,000 transients per slice were collected.

The VOCS data were acquired using the same experiment and parameters, however due to the lack of automation with this approach the experiment time was considerably longer ( $\approx 2$  weeks).[104] The acquired SEHS spectra were sampled at regular intervals throughout the 3.2 MHz lineshape also using a  $\frac{\pi}{2} - \tau - \pi - \tau$  spin echo experiment, however softer  $8 \mu\text{s}$  ( $\frac{\pi}{2}$ ) -  $16 \mu\text{s}$  ( $\pi$ ) pulses were employed. For this approach the intensity of the echo top was then plotted against the central irradiation frequency which defined each data point. As only a coarse sample of the lineshape was acquired, the total experiment time was  $\approx 2$  working days.

The  $^{195}\text{Pt}$   $T_1$  measurements were undertaken using the common saturation-recovery pulse method which employed a pre-saturation comb of 100  $5 \mu\text{s}$  pulses separated by a  $5 \mu\text{s}$  inter-pulse spacing. This was followed by incremented delays varying in length between  $5 \mu\text{s}$  to  $15,000 \mu\text{s}$  for the metals, and 0.01 s to 2 s for the clusters.

$^{119}\text{Sn}$  magic angle spinning (MAS) NMR measurements were conducted at a magnetic field of 9.4 T (Larmor frequency of 148.7 MHz) using a Bruker DSX-400 spectrometer. These data were acquired using a Bruker 3.2 mm double-air-bearing MAS probe in which rotational frequencies of 12 kHz were implemented. All PtSn intermetallic samples were mixed in a 1 : 1 ratio (by weight) to reduce sample conduction and thus facilitate MAS operation, and prevent sample agglomeration. Single pulse experiments were used for these  $^{119}\text{Sn}$  measurements, where  $\frac{\pi}{4}$  pulses of  $1 \mu\text{s}$  duration were separated by recycle delays of 0.1 s. All measurements were referenced to a secondary solid sample of  $\text{Cy}_4\text{Sn}$  (located upfield at  $\delta_{iso} = -97.35\text{ppm}$ ) with respect to the primary IUPAC reference of  $\text{Me}_4\text{Sn}$  ( $\delta = 0$  ppm). [179] The  $^{27}\text{Al}$ ,  $^{45}\text{Sc}$ , and  $^{93}\text{Nb}$  static NMR data from these metals and the respective Pt alloy

Nuclei	Frequency	Pulse Width	Tip	Recycle
		( $\pi/2$ )	Angle	Delay
	MHz (B <sub>0</sub> )	$\mu$ s		s
<sup>195</sup> Pt	64.1 (7.05 T)	5.0	$\pi/2$	*
<sup>119</sup> Sn	148.7 (9.4 T)	11	$\pi/4$	0.1
<sup>93</sup> Nb	146.7 (14.1 T)	19	$\pi/4$	0.1
<sup>45</sup> Sc	145.6 (14.1 T)	27	$\pi/4$	0.1
<sup>27</sup> Al	156.3 (14.1 T)	38	$\pi/12$	0.1 <sup>a</sup>

Table 4.1: The experimental NMR Parameters used for the discussed nuclei. \* The relaxation times for the various platinum nanoparticles, intermetallics and alloys is given in table 4.5. <sup>a</sup> The recycle delay utilised for the Pt<sub>13</sub> clusters was considerably longer as illustrated in figure 4.4.

systems were acquired at 14.1 T (Larmor frequencies of 156.3, 145.6 and 146.7 MHz, respectively,) using a Bruker Avance II-600 spectrometer. All Pt alloy samples were also mixed with MgO (1 : 1 by weight) to reduce sample conduction and probe detuning issues. These experiments were performed in a Bruker 5 mm static probe using  $\frac{\pi}{2} - \tau - \pi - \tau$  spin echo methods. All data were referenced to their respective primary aqueous references as given in IUPAC guidelines shown in reference [52]. The sub skin depth metal meshes were all purchased from Sigma-Aldrich. All metal mesh and alloyed systems had rapid relaxation times of 0.1 s; with the <sup>27</sup>Al data achieved for the alumina coated clusters completed at a relaxation time of 1 s. The experimental conditions used in these experiments are shown in table 4.1.

### 4.3 Results and Discussion

The broad line Knight shifted platinum metal shown as the sharp upfield resonance in figure 4.1 is shown at the same location as bulk platinum metal ( $-35,350$  ppm, 1.138 G/kHz) with the surface oxide occurring  $\approx 3.0$  MHz downfield at  $+1,750$  ppm.

#### 4.3.1 Theory Versus Field Sweep Fourier Transform NMR

The metal centre of the nanoparticle has translational symmetry which is no longer present at the surface sites meaning the metal sites highest occupied orbital is very close in energetic terms to its ground state orbital hence a Knight shift contribution is present caused by the Pauli-like paramagnetism. At the surface the difference between the ground and highest occupied orbitals becomes sufficient that thermal



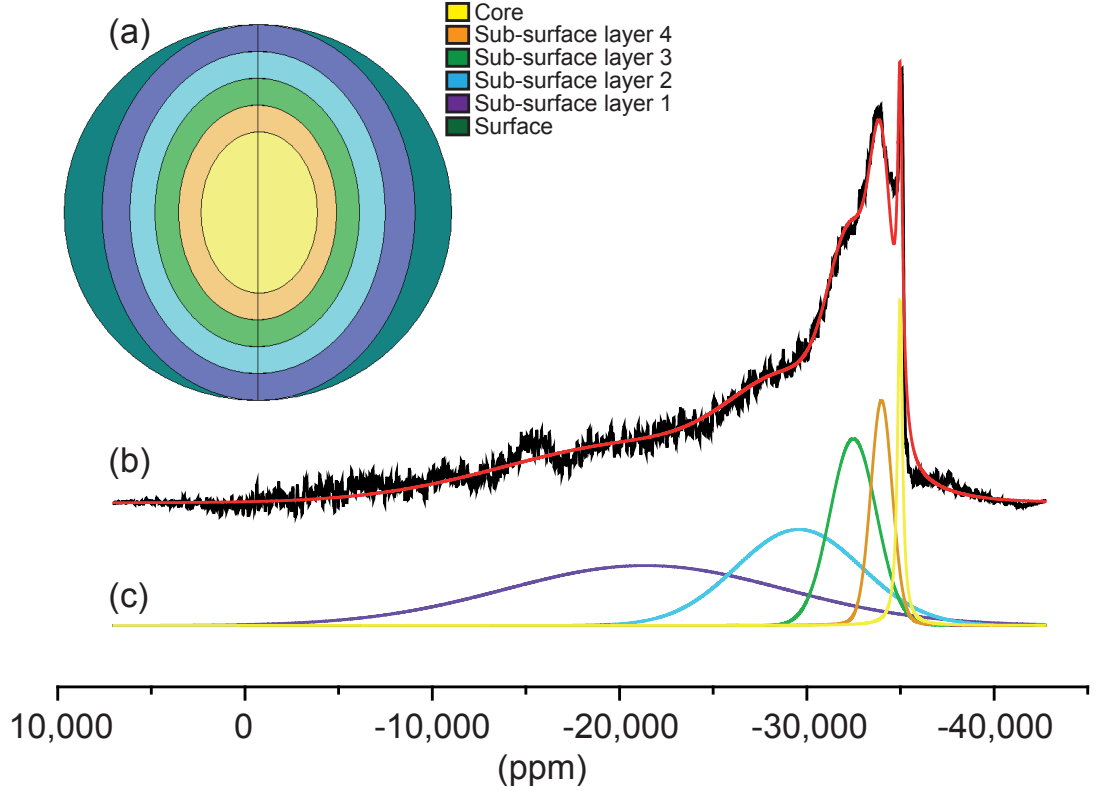


Figure 4.1: A NMR spectrum of a 5 nm platinum nanoparticle supported on carbon black. The layered shells present in a platinum nanoparticle are shown in (a), which gives the  $^{195}\text{Pt}$  FSFT spectra shown in (b) and finally in (c) is the deconvolution into each of the respected layers shown in (a). This diagram is re scaled and adapted from L. E. Barret thesis [180].

excitation to this level is less likely; giving a very much decreased Knight shift. Hence, distinguishing between the local densities of state at the various subsurface sites across the nanoparticle is shown in Figure 4.1. [179]

Figure 4.1 illustrates the deconvoluted unsupported 5 nm platinum nanoparticle, the result shows five shells are present with the inner three combined from the literatures model for simplicity. On moving to higher field the d-electron local density of states (LDOS) shows a monotonic decrease causing a shift and broadening of the spectra. This effect is enhanced by the platinum atoms in each region will have a perturbing effect from the neighbouring regions. The simulated spectrum is modelled against a theoretical nanoparticle of  $N_T = 3871$  atoms (4.81 nm diameter) representing the average nanoparticle size of 5 nm determined by Scherrer analysis of the XRD data.

Shift (ppm)	Theoretical $I$ (%)	Field Swept $I$ (%)	VOCS $I$ (%)	SEHS <sup>a</sup> $I$ (%)
( $\pm 100$ )	( $\pm 2$ )	( $\pm 2$ )	( $\pm 2$ )	( $\pm 5$ )
-35350	6	5	6	9
-34000	10	11	10	10
-32500	18	19	18	10
-29500	27	27	27	44
-21400	39	38	39	26

Table 4.2: Theoretical and experimental values for the relative intensities ( $I$ ) of the different regions based on a total atom number  $N_{tot} = 923$  (seven layers simplified to five). <sup>a</sup> - Due to lack of resolution, deconvolution of these peaks becomes incredibly difficult as gaps between sampled echo are joined by straight lines making a Gaussian fit inaccurate.

#### 4.3.2 Comparison of Commonly used Wideline Reconstruction Techniques

When the result in Figure 4.1 is compared with other wideline acquisition techniques, as shown in Figure 4.2, a good agreement between VOCS and FSFT NMR is revealed. Each region has been fitted using a 50 % Gaussian 50 % Lorentzian line shape to represent the dispersion of environments experienced by the platinum atoms within these layers. The success of each fit is illustrated in Table 4.2. The field sweep and VOCS methods show minimum errors when compared to the theoretical values, however due to the more dispersed sampling of the SEHS a larger error is present in the outer layers of the shell.

The three spectra have a significant number of similarities along with some key differences. Of most concern is the difference observed in the intensity of the bulk resonance at  $-35,350$  ppm. The VOCS approach shows no observed error in the intensity when compared with a theoretical nanoparticle of 3871 atoms. Conversely, the SEHS method shows a much larger discrepancy which can be eradicated by recording more data points, however this becomes very time consuming and thus eliminates the main advantage of SEHS.

The second obvious discrepancy is the oxide peak observed solely in the SEHS sample and is not present in the VOCS or FSFT methods. Previous work by Tong *et al.* has stated that unsupported catalysts show no surface effects, it is assumed that Tong *et al.* was referring to unsupported blacks that were electrochemically reduced before the NMR experiment and this is a possible reason why we do not

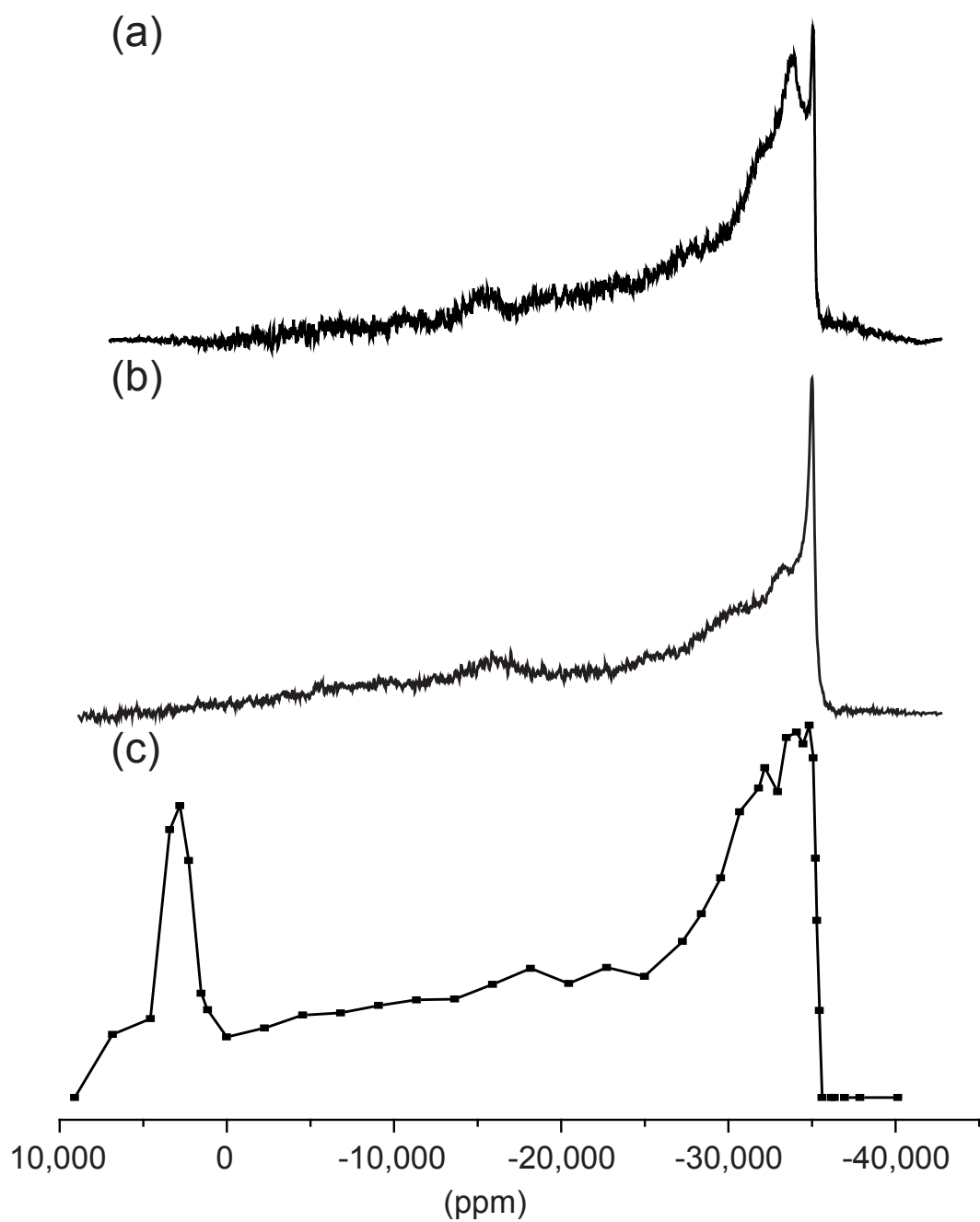
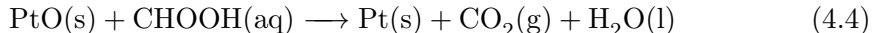


Figure 4.2: A 5 nm platinum nanoparticle compared by three commonly used wide-line techniques: (a) FSFT, (b) VOCS and (c) the literature heavy SEHS method. Diagram (a) is re scaled and adapted from L. E. Barret's thesis [180] and diagram (c) is edited from Simon Orr's [181].

see the same results and are able to detect the surface effects along with the oxide layer. [160, 161] Chemical reduction was attempted with an excess of formic acid shown in the chemical equation below; however it was not possible to tune the probe as the reduction process had an annealing effect, thus forming continuous volumes of conducting platinum with effective diameters greater than the skin depth. This may also be a reason for discrepancies with Tong’s results.



As the sample was oxidised this explains the appearance of platinum oxide peak at 1,750 ppm. It is expected that a large proportion of the surface layer is oxide due to the catalytic ability of platinum. However the sites attributable to the oxide layer(s), depending on the depth of oxide penetration, are likely to be broad due to their proximities to edges and corners of the nanoparticles. Such local structures would cause a change in the local electron structure between the oxide and the platinum surface giving an increased dispersion of sites which would lead to the resonance being broader than that of the non-oxidised Knight shifted surface.

#### 4.3.3 Field Sweep Fourier Transform (FSFT) NMR comparison Versus Spin Echo Height Spectroscopy (SEHS) NMR

Figure 4.3 shows a comparison of FSFT technique against the SEHS technique which dominates the reports from such systems in the literature for four model nanoparticles. The results have been simulated against model particle sizes of 14.90, 8.01, 4.81 and 1.62 nm which correspond to 33, 18, 11 and 4 platinum layers respectively. At first glance there appears to be a large disparity between the sets of data with the bulk resonances found in the FSFT method being considerably narrower than those in the SEHS process. As explained previously, this is due to the soft echo scheme not recording the narrowest part of the lines spectral features as the data points sampled are too far apart. All four FSFT spectra were fitted using the shell model and compared to theoretical particles of similar diameter and the results are shown in Table 4.3. The healing length for the simulations was defined by the positions of the sub-surface 1 and 2 peaks and this was fixed to 1.5 nm for all the samples. The simulated Gaussian widths were allowed to vary to fit the data which increased monotonically as the layers approached the surface.

For (d), (e) and (f) a clear trend is followed of diminishing bulk platinum content with an obvious increase in sub-surface and surface resonances as the particle size decreases. This is expected as the quantity of nuclei experiencing the bulk state

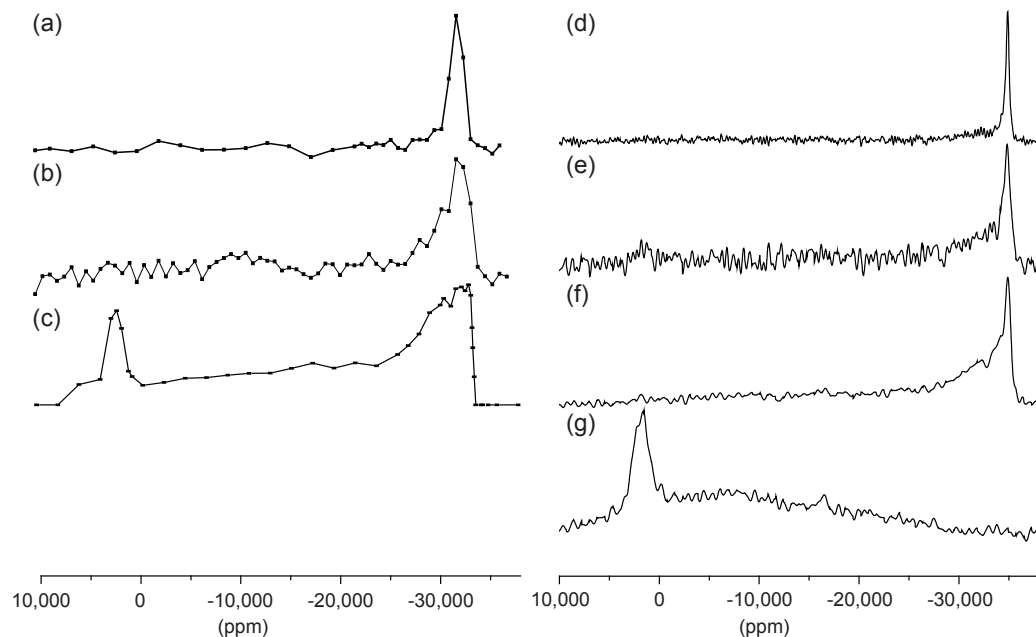


Figure 4.3: A comparative illustration of the commonly used SEHS (a-c) wideline technique against the FSFT (d-g) technique for varying platinum particle sizes. The particle sizes shown are (a) and (g) are a 15 nm, (b) and (e) 7.7 nm, (c) and (f) 5 nm and finally (g) is a FSFT of a 1.8 nm particle. The SEHS result of a 1.8 cannot give a true reflection on the broad outer layers of the particle and is hence not shown. This data is checked, edited and re-scaled from Simon Orr's thesis [181].

decreases with decreasing particle diameter. The final spectrum (g) shows that there is no bulk platinum present in a 1.8 nm platinum particle and all the nuclei sit as either surface atoms or one to two layers below it. In a simplified model this is an ideal arrangement for surface catalysis as none of the platinum is wasted in its bulk format; however bulk-surface interactions may also define the catalytic activity.

Although agreement between the deconvoluted particle size and the theoretical model is good there are some discrepancies that have to be taken into account. The intensity of the bulk peak when compared to the theoretical model is considerably lower than predicted, a trend repeated in other FSFT experiments (as above when compared to VOCS). A possible reason for this lays with the limits of the models inability to distinguish between layers close enough to the bulk shift. The simplest explanation for the intensity in the bulk being shifted towards the sub-surface layers is that the geometry of the particles is non-spherical. As a particle deviates from spherical a small proportion of the nuclei will be found at the bulk resonance position for the same overall volume of particle. The reduced symmetry of

such a particle requires a more sophisticated model than is being proposed here and no such treatment was found in the literature possibly due to relativistic complications with heavy nuclei such as platinum. It can be stated from the data collected here that loss of symmetry is evident in particles above 5 nm and on supported nanoparticles.

As previously mentioned spectrum (g) contains no bulk-like nuclei which is also confirmed by an increase in the relaxation time, however a higher than expected ratio of surface to sub-surface signals are observed, suggesting that a perfect 1.62 nm four layered model might not be present. This could be due to defects or vacancies in the particle that are increasing the surface area. A significant proportion of the particle surface has oxidised as shown with the PtO resonance at 1,750 ppm. To observe a surface resonance the resultant oxide peak would need to have a breadth smaller than that of the Knight shift between the surface and the first sub surface layer. This has been proposed only to take place in electrochemically cleaned surfaces. [157] Therefore the formation of the platinum oxide is proposed to distort the shape of the nanoparticle as the layer can differentially form and/or penetrate into the particle. With small nanoparticles the surface area must be sufficiently large to contain a substantial amount of well-defined oxide sites making it observable as a separate resonance. Therefore it can be presumed that  $\approx 50\%$  of the surface is oxidised to form a well defined oxide site whilst the other  $\approx 50\%$  is not apparent and is broadened into the sub surfaces due to the oxide forming on edges and corners.

While spectra (d) and (e) contain large enough particles that an oxide layer does not have the intensity to be observed, spectrum (f) however should contain a visible oxide layer as also observed in (g). It has been proposed that the orientation of the surface atoms has an effect on its catalytic activity which could be dependent on the particle size. If this is the case the 5 nm particle may be free from oxide effects or more likely is that the oxide has become broadened due to it being no longer cubo-octahedral.

Nanoparticle size estimate by Scherrer analysis	Oxide	Surface		Sub Surface Layer 1		Sub Surface Layer 2		Sub Surface Layer 3		Bulk	
		Fit	Model	Fit	Model	Fit	Model	Fit	Model	Fit	Model
	1,750 ppm		-21,40 ppm		-29,500 ppm		-32,500 ppm		-34,000 ppm		-35,350 ppm
			0								
			Fit								
(nm)	( $\pm 1\%$ ) <sup>e</sup>	( $\pm 3\%$ )		( $\pm 14\%$ )		( $\pm 9\%$ )		( $\pm 7\%$ )		( $\pm 17\%$ )	
15.0 <sup>a</sup>	2.0	8.4	8.9	8.1	8.4	23.8	15.2	24.7	13.3	36.8	54.2
7.7 <sup>b</sup>	6.6	15.7	16.2	14.2	14.3	26.5	23.6	20.3	17.6	16.7	28.4
5.0 <sup>c</sup>	0.3	22.6	25.9	17.7	21.0	30.0	29.3	21.0	15.9	8.5	8.0
1.8 <sup>d</sup>	19.5	65.6	62.6	14.9	28.6	0.0	8.9	0.0	8.9	0.0	0

Table 4.3: A comparison of the theoretical model against the deconvolution of the platinum sweeps for various platinum nanoparticle sizes. <sup>a,b,c,d</sup> - Comparison of relative peak intensities of fits of figure 4.3 (<sup>d,e,f,g</sup>) compared to those described in the layer model. Model particle sizes are as follows: a. 14.90 nm (33 layers), b. 8.01 nm (18 layers), c. 4.81 nm (11 layers) and d. 1.62 nm (4 layers). <sup>e</sup> - the maximum error observed for that respective nanoparticle layer.

#### 4.3.4 Platinum Clusters

The synthetic pathway for creating specific sized clusters is difficult and usually a distribution of particle sizes are present; this is indicated in the particle size analysis by aberration corrected TEM. There are very few reports of such clusters in the literature because of the difficulty in preparing them. A perfect cubo-octahedral 13 atom two layer nanoparticle would have a diameter of 0.72 nm. The mean cluster (figure 4.4 c) size is 0.73 nm with a range of 0.3 - 2.0 nm. The present dispersion means that some of the platinum nanoparticles will not be 13 atoms large and hence may contain conduction electrons if they are larger than 13 atoms. Proportions of the clusters are smaller than the required magic number clusters, this means they would deviate from cubo-octahedral; this would cause an anisotropy and hence broaden the resonance as well.

The  $^{195}\text{Pt}$  spectra (figure 4.4 a) instead of showing the predicted two narrow peaks, shows a distribution of sites. The resonance has a centre of gravity appearing at approximately  $-7,400$  ppm and has a span in the region of  $10,000$  ppm. This span is a direct product of the range of platinum sites caused by such a range of particle sizes.

The sample was sealed with trialkyl aluminium to prevent oxidation and the clusters deviating from the desired cubo-octahedral result and hence to maintain the translational symmetry. It has been suggested that trialkyl aluminium weakly bonds to platinum with no electron overlap. If this statement is correct then the trialkyl aluminium should give a single peak, the corresponding  $^{27}\text{Al}$  static resonance (figure 4.4 b) appears at  $15.3$  ppm with a second additional peak at  $137.4$  ppm. These peaks are not distorted or Knight shifted and can be concluded to have no or minimal interaction with the internal platinum clusters.

The  $T_1$  relaxation (figure 4.4 d) from the saturation recovery experiment is shown to be  $0.171$  s; this is very much longer than for metallic platinum. Bulk platinum metal has a determined relaxation time of  $66\ \mu\text{s}$  at  $298$  K. This slower relaxation at room temperature indicates that the relaxation mechanism is no longer wholly electronic. These slower relaxation times suggest that there is no longer any conducting electron density; which suggests the line is no longer Knight shifted.

As the resonance is not the two narrow peaks with a 12:1 ratio as expected (caused due to the distribution) then it is difficult to determine the actual isotropic shift of  $\text{Pt}_{13}$  clusters. Instead we can only comment on the centre of gravity of the distribution. This structure with no Knight shift is approximately  $-7,400$  ppm ( $-0.73\%$ ) shifted from the six coordinated primary reference used to determine the Knight shift. Hence we are able to estimate the contribution of the Knight shift to



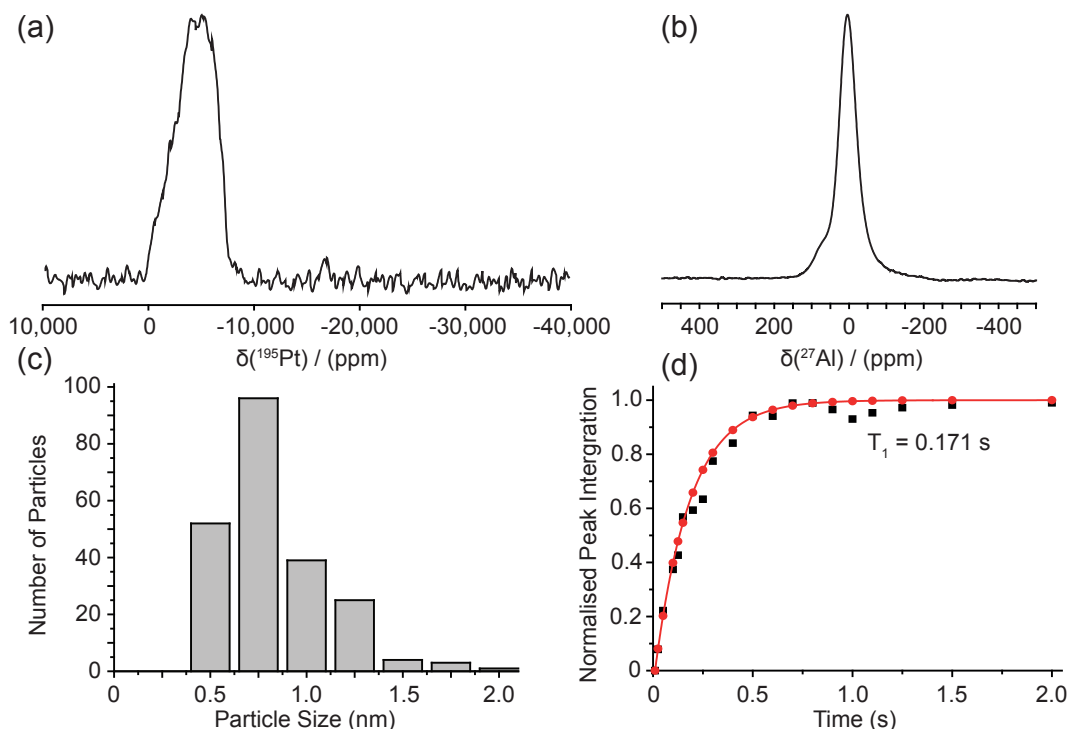


Figure 4.4: Platinum 13 clusters. The platinum FSFT result is shown in (a), whilst (b) shows the aluminum spectra for the trialkyl aluminum coating, (c) is the particle size determination as completed by aberration corrected TEM studies and (d) shows the  $T_1$  relaxation time of the platinum clusters as determined by a saturation recovery experiment.

the overall position observed for the platinum nanoparticles taking into account the chemical shift of a closely related insulating structure is  $-7,400$  ppm.

#### 4.3.5 Platinum-Tin Intermetallic Nanoparticles

The  $\text{Pt}_3\text{Sn}$  shown in figure 4.5 (a), shows three  $^{195}\text{Pt}$  resonances distributed throughout the chemical shift range, the downfield platinum metal line shape begins at  $\approx -35,000$  ppm and extends to  $\approx 5,000$  ppm suggesting sub 7 nm platinum particles are present in the catalyst (48 % abundant). At a higher field a Knight shift anisotropy (KSA) broadened resonance is present at  $+9,913$  ppm signifying a far more ordered environment is present when compared to previous bimetallics studied which is identified as the  $\text{Pt}_3\text{Sn}$  bimetallic (44 %). The second KSA resonance present is attributed to a  $\text{PtSn}$  contaminant (8 %) within the sample. Platinum-tin phase diagrams show the associated difficulties with making pure  $\text{Pt}_3\text{Sn}$ . As the chemical shift and Knight shift are difficult to separate from each other, the total

Platinum system	$\Delta\delta_{\text{iso}}^{\text{a}}/$ ppm	$\delta_{11}/$ ppm	$\delta_{22}/$ ppm	$\delta_{33}/$ ppm	$\Omega^{\text{b}}/$ ppm	$\kappa^{\text{b}}$	$\Delta\delta$ ppm	$\eta$
	( $\pm 25$ )	( $\pm 25$ )	( $\pm 25$ )	( $\pm 25$ )	( $\pm 25$ )	( $\pm 0.005$ )	( $\pm 25$ )	( $\pm 0.005$ )
$^{195}\text{Pt}_3\text{Sn}$	-9913	-7986	-10870	-10883	2897	-0.99	-2891	0.0067
	-2122	-1767	-1823	-2777	1010	0.89	-981	0.0870
$^{195}\text{PtSn}$	-2474	-1646	-2290	-3474	1828	0.30	-1506	0.6414
$\text{Pt}_3^{119}\text{Sn}$	-509	-396	-507	-626	230	0.04	-174.5	0.9541
$\text{Pt}^{119}\text{Sn}$	-745	-	-	-	-	-	-	-

Table 4.4: Experimentally measured  $^{195}\text{Pt}$  and  $^{119}\text{Sn}$  NMR interaction parameters for  $\text{Pt}_Y\text{Sn}_X$  bimetallics systems. The conventions shown are taken from section 2.3.5 in this thesis.

shift can only be presumed to be a combination of both effects contributing to the resonances overall shift. The shift is representative of platinum clusters in the literature which suggests a more dominant chemical shift effect is present over the Knight shift. This is also indicated by the resonance being present in the sub-surface one and surface regions of the chemical shift range.

The addition of tin causes a change in line shape from the core shell dispersion seen in the previous monometallic platinum nanoparticles to an anisotropic line shape now seen in these bimetallics. This suggests that more ordered environments that are constant throughout the sample rather, than the atomic disorder shown in alloys.

The 1 : 1 plat-tin (4.5 (b)) carbon supported catalyst shows one resonance which has a good agreement with the contaminant present in the 3 : 1 sample. This means both can be attributed to  $\text{PtSn}$ , their deconvolutions are shown in 4.4 confirming these conclusions. As with the  $\text{Pt}_3\text{Sn}$  material an anisotropic line shape dominated by shift effects suggesting an ordered environment throughout the sample, this is confirmed by the diffraction pattern which shows a super lattice line.

Tin NMR has been comprehensively studied throughout the literature for monometallic and bimetallic samples. Tin metal is +1 % Knight shifted from its primary reference, with the monoxide and dioxide both appearing at lower frequency. The  $\text{Pt}_3^{119}\text{Sn}$  resonance, as shown in figure 4.5 (c), appears at  $-509$  ppm with an expected KSA line shape present due to the ordered sample. One resonance is present possibly due to the low amount of  $\text{PtSn}$  contaminant present not being sufficient to produce a visible signal. The chemical/Knight shift is consistent with metal clusters suggesting a limited Knight shift contribution.

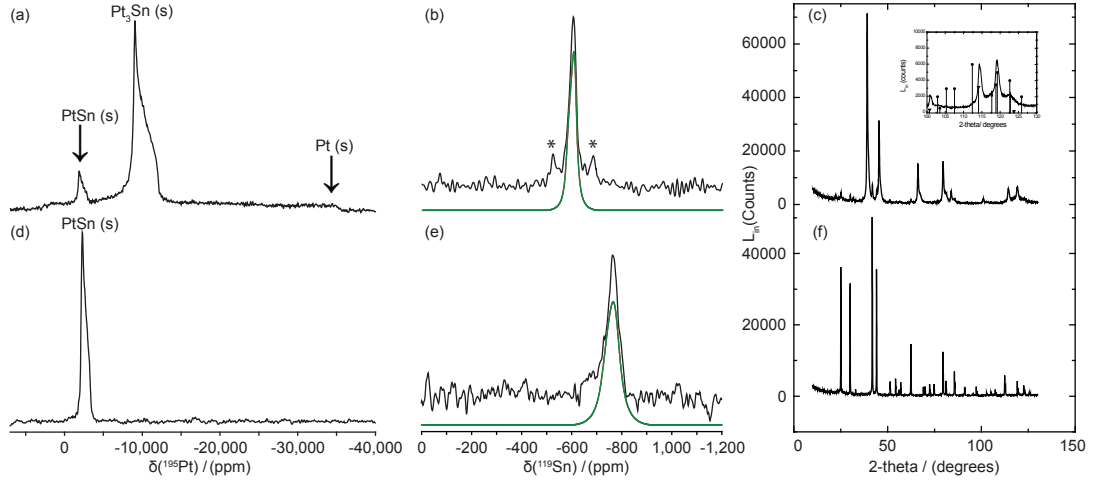


Figure 4.5: A multi-nuclear NMR study of 7 nm platinum- tin nanoparticles with varying amount of platinum, (a) and (d) show  $\text{Pt}_3\text{Sn}$  with (b) and (e) showing  $\text{PtSn}$ . The spectra on the left are completed by  $^{195}\text{Pt}$  FSFT NMR and the right by  $^{119}\text{Sn}$  MAS (12 kHz) NMR. X-ray diffraction patterns of (c)  $\text{Pt}_3\text{Sn}$  on carbon and (d)  $\text{PtSn}$  on carbon samples. Insert shows an expansion of the  $\text{Pt}_3\text{Sn}$  pattern, together with reference reflections from pure Pt (square),  $\text{Pt}_3\text{Sn}$  (circle) and  $\text{PtSn}$  (triangle).

Comparatively the  $\text{PtSn}$  (d) shows a single narrow resonance which is down-field shifted from the  $\text{Pt}_3\text{Sn}$ . The narrow peak suggests a well ordered sample with limited dispersion and the tin occupying a symmetric site. As a small shift anisotropy can only be measured due to the small half width of the resonance. As the corresponding platinum resonance is half the span of the 3 : 1 sample then this could be reflected in the tin spectrum meaning the anisotropy is also very small.

The three  $^{195}\text{Pt}$  NMR resonances shown by the  $\text{Pt}_3\text{Sn}$  sample and their assignment to a main phase of  $\text{Pt}_3\text{Sn}$  and minor phases of  $\text{PtSn}$  and  $\text{Pt}$  agree perfectly with the XRD pattern (figure 4.5) of the sample. This also shows a major phase of cubic  $\text{Pt}_3\text{Sn}$  (19 nm average crystallite size) and minor phases of  $\text{PtSn}$  (8 nm) and  $\text{Pt}$  (6 nm). The single  $^{195}\text{Pt}$  NMR resonance shown by  $\text{PtSn}$  also agrees with the XRD which only shows a very crystalline  $\text{PtSn}$  phase (99 nm).

#### 4.3.6 Platinum Alloy Nanoparticles

The  $\text{Pt}_3\text{X}$  (where X is a *p*- or *d*- block metal) systems show significantly disordered line shapes, such that the overall KSA seen in the  $\text{Pt}_x\text{Sn}_y$  intermetallics is no longer observable. Instead a typical broad dispersed lineshape is observed which suggests the alloys contain a variety of different local  $^{195}\text{Pt}$  sites. Figure 4.7 shows the  $^{195}\text{Pt}$  spectra for a variety of platinum alloys, also present is the corresponding X nuclei in

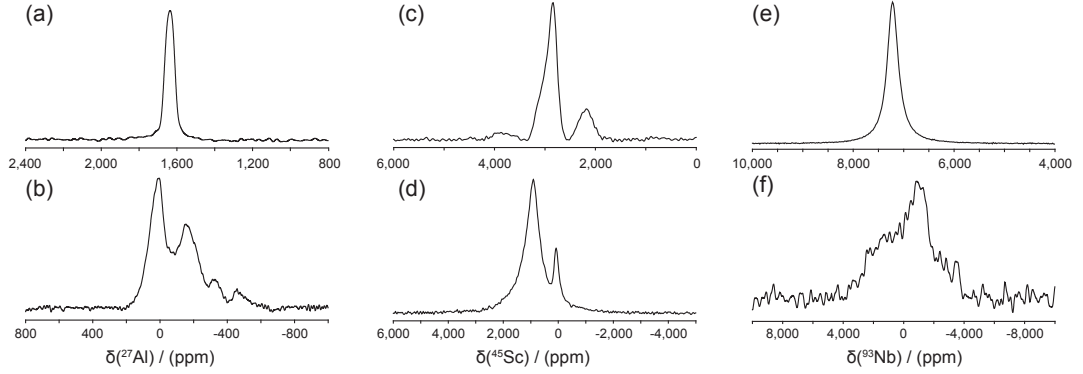


Figure 4.6: Solid state static NMR (14.1 T) spectra of the  $^{27}\text{Al}$ ,  $^{45}\text{Sc}$ , and  $^{93}\text{Nb}$  metals shown in (a), (c) and (e) and their respected  $\text{Pt}_3\text{X}$  alloys shown below them in (b), (d) and (f).

the alloy and 4.6 shows the corresponding X resonances from the  $\text{Pt}_3\text{X}$  nucleus along with the Knight shifted  $^{27}\text{Al}$ ,  $^{45}\text{Sc}$ , and  $^{93}\text{Nb}$  from pure metal meshes. These have been previously recorded during the early days of solid state NMR; here we present the data in ppm format against their primary IUPAC references. The  $^{47/49}\text{Ti}$  and  $^{91}\text{Zr}$  metals have been relatively recently reported in the literature and to the best of our knowledge the unfavourable quadrupole moment of  $^{177/179}\text{Hf}$  means there is no published literature on this nucleus. [172, 182]

The  $^{27}\text{Al}$ ,  $^{45}\text{Sc}$ , and  $^{93}\text{Nb}$  metals all show varying degree of positive Knight shifts (figure 4.6 (a), (c) and (e) respectively). The electron heavy  $^{93}\text{Nb}$  as expected show the largest Knight shift of 7.2 %. Whilst the lighter  $^{27}\text{Al}$  and  $^{45}\text{Sc}$  metals give reduced Knight shifts of 1.6 and 2.8 % respectively. The  $^{45}\text{Sc}$  metal also shows a KSA resonance ( $\delta_{iso} = 2882$ ,  $\delta_{11} = 3152$ ,  $\delta_{22} = 2833$  and  $\delta_{33} = 2663$  ppm) suggesting it is an non-axially symmetric metal.

Platinum on alumina is probably the most commonly used catalyst in industry today; it is known from surface science studies that these platinum nanoparticles if heated above 800 K can form a  $^{195}\text{Pt}$  alloyed surface. [183] The  $\text{Pt}_3\text{Al}$  (4.7 (a)) alloy shows two  $^{195}\text{Pt}$  resonances; a broad with a centre of gravity at  $-9,544$  ppm which spans between  $-4,000$  and  $-12,000$  ppm and a much smaller much more ordered site appearing at  $-14,400$  ppm. There is no excess platinum metal in any of the alloy samples due to the lack of platinum nanoparticle distribution which has been previously shown to occur in the  $-35,350$  to  $+1,750$  ppm range. The shift position is comparable to the ordered  $\text{Pt}_3\text{Sn}$  sample previously discussed. The  $^{27}\text{Al}$  NMR (figure 4.6(b)) spectrum show four distinct resonances ranging from 100 ppm to  $-300$  ppm. Previous work by Smith *et al.* has shown  $\text{Ti}_3\text{Al}$  alloys (Ti has a

similar size ionic radius as Pt) have interesting structural variations, the phase diagram shows the possibility of the formation of  $\alpha_2$ ,  $\alpha$  and  $\beta$  phases with increasing temperature for fixed atomic Al percentage. [48, 184] Although it is difficult to determine which phases are being represented at each chemical shift without varying the atomic percentage of aluminium in the alloy, the phase diagram illustrates the associated difficulties with generating pure phase platinum-aluminium alloys. [185]

The  $^{195}\text{Pt}$  NMR spectra for the  $\text{Pt}_3\text{Sc}$  sample (4.7 (b)) show similar resonances as the previous  $\text{Pt}_3\text{Al}$ . The only marked difference is the narrower width of the major peak at  $-9,340$  ppm. This suggests the sample is slightly more ordered than the corresponding platinum-aluminium alloy. The  $^{45}\text{Sc}$  NMR spectrum (figure 4.6(d)) shows two distinct Gaussian resonances, a very much narrower smaller peak (8%) appearing at 85 ppm and a broader peak (92%) with a shift of 935 ppm.

The platinum result for the  $\text{Pt}_3\text{Nb}$  nanoparticles (4.7 (c)) shows an apparent shift ( $-618$  ppm) in the resonance when compared with the  $\text{Pt}_3\text{Al}$  and  $\text{Pt}_3\text{Sc}$  samples. The  $^{93}\text{Nb}$  NMR spectrum (figure 4.6(e)) of the alloy shows a very broad disordered single peak stretching over 8,000 ppm with a centre of gravity around 0 ppm.

The  $\text{Pt}_3\text{Ti}$ , Hf, Zr alloys (4.7 (d,e,f) respectively) show a similar centre of gravity shift as the  $\text{Pt}_3\text{Nb}$ . Although all three lines are significantly more ordered than the niobium alloy. The  $\text{Pt}_3\text{Zr}$  alloy shows a very ordered environment with a comparable width to the 1 : 1 PtSn sample. Although the shift is similar to that of the PtSn, a 1 : 1 alloy cannot have formed due to the lack of presence of platinum metal. If a 1 : 1 alloy had formed, 50 % of the sample would just be bare platinum nanoparticles and as the entire chemical and Knight shift range was swept for all the samples and the typical platinum lineshape discussed above is not present a 3 : 1 alloy must be represented here.

A hint at helping to understand whether the apparent change of shift from the  $\text{Pt}_3\text{Sn}$ , Al, Sc bimetallics to the  $\text{Pt}_3\text{Nb}$ , Ti, Hf, Zr bimetallics is due to the changing density of states is to measure their spin-lattice ( $T_1$ ) relaxation times. Table 4.5 shows the results from a saturation recovery experiment using the highest peak intensity of the resonance for the series of bimetallics. The Pt nanoparticle result is observed across the entire 3 MHz wide line for each particle size. This shows that by combining platinum metal with another element dramatically decreases the relaxation rate and hence the overall shift of the line as the conduction electron density will also decrease which also fits with the observed decrease in the Knight shift. Within the series of binary materials their relaxation times increase by an order of magnitude when moving from the  $-600$  ppm shifted resonances to the

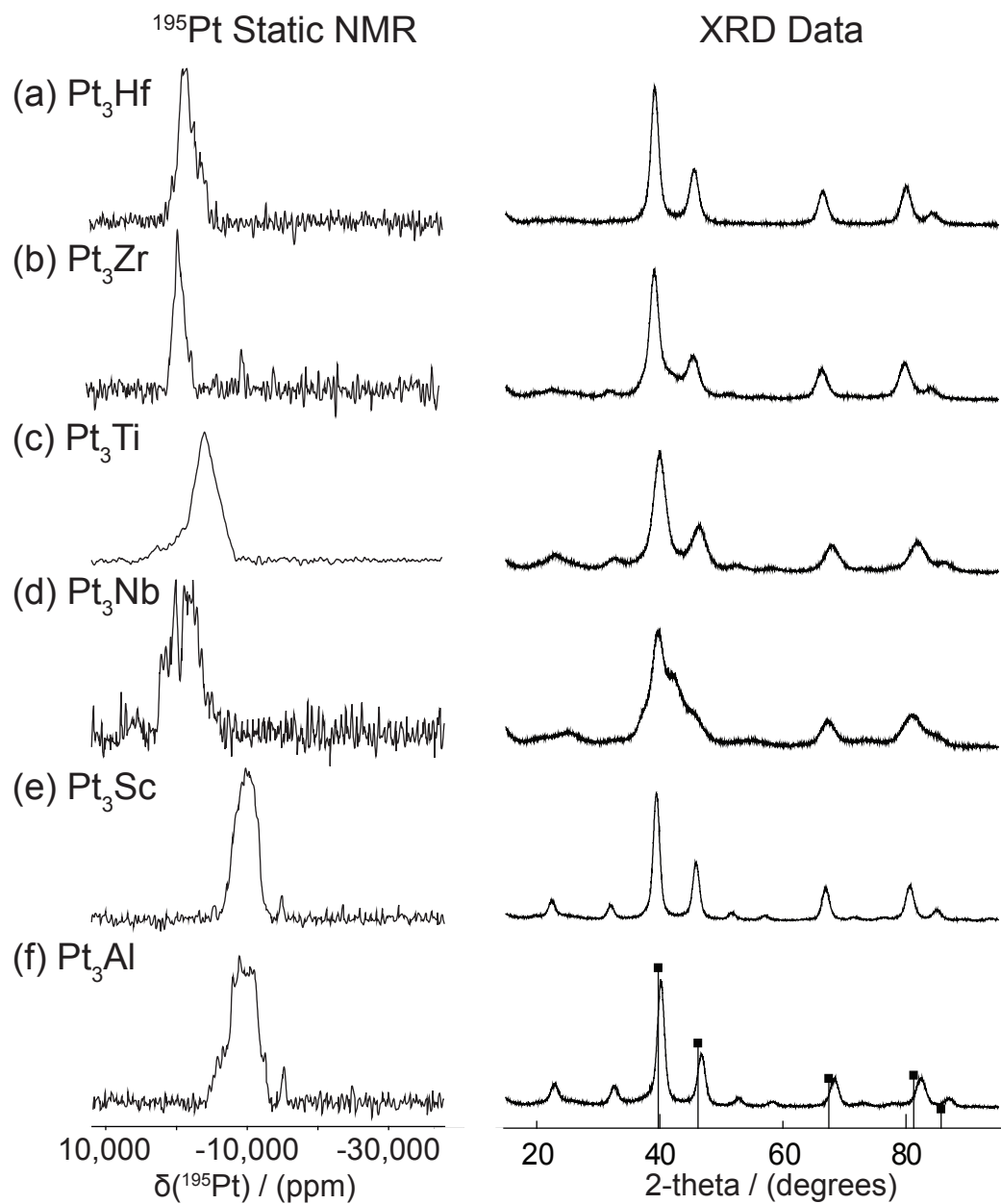


Figure 4.7: FSFT spectra and X-ray crystallographic study on a series of  $\text{Pt}_3\text{X}$  alloys; (a)  $\text{Pt}_3\text{Al}$ , (b)  $\text{Pt}_3\text{Sc}$ , (c)  $\text{Pt}_3\text{Nb}$ , (d)  $\text{Pt}_3\text{Ti}$ , (e)  $\text{Pt}_3\text{Hf}$  and (f)  $\text{Pt}_3\text{Zr}$ .

Sample	Centre of Gravity	$^{195}\text{Pt } T_1$ relaxation
	(ppm)	$\mu\text{s } (\pm 25)$
Pt Nanoparticle	-35,350 to 1,750	66
PtSn	-2,211	4291
Pt <sub>3</sub> Sn	-9,913	7549
Pt <sub>3</sub> Al	-9,544	2629
Pt <sub>3</sub> Sc	-9,340	3921
Pt <sub>3</sub> Nb	-618	478
Pt <sub>3</sub> Ti	-4,056	415
Pt <sub>3</sub> Hf	-2,711	298
Pt <sub>3</sub> Zr	-2,423	917

Table 4.5: The  $T_1$  relaxation times as determined by a saturation recovery experiment and fitted by a single exponent. The Pt nanoparticle result is achieved across the entire platinum range for all nanoparticle sizes.

-9,500 ppm shift lines. This also suggests that there is change in the electron density in the conduction band, and that there are likely to be contributions of different signs contributing to the observed effects as the smaller shift has more efficient relaxation. Also the observed changes are far more dependent on the conduction electrons and hence the Knight shift effects rather than changes associated with structural arrangement around the site; i.e. the chemical shift effects.

A point to note is that the shift seen here, which has been shown to be caused by a change in the conduction electrons, can also be confirmed by the presence of a decreased amount of  $d$ -electrons. The  $p$ -block metals which have alloyed with the platinum appear at approximately -9,500 ppm, whilst the  $d$ -electron heavy nuclei appear at -600 ppm. This can be seen on moving from aluminium which only has  $p$ -electrons and a centre of gravity of -9,544 ppm, to scandium which has one  $d$ -electron and a shift of -9,340 ppm, to titanium with two  $d$ -electrons and a total shift of -4,056 ppm and finally to other extreme of the  $d$ -electron heavy niobium appears at -618 ppm. This is clearly not reserved to the outer electrons as the zirconium and hafnium results do not have the same shifts as titanium which is in the same group.

The XRD of all the Pt alloy samples (except Pt<sub>3</sub>Nb, figure 4.7) show cubic structures with the expected lattice parameters of the nominal compositions. The Pt<sub>3</sub>Nb also appears to show a cubic structure, however, as the expected structure of Pt<sub>3</sub>Nb is orthorhombic, it is not clear whether an alloy structure has been formed.

All the alloys except  $\text{Pt}_3\text{Hf}$  and  $\text{Pt}_3\text{Nb}$  show some evidence of ordering due to the presence of superlattice reflections.

The XRD of the  $\text{Pt}_3\text{Al}$  sample shows a single ordered cubic alloy with a partially ordered structure. The measured lattice parameter,  $3.876\text{\AA}$  is very close to the literature value of  $3.8775\text{\AA}$ . The diffraction pattern of the  $\text{Pt}_3\text{Sc}$  sample shows a single ordered cubic alloy with a well ordered structure with a measured lattice parameter of  $3.949\text{\AA}$  close to the literature value of  $3.958\text{\AA}$ .

The XRD of the  $\text{Pt}_3\text{Nb}$  sample appears to show a cubic phase with very broad reflections, either suggesting a mixture of similar phases or a highly disordered single phase. As commented above, a orthorhombic phase is expected for bulk  $\text{Pt}_3\text{Nb}$  alloys. High resolution TEM was performed on the sample and this showed the presence of on average 5 nm particles containing both Pt and Nb. Given that the  $^{195}\text{Pt}$  nmr spectrum shows a significant shift in the Pt resonance, this suggests more unambiguously than the XRD that the Pt and Nb have alloyed. The patterns from the  $\text{Pt}_3\text{Ti}$ ,  $\text{Pt}_3\text{Zr}$  and  $\text{Pt}_3\text{Hf}$  series shows similarly well alloyed cubic phases with a decrease in ordering down the group, with  $\text{Pt}_3\text{Ti}$  showing the largest degree of superlattice reflections with  $\text{Pt}_3\text{Hf}$  showing none.

## 4.4 Conclusions

In summary, we have shown it is possible to accurately reconstruct a 3.2 MHz wide  $^{195}\text{Pt}$  resonance in platinum nanoparticles. This has then been deconvoluted to give information regarding the number of atoms present in the nanoparticle; this has been confirmed by the number of atoms present in a cubo-octahedral model of the nanoparticle. The deconvolution of these field swept spectra show very good agreement with the expected number of platinum atoms in these model samples. The errors from the SEHS and SEIS methods that dominate the reports in the literature mean that accurate prediction of the particle size is not possible from these approaches. Although VOCS is the preferred method of lineshape reconstruction, the time scale benefits of a FSFT method outweigh the minor inaccuracies in the lineshape reconstruction.

The  $\text{Pt}_{13}$  clusters showed a discernable shift difference from the primary reference. This suggests that quoting the Knight shift with respect to the commonly used IUPAC reference may give large errors when compared to a more appropriate non-conducting small cluster with an identical number of neighbouring atoms. The exact shift could not be determined due to the difficulty of making such a sample without a distribution of particle size.



Intermetallic platinum-tin nanoparticles showed an ordered environment with a Knight shift anisotropy suggesting an ordered environment with no observable dispersion. Multinuclear studies allude to this order with very small anisotropic interactions in the case of the  $^{119}\text{Sn}$  resonances.  $\text{Pt}_3\text{Sn}$  shows a large axially symmetric anisotropic interaction when compared to the smaller axially symmetric interaction in  $\text{PtSn}$ . The platinum and tin spectra are to a lower frequency shifted with an excess of platinum when the platinum:tin ratio equilibrates then a deshielded shift is observed.

The alloyed platinum systems show a variety of shifts which are dependent on the conduction electrons of the system and the number of d-electrons in the alloyed X-element. The shift becomes more positive with a greater number of *d*-electrons in the X alloyed atoms.

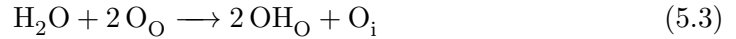
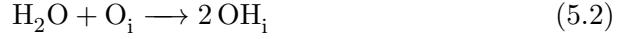
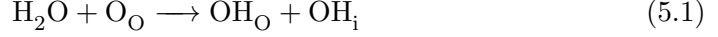
## Chapter 5

# Apatite Oxide Ion Conductors

### 5.1 Introduction to Solid Oxide Fuel Cells and Apatite Oxide Ion Conductors

Rare-earth apatite materials, of general formula  $\text{La}_{8+x}\text{M}_{2-x}(\text{XO}_4)_6\text{O}_{2y}$  (where M is a metal and X is a *p*-block element such as P, Si and Ge), have recently attracted attention as candidates for solid electrolytes in solid oxide fuel cell applications. Silicate and germanate types show a similar conductivity at decreased operational temperatures, when compared to conventional yttria-stabilised zirconia (YSZ). Whilst higher conductivities have been reported for these apatites at moderate temperatures. A variety of compositions have been synthesized and the lanthanum silicates and germanates were shown to have the most promising conduction properties. The introduction of cation vacancies or oxygen excess ( $y \geq 0$ ) were found to be the most promising conductors with the latter exhibiting the highest conductivities. [186–192] This behaviour is attributed to the conduction of interstitial oxide ions present in the structure. The lanthanum silicate/germanate apatites are composed of isolated  $\text{SiO}_4/\text{GeO}_4$  tetrahedra that are arranged to create two distinct channels along the *c*-axis. The smaller of these channels is occupied by La cations and the larger channel contains La and oxygen anions. In the samples with cation vacancies or oxygen excess, there are six crystallographic oxygen positions as shown in figure 5.1. Oxygens 1-4 are located in the  $\text{SiO}_4/\text{GeO}_4$  tetrahedra, oxygen 5 is found in the channels along the *c* axis and oxygen 6 is an interstitial oxide ions ( $\text{O}_i$ ). The exact position of this  $\text{O}_i$  is unknown due to the local disorder it brings to the structure; limiting the resolution of the powder diffraction studies. The wet samples studied here were prepared by annealing in air at temperatures below 200 °C. There is evidence for enhanced conductivity of oxygen excess germanate apatites in wet

atmospheres. [193–196] It was recently proposed that in these systems the incorporated water molecules react with oxygen, as summarized in the following equations: [197, 198]



where  $\text{O}_\text{O}$  and  $\text{OH}_\text{O}$  are oxide and hydroxide ions located in the channels and  $\text{O}_\text{i}$  and  $2 \text{OH}_\text{i}$  are the interstitial oxide and hydroxide ions. Hence, as shown in 5.3, incorporation of water into an apatite system will result in occupancy of interstitial oxide ions and these should be present in all of the wet apatite samples. However, in the dry stoichiometric oxygen sample, there should only be oxygens present in the  $\text{SiO}_4/\text{GeO}_4$  tetrahedra and in the channels.

Using atomistic modelling studies, the position of these interstitial ions were located near the silicate/germanate tetrahedra (5.1) units and not as expected in the channels, which is evident for modelling studies on a hydroxyapatite system. [199] The obvious position for the  $\text{O}_\text{i}$  to be located is the defect rich *c*-axis channel which runs through the centre of the structure. High resolution neutron powder diffraction (NPD) has experimentally hinted at this location of the interstitial oxide ions in silicate systems, observing a large degree of oxygen disorder and excess scattering density along the channels and around the silicate unit. [193–196] NPD studies on germanate apatites found that the proposed position of the interstitials are located closer to the framework walls than in the silicate systems. This is due to germanium having a larger ionic radius and hence a greater capacity for the oxide ion when compared to the smaller silicon centre. [1, 190, 196, 198, 200–203]

Previous studies of alkaline earth metal doped apatite silicates using  $^{29}\text{Si}$  magic angle spinning (MAS) NMR revealed one resonance in the samples with stoichiometric oxygen content and two or more resonances in those with oxygen excess. [197, 204, 205] This second resonance is assigned to silicate groups located close to interstitial oxide ions, consistent with computer modelling studies. The use of  $^{29}\text{Si}$  NMR is a facile method for indirect detection of the interstitial oxygen sites in the silicate apatites. However, germanates have been shown to offer increased conductivity at lower operational temperatures than silicon. Germanium-73 ( $I = \frac{9}{2}$ ) has a low natural abundance ( $\approx 7.7\%$ ), large quadrupole moment ( $Q = -19.6 \times 10^{-30} \text{ m}^2$ ) and small gyromagnetic ratio (3.49 MHz at 2.348 T), which makes the elucidation

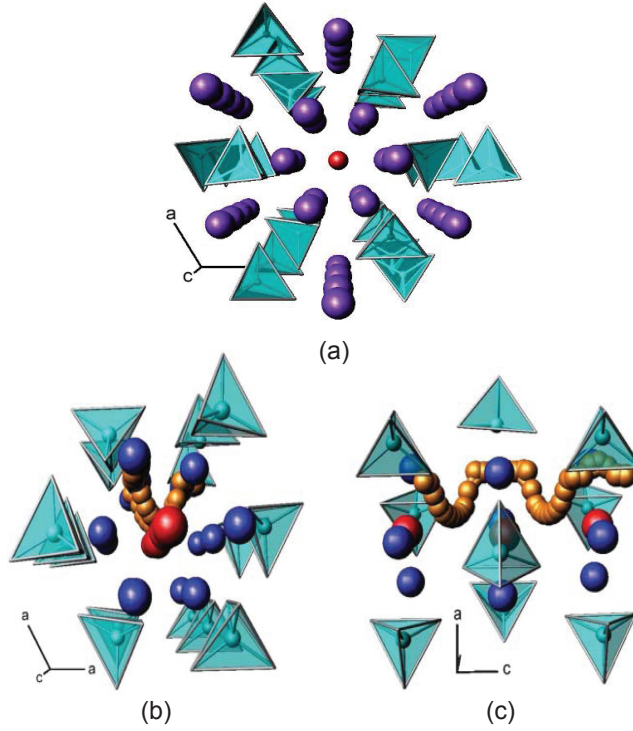


Figure 5.1: The structure of a rare earth apatite, (a) shows the view down the  $c$ -axis. The blue spheres represent the  $\text{La}_{8+x}\text{M}_{2-x}$  atoms, the green tetrahedra represent the  $\text{XO}_4$  polyhedron and the channel oxygens are displayed in red. The density functional theory calculated conduction pathway is displayed in (b) down the  $c$ -axis and (c) along the  $c$ -axis, it is noted that the conduction pathway does not come into contact with the channel oxygens. The crystal system is system hexagonal dipyramidal ( $6/m$ ).

tion of multiple germanium sites by SSNMR quite challenging. Here we utilize the oxygen-17 ( $I = \frac{5}{2}$ ) nucleus, which is present in large amounts in these samples (after isotropic enrichment), to elucidate the different oxygen local environments and directly detect the proposed interstitial oxide ions. [52] The  $^{17}\text{O}$  nucleus has been demonstrated to be a very good probe of oxide based materials structure because of its large chemical shift range, the major disadvantage is the low natural abundance of the  $^{17}\text{O}$  isotope (0.037%) meaning isotopic enrichment is required. Despite the quadrupolar nature of this nucleus ( $Q = -2.56 \times 10^{-30} \text{ m}^2$ ) the overall size of the  $^{17}\text{O}$  quadrupole interaction and the resultant quadrupole coupling constants ( $C_Q$ ) in these materials is sufficiently small such that conventional MAS alone can be applied for resolution enhancement. [52, 56, 107, 108, 206–210]

Greater resolution can be supplied to multiple site samples by multiple quan-

tum (MQ) MAS and double rotation (DOR) experiments. Although the quadrupolar information is known to give information on the symmetry of the  $I = \frac{5}{2}$  nuclei's environment, it is often desirable to remove this piece of information to gain insight into the other interactions present or to achieve higher resolution. MQMAS is a two dimensional echo experiment (see section 3.4.8 for a complete description) involving transitions between non-consecutive energy levels during the excitation of the spin system during the first solid pulse, the MQ coherence generated from the first pulse is then converted back into the observable state by a series of hard and soft pulses. By completing this coherence pathway the resultant two dimensional resonance should give accurate chemical shift information which is free from both first and second order quadrupole broadening effects. [39] DOR (see section 3.4.10) requires the mechanical spinning of a sample at two angles (the magic angle of  $54.7^\circ$  and  $30.6^\circ$ ). This provides a double modulation of the second order quadrupole frequency with the result being a decreased line width and an enhancement in resolution. Here we provide both these techniques to attempt to characterize the NMR parameters of the oxygen sites involved in the formation of rare earth apatites. Sideband suppression by pulse synchronization is also applied to the experiment to give enhanced resolution. [30, 129, 211]

This study draws on a combined SSNMR and DFT (GIPAW - CASTEP, see section 3.5) investigation into various apatites with the maximum number of interstitials per unit cell with the silicate  $\text{La}_{9.6}\text{Si}_6\text{O}_{26.4}$  and germanate  $\text{La}_8\text{Y}_2\text{Ge}_6\text{O}_{27}$  to no  $\text{O}_i$  sites present in the sample with silicate  $\text{La}_8\text{Ca}_2\text{Si}_6\text{O}_{26}$  and the germanate  $\text{La}_8\text{Ca}_2\text{Ge}_6\text{O}_{25.75}$ ; with the range filled with varying X substituents added to increase or decrease the number of interstitials present. The rare earth apatites were studied under wet and dry conditions and from the changes in the corresponding  $^{17}\text{O}$  MAS NMR spectra; an unequivocal assignment of the interstitial oxide ions is possible. All the  $^{17}\text{O}$  was incorporated into the sample by hydrothermal reactions during the  $\text{H}_2\text{O}$  incorporation stage of oxide ion interstitial annealing. Information about the defect properties in these systems is essential to develop an understanding of their macroscopic conductivity behaviour and to improve upon their characteristics. Both the silicate and germanate apatites have been shown to incorporate significant amounts of water on annealing and  $^1\text{H}$  MAS NMR spectra confirm the presence of mobile water and hydroxyls in the samples. [190]

## 5.2 Experimental and Synthesis

### 5.2.1 Synthesis and Sample Preparation

All samples were synthesized from stoichiometric amounts of high purity  $\text{La}_2\text{O}_3$ ,  $\text{Y}_2\text{O}_3$ ,  $\text{CaCO}_3$  and  $\text{SiO}_2$  or  $\text{GeO}_2$ . These were ground together and heated (1100 °C, 12 hours) before being reground and refined (1100 °C, 12 hours). The resultant product was then ball milled before final heating took place at 1300 °C for 2 hours. The required  $^{17}\text{O}$  enrichment was completed by hydrating the samples with 0.5  $\text{cm}^3$  water (10 - 90%  $^{17}\text{O}$  labelled) under low temperature conditions hydrothermal conditions (200 °C). After 48 hours, the samples were dehydrated to ensure equilibrated exchange.

### 5.2.2 Density Functional Theory

Molecular dynamics (MD) simulations used the DLPOLY code with shell-model ionic potentials, and were carried out at higher temperatures than the NMR experiments, which allowed for high-quality statistics from long simulation timescales. [212] DFT calculations used the VASP code for the geometry optimizations, and the GIPAW-based NMR-CASTEP code for the electric field gradient and isotropic shift calculations.[213, 214] VESTA was used for analysis of the results. [215] The methods used here have been applied successfully to fuel cell materials and other related oxides. [186–191, 216]

### 5.2.3 Solid State NMR

The  $^{17}\text{O}$  spectra were acquired at Larmor frequencies 40.68, 52.23, 67.78, 81.34 and 108.49 MHz using Varian Infinity Plus 300 (7.05 T), Bruker AV-400 (9.4 T), Bruker AV-500 (11.7 T), Bruker AV-600 (14.1 T) and Varian Infinity Plus 800 (18.8 T) spectrometers respectively. A 3.2 mm double resonance Bruker MAS probe was used at 7.1 to 14.1 T, facilitating spinning frequencies in the range of 12.5 to 20 kHz. A 4 mm double channel Varian MAS probe with a spinning frequency of 12.5 kHz was used at 18.8 T. With multiple magnetic field data, the quadrupolar parameters can be extracted. An example of this is the quadrupolar coupling constant ( $C_Q$ ) can be estimated, or more accurately a combination of  $C_Q$  and the quadrupolar asymmetry parameter  $\eta_Q$  termed  $P_Q$  the quadrupolar effect parameter defined as:

$$P_Q = C_Q \sqrt{1 + \frac{\eta_Q^2}{3}} \quad (5.4)$$

The  $P_Q$  may be extracted from the gradient of the plot the centre of gravity ( $\delta_{cg}$ ) of the  $^{17}\text{O}$  resonance against the squared inverse of the magnetic field ( $\frac{1}{B_0^2}$ ), given as:

$$\delta_{cg} = \delta_{iso} - 6000 \frac{C_Q \sqrt{1 + \frac{\eta_Q^2}{3}}}{\left(\frac{\gamma}{2\pi}\right)^2} \cdot \frac{1}{B_0^2} \quad (5.5)$$

Where the  $\delta_{cg}$  represents the centre of gravity (position weighted mean taking into consideration all distributions) and the  $\delta_{iso}$  is the isotropic chemical shift, which is the average of the three principal components of the chemical shift tensor as described by the shielding produced due to electron density inside a magnetic field, this is more thoroughly described in section 2.3.5.

All spectra are reported against a primary reference of 10% labelled  $\text{H}_2^{17}\text{O}$  ((1),  $\delta_{iso}$  0 ppm). All  $^{17}\text{O}$  spectra were acquired with a rotor synchronized solid-echo sequence, using selective (solid)  $\frac{\pi}{2}$  pulse durations scaled from non-selective solution value measured on  $\text{H}_2^{17}\text{O}$  by dividing the duration by  $I + \frac{1}{2}$ . A duration between 1.5 - 2.0  $\mu\text{s}$  was achieved and a recycle delay of 5 seconds employed, with a total of 17000 to 74000 transients collected. Triple Quantum MAS (3QMAS) was completed at a Larmor frequency of 81.34 MHz (14.1 T) with a 3.2 mm double-resonance Bruker MAS probe with spinning frequency of 15 kHz. MQMAS experiments were recorded using a three pulse Z-filter pulse sequence. A non-selective 5.0  $\mu\text{s}$   $\frac{3\pi}{2}$  excitation and 1.5  $\mu\text{s}$   $\frac{\pi}{2}$  conversion pulse was followed by two 40.00  $\mu\text{s}$  selective  $\frac{\pi}{2}$  pulses. The Double Rotation (DOR) experiment was completed at 81.341 MHz (Bruker AV-600 at 14.1 T) using a Samoson DOR probe with an internal spinning frequency of 1.5 kHz and an external spinning frequency of 7.0 kHz.

The  $^{29}\text{Si}$  SSNMR spectra were collected at the Larmor frequency 59.58 MHz with a Bruker 7 mm double resonance MAS (5 kHz) probe on a Varian Infinity Plus 300. All the spectra were referenced to the secondary solid reference of Kaolinite solid,  $\delta_{iso} = -92$  ppm with respect to tetramethylsilane (TMS, 0 ppm). A recycle delay of 2 minutes was used to collect between 700 and 800 transients.

The  $^1\text{H}$  spectra were acquired at a Larmor frequency of 500.10 MHz using a Bruker AV-III (11.7 T) spectrometer. For the wet samples, a 2.5 mm triple-resonance Bruker MAS probe was used, with a spinning frequency of 30 kHz. For the dried samples, a 4 mm triple-resonance Bruker probe was used, with a rotating frequency of 12 kHz. All spectra were referenced to adamantane ((s), 1.63 ppm with respect to TMS, 0 ppm). The  $^1\text{H}$  spectra were acquired using a  $\frac{\pi}{2}$  pulse length of 2.5  $\mu\text{s}$  and a recycle delay of 3 seconds. A total of 256 transients were acquired in each case.  $^1\text{H}$  DQF MAS experiments were performed with one cycle of the Back-to-Back

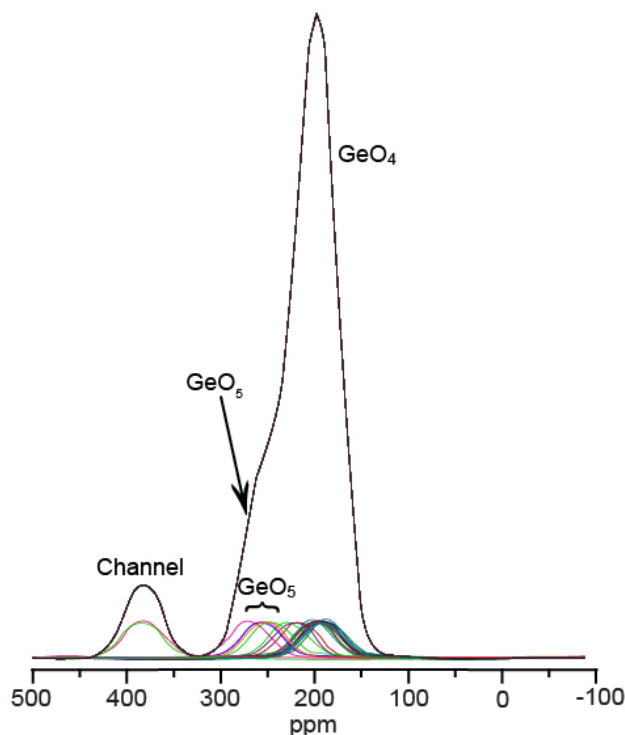


Figure 5.2: The Density Functional Theory  $^{17}\text{O}$  CASTEP determined NMR spectra for sample  $\text{La}_8\text{Y}_2\text{Ge}_6\text{O}_{27}$ . This spectrum is achieved by geometry optimising the apatite structure shown in figure 5.1 (a) with an additional oxide ion in the unit cell. The result shows no increased intensity in the channel region of the apatite, however an additional peak is formed which is attributed to the formation of a  $\text{GeO}_5$  sub-unit. See A.1 for more discussion on the simulation program.

(BaBa) recoupling sequence to determine the motion of the protons present in the samples.

## 5.3 Results and Discussion

### 5.3.1 Modelling and DFT of Rare Earth Apatite Conduction

Computer modelling studies have previously demonstrated the important role of the silicate/germanate tetrahedra in the high oxide ion conductivity in apatite systems. [187, 199, 217, 218] Molecular dynamics calculations (figure 5.1) show that the migration of the oxide ions occurs via a co-operative displacement of the  $\text{GeO}_4$  tetrahedra, where the oxide interstitial is passed from one  $\text{GeO}_4$  unit to the next by a rotation of the tetrahedra. Figure 5.2 shows the density functional theory (DFT) calculations via the CASTEP code was performed on a fully relaxed ox-



ide ion incorporated  $\text{La}_8\text{Y}_2\text{Ge}_6\text{O}_{27}$  apatite supercell (2:3:3). [214] The results show three resonances, the two downfield shifted channel oxygens form a narrow resonance whilst the main resonance comprises of twenty  $\text{GeO}_4$  tetrahedra and there are five downfield shifted oxygens attributed to the  $\text{GeO}_5$  interstitial site. A clear separation at a MAS spinning speed of 20 kHz between the  $\text{GeO}_4$  and  $\text{GeO}_5$  resonances than the gauge including projector augmented waves (GIPAW) calculated spectra.

### 5.3.2 Rare Earth Apatite Silicates

The silicate apatites shown in figure 5.3 depict the  $^{29}\text{Si}$  MAS NMR spectra on the left and the  $^{17}\text{O}$  MAS NMR spectra on the right. A stoichiometric sample of  $\text{La}_8\text{Ca}_2\text{Si}_6\text{O}_{26}$  shown in (a) indicates that there is no obvious sign of  $\text{O}_i$  interstitials, giving a single  $^{29}\text{SiO}_4$  resonance present at  $\delta_{iso} = -83$  ppm. Calcium's small size prevents the addition of an interstitial due the lack of room to accommodate the extra oxygen ion and hence only a single peak is observed which is representative of the framework tetrahedra. Previous literature results show that  $\alpha\text{-La}_2\text{Si}_2\text{O}_7$  gives a single NMR signal at  $\delta_{iso} = -83.2$  ppm, which shows good agreement with our results here. [219] The corresponding oxygen spectrum (e) shows two distinct resonances, the larger upfield peak at  $\delta_{cg} \approx 190$  ppm is attributed to the oxygens present in the  $\text{Si}^{17}\text{O}_4$  tetrahedra, whilst the single sharp downfield resonance at  $\delta_{cg} \approx 380$  ppm can be deduced to be the c-axis channel oxygens which run through the structure. The narrow lines suggest a well ordered sample with limited dispersion meaning few Frenkel-type defects present in the apatite. The poor signal to noise can be attributed to the lack of  $^{17}\text{O}\text{-H}_2\text{O}$  uptake during the hydrothermal conduction. This gives firm insight into the conduction properties of the material, a good conductor would have an increased oxygen uptake as rare earth apatites are known to be oxide ion conductors.

As the amount of calcium in the sample decreases to form the oxygen excess sample,  $\text{La}_9\text{CaSi}_6\text{O}_{26.5}$ , an additional low frequency peak at  $\delta_{iso} = -85$  ppm is observed in the silicon spectrum. The peak can be attributed to being the interstitial oxide ion present in the sample. The interstitial has not formed the previously suspected  $\text{SiO}_5$  environment as this would give a distinct resonance at  $\delta_{iso} \approx 150$  ppm, instead a shoulder is seen on the major  $\text{SiO}_4$  peak which is denoted as  $\text{SiO}_{4+1}$  in this manuscript; a silicon tetraoxide with an extra oxygen within its local environment. This is commonly seen in silicon Q-species where the next nearest neighbour of the silicon directly affects the silicon oxide shift. [48] This indicates that the  $\text{O}_i$  ion is not able to penetrate the tetrahedra, however as the silicon spectrum does show an obvious resonance and NMR is used to determine local structure, then the  $\text{O}_i$

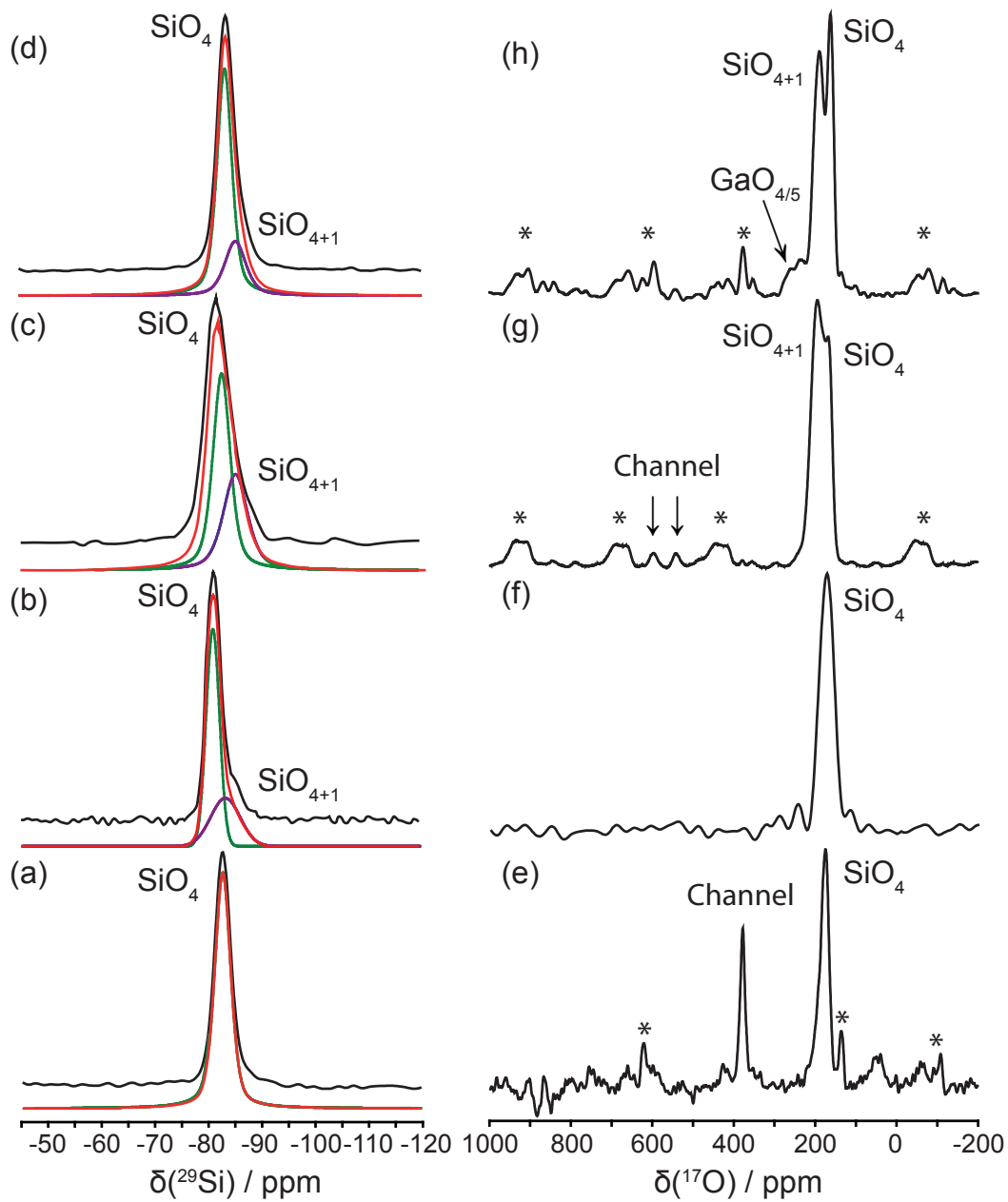


Figure 5.3: The  $^{29}\text{Si}$  MAS (left) and  $^{17}\text{O}$  MAS (right) NMR spectra of rare earth silicate oxide ion conductors. Sample (a)(e)  $\text{La}_8\text{Ca}_2\text{Si}_6\text{O}_{26}$ , (b)(f)  $\text{La}_9\text{CaSi}_6\text{O}_{26.5}$ , (c)(g)  $\text{La}_{9.6}\text{Si}_6\text{O}_{26.4}$  and (d)(h)  $\text{La}_{10}\text{Si}_4\text{Ga}_2\text{O}_{26.5}$ . \* spinning sidebands

must be within two bond lengths of the silicon centre. The  $^{17}\text{O}$  SSNMR spectrum of the mono-calcium (f) apatite shows a single slightly broader resonance ( $\delta_{cg} \approx 190$  ppm) which is identified with the oxygens surrounding the silicon centre being in a similar environment. The lack of a channel resonance is due to the lack of labelled oxygen-17 take up from the bottom up synthesis method. As the labeling method was effectively completed by the oxide conduction mechanism then it can be presumed that this near linear channel running through the sample is not present in the oxide ion conduction process. The increased signal to noise also shows that a greater amount of label has been absorbed by the sample during low temperature hydrothermal conduction.

The  $\text{La}_{9.6}\text{Si}_6\text{O}_{26.4}$  (shown in c) ion conductor shows an increased amount of  $\text{SiO}_{4+1}$  ( $\delta_{iso} = -85$  ppm) in the silicon spectra, this is due to that the lack of small calcium ions gives more space for  $\text{O}_i$ . The oxygen-17 (g) result gives four distinct shifts; the two resonances are determined to be the  $\text{SiO}_4$  ( $\delta_{cg} \approx 190$  ppm) and the  $\text{SiO}_{4+1}$  ( $\delta_{cg} \approx 220$  ppm) sites. The intensities are once again skewed towards the environments which contribute most to the conduction of the oxide ions. The two downfield peaks show the two oxygens present along the channels, the poor signal to noise is attributed to the lack of a role played by these sites in conduction. The differing environments of the channels can be assigned to one of the *c*-axis oxygens being closer to the interstitial oxygen producing a more shielded environment. The increased signal to noise here is not representative of the conduction properties as 90%  $^{17}\text{O}$  enriched water was employed for this sample, whereas 20% enrichment was used for all others.

The final silicon spectrum of  $\text{La}_{10}\text{Si}_4\text{Ga}_2\text{O}_{26.5}$  (shown in d) once again shows the formation of the  $\text{O}_i$  at  $\delta_{iso} = -85$  ppm, however a decreased amount is observed due to doping of the larger more accommodating gallium centre in the apatite. No channels are observed in the spectrum, which indicates that these are also not involved in the motion of the oxide ion through the sample. The two high frequency peaks can be deduced to be the  $\text{SiO}_4$  (190 ppm) and  $\text{SiO}_{4+1}$  (220 ppm). The broadened peak present at the base of these two sharp resonances is the  $\text{GaO}_{4/5}$  site ( $\delta_{cg} \approx 250$  ppm); due to lack of resolution it cannot be determined whether one or both of these environments are present. The lack of resolution is due to the dispersion caused by the variable Ga-O bond distances in gallium tetrahedra. [220, 221] It is presumed both environments are present due to the decrease in intensity of the  $\text{SiO}_{4+1}$  environment in the  $^{29}\text{Si}$  MAS NMR spectrum.

As silicon NMR is a facile method of measuring the interstitial content of these apatites then the ratio between the deconvoluted  $\text{SiO}_4$  and  $\text{SiO}_{4+1}$  peak should

indicate how many  $O_i$ s are present per unit cell, this should also directly compare with the conduction properties of the apatite presuming no other conduction mechanism is present (i.e. defect conducting). Quantitatively the stoichiometric  $La_8Ca_2Si_6O_{26}$  sample has no obvious interstitials and hence contains only  $SiO_4$  framework tetrahedra, the  $La_9CaSi_6O_{26.5}$  sample is shown to be 33%  $SiO_{4+1}$ , the  $La_{9.6}Si_6O_{26.4}$  is 40%  $SiO_{4+1}$  and the  $La_{10}Si_4Ga_2O_{26.5}$  sample is 26%  $SiO_{4+1}$ ; an immeasurable amount of the final sample could form a gallium interstitial site ( $GaO_5$ ). The shift of this  $GaO_5$  site cannot be determined from the literature or this study and hence drawing comparisons on the structural characteristics and conduction may not be accurate for this sample. Another point of note is that when the initial shift of the  $SiO_4$  environment in the stoichiometric sample is upfield at  $\delta_{iso} = -83$  ppm when compared to samples containing the interstitials ( $\delta_{iso} = -80$  ppm); the interstitial remains at  $\delta_{iso} = -85$  ppm throughout. Previous work has shown that defects in the samples can give a positive ppm shift to silicon spectra, as shown here by the amount of oxygen present (determined by gravimetric analysis) in the apatites that despite large amounts of  $O_i$  the amount of oxygen remains at less than one extra oxygen per unit cell. Thus, there is presumed to be large amounts of Frenkel-type defects in the samples causing this silicon shift, this has also been confirmed previously in the literature by NPD. [1]

### 5.3.3 Rare Earth Apatite Germanates

Figure 5.4 shows the  $^{17}O$  NMR spectra do not have the clearly defined discontinuities typical of  $^{17}O$  MAS NMR spectra of highly crystalline or ordered systems. The lineshapes present in these samples, particularly for the resonances of the low frequency  $GeO_4$  and  $GeO_5$  sites are asymmetrically broadened with a tail to low frequency which is characteristic of a distribution of quadrupolar interactions. The three different oxygen local environments in the lanthanum germanates are  $Ge-O-La/Y_3$ ,  $OLa_3$  and  $Ge_2-O-La/Y_3$  for the oxygens in the  $GeO_4$  tetrahedra, the channel oxygens and the interstitial oxygens respectively. From studies of  $GeO_2$ ,  $La_2O_3$  and  $Y_2O_3$  environments, the  $^{17}O$  chemical shifts for  $OGe_2$ ,  $OLa_4$  and  $OY_4$  environments appear at 70, 584 and 383 ppm respectively. [48, 222, 223]

The  $La_{7.5}Ca_{2.5}Ge_6O_{25.75}$  (5.4 a) sample is an oxygen deficient ion conductor with a stoichiometric chemical formula. This sample is directly comparable to its silicate sister  $La_8Ca_2Si_6O_{26}$ . Only a single  $^{17}O$  resonance is observable at  $\delta_{cg} \approx 160$  ppm. Unlike the corresponding stoichiometric silicate the channel oxygen is absent, this can be credited to the increased conduction properties of the germanates when compared to the silicates, meaning the increased signal to noise of the major con-

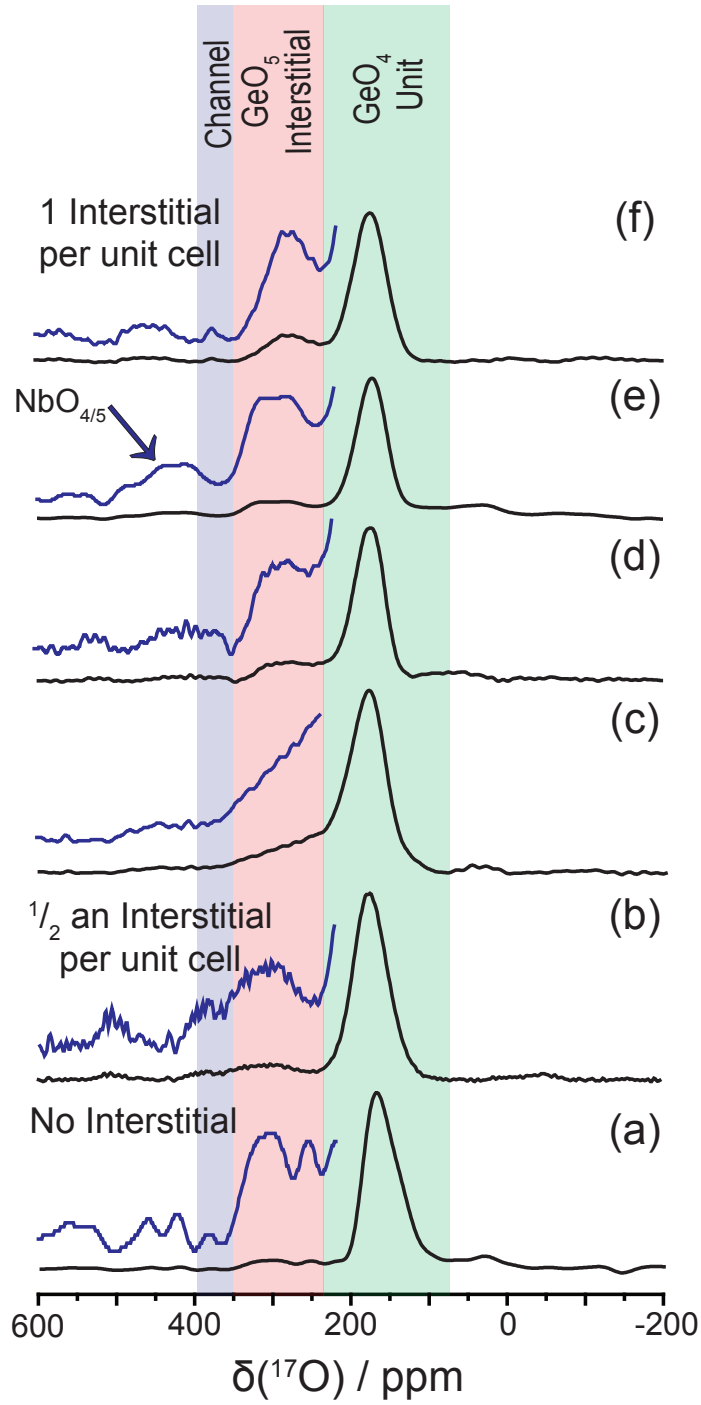


Figure 5.4: The  $^{17}\text{O}$  MAS spectra of (a)  $\text{La}_{7.5}\text{Ca}_{2.5}\text{Ge}_6\text{O}_{25.75}$ , (b)  $\text{La}_8\text{CaYGe}_6\text{O}_{26.5}$ , (c)  $\text{La}_8\text{Bi}_2\text{Ge}_6\text{O}_{27}$ , (d)  $\text{La}_{9.67}\text{Ge}_6\text{O}_{26.5}$ , (e)  $\text{La}_{9.83}\text{Ge}_{5.5}\text{Nb}_{0.5}\text{O}_{26.5}$  and (f)  $\text{La}_8\text{Y}_2\text{Ge}_6\text{O}_{27}$  acquired at 14.1 T with the positions of the expected, as derived from the CASTEP results,  $\text{GeO}_4$ ,  $\text{GeO}_5$  and channel regions highlighted in green, red and blue respectively. The areas from 250 to 600 ppm have been expanded and overlaid in dark blue for each of the samples to illustrate the channel regions.

ducting and therefore  $^{17}\text{O}$  enriched framework oxygens dwarfs the small channel oxygens; which are not present in the oxide ion conduction mechanism. Essentially the peak present here is at natural  $^{17}\text{O}$  abundance and can only be viewed in the blue expansion of the region. The single large peak can be assigned to the framework  $\text{GeO}_4$  tetrahedra; rutile- $\text{GeO}_2$  has been shown to occur at an isotropic shift of  $\delta_{iso} \approx 160$  ppm. [223] On replacing the calcium content with the larger atomic radii of yttrium to form  $\text{La}_8\text{CaYGe}_6\text{O}_{26.5}$  (5.4 b) a second upfield resonance becomes visible at  $\delta_{cg} \approx 295$  ppm. The oxygen excess (gravimetric analysis) of the determined structural formula suggests the formation of an interstitial aiding the peak assignment. The large size of the germanium centre means that the tetrahedra (co-ordination number 4) site on addition of the interstitial can become a co-ordination number 5 site, this can also be seen by the increase in chemical shift from 220 ppm in  $\text{SiO}_{4+1}$  to 295 ppm in the  $\text{GeO}_5$  site. When integrated the peaks show a ten  $\text{GeO}_4$  to one  $\text{GeO}_5$  ratio, suggesting that every other cell contains an interstitial oxygen environment, as indicated in the gravimetrically determined empirical formula.

The  $\text{La}_8\text{Bi}_2\text{Ge}_6\text{O}_{27}$  (5.4 c) sample contains one oxygen interstitial per unit cell; this is noted due to the increased intensity of the upfield  $\text{GeO}_5$  resonance. Once again, no obvious channel oxygens are visible suggesting all the enrichment is happening in the framework sites and not the near linear oxygen channels running through the centre of the structure. Without doping the metal sites of the structure you can form the defect heavy  $\text{La}_{9.67}\text{Ge}_6\text{O}_{26.5}$  apatite (5.4 d), by mass there is  $\frac{1}{2}$  an interstitials per unit cell. It worth noting that as there is one lanthanum cation vacancy per three cells; this can give a broadening to the peak as greater chemical shift dispersion is present. Unlike the silicon spectra the oxygen chemical shifts are not susceptible to cation vacancies which are incorporated in the structure. The  $\text{La}_{9.83}\text{Ge}_{5.5}\text{Nb}_{0.5}\text{O}_{26.5}$  apatite (5.4 e) has an extra high frequency resonance at  $\delta_{cg} \approx 460$  ppm; this has been attributed to framework  $\text{NbO}_4$  or  $\text{NbO}_5$  interstitials. Work by Bastow *et al.* and Bunker *et al.* has shown the  $^{17}\text{O}$  SSNMR chemical shifts of niobate sites occur between  $\delta_{iso} = 350$  and 504 ppm. [224, 225]

In the  $\text{La}_8\text{Y}_2\text{Ge}_6\text{O}_{27}$  (5.4 f) case there are three distinct chemical shifts that correspond to the calculated three different oxygen local environments. Since the oxygens in the  $\text{GeO}_4$  tetrahedra are closest to the Ge centres, the  $^{17}\text{O}$  resonance at lowest frequency is consistent with this local environment. Based on considerations of stoichiometry, the relative intensities of the channel and interstitial oxide ions should be 8 and 4% (two and one per formula unit) respectively. This confirms that the resonance at intermediate frequency ( $\delta_{cg} \approx 300$  ppm) corresponds to the channel oxygens. However, since sample enrichment was accomplished by reaction

of the apatites with labelled water, the relative intensities of the resonances must be taken with some caution. Unfortunately,  $^{17}\text{O}$  enrichment of the reactants, to allow incorporation of labelled  $^{17}\text{O}$  from the bottom up, was not possible due to the high firing temperatures required for the synthesis of all the presented apatite systems.

The linewidths of all the  $^{17}\text{O}$  resonances in these germanium apatite oxide ion conductors increases with magnetic field strength, meaning the chemical shift dispersion is the broadening mechanism, although some dispersion in the second order quadrupole broadening of these resonances may be contributing. Chemical shift dispersion is caused by the static variety of bond lengths around the Ge centres and by mobile dispersion caused by the movement of the oxide ion through the structure. This supports the conclusion that there is a distribution of oxygen sites. The high frequency resonance of the channel species has been calculated to be very narrow and is shown here as a narrower peak suggesting a very ordered oxygen environment due to the perceived lack of mobility and dispersion.

#### 5.3.4 $P_Q$ Calculations

To extrapolate information from this multiple  $B_0$  field data, i.e. isotropic shift ( $\delta_{iso}$ , ppm) and quadrupole coupling parameter ( $P_Q$ ), these were calculated by comparing the apparent shifts of the resonances against the inverse of the field squared, as indicated in figure 5.5 and the results given in table 5.1. [30, 129, 211, 226] The quadrupole parameter ( $P_Q$ ) derived for the  $\text{SiO}_4$  groups (2.1 - 2.4 MHz) shows that there is a minimum amount of variation within the second order quadrupole interaction. This suggests a very ordered environment and this feature is also seen in the one pulse MAS spectra as it contains narrow resonances. The  $\delta_{iso}$  ( $y$ -axis intercept) falls in a narrow range between 171 - 185 ppm. The corresponding  $\text{SiO}_{4+1}$  environments have decreased  $P_Q$ s with a range between 1 to 2 MHz. As the interstitial is presumed to act like a bridging oxygen this low  $P_Q$  is a surprising result; work is still on going to use DFT to calculate this observation. The channel oxygens have much more variable  $P_Q$  over a range 0.5 to 3 MHz, which is expected due to the amount of disorder generated by Frenkel-type defects running through the central oxygen axis. As the  $c$ -axis channel is surrounded by large M cations this creates a less shielded environment, hence why the isotropic shifts are greater than 380 ppm.

The corresponding germanates show a similar trend with the  $\text{GeO}_4$  giving quadrupole coupling parameters between 3 - 4 MHz with isotropic shifts ranging from 180 to 205 ppm. The interaction for interstitials is once again much smaller ( $\approx 1$  MHz) and the isotropic shift is downfield ( $\delta_{iso} \approx 300$  ppm) except for the

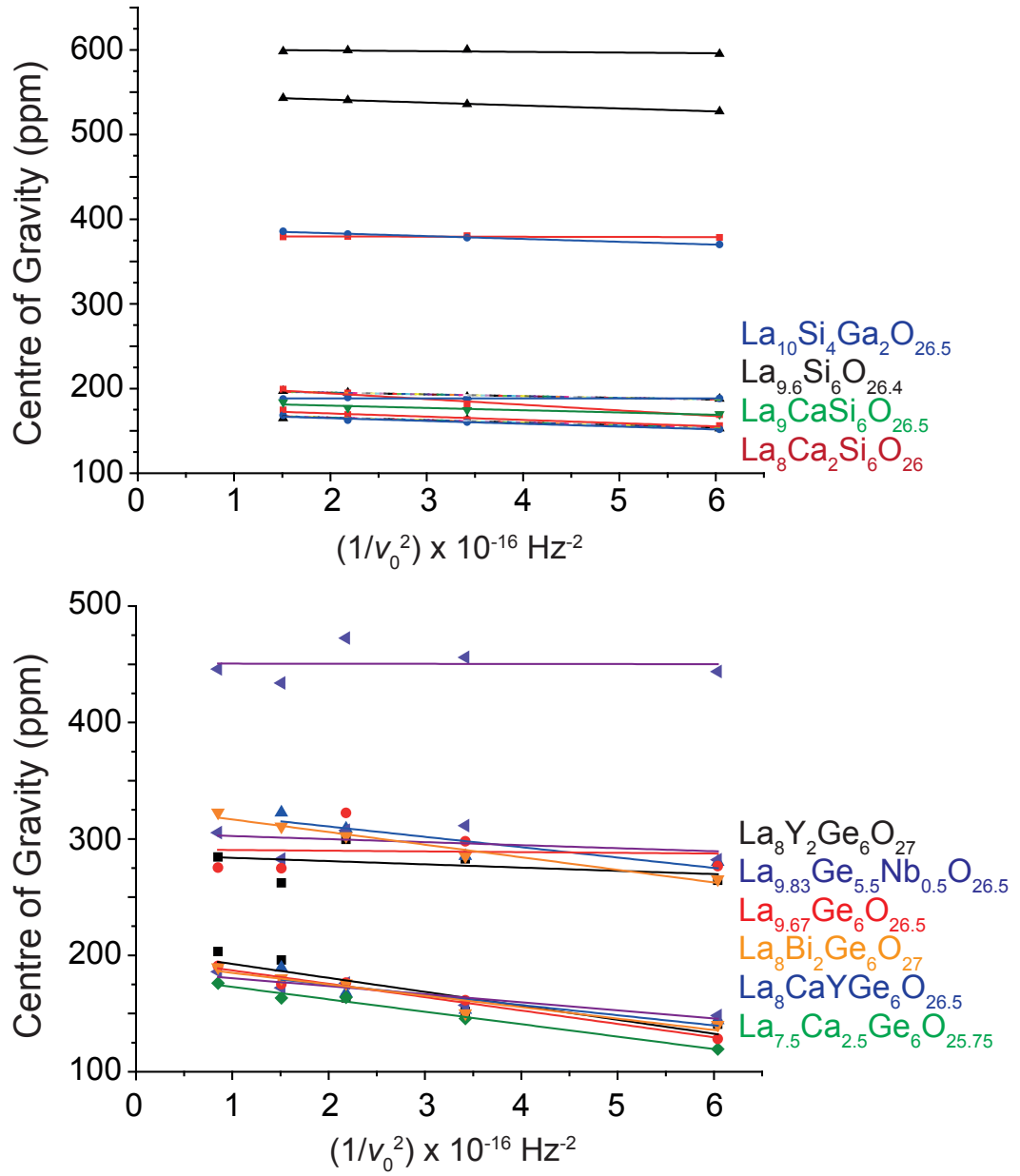


Figure 5.5: A plot of the inverse of the squared Larmor frequency against centre of gravity of the resonance for the various silicates apatites (left) and the various germanate apatites (right)



Nb case in which two interstitials are present corresponding to the formation of a  $\text{NbO}_{4/5}$  site. The errors present on this data are caused due to mobile chemical shift dispersion due to the variation in water content by variations in humidity.

Apatite system	Peak assignment	$\delta_{\text{iso}}^a$ ppm	$\delta_{\text{iso}}^b$ error ppm	$P_Q^b$ MHz	$P_Q^b$ error MHz	$\delta_{\text{iso}}^b$ ppm	$\delta_{\text{iso}}^b$ error ppm	$C_Q^b$ MHz	$C_Q^b$ error MHz	$\eta_Q^b$	$\eta_Q^b$ error	NMR-CASTEP
Silicates		$P_Q$				3QMAS						$\delta_{\text{iso}}$ $C_Q$ $\eta_Q$
$\text{La}_8\text{Ca}_2\text{Si}_6\text{O}_{26}$	$\text{SiO}_4$	178.3	$\pm 2.4$	2.52	$\pm 0.43$							
	channel <sup>A</sup>	380	$\pm 0.8$	0.55	$\pm 0.69$							
	$\text{SiO}_4^*$	185.3	$\pm 2.9$	2.12	$\pm 0.61$							
	$\text{SiO}_4$	171.6	$\pm 2.7$	2.22	$\pm 0.54$							
	$\text{SiO}_{4+1}$	199.3	$\pm 1.9$	1.85	$\pm 0.47$							
$\text{La}_{10}\text{Si}_4\text{Ga}_2\text{O}_{26}$	channel	548.2	$\pm 0.5$	2.40	$\pm 0.08$							
	channel	600.9	$\pm 2.0$	1.17	$\pm 0.78$							
	$\text{SiO}_4$	171.7	$\pm 1.9$	2.35	$\pm 0.37$							
	$\text{SiO}_{4+1}$	188.3	$\pm 1.0$	0.06	$\pm 7.57$							
	channel	390.1	$\pm 0.6$	2.37	$\pm 0.11$							
<b>Germanates</b>												
$\text{La}_{7.5}\text{Ca}_{2.5}\text{Ge}_6\text{O}_{25.7}$	$\text{GeO}_4^*$	183.6	2.8	4.22	0.96	180	16	4.3	0.6	0.4	0.1	
$\text{La}_8\text{CaYGe}_6\text{O}_{26.5}$	$\text{GeO}_4$	192.3	11.9	3.82	1.45							
	$\text{GeO}_5^\square$	328.5	12.0	3.85	1.40							
$\text{La}_{9.67}\text{Ge}_6\text{O}_{26.5}$	$\text{GeO}_4$	198.6	3.4	4.38	0.07							
	$\text{GeO}_5$	291.1	19.6	1.02	2.21							
$\text{La}_8\text{Bi}_2\text{Ge}_6\text{O}_{27}$	$\text{GeO}_4$	194.7	6.0	4.04	0.35							
	$\text{GeO}_5$	327.5	3.6	4.24	0.42							
$\text{La}_8\text{Y}_2\text{Ge}_6\text{O}_{27}$	$\text{GeO}_4$	204.6	11.6	4.47	1.66	185	19	4.6	0.5	0.4	0.1	192 4.7 0.2
	$\text{GeO}_5$	286.5	13.1	2.41	0.82	292	24	2.8	0.2	0.5	0.2	342 0.8 0.5
$\text{La}_{9.83}\text{Ge}_5\text{Nb}_{0.5}\text{O}_{27}$	$\text{GeO}_4$	187.4	4.8	3.40	0.61	196	20	4.3	0.6	0.6	0.3	
	$\text{GeO}_5$	305.1	12.5	2.09	0.89	329	28	2.9	0.3	0.6	0.1	
	$\text{NbO}_5$	450.7	13.9	0.40	4.66							

Table 5.1: Experimentally measured and NMR-CASTEP DFT calculated 17O NMR interaction parameters for various apatite systems. <sup>\*</sup>- $\text{SiO}_4$  and  $\text{GeO}_4$  framework tetrahedra,  $\square$ -  $\text{SiO}_{4+1}$  and  $\text{GeO}_5$  interstitials,  $\Delta$ - c axis channel oxygens. <sup>a</sup> -  $P_Q$  derived from  $P_Q = C_Q \sqrt{1 + \frac{\eta_Q^2}{3}}$ , with the isotropic shift obtained from the intercept of the plot apparent shift against the inverse of the field. <sup>b</sup> - EFG tensor conventions derived for 3QMAS simulations:  $V_{33} \geq V_{22} \geq V_{11}$ ,  $C_Q = \frac{e^2 q Q}{h}$ ,  $\eta_Q = \frac{V_{11} - V_{22}}{V_{33}}$  ( $1 \leq \eta_Q \leq 0$ ).

### 5.3.5 The 3QMAS spectra of highly labelled Apatite Ion Conductors

The 3QMAS (figure 5.6) of the silicate sample shows two distinct sites in the one dimensional experiment, these are fully separated in the two dimensional MQMAS, showing two peaks,  $\text{SiO}_4$  and  $\text{SiO}_{4+1}$  with a similar  $C_Q$  and  $\eta_Q$ . However, larger chemical shift dispersion is shown for the  $\text{SiO}_{4+1}$  peak due to the variation in the bond lengths and bond angles around silicon centre. A single  $\text{GeO}_4$  peak is observed for the  $\text{La}_{7.5}\text{Ca}_{2.5}\text{Ge}_6\text{O}_{25.75}$  stoichiometric case showing very little chemical shift dispersion and a larger quadrupolar coupling range.  $\text{La}_8\text{Y}_2\text{Ge}_6\text{O}_{27}$  indicates two very distinct resonances, a quadrupolar dominated  $\text{GeO}_4$  framework site ( $C_Q \approx 4.6$  MHz and  $\eta_Q \approx 0.4$ ) and a chemical dispersion interstitial ( $C_Q \approx 2.8$  MHz and  $\eta_Q \approx 0.5$ ). This observation suggests the interstitial forces more disorder on the lineshape due to its asymmetric environment and mobility throughout the material. The  $\text{La}_{9.83}\text{Ge}_{5.5}\text{Nb}_{0.5}\text{O}_{26.5}$  apatite shows the formation of the framework  $\text{GeO}_4$  and  $\text{NbO}_4$  sites as well as the  $\text{GeO}_5$  and  $\text{NbO}_5$  interstitials. The results show the same trend as the lanthanum-yttrium apatite with the mobile interstitial giving large chemical shift dispersion in comparison to the framework tetrahedra.

### 5.3.6 The Double Rotation spectra of of highly labelled Apatite Ion Conductors

The DOR spectrum, as shown in figure 5.7, reduces the second order quadrupole broadening by spinning the sample at two angles. The spectra of the stoichiometric  $\text{La}_{7.5}\text{Ca}_{2.5}\text{Ge}_6\text{O}_{25.75}$  (5.7 b) sample removes the second order quadrupole broadening and hence increases the spectral resolution. The samples containing the interstitials 5.7 a, c and d have no obvious decreased line width and increased resolution. This is due to the mobility of the interstitial causing an increased chemical shift dispersion which now dominates the lineshape and is not removed by DOR. This mobile disorder overcomes the quadrupole coupling and hence the linewidth cannot be narrowed by solely reducing the first and second order quadrupole couplings. This gives increased evidence for the interstitial being responsible for the conductivity of the sample, due to its high chemical shift dispersion and is probably due to mobility. The sample without the interstitial (5.7 b) has limited oxide ion mobility and is therefore a more rigid structure and hence can be broken up into its individual framework oxygen sites.

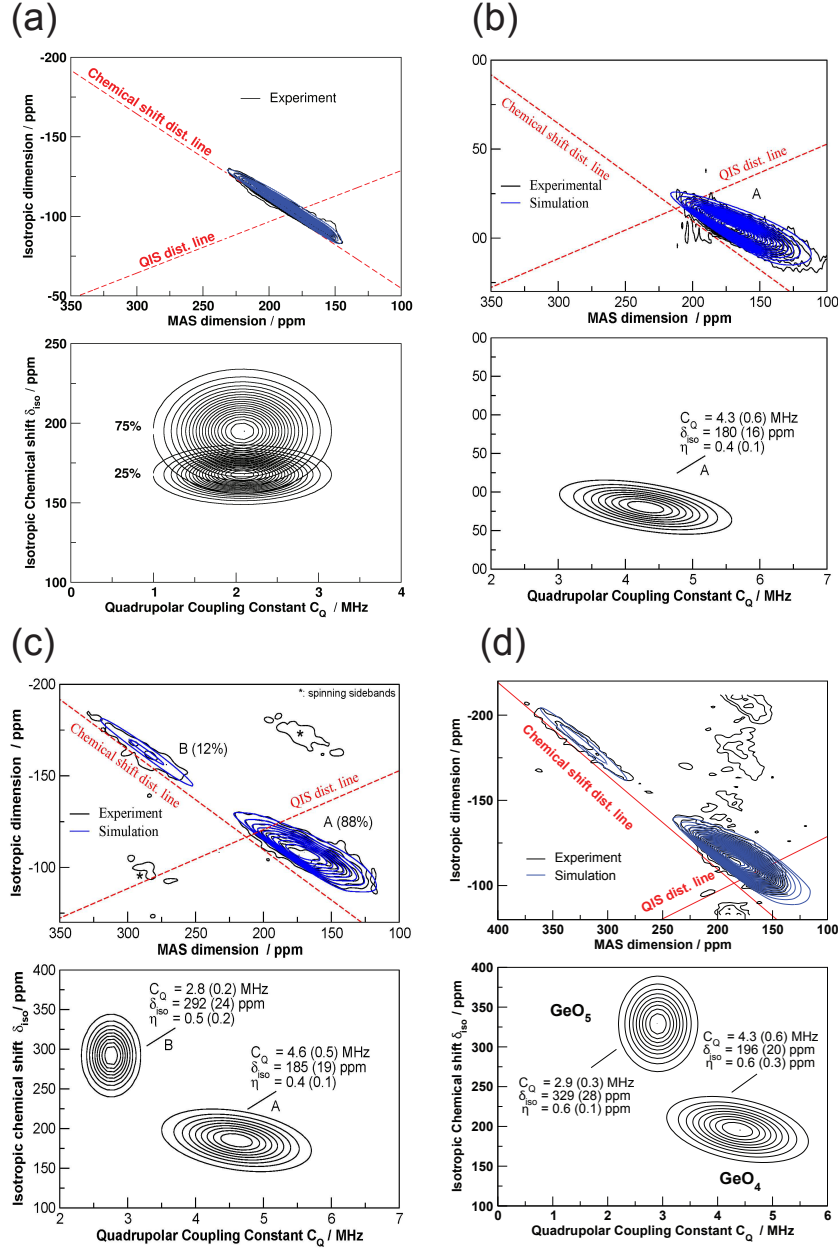


Figure 5.6: 3QMAS (15 kHz) experiments on a highly (90% +)  $^{17}\text{O}$  labelled (a)  $\text{La}_{9.6}\text{Si}_6\text{O}_{26.4}$ , (b)  $\text{La}_{7.5}\text{Ca}_{2.5}\text{Ge}_6\text{O}_{25.75}$ , (c)  $\text{La}_8\text{Y}_2\text{Ge}_6\text{O}_{27}$  and (d)  $\text{La}_{9.83}\text{Ge}_{5.5}\text{Nb}_{0.5}\text{O}_{26.5}$  apatite samples to elucidate the different isotropic chemical shifts,  $C_Q$  and  $\eta_Q$  information. The top spectra for each sample is the sheared data achieved with a blue overlying simulation and the red quadrupolar and isotropic shift axis dotted on. The bottom spectra represent the simulation with the a mathematical operation performed to deduced the quadrupolar coupling axis and the isotropic shift axis.

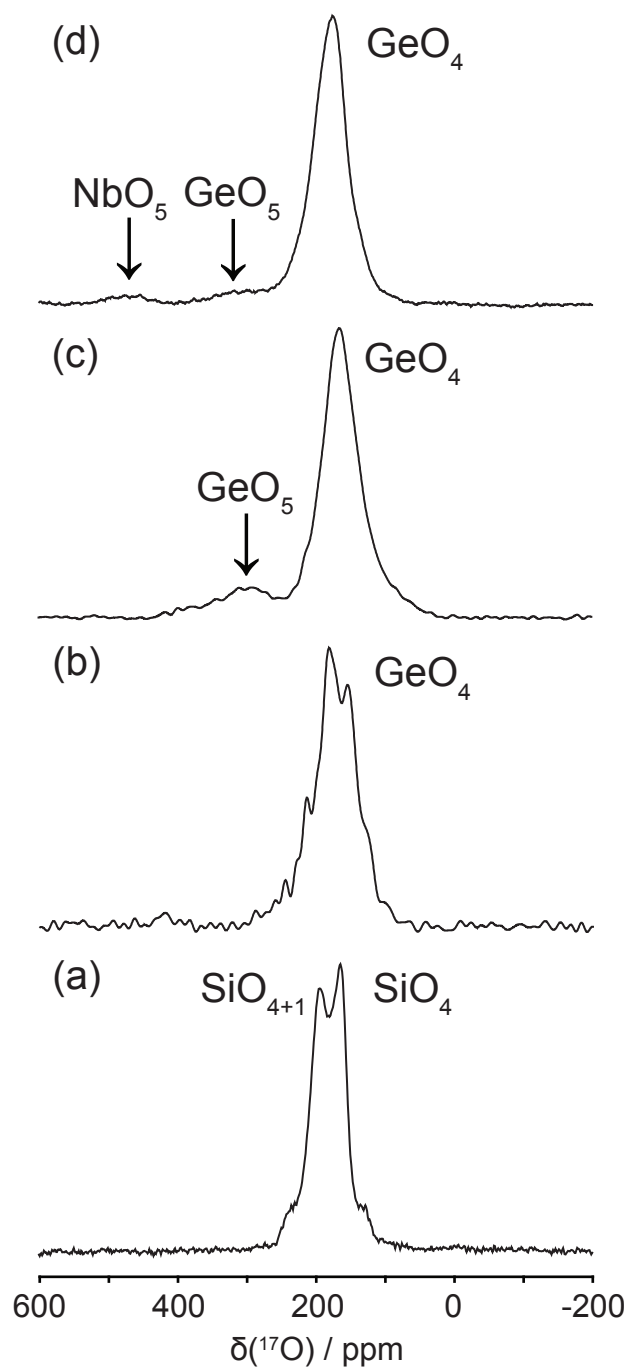


Figure 5.7: DOR spectra of the highly (90% +  $^{17}\text{O}$ )labeled apatites (a)  $\text{La}_{9.6}\text{Si}_6\text{O}_{26.4}$ , (b)  $\text{La}_{7.5}\text{Ca}_{2.5}\text{Ge}_6\text{O}_{25.75}$ , (c)  $\text{La}_8\text{Y}_2\text{Ge}_6\text{O}_{27}$  and (d)  $\text{La}_{9.83}\text{Ge}_{5.5}\text{Nb}_{0.5}\text{O}_{26.5}$ .

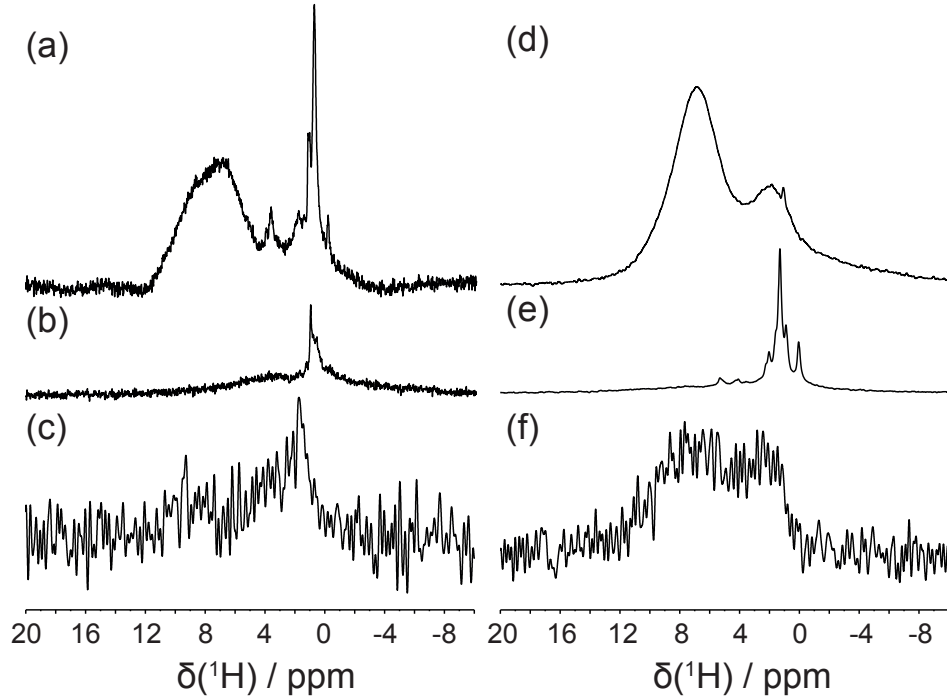


Figure 5.8: The proton ( $^1\text{H}$ ) MAS spectra of (a) wet, (b) dried and (c) BaBa of  $\text{La}_{7.5}\text{Ca}_{2.5}\text{Ge}_6\text{O}_{25.75}$  and the corresponding spectra for  $\text{La}_8\text{Y}_2\text{Ge}_6\text{O}_{27}$  in (d), (e) and (f).

### 5.3.7 Proton Motion Studies

The  $^1\text{H}$  MAS NMR spectra of wet and dried  $\text{La}_8\text{Y}_2\text{Ge}_6\text{O}_{27}$  are shown in Figure 5.8. In the wet sample (5.8 d), the resonances are located at  $\delta_{iso} = 1, 2$  and  $7$  ppm. The broad resonance at  $7$  ppm is assigned to physisorbed water located within the crystal structure. The two resonances at lower frequency correspond to hydroxide ions. In a study of the  $^1\text{H}$  environments in hydroxyapatite, the presence of structural OH and surface adsorbed water was reported. [207, 227–230] Here, the water occupies sites within the structure and is not just located on the surface. This is consistent with the location suggested by X-ray diffraction studies, where changes in the unit cell parameters show that water incorporation occurs at the interstitial sites within the  $\text{GeO}_4$  framework. The multiple hydroxyl resonances correspond to a variety of local environments and support the location of hydroxide ions in both channel and interstitial positions 5.1, 5.2 and 5.3. Also present in (5.8 c) is a  $^1\text{H}$  MAS double quantum filtered (DQF) spectrum using the Back-to-Back (BaBa) pulse sequence. [231] In this experiment, protons that are mobile on the timescale of the pulse sequence are motionally averaged and filtered from the

spectra. For  $\text{La}_8\text{Y}_2\text{Ge}_6\text{O}_{27}$ , the sharp resonance corresponding to the hydroxide ions ( $\delta_{iso} = 1$  ppm) is completely filtered out, meaning they are moving faster than  $33 \mu\text{s}$ . The broad resonances for hydroxide ions and adsorbed water also appear to be highly filtered out, evidence of some mobility of the hydroxides and water molecules within the sample. The  $^1\text{H}$  spectrum of the dry sample (e) shows that the water molecules are completely removed from the sample but that some residual hydroxide ions remain. If the hydroxide ions are located in the channels, as proposed in 5.3, you would expect all of the ions to be removed easily via the channels along the  $c$ -axis. There must be hydroxide ions located in the interstitial positions as well 5.1 and 5.2, explaining why it is not possible to completely remove all the hydroxides at temperatures as high as  $500^\circ\text{C}$ . The hydroxide resonances have narrowed significantly in the dry sample, suggesting that the  $^1\text{H}$ - $^1\text{H}$  dipolar coupling interaction is much weaker. This is consistent with hydroxide ions being located in the interstitial positions, more isolated from each other within the structure.

The  $^1\text{H}$  MAS NMR spectra of wet (5.8 a) and dry (5.8 b)  $\text{La}_{7.5}\text{Ca}_{2.5}\text{Ge}_6\text{O}_{25.75}$  are included in Figure 5.8. In comparison to the proton content in  $\text{La}_8\text{Y}_2\text{Ge}_6\text{O}_{27}$ , the types of proton environments are similar physiosorbed water and hydroxides. The concentration of protons in  $\text{La}_{7.5}\text{Ca}_{2.5}\text{Ge}_6\text{O}_{25.75}$  is much lower than in  $\text{La}_8\text{Y}_2\text{Ge}_6\text{O}_{27}$ . This is consistent with recent thermogravimetric analysis (TGA) data where the stoichiometric germanate sample showed much lower water content than the oxygen excess systems. Moreover, the  $^1\text{H}$  resonances in  $\text{La}_{7.5}\text{Ca}_{2.5}\text{Ge}_6\text{O}_{25.75}$  are narrower, implying that the protons are more isolated in this system. The DQF spectrum of  $\text{La}_{7.5}\text{Ca}_{2.5}\text{Ge}_6\text{O}_{25.75}$  (5.8 c) shows that most of the protons are moving faster than  $33 \mu\text{s}$ . The lower concentration of water molecules in the stoichiometric sample could result in a greater ease of motion within the lattice structure.

## 5.4 Conclusions

Since oxygen enrichment in the samples studied here was achieved by reaction of the sample with labelled water, the sites detected using  $^{17}\text{O}$  MAS NMR must have exchanged with the labelled water. As described above, water incorporation into the apatites preferentially occurs at interstitial sites within the  $\text{Si}/\text{GeO}_4$  framework rather than down the oxygen channels. The labelled water must then be exchanging with the channel oxygens, forming interstitials according to 5.3. These  $^{17}\text{O}$ -enriched interstitial oxide ions are moving through the channels by exchanging with the  $\text{Si}/\text{GeO}_4$  tetrahedra to form intermediate  $\text{SiO}_{4+1}/\text{GeO}_5$  environments. Thus the water in the interstitials is close to enough to the tetrahedra to exchange directly.

This explains the intense  $^{17}\text{O}$  resonance attributed to the  $\text{Si}/\text{GeO}_4$  tetrahedra and  $\text{SiO}_{4+1}/\text{GeO}_5$  unit. This is the first direct experimental evidence confirming that the germanate substructure is involved directly in the conduction of the interstitials. This supports the conclusion that conduction of the interstitial oxide ions occurs in a non-linear pathway, involving oxygens in the tetrahedra. It is also possible to quantify the size of the  $C_Q/P_Q$  and  $\eta_Q$  by variable field, two dimensional 3QMAS and multiple angle spinning methods. These show that the tetrahedra present in both silicates and germanates have quadrupole coupling constants almost twice that of the corresponding  $\text{SiO}_{4+1}/\text{GeO}_5$ . This has been firmly supported by the density functional theory CASTEP data, suggesting that the introduction of the bridging interstitial brings higher symmetry to the local environment.



## Chapter 6

# A Multinuclear Solid State NMR, DFT and Diffraction study of Tight Hydrogen Bonds in Group IA Hemibenzoate

### 6.1 Introduction to Solid State NMR and the Measurement of Hydrogen Bonding

The study of hydrogen bonding in small organic and biological molecules by  $^1\text{H}$ ,  $^{13}\text{C}$  and  $^{15}\text{N}$  solid state nuclear magnetic resonance (SSNMR) has become very common place in the past few decades. [232–237] Hydrogen bonding has an important role in higher order structure formation in proteins, DNA, RNA and polymers.[238–240] Hydrogen bonding is commonly studied by infra-red (IR) spectroscopy, solution state NMR and neutron diffraction.[241–243] Neutron diffraction, although difficult, is a facile method of measuring the hydrogen bonding interaction as it gives precise bond lengths and atomic positions.[244] The IR stretching frequencies have been shown to be proportional to these distances determined by neutron diffraction, however it suffers from the limitation of resolution when multiple hydrogen bonded sites are present in the sample. Here we present a multinuclear solid state nuclear magnetic resonance (SSNMR), X-ray diffraction (XRD) and density functional theory (DFT) study of the hydrogen bonding in benzoic acid (BZA) and its corresponding Group 1A (Li, K, Rb and Cs) hemibenzoate salts (HB). SSNMR is a powerful tool for elucidation of structure in materials and complements the long-

range structural information obtained by XRD by providing a local picture of the environment around the nucleus. Most SSNMR experiments have focused on the much favoured spin -  $\frac{1}{2}$  nuclei such as  $^1\text{H}$ ,  $^{13}\text{C}$ ,  $^{15}\text{N}$  and  $^{29}\text{Si}$ . However over the past two decades a protocol to establish NMR studies of  $^{17}\text{O}$  ( $I = \frac{5}{2}$ ) and other quadrupolar nuclei ( $I \geq \frac{1}{2}$ ) have become more common place.[56, 245] Recently,  $^{17}\text{O}$  SSNMR studies for inorganic solids have become more frequent ever since the initial work by Oldfield and natural abundance studies on very simple oxides by Bastow and Stuart. [222, 246] In inorganic materials the electric field gradient (EFG) tends to be very small due to high symmetry, resulting in relatively high resolution magic angle spinning (MAS) spectra, this makes  $^{17}\text{O}$  an ideal candidate for studying complex oxide structures such as  $^{17}\text{O}$  labelled pervoskites and apatites. [1, 247]

Recently the description of a hydrogen bond has changed to take into consideration the broad range of bonds formed by hydrogen and to eliminate other interactions which can be mistaken for hydrogen bonds, such as permanent multipoles, inductive forces and London dispersion. The description provided by IUPAC is given as:

The hydrogen bond is an attractive interaction between a hydrogen atom from a molecule or a molecular fragment  $\text{X}-\text{H}$  in which X is more electronegative than H, and an atom or a group of atoms in the same or a different molecule, in which there is evidence for bond formation. [248]

Firstly the authors note that they are not defining the word 'bond' in this statement. Another point is the word 'attractive', this word is important in the solid state context as it takes into consideration the stabilisation and geometry of the crystal system caused by the hydrogen bond formation. [249] A case in point is the very short bond distances sometimes observed in  $\text{C}-\text{H} \cdots \text{O}$  contacts, however these interactions are destabilising and hence unattractive. This means they are not forming hydrogen bonds.

Some of the criteria to measuring hydrogen bonding are also explained. The hydrogen bond ( $\text{X}-\text{H} \cdots \text{Y}-\text{Z}$ ) is usually linear ( $180^\circ$  with a minimum angle of  $110^\circ$ ), the  $\text{X}-\text{H}$  bond usually increases with with bond formation causing a red shift in the infrared stretching frequency and the proton resonances observed by NMR give very characteristic deshielded signatures. [248–250]

There is a copious amount of previous work on hydrogen bonded biological systems, the motivation for this work is that hydrogen bonding plays an important role in high order molecular tertiary and quaternary structure formation in proteins and DNA. Thus, simple organic molecules and amino acids have been used as model

systems to gain insights into much larger biological and pharmaceutically significant samples. Hydrogen bond distances in simple molecules have been correlated to their deshielded isotropic resonances observed in their respective proton NMR spectra (10 – 25 ppm); however due to poor resolution caused by dipole-dipole coupling, deconvoluting multiple hydrogen bonded sites in the solid state becomes difficult. Harris and co-workers determined the  $^1\text{H}$  isotropic shift of the proton involved in the hydrogen bond for a series of carboxylic acids; the  $\delta_{iso}$  for BZA was determined to be 12.7 ppm.[251] These results were correlated with oxygen-oxygen distances across the hydrogen bond. Gobetto *et al.* showed that it is also possible to correlate the isotropic  $^1\text{H}$  and  $^{15}\text{N}$  chemical shifts with determined N–O distances of the atoms involved in the NH—O hydrogen bond.[252]

It has been deduced that the 'strength' of a hydrogen bond at certain sites within a structure can be determined via the chemical shift (CS) tensorial components from the anisotropy observed in SSNMR spectrum. [234, 235, 253] Traditionally, the tensorial CS components describe the chemical shift variation with the sample orientation. To observe directly the classic chemical shift anisotropy (CSA) resonance either slow MAS (1 – 3 kHz) or a static SSNMR experiment is implemented; as the interaction is reduced or removed during MAS. [55] Static SSNMR has the advantage of giving excellent lineshape simulations to achieve the span and skew data; it has the disadvantage of broadening the resonances by orders of magnitude making it difficult to separate multiple environments. However, if other interactions are present (e.g. homonuclear, dipolar and quadrupolar) they will also contribute to broadline data, this complicates the interpretation. The obvious way around these disadvantages is to selectively isotopically enrich the samples at the desired chemical site. Conversely, slow MAS can be used to distinguish between multiple carbon anisotropies; however it does have the disadvantage of giving larger errors in the spectral simulation of the anisotropy.

For  $^{13}\text{C}$  SSNMR the  $\delta_{11}$  component of the line represents the least shielded resonances and has previously been shown to decrease in ppm when deprotonated and increase in ppm when protonated. The  $\delta_{33}$  parameter is the most shielded and shown to be orthogonal to the  $\text{CO}_2\text{H}$  functional group. The  $\delta_{22}$  parameter sits near the C=O bond and varies considerably with the hydrogen bond length. Likewise, the CS tensorial components of the oxygen SSNMR resonance follow a similar trend and have been shown to give considerable variations with decreasing hydrogen bond length.

Tensor data in NMR has a significant advantage over the isotropic shift as the tensor components have a larger magnitude of variation and hydrogen bonding has

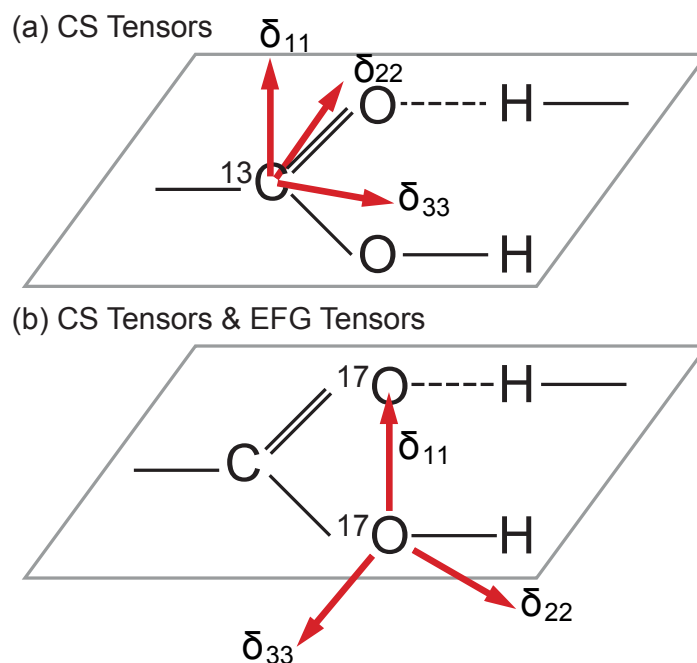


Figure 6.1: The diagram shows a tensorial representation of the chemical shift (CS) anisotropies for  $^{13}\text{C}$  (a) and  $^{17}\text{O}$  nuclei (b) involved in carboxylic acid hydrogen bonded systems. The following conventions are applicable for the various tensorial parameters. The terms used in the convention are described in section 2.3.5.

been shown to only affect certain parameters of the three tensor components. Results by McDermott have shown a strong correlation between the hydrogen bond distance between carboxyl groups and amine, as derived from neutron diffraction, and the  $\delta_{22}$  component of the static  $^{13}\text{C}$  NMR spectrum of the carboxyl group. [1d, 10a] This group has found that the  $\delta_{11}$  and  $\delta_{22}$  components of the chemical shift tensor at the O–H and C=O respectively, are aligned nearly parallel with the strong H-bond and shift away as the hydrogen bond length increases and strength decreases. [245, 254] Wu and Yamada have completed  $^{17}\text{O}$  SSNMR studies on a range of small organic molecules as well as BZA and potassium hemibenzoate (KHB) yielding quadrupole coupling parameters for the multiple oxygen sites present in each, these results have confirmed previous nuclear quadrupole resonance (NQR) results. [255–257] From this the tensorial interactions were deconvoluted to show that the hydrogen bond distance is reflected in the anisotropic parameters.

BZA and its alkali metal hemibenzoates have been classically used as a description for hydrogen bonding. BZA was originally discovered in the form of gum benzoin by Nostradamus in the 15 th Century with the structure being comprehensively described by Goodwin *et al.* in 1955. [258, 259] SSNMR studies have

been completed to yield results on rate of proton transfer between the two hydrogen bonded oxygen groups, to determine the heteronuclear dipolar coupling and a through bond characterisation. [260] Tightly hydrogen bonded systems have two types of intermolecular bonds between the carboxylic groups; these have been confirmed by work on their crystal structures.[261] Type A occurs when two carboxyl groups are related by a symmetry element of the crystal meaning there is effectively one oxygen environment present. A classic example of this is the proton in  $\text{NaHF}_2$  and  $\text{KHF}_2$ , in each case the  $\text{FHF}^-$  ion lies across a centre of symmetry.[261] This indicates the proton bonded between the two oxygens is in a centred symmetrical position. Type B is relevant when the two carboxyl groups have structural differences and are not symmetry related forming an ionised and deionised formation. This indicates the proton must be closer to one of the oxygen groups than the other, effectively creating two different oxygen environments, as with BZA.

## 6.2 Experimental

### 6.2.1 Sample Preparation

BZA was prepared from a microwave hydrolysis (433.15 K, 16 bar, 15 mins) of  $\alpha,\alpha,\alpha$ -trichlorotoluene with +90 %  $^{17}\text{O}$  labelled water. The resulting product was allowed to cool to room temperature and the excess pressure released liberating the  $\text{HCl(g)}$ . The resultant mixture was again heated in the microwave reactor to 433.15 K for 45 minutes at 16 bar, the products pressure was once again released upon cooling. Depending on the degree of conversion to BZA (as determined by GC-MS analysis), a further amount of  $^{17}\text{O}$ -labelled water was added (typically 50 – 100  $\mu\text{L}$ ), and the mixture treated under the same microwave conditions (45 mins). This was repeated, if necessary, until GC-MS showed almost complete conversion to benzoic acid. Crude product was recrystallized from heptane, typical isolated yield of 94 %. The potassium hemibenzoate (KHB), rubidium hemibenzoate (RbHB) and caesium Hemibenzoate (CsHB) were prepared from two methods. Method A involved potassium hydroxide in water (1 mL) being added to a hot solution of  $^{17}\text{O}$ -labelled benzoic acid in ethanol (2 mL) and the immediately formed precipitate heated for 5 minutes. Water was added until a solution was just formed, and the product left to crystallise. In the second method, B, potassium hydroxide in methanol was added to a hot solution of  $^{17}\text{O}$ -labelled benzoic acid in THF (2.5 mL) and the immediately formed precipitate heated for 5 minutes. Methanol was added until a solution was just formed, and the product left to crystallise. Further synthetic details and characterisation are present in the appendix.

### 6.2.2 Crystallography

All crystallography was completed at Nottingham Trent University (NTU) by Prof. John Wallis. X-ray diffraction datasets were measured on a Bruker-Nonius FR591 diffractometer equipped with a rotating anode and a Bruker-Nonius Roper CCD camera (National Crystallography Service, Southampton University, UK). The orthorhombic polymorph of caesium hemibenzoate was measured on an Oxford Diffraction Xcalibur diffractometer equipped with a Sapphire CCD detector at NTU. Crystal cooling was provided by an Oxford Cryosystems Cryostream low temperature system. Crystal structure solution and refinement were carried out with SHELXS and SHELX programs using the XSEED interface.[262, 263] Non-hydrogen atoms were assigned anisotropic displacement parameters. All hydrogen atom positions were determined geometrically and refined with a riding model, except as follows: lithium hemibenzoate and sodium benzoate. Two benzoic acid: coordinates of the (O)H atoms refined; potassium hemibenzoate: two (O)H positions, related by a centre of symmetry in the middle of the O—O vector, refined with half occupancies; rubidium hemibenzoate and both polymorphs of caesium hemibenzoate: electron density corresponding to the (O)H atom located on a two-fold axis and equidistant from two O atoms (O—O: (Rb) 2.455 Å, (Cs monoclinic) 2.457 Å, (Cs orthorhombic) 2.457 Å) and only the y coordinate refined in each case. In the rubidium and caesium cases, these (O)H positions may be misleading, and may be rather an average of a disorder between two positions in which the H atom lies closer to one O atom or the other. Molecular illustrations were made with Mercury and POV-Ray. [264] The full crystal data recorded is present in the appendix section of this thesis.

### 6.2.3 Solid State NMR

The  $^1\text{H}$  MAS (27.5 kHz, 500.1 MHz) SSNMR was completed on a Bruker Avance III 11.7 T spectrometer; all samples were referenced to the primary standard of tetramethylsilane (TMS, 1,  $\delta_{iso} = 0$  ppm). [265] The  $^{13}\text{C}$ -Carboxy labelled benzoic acid was purchased from Sigma Aldrich and the corresponding salts were synthesised as previously discussed. Variable MAS  $^{13}\text{C}$  NMR was completed at 100.3 MHz (9.4 T) using a Bruker 3.2 mm dual channel probe. A variable amplitude cross polarisation from the  $^1\text{H}$  nuclei was utilised with a contact time of 900  $\mu\text{s}$  and proton  $90^\circ$  pulse of 3.00  $\mu\text{s}$ . Various spinning frequencies of 0.8, 1.5 and 12 kHz were used to allow a detailed sideband analysis and hence to determine the CSA. Sideband manifold spectral simulation was completed on the solids line analysis

function available in TOPSPIN 2.1.

The  $^{17}\text{O}$  spectra were acquired at Larmor frequencies of 52.23 and 81.34 MHz using an AV-400 (9.4 T) and a Bruker AV-600 (14.1 T) spectrometers respectively. A 2.5 mm Bruker double resonance (HX) probe was used on both spectrometers with a magic angle spinning (MAS) frequency of 27.5 kHz facilitated. The spectra are reported against a primary reference of  $\text{H}_2^{17}\text{O}$  (l),  $\delta_{iso} = 0$  ppm). All  $^{17}\text{O}$  spectra were acquired with a rotor-synchronized solid-echo sequence, using selective (solid)  $\frac{\pi}{2}$  pulse durations (scaled from a selective (solution) values measured on 10 %  $\text{H}_2^{17}\text{O}$  by  $(I + \frac{1}{2})$  of 1.0 - 1.5  $\mu\text{s}$  and a recycle delay of 1 second. The triple quantum MAS (3QMAS) spectra were achieved at 81.34 MHz using a double resonance Bruker 2.5 mm probe with a MAS frequency of 27.5 kHz. All 3QMAS experiments were recorded using a three pulse Z-filter pulse sequence. A non-selective 5.0  $\mu\text{s}$   $\frac{3\pi}{2}$  excitation and 1.5  $\mu\text{s}$   $\frac{\pi}{2}$  conversion pulse was followed by two 40.00  $\mu\text{s}$  selective  $\frac{\pi}{2}$  pulses. DOuble Rotation (DOR) experiment was completed at 81.341 MHz (Bruker AV-600 at 14.1 T) and 115.250 MHz (Bruker AVIII-850 at 20.0 T) both using a Samoson DOR probe with an outer rotor spinning frequency varying between 1.2 - 1.8 kHz and an internal rotor spinning frequency of 5.8 - 8.8 kHz.

The  $^7\text{Li}$  result was achieved on a Bruker AV-III 500 (11.7 T) spectrometer with a Bruker HX 3.2 mm giving a MAS frequency of 20 kHz. A one pulse experiment with a solid pulse of 1.50  $\mu\text{s}$  was determined from 9.6 M  $\text{LiCl}_{(\text{aq})}$  solution ( $\delta_{iso} = 0$  ppm) and a recycle delay of 60 seconds was determined. Multiple field static potassium NMR was achieved at 18.66 MHz on a Bruker AV-400 (9.4 T) using a 9.5 mm low gamma Varian MAS probe and 27.97 MHz on a Bruker AV-600 (14.1 T) using a Bruker 10 mm static probe. All spectra were referenced to 0.1 M  $\text{KCl}_{(\text{aq})}$  ( $\delta_{iso} = 0$  ppm) and the pulses were scaled by  $I + \frac{1}{2}$  to give representative solid pulse of 5  $\mu\text{s}$ . Static rubidium NMR were collected at 65.25, 130.50 and 196.13 MHz on Varian Infinity 200 (4.7 T), Bruker AV-400 (9.4 T) and a Bruker AV-600 (14.1 T) spectrometers respectively. All three were obtained using a Bruker 10 mm static probe and were referenced to  $\text{RbCl}_{(\text{s})}$  ( $\eta = 0$ ,  $\delta_{iso} = 0$ ). All three  $^{87}\text{Rb}$  spectra were acquired with a rotor-synchronized solid-echo sequence, using a selective (solid)  $\frac{\pi}{2}$  pulse durations of 1.0  $\mu\text{s}$  and a recycle delay of 0.25 seconds.  $^{133}\text{Cs}$  results were obtained at frequencies of 52.32 and 78.62 MHz using a HX Bruker 3.2 mm probe on a Bruker AV-400 (9.4 T) and a Bruker AV-600 (14.1 T) spectrometers respectively. A MAS frequency of 10 kHz was employed at both resonances and a one pulse sequence using selective (solid)  $\frac{\pi}{2}$  pulse durations which were scaled from non-selective ( $\eta = 0$ ) values measured on  $\text{CsCl}$  (18 ppm, 1 M  $\text{CsNO}_{3(\text{aq})}$ ,  $\delta_{iso} = 0$  ppm) by  $(I + \frac{1}{2})$  of 2.0  $\mu\text{s}$  and a recycle delay of 5 seconds was used. The basic solid

salts of  $\text{LiCl}_{(s)}$ ,  $\text{KCl}_{(s)}$ ,  $\text{RbCl}_{(s)}$  and  $\text{CsCl}_{(s)}$  were also running during their respective experiments to compare with DFT calculations discussed below. All quadrupolar MAS NMR spectra were simulated with the freely available DMFit program. [266]

#### 6.2.4 Computational Aspects

The ab initio density functional theory (DFT) calculations were carried out using CASTEP 5.52 at the HECToR high-performance computing cluster and at the University of Warwick centre for scientific computing cluster Francesca. [214]

This code employs Kohn-Sham DFT using periodic plane-waves under the pseudopotential approximation. The correlation generalized gradient approximation for the exchange correlation energy was employed using the Perdew-Burke-Ernzerhof (PBE) functional. [136, 267] The action of the valence electrons was defined by on-the-fly pseudopotentials generated by Accelrys Software Materials Studio. A minimum standard basis set convergence of 0.3675 mHa ( $\text{Ha} = \text{Hartrees}$ ,  $\approx 0.0005\%$  of  $kT$  at room temperature ( $25^\circ\text{C}$ )) per atom was set for the each of the systems under investigation. Energy minimization calculations were repeated to determine the plane-wave cut-off energy and the  $\mathbf{k}$  point sampling of the Monkhorst-Pack of the first Brillouin zone required for such a convergence. This level of convergence was achieved using a plane wave cut-off energy of 900 eV for the Li, Rb and Cs hemibenzoates and 950 eV for the KHB, as well as using  $\mathbf{k}$ -point Monkhorst-Pack spacing of 0.075 for the K and Li systems and 0.1 for the Cs and Rb hemibenzoates. At this level of accuracy it was assumed that the NMR parameters would have been fully converged.

Geometry optimisation and hydrogen optimisation calculations were performed on all the systems. For these structural optimisations the lattice parameters were kept fixed whilst the atomic positions were allowed to relax to a force tolerance of  $0.05 \text{ eV } \text{\AA}^{-1}$  and a total energy per atom of  $1 \times 10^{-5} \text{ eV}$ .

The pseudopotential approximation only allows for an explicit treatment of the valence electrons, yet the chemical shielding tensor depends critically on the details of the all-electron wave function at the nucleus. The gauge-including projector augmented-wave (GIPAW)-DFT method and the projector augmented-wave (PAW) method were used to reproduce the results of an all electron calculation of the chemical shifts and electric field gradient respectively under the pseudopotential approximation for the original and geometry optimised systems. [268, 269]

The equilibrium density is related to the negative exponential of the energies of the independent particle states, whereas the density is directly related to the NMR parameters. The lower sensitivity of the density with respect to energy means



that convergence at the milli-Hartree per atom level specified earlier should directly imply convergence of the NMR parameters. Subsequently each of the systems were run with the same cut-off energy and k-point sampling as specified by the energy minimisation calculations earlier.

In order to calculate the isotropic chemical shifts  $\delta_{iso} = -[\sigma - \sigma_{ref}]$ , where  $\sigma$  is the isotropic shielding and  $\sigma_{ref}$  is the isotropic chemical shift of the same nucleus in a reference frame, separate GIPAW-DFT calculations were run on a set of references; benzoic acid (Cambridge database reference code - BENZAC07), alanine (LALNIN24), LiCl (44273), KCl (44281), RbCl (44285) and CsCl (44289). [270–272] These calculations used the same basis set convergence (0.3675 mH) as the original calculations in order to minimise the propagation of errors. Due to the cubic nature of the chlorides and small unit cells of the references in general the calculations could be completed with 16 cores at the now defunct Francesca high-performance computing cluster.

In order to fix the chemical shift scale for  $^{17}\text{O}$  it was assumed that the summed isotropic chemical shifts established experimentally should be equal to the theoretical values calculated computationally. Then the chemical shielding values calculated with CASTEP were summed over for each site and the chemical shifts were taken away in order to produce  $\sigma_{ref} = 260.4$  ppm. The same principle was applied for the proton and carbon NMR giving  $^1\text{H}$   $\sigma_{ref} = 30.0$  ppm and  $^{13}\text{C}$   $\sigma_{ref} = 168.0$  ppm. For the metal nuclei the references LiCl, KCl, RbCl and CsCl were used to set a zero from which the benzoate systems could be calibrated.

## 6.3 Results and Discussion

### 6.3.1 Crystallography

The crystallographic structure determination of BZA has been previously completed by numerous workers; we have chosen to use the relatively recent study by Wilson using neutron diffraction at 20 K for density functional theory calculations. [272] The crystal structures of the corresponding group IA metal hemibenzoates are shown in figure 6.2 and their crystal packing illustrated in figure 6.3.

LiHB crystallises in space group P-1, with one lithium cation, a benzoate anion and a benzoic acid moiety all of which are crystallographically unique. Two lithiums and one oxygen (O4) from two of the benzoate anions form a centrosymmetric  $\text{Li}_2\text{O}_2$  rectangle, and the second O atom (O3) from the two benzoates act as coordinating ligands to the next  $\text{Li}_2\text{O}_2$  rectangles in the  $+a$  and  $-a$  directions to form a linear coordination polymer. A benzoic acid molecule completes the struc-

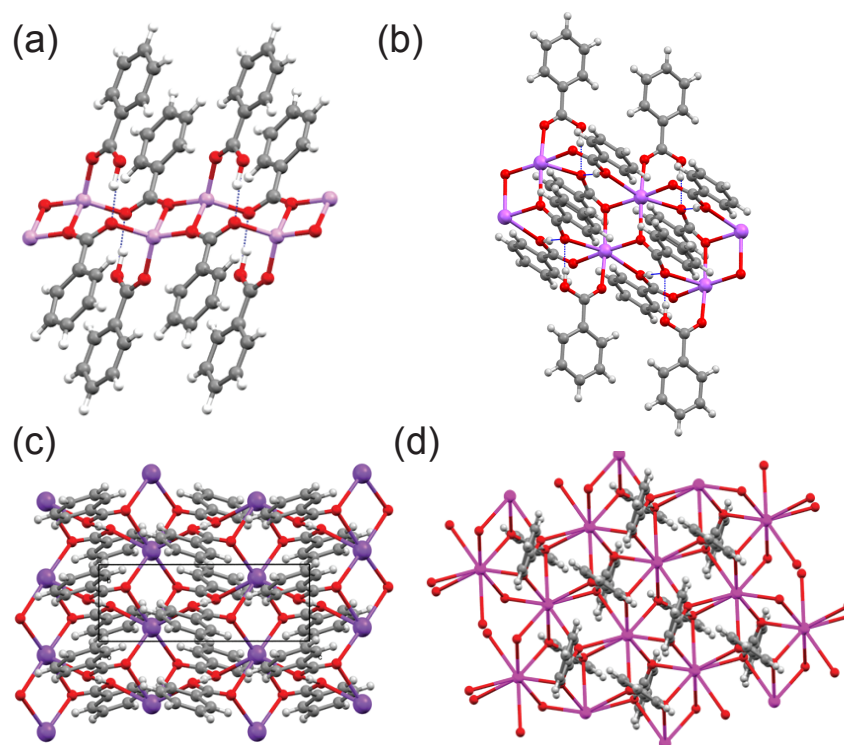


Figure 6.2: The crystal structures of (a) 1-dimensional co-ordination polymer formed by LiHB. The benzoate anions bridge two lithiums, benzoic acid molecules complete the coordination, (b) A view of a layer of potassium ions showing their involvement in two coplanar  $K_2O_2$  rectangles where the participating O atoms are not involved in a hydrogen bond, (c) The rubidium/oxygen network containing where each rubidium is involved in four  $Rb_2O_2$  rectangles.

ture, with the carbonyl O atom (O2) providing the fourth coordination site at the lithium, and the  $-OH$  group forming a hydrogen bond with the benzoate O atom (O3) ( $O\cdots O$ : 2.613 Å,  $OH\cdots O$ : 1.58 Å, angle at H:  $169.8^\circ$ ) which links the rectangles and so completes an eight membered ring involving four O, two C one Li and one H atom. There are thus four distinct oxygen atom environments: an OH (O1), a C=O group (O2) which coordinates one lithium, and two benzoate O atoms, one of which (O3) coordinates one Li ion and forms a hydrogen bond, while the second (O4) coordinates two Li ions. The coordination polymers lie side by side in the  $-b$  and  $+b$  directions to form a layer in the  $ab$  plane, and the interface between the layers in the  $-c$  and  $+c$  directions involves only the benzene rings but with no interdigitation of aromatic residues. Within a layer benzene rings of the benzoic acid and benzoate residues lie at an angle of  $8.8^\circ$ .

From the sodium benzoate/benzoic acid system Flammersheim has identified

two 1 : 2 complexes and one 2 : 1 complex, but no 1 : 1 hemibenzoate has been prepared. [273] We isolated crystals of the 1 : 2 complexes, which crystallised in space group P21/c and forms coordination polymers oriented along the *a* axis. Adjacent coordination polymers in the *b* direction are related by a unit cell translation, while adjacent chains in the *c* direction are related by the *c* glide plane perpendicular to *b*. One sodium ion, one benzoate ion and two benzoic acid molecules are crystallographically unique. Two sodium ions and two oxygens (O2A) from different benzoate molecules form Na<sub>2</sub>O<sub>2</sub> rectangles which are linked together in two ways. The second benzoate oxygen atom (O1A) coordinates to a Na ion of the next rectangle, and a benzoic acid coordinates Na ions of adjacent rectangles by its carbonyl oxygen (O2B) and by its hydroxyl oxygen (O1B). The hydroxyl group also forms a hydrogen bond with a neighbouring linking benzoate O atom (O1A). Thus a benzoate ion and a benzoic acid molecule link the edges of two rectangles and form an eight membered ring (two Na, four O, and two C atoms), with a hydrogen bond across the centre of the ring. Two such arrangements link each adjacent pair of Na<sub>2</sub>O<sub>2</sub> rectangles. The second benzoic acid approaches the coordination polymer backbone roughly perpendicular to the first and the carbonyl O atom (O2C) provides the sixth coordination to sodium, while the hydroxyl group forms a second hydrogen bond to the bridging benzoate O atom (O1A). There are thus two distinct benzoate oxygens, one involved in the Na<sub>2</sub>O<sub>2</sub> rectangle, and the other making a single coordination to sodium and making two hydrogen bonds. The two benzoic acid molecules are not equivalent either, one coordinating a sodium ion at both O atoms and the other just coordinating a single sodium via the carbonyl O atom. We were not able to find a reproducible way of isolating this phase, so did not undertake any SSNMR studies.

The potassium ions present in the KHB sample are organised in layers perpendicular to the *a* axis (Figure 6.3 c). There are chains of coplanar K<sub>2</sub>O<sub>2</sub> rectangles which share potassium ions running along the *b* direction. The oxygens which bridge two potassiums are not involved in hydrogen bonding, and these K–O bonds are 2.6895(14) and 2.8110(14) Å long. The lines of rectangles are linked by pairs of benzoate oxygens which coordinate potassium (K–O 2.7638(14) Å) and are hydrogen bonded to each other. These two O atoms are 2.452 Å apart, and related by a centre of symmetry. Two centrosymmetrically related positions for the hydrogen atom were located in the difference electron density map, which are 50 % occupied. The potassium is a six-coordinate site. The benzene rings project to either side of the layer (Figure 6.2 c), and are related by a unit cell translation in the *b* direction, and by the *c* glide plane in the *c* direction, with the best planes of the latter related

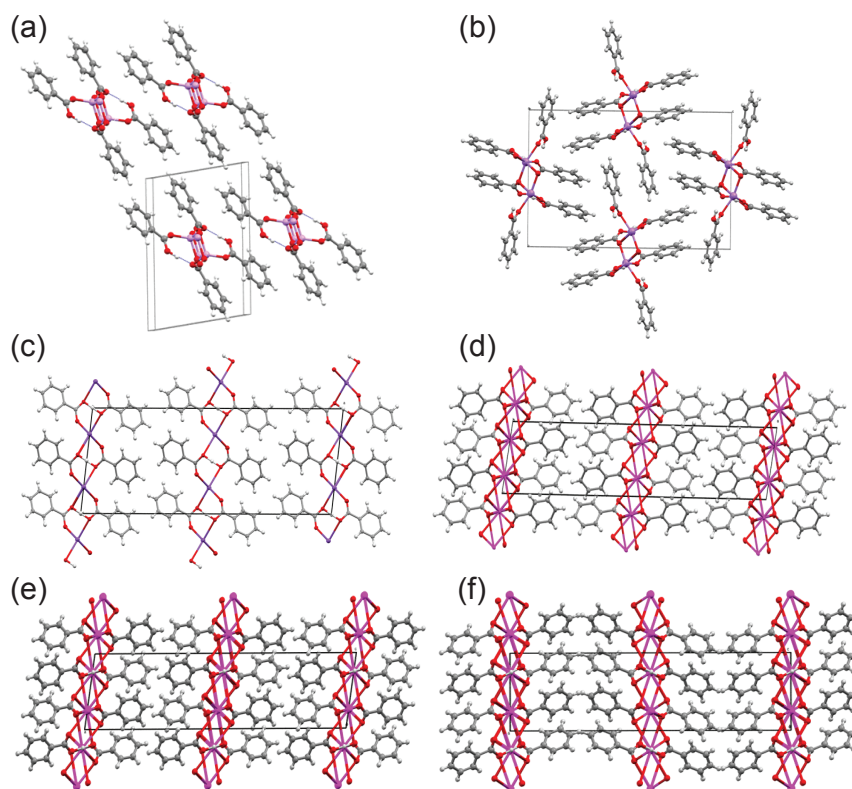


Figure 6.3: The packing structures of (a) LiHB viewed in the  $bc$  plane, (b) sodium benzoate/benzoic acid 1 : 2 complex viewed down the  $a$  axis, with  $c$  axis horizontal, showing the 1-dimensional coordination polymers, (c) KHB viewed down  $b$  axis. Note that the (O)H atom position is an average of two positions on the O—O vector. (d) monoclinic phase of RbHB viewed down  $b$  axis, (e) monoclinic phase of CsHB viewed down  $b$  axis and (f) orthorhombic phase of CsHB viewed down  $b$  axis.

benzene rings lies at  $49.1^\circ$ .

Rubidium hemibenzoate crystallises in the monoclinic space group  $C2/c$  with the eight-coordinated rubidium ions organised in layers and coordinated by benzoate and benzoic acid molecules, and the benzene rings project to either side of the layer (Figure 6.3 d). These layers are packed along the long  $a$  axis ( $29.03 \text{ \AA}$ ). The rubidium ion lies on a 2 fold axis, and the benzoate and benzoic acid molecules are hydrogen bonded. In the  $C2/c$  space group the average position of the hydrogen lies on a twofold axis, though it is likely to be disordered between two positions either side of the average. Referring to the ligands only as benzoate, then each benzoate oxygen coordinates two rubidium ions, so each benzoate coordinates four rubidiums. The rubidium/oxygen network is composed of a series of  $Rb_2O_2$  rectangles, thus, each rubidium is part of four such rectangles extended in two dimensions. There are four

crystallographically different Rb–O distances (2.9641(18), 2.9956(19), 3.1561(19) and 3.210(2) Å). The acidic hydrogen atom lies inside this network bridging between two Rb<sub>2</sub>O<sub>2</sub> rectangles, with the hydrogen lying between two oxygen atoms 2.455 Å apart. The bonds from these oxygens to rubidium are the two longer ones of the set of four. The benzene rings make edge to face contacts with each other, with the planes of benzenes related by the *c* glide lying at 76.8° to each other.

The CsHB analogue has two polymorphs, one monoclinic in space group C2/c and one orthorhombic in space group Pbcn, though their overall crystal packing arrangements are similar (Fig 6.3). The monoclinic form is very similar to that of rubidium hemibenzoate, with the caesium cations linked by four Cs<sub>2</sub>O<sub>2</sub> rectangles into a layer. The Cs–O distances are (3.0631(13), 3.0660(14), 3.2230(14) and 3.2459(15) Å, and as for the rubidium salt, the two longer Cs–O distances corresponded to the oxygens involved in the hydrogen bonding. These two oxygen atoms are 2.457(2) Å apart. The benzene rings project from the surface of each layer. The best planes of the two crystallographically distinct rings lie at 83.02° to each other, and the benzene planes lie at 79.7° to the plane of the caesium ions.

The orthorhombic phase of CsHB has a very similar crystal structure to the monoclinic phase. The cell parameters are very similar with the exception of the  $\beta$  angle (90 v 99.97°). There is the same mode of linking of cesiums with bridging oxygens into Cs<sub>2</sub>O<sub>2</sub> rectangles. The Cs–O bond lengths are a little different (3.063(2), 3.090(2), 3.231(2) and 3.286(2) Å) and in most cases slightly longer than in the monoclinic case. The O—O distance between hydrogen bonded oxygen atoms is identical to the monoclinic case, and the relative orientations of the benzene rings are almost the same (interplanar angle 82.63°). The benzene ring planes lie at 76.90° to the plane of the caesium ions cf. 79.66° for the monoclinic phase.

### 6.3.2 Proton One Dimensional NMR

The proton MAS NMR spectra of the BZA and its corresponding hemibenzoates (figure 6.4 and table 6.1) show multiple Gaussian peaks which represent each of the individual proton environments in the sample. The majority of the resonances in the sample are from the aromatic regions; however there is a distinct downfield peak which is descriptive of a deshielded proton present across belonging to a hydrogen bond. The BZA and LiHB samples show a resonance at 13.2 and 13.0 ppm respectively, these are weak hydrogen bonds. The previous BZA shift of 12.7 ppm via a CRAMPS MAS method, given by Harris was completed in 1988 and hence suffered from poor resolution because of slower MAS frequencies and low magnetic fields. [251] The addition of the large cations causes a dramatic shift in the res-

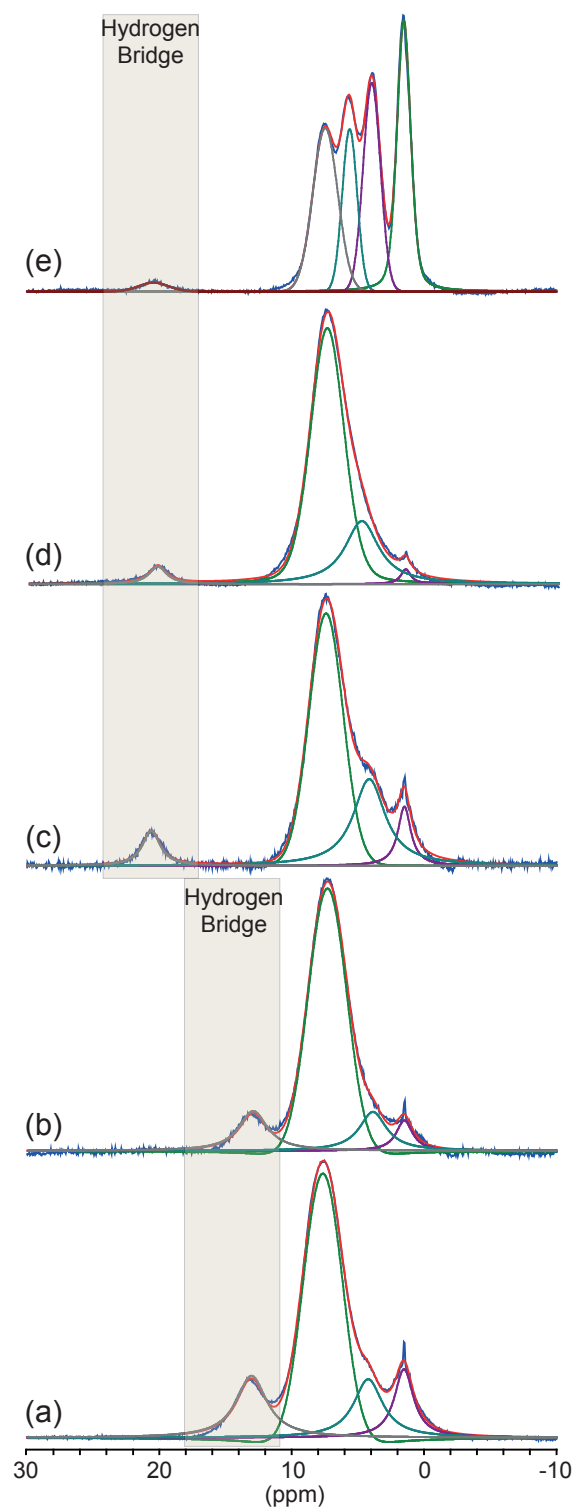


Figure 6.4: The 1-dimensional MAS spectra of the protons in (a) BZA, (b) LiHB, (c) KHB, (d) RbHB and (e) CsHB, the highlighted regions show the proton involved in the hydrogen bond.

onance position to the downfield region of 20.8, 20.2 and 20.9 ppm for the KHB, RbHB and CsHB acids respectively. These large deshielded shifts are indicative of very tight hydrogen bonds. This large high frequency shift is representative of the change in coordination around the alkali earth metal centre, the benzoic acid is a dimer as deduced from the crystallographic study, the lithium hemibenzoate forms a tetramer and sodium hemibenzoate forms a hexamer. On moving to larger nuclei the (i.e. K, Rb and Cs) the complex forms a dimer, sharing one alkali metal per benzoate. The ionic radii of proton and  $\text{Li}^+$  are similar and there is a step in radii to  $\text{K}^+$  before a gradual increase for  $\text{Rb}^+$  and  $\text{Cs}^+$ . This step is reflected in the proton shifts of the MAS NMR spectra.

The ab initio calculations on the geometry optimised CIFs via GIPAW-CASTEP confirm this trend; a comparison of these calculations completed on the proton only optimised CIFs (A.2) and the XRD CIFs (A.3) are present in A. They show a step in the chemical shift as you move from Li to K, Rb and Cs. The CASTEP calculations results confirm that the BZA dimer has an increasingly deshielded proton when directly compared to the LiHB. The CASTEP also confirms the large 8 ppm shift to higher frequency as you move from the LiHB to the K/Rb/CsHB samples. The hydrogen bonding in the BZA and LiHB samples can be described as weak in this instance, whilst the bonds in the heavier group IA alkali metal hemibenzoates can be described as strong for the purpose of this study.

Sample	$\delta_{\text{iso}}(\text{MAS})$	$^1\text{H}^{[a]}$	$\delta_{\text{iso}}$ $^1\text{H}^{[a]}$	$\delta_{\text{iso}}(\text{MAS})$ $^{13}\text{C}^{[b]}$	$\delta_{\text{iso}}(\text{CSA})$ $^{13}\text{C}^{[b]}$	$\delta_{11}$ $^{13}\text{C}$	$\delta_{22}$ $^{13}\text{C}$	$\delta_{33}$ $^{13}\text{C}$	$\delta_{\text{iso}}$ $^{13}\text{C}^{[c]}$	$\delta_{11}$ $^{13}\text{C}$	$\delta_{22}$ $^{13}\text{C}$	$\delta_{33}$ $^{13}\text{C}$
	$=\text{O} \cdots ^1\text{HO}$	$=\text{O} \cdots ^1\text{HO}$	$=\text{O} \cdots ^1\text{HO}$	$^{13}\text{COOH}$	$^{13}\text{COOH}$	$^{13}\text{COOH}$	$^{13}\text{COOH}$	$^{13}\text{COOH}$	$^{13}\text{COOH}$	$^{13}\text{COOH}$	$^{13}\text{COOH}$	$^{13}\text{COOH}$
	ppm/ $\pm 0.25$	CASTEP		ppm/ $\pm 0.5$	ppm/ $\pm 2.0$	ppm/ $\pm 2.0$	ppm/ $\pm 2.0$	ppm/ $\pm 2.0$	CASTEP	CASTEP	CASTEP	CASTEP
BZA	13.2	14.5		172.2	172.3	222.7	187.08	107.0	172.2	246.2	173.7	96.8
LiHB	13.0	13.2		173.5	173.5	226.6	189.2	104.6	171.8	240.6	179.9	95.0
KHB	20.8	21.2		176.3	174.7	237.1	179.3	107.6	175.8	246.7	177.6	103.1
RbHB	20.2	20.7		176.0	176.0	242.8	178.4	106.9	175.1	243.1	183.9	98.2
CsHB	20.9	21.1		173.2	173.2	241.8	168.6	109.3	172.5	232.7	192.0	92.8

Table 6.1: The experimental and DFT (CASTEP) determined anisotropic parameters for the carboxyl labelled  $^{13}\text{C}$  benzoic acid and hemibenzoates. [a] is simulated from the fast  $^1\text{H}$  MAS NMR spectra achieved in 6.4 and [b] is achieved from  $^{13}\text{C}$  sideband manifold simulation of the spectra 6.5



### 6.3.3 Carbon Chemical Shift Anisotropy Determination

The central carbon on the carboxylic was 100 %  $^{13}\text{C}$  labelled to complete comprehensive anisotropic studies. This involved slow magic angle spinning followed by sideband intensity fitting (figure 6.5 and table 6.1). The anisotropic data gives tensorial information for the carbon site which has been shown to be proportional to the strength of the hydrogen bond. This is shown markedly in this data series. The change in  $\delta_{22}$  tensors as you move from the BZA dimer ( $\delta_{22} = 187.1$  ppm) to the weaker hydrogen bond of the LiHB ( $\delta_{22} = 189.2$  ppm) and onto the strong hydrogen bonds of KHB, RbHB and CsHB ( $\delta_{22} = 179.3$ ,  $178.4$  and  $168.6$  ppm respectively) reflect the proton shifts shown in  $^1\text{H}$  MAS NMR. They confirm that the BZA and LiHB are comparatively weak hydrogen bonds whilst the K, Rb and Cs analogues are far stronger bonds. The  $^{13}\text{C}$  isotropic shift ( $\delta_{iso}$ ) calculated by simulation of the fast MAS spectra and by averaging the tensorial components shows good agreement; however both show limited correlation with the proton shifts of the hydrogen bond and the  $\delta_{22}$  tensor of the slow MAS  $^{13}\text{C}$  spectra. The  $\delta_{11}$  tensor component, which runs perpendicular to the hydrogen bond, shows no appreciable correlation with the hydrogen bond strength. The  $\delta_{33}$  shows no correlation with the proton shifts or the  $\delta_{22}$  tensor; this is because the  $\delta_{33}$  tensor is directed away from the plane of the bond.

The DFT calculations (table 6.1) confirm the trend observed in the MAS spectra. However, the  $\delta_{22}$  parameters show a decrease as you move from BZA to the heavier alkali metal salts. A significant error is seen in the LiHB case, this could be propagated from the change in coordination number to a tetramer. Both the  $\delta_{11}$  and  $\delta_{33}$  show similar uncertainty from which no conclusions can be drawn. The average of these terms gives the isotropic shift which shows good agreement with the observed isotropic shifts also present in table 6.1.

### 6.3.4 $^{17}\text{O}$ -Oxygen Spectra, Simulations and MQMAS

The oxygen sites present directly in the hydrogen bond are an excellent solid state NMR indicator for the symmetry of the site and the anisotropic terms present in these spectra have been shown to also provide insight into the strength of the hydrogen bond. The observed MAS NMR spectra for the  $^{17}\text{O}$  labelled hemibenzoates are shown in figure 6.6; the simulations and their sum are shown below in colour. In general, simple carboxylic acids contain two oxygen environments, a carbonyl ( $\text{C}=\text{O}$ ) and a hydroxyl ( $\text{O}-\text{H}$ ); it would be expected that both these sites would give different isotropic shifts ( $\delta_{iso}$ ), quadrupole coupling constants ( $C_Q$ ) and asymmetry parameters ( $\eta$ ). Previous work by Wong *et al.* has suggested that the carbonyl

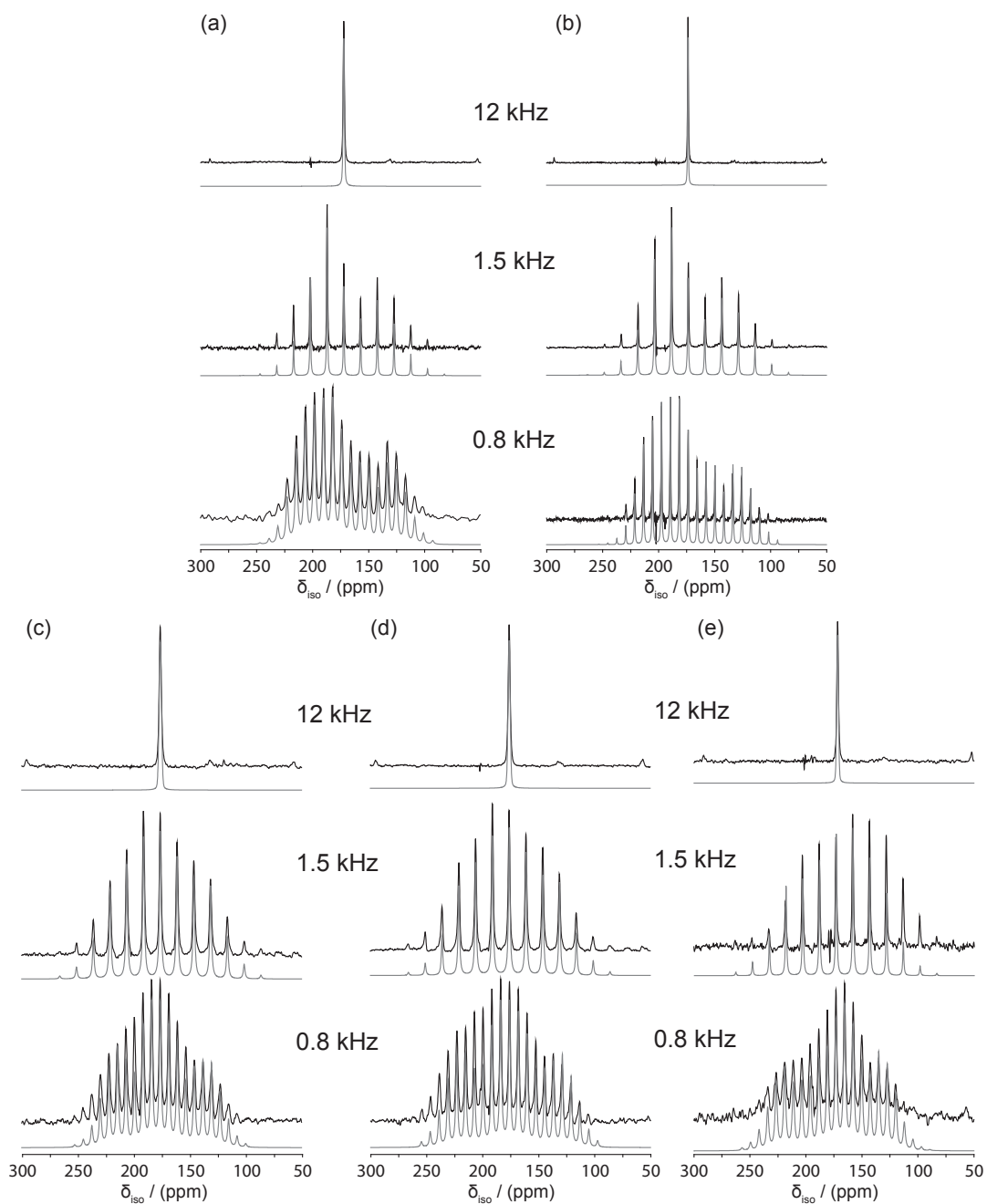


Figure 6.5: The 1-dimensional slow MAS spectra of the  $^{13}\text{C}$  labelled carboxy carbon in (a) BZA, (b) LiHB, (c) KHB, (d) RbHB and (e) CsHB, the spectral simulations shown in grey are explained in figure 2.4.

groups have  $\delta_{iso(17O)}$  between 310 to 340 ppm, whilst the hydroxyl is shown to have an  $\delta_{iso(17O)}$  range of 170 to 190 ppm. [254] Due to the distortion of carbonyls their oxygen sites are suggested to have  $C_Q$ 's greater than 7 MHz, with the corresponding hydroxyls would be found in the 6.5 to 7 MHz range.

The  $^{17}O$  labelled BZA spectrum has been previously collected by Wu. [255] Due to signal to noise limitations Wu evaluated the spectrum as a single site with  $\delta_{iso} = 230$  ppm,  $C_Q = 5.7$  MHz and  $\eta = 1.0$ ; this would suggest that BZA is an A type hydrogen bond. More recently, Hagaman has shown that there are two sites present with  $\delta_{iso} = 236$  ppm,  $C_Q = 5.4$  MHz and  $\eta = 0.99$  and  $\delta_{iso} = 233$  ppm,  $C_Q = 5.6$  MHz and  $\eta = 0.98$ ; this suggest that as both oxygen sites are inequivalent then the proton cannot be shared in the bond and a B type hydrogen bond is present. [274] The results presented here (figure 6.6, table 6.2) confirm the observed two sites, these can be observed by the two shoulders present on the spectrum at 14.1 T and these cannot be simulated into a single site. The deconvoluted parameters give  $\delta_{iso} = 236$  ppm,  $C_Q = 6.0$  MHz and  $\eta = 0.92$  and  $\delta_{iso} = 225$  ppm,  $C_Q = 5.6$  MHz and  $\eta = 0.81$ . These are in good agreement with Hagaman's results. Discrepancies may be caused by the chemical shift anisotropy contribution to the line, and also our samples have a larger  $^{17}O$  content (Hagaman  $\approx 35$  %, BZA  $\approx 86$  %) and differing MAS frequencies (Hagaman 15 – 20 kHz, BZA 27.5 kHz). The 3QMAS spectra of the labelled BZA sample shows two observable sites, however due to a significant overlap it is not possible to deconvolute these spectra and determine any  $C_Q$  or  $\eta$  information. The CASTEP results also confirm the presence of two sites (as shown in table 6.2), although the calculation suggests a slightly higher  $C_Q$  of 7.63 and 7.45 MHz and lower  $\eta$  of 0.43 and 0.10 respectively. The errors in the  $C_Q$  and  $\eta$  can be explained by the overall lineshape and by previous results.

The LiHB (figure 6.6 b) sample has been shown by the previous crystallographic studies to contain four distinct oxygen sites. From the resultant MAS  $^{17}O$  spectra, four distinct sites can be observed at 14.1 T. The two hydroxyl groups are shown to be similar to the benzoic acids sites with  $C_Q$ s of 6.21 and 4.70 MHz and asymmetries ( $\eta$ ) of 0.88 for both sites. The other two sites are shown to have higher  $C_Q$ s of 12.36 and 7.94 MHz with asymmetries of 0.08 and 0.40 for both. These can both be fitted with confidence due to the features present in the spectra. The DFT agrees with the observation of the four distinct sites and the  $\delta_{iso}$  calculated shifts gives good agreement with the simulated data.

The larger group IA alkali metal hemibenzoates revert back to the two oxygen site environment model. KHB samples have been previously studied by Wu. [275] Their results show two oxygen sites with the potassium bound site having the NMR

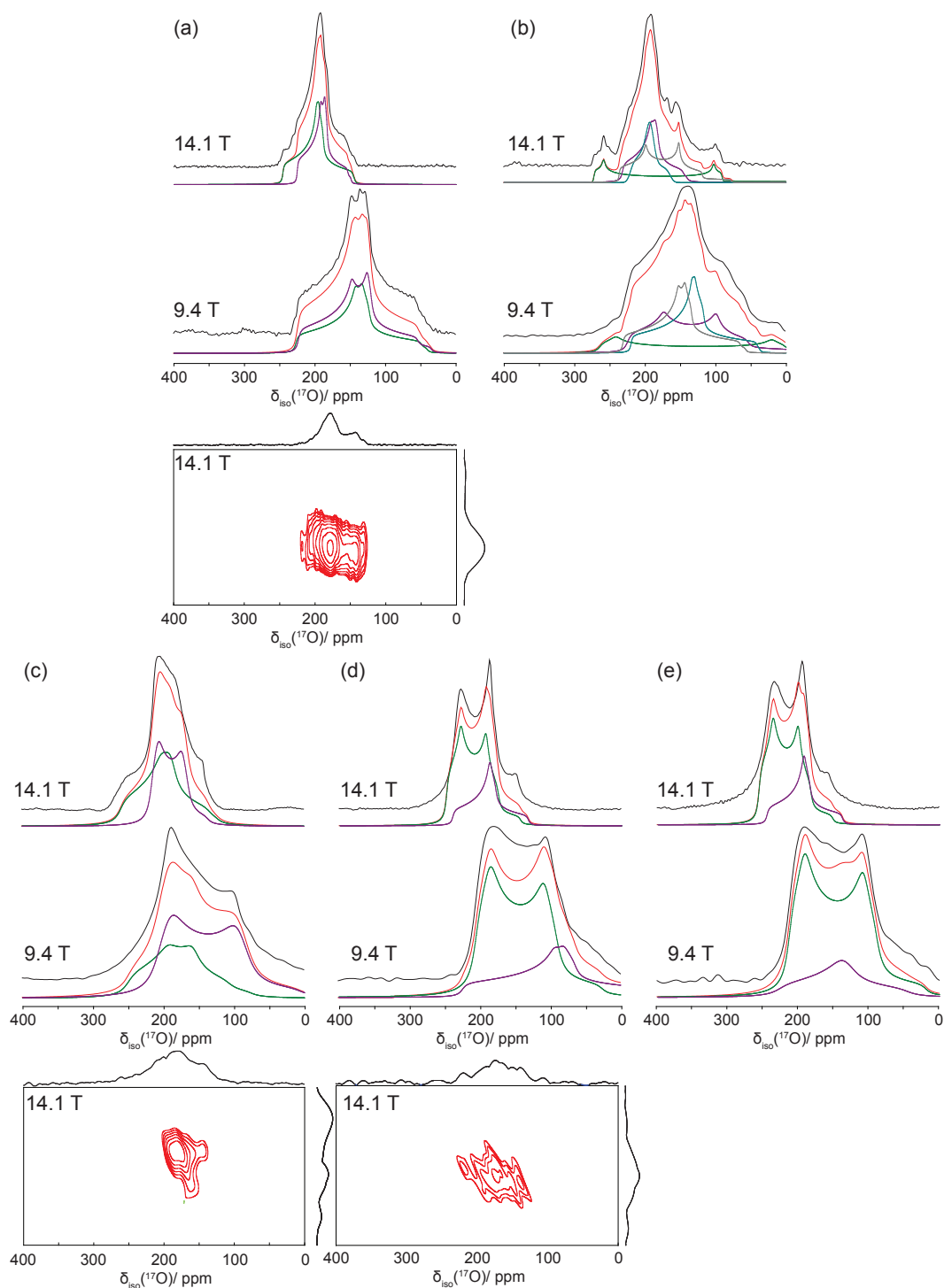


Figure 6.6: A MAS solid state NMR study of the labelled BZA and its corresponding hemibenzoates; (a) BZA, (b) LiHB, (c) KHB, (d) RbHB and (e) CsHB, the spectral simulations are shown below each resonance at each field. The bottom two dimensional spectra are the attempted 3QMAS; these highlight the overlap in  $C_Q$  and  $\delta_{iso}$  making simulations very difficult.

		<sup>17</sup> O NMR Experimental			<sup>17</sup> O CASTEP				
System	Site	$\delta_{\text{iso}}$ (MAS)	$C_Q$	$\eta$	$\delta_{\text{iso}}$ (PQ)	$P_Q$	$\delta_{\text{iso}}$ (MAS)	$C_Q$	$\eta$
		ppm/ $\pm 3.0$	MHz/ $\pm 0.5$	/ $\pm 0.05$	ppm/ $\pm 3.0$	MHz/ $\pm 0.5$	ppm	MHz	
BZA	1	236.54	5.96	0.92	262.8	8.54	335.98	7.45	0.10
	2	224.78	5.61	0.81	242.5	7.66	229.92	7.63	0.43
LiHB	1	315.78	12.36	0.08	303.35	10.04	328.74	7.50	0.18
	2	236.40	7.94	0.40	257.44	9.12	270.53	7.65	0.70
	3	236.32	6.21	0.88	257.19	9.67	260.78	7.96	0.55
	4	220.88	4.70	0.88	251.19	9.64	229.24	8.54	0.31
KHB	1	257.58	7.40	0.69	285.86	8.28	287.04	8.63	0.30
	2	227.37	6.41	0.16	187.12	3.71	222.25	6.45	0.58
RbHB	1	255.67	6.96	0.32	-	-	286.75	6.54	0.56
	2	239.68	6.37	0.99	-	-	206.76	8.85	0.23
CsHB	1	233.59	6.44	0.18	352.79	12.27	277.69	8.72	0.14
	2	226.70	5.51	0.99	254.53	11.07	195.18	6.86	0.42

Table 6.2: The experimental and DFT (CASTEP) determined isotropic shift and quadrupolar parameters calculated by the spectral simulations shown in figure 6.6, the calculated DOR results shown in figures 6.7 and 6.8, which can be compared to the DFT calculated results in the final columns labelled CASTEP.

parameters  $\delta_{iso} = 287$  ppm,  $C_Q = 8.30$  MHz and  $\eta = 0.23$  and the hydrogen bonded site with  $\delta_{iso} = 213$  ppm,  $C_Q = 5.90$  MHz and  $\eta = 0.55$ . The spectral simulations here found the potassium bound oxygens to give the following parameters;  $\delta_{iso} = 257$  ppm,  $C_Q = 7.40$  MHz and  $\eta = 0.69$ . The hydrogen bonded site limitations agree with that of Wu and show a decrease in both shift and quadrupole coupling constant:  $\delta_{iso} = 227$  ppm,  $C_Q = 6.41$  MHz and  $\eta = 0.16$ . Possible discrepancies between the results could be a result of significantly differing  $^{17}\text{O}$  enrichment; here we present results with 86 % enrichment whilst Wu was limited to 40 %; this point is also commented on by Hagaman. The calculated results agree with trend of the potassium bound oxygens giving a higher shift (287 ppm) and  $C_Q$  (8.63 MHz), whilst the hydrogen bonded oxygens give a decreased shift (222 ppm) and  $C_Q$  (6.45 MHz). A point of note is that similarly Wu's calculated data on KHB generally overestimated the  $C_Q$  and showed a range of results for the  $\delta_{iso}$  and  $\eta$  terms. In a very general sense, the data achieved here also showed a similar trend, although the isotropic shift data is within the expected error, suggesting there are possible issues with the geometry optimisation methods in the DFT calculation.

The RbHB and CsHB both give very similar lineshapes. This is expected as the local environments confirmed by XRD are comparable. The Rb and Cs bound oxygens appear at  $\delta_{iso} = 255$  and 233 ppm with  $C_Q$ s of 6.96 and 6.44 MHz and  $\eta_Q$  of 0.32 and 0.18 respectively. The oxygens present in the hydrogen bond again have a decreased isotropic shift and  $C_Q$ ; with the Rb simulated parameters  $\delta_{iso} = 239$  ppm,  $C_Q = 6.37$  MHz and  $\eta = 0.99$  and for Cs give a  $\delta_{iso} = 226$  ppm,  $C_Q = 5.51$  MHz and  $\eta = 0.99$ . The CASTEP calculated results agree with the trend; however errors are once again apparent. This larger inaccuracy may be due to the Rb and Cs pseudopotentials having limitations; both these nuclei are quite large and contain a large amount of electrons such that relativistic complications may occur.

### 6.3.5 Double Rotation

The double rotation (DOR) experiment involves spinning the sample about two angles to satisfy both the  $P_2$  and  $P_4$  (2.2) terms of the Legendre polynomial. This not only reduces the first order quadrupole broadening but can also reduce the second order broadening by spinning at the second angle. [30, 129, 211] An advantage of DOR is that the observed shift of the resonance (centre of gravity,  $\delta_{cg}$ ) can be used to give information about the  $^{17}\text{O}$  parameters which have been experimentally determined; this is due to the  $\delta_{cg}$  being dependant on the magnetic field ( $B_0$ ) through second order quadrupole effects for a spin  $I = \frac{5}{2}$  nucleus such that:

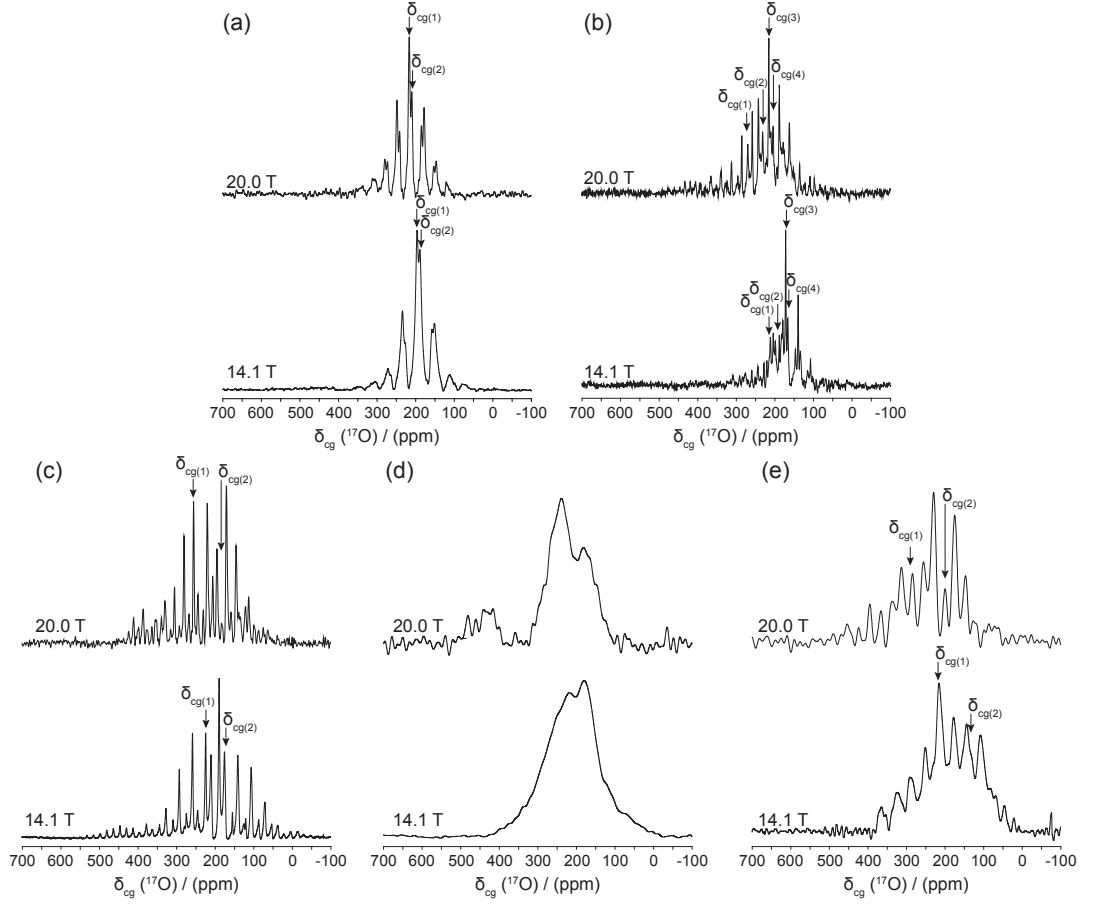


Figure 6.7: A DOR solid state NMR study of the labelled BZA and its corresponding hemibenzoates: a) BZA, (b) LiHB, (c) KHB, (d) RbHB and (e) CsHB, the spectra simulations are shown below each resonance at each respected fields. The  $\delta_{cg}$  show the centre of gravity of the peak at each field, at infinite  $B_0$  this would represent the isotropic shift.

$$\delta_{cg} = \delta_{iso} - \frac{3}{500} \frac{P_Q^2}{v_0^2} \times 10^6 \quad (6.1)$$

Where  $v_0$  is the Larmor frequency and  $P_Q = C_Q(1 + \eta_Q^2/3)^{\frac{1}{2}}$ . Multiple field (20.0 T and 14.1 T) data is required to determine the isotropic shift ( $\delta_{iso}$ ) and quadrupole coupling parameter as:

$$\delta_{iso} = \frac{v_0^2 \delta_{cg1} - v_0^2 \delta_{cg2}}{v_0^2 - v_0^2} \quad (6.2)$$

and

$$P_Q^2 = \frac{500}{3} \nu_0 1^2 \nu_0 2^2 \left( \frac{\delta_{cg1} - \delta_{cg2}}{\nu_0 1^2 - \nu_0 2^2} \right) \times 10^{-6} \quad (6.3)$$

Where  $\delta_{cg1}$  and  $\delta_{cg2}$  are the centre of gravity of the resonances at the multiple fields. The double rotation results are shown in figure 6.7, with the peak centres of gravity ( $\delta_{cg}$ ) indicated. The peaks positions were isolated from the spinning sidebands by variable spinning frequency experiments (outer rotor frequency between 1.2 – 1.8 kHz). The  $\delta_{iso}$  and  $P_Q$  determinations are shown in the figure 6.8 and the parameters given in table 6.2.

The resolution achieved by the DOR experiment is excellent (FWHM  $\approx$  230 Hz,  $\approx$  2 ppm) and highlighted by the BZA results (figure 6.7 a) . No proton decoupling was employed as the motion of the hydrogen bonded proton is on the time scale of the experiment, which effectively recouples the proton to the oxygen causing broadening of the resonance; this is also present in the MAS spectra and hence these were completed without decoupling. The centre of gravity ( $\delta_{cg}$ , ppm) resonances are determined by varying spinning frequency, this spectra also illustrates the change in shift with magnetic field. The isotropic shift is effectively the centre of gravity at infinite magnetic field (as observed in the graph shown in figure 6.8) and is given as  $\delta_{iso} = 262.8$  ppm for the carbonyl and 242.5 ppm for the hydroxyl oxygen. This is confirmed with  $P_Q$  showing an expected higher 8.54 MHz coupling for the carbonyl, which reduces to 7.66 MHz for the hydroxyl oxygen. The  $^{17}\text{O}$  MAS NMR (figure 6.6) lineshapes suggest the quadrupole asymmetry parameter ( $\eta$ ) can vary in these organic oxygen environments. The maximum contribution it can make to the  $P_Q$  is 1.154 MHz (presuming  $\eta = 1$ ), therefore it is not possible to directly compare with the  $C_Q$  results previously determined. The  $\delta_{iso}$  terms show a distinct trend across the MAS, DOR and DFT calculated parameters.

The LiHB DOR spectra (figure 6.7 b) illustrate it is possible to distinguish between all four sites. The  $\delta_{iso}$  show a correlation (table 6.2) previously determined by the MAS  $^{17}\text{O}$  experiments and the DFT calculated parameters. It would be expected that the two benzoate oxygen atoms have similar isotropic shift and quadrupole coupling parameter. These are shown as site 2 and 3 in table 6.2 and are confirmed by all three NMR spectral simulation techniques. As previously discussed, the carbonyl tends to have higher isotropic shift and quadrupole coupling parameters and hence site 1 is shown to agree with this trend; with the hydroxyl given as site 4 also agreeing with the previous results.

The KHB shows the two observed environments, with the oxygen bound to the K group labelled as site 1 in table 6.2; it shows a remarkable similarity to the



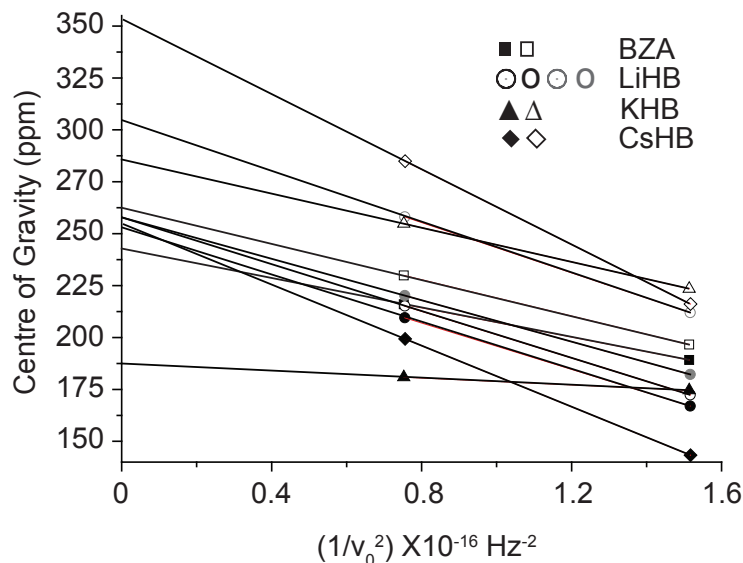


Figure 6.8: The quadrupole coupling parameter and isotropic shift plots for the BZA and the series of group IA hemibenzoates.

calculated DFT parameters. The hydroxyl (site 2) shows a decreased shift and  $P_Q$  as also derived from the MAS NMR spectra and calculated parameters. For RbHB DOR does not reduce the second order quadrupole broadening, this can only be due to increased disorder at the oxygen sites; by applying excess line broadening (1 kHz) to the CsHB DOR spectra (figure 6.7 e) it is possible to achieve the same spectra. From this it can be presumed that the RbHB DOR would give the same results as the CsHB as seen in the MAS NMR cases. In the CsHB case it is just possible to observe two distinct sites, although one of the sites is clearly has not narrowed as much as the other. The parameters achieved from this multiple field analysis contain larger errors due to the increased line widths, however they both support the previous observations that the metal ion bound oxygen has the higher shift and  $P_Q$ , whilst the hydrogen bonded site gives a lower shift and  $P_Q$ . A further field analysis could possibly limit these errors; however due to the design of the DOR probe it is not possible to complete this.

### 6.3.6 NMR of the Group IA Metal Hemibenzoates

The solid state NMR analysis of the central alkali metals was completed to gain an insight into the increasing hydrogen bond angle at the dimer's centre. As the size of the alkali metal increases the bond angle at the hydrogen bond centre varies quite considerably, as shown in table X, this is directly proportional to the change in the

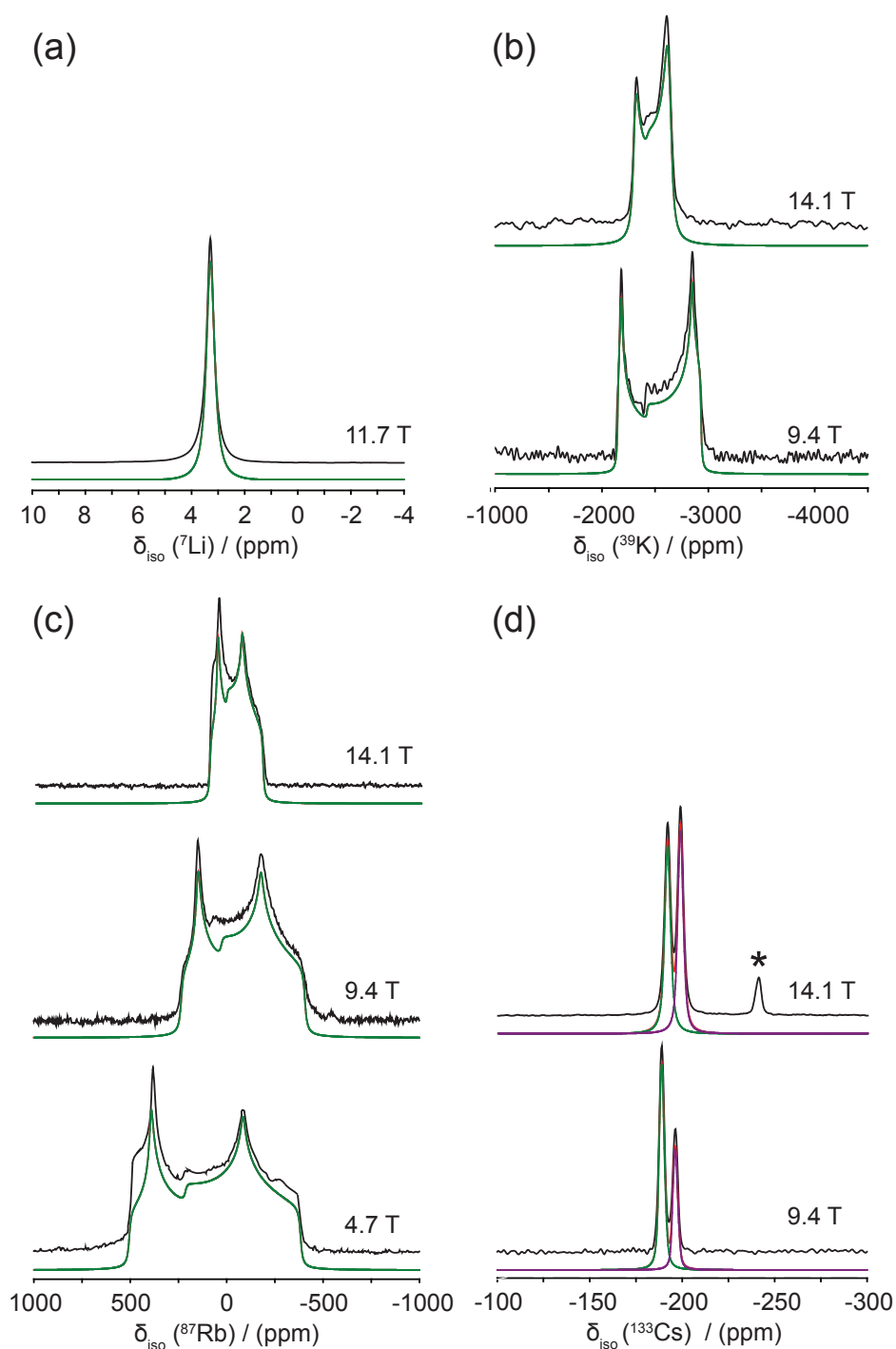


Figure 6.9: The solid state NMR spectra of the group IA metals, (a) MAS (27.5 kHz) of  ${}^7\text{Li}$ , (b) multiple field static  ${}^{39}\text{K}$ , (c) multiple field static  ${}^{87}\text{Rb}$  and finally (d)  ${}^{133}\text{Cs}$  MAS (10 kHz) at multiple fields. The resultant simulations are shown below each spectra in green and purple. \* shows the presence of caesium benzoate in the compound.

Sample	Nuclei	$\delta_{iso(MAS)}$ or $\delta_{(static)}^*$	$C_Q$	$\eta$	$\delta_{iso (MAS)}$	$C_Q$	$\eta$
		ppm	MHz		CASTEP	CASTEP	CASTEP
LiHb	$^7\text{Li}$	3.38	0.39	0.04	0.98	0.39	0.04
KHB	$^{39}\text{K}$	-2,431*	1.38	0.09	-2,380	1.24	0.08
RbHB	$^{87}\text{Rb}$	-82.08*	10.12	0.34	-173.8	9.41 $^\square$	0.69
CsHB	$^{133}\text{Cs}^{(m)}$	-188.2	0.34	0.79	-184.5	0.34	0.79
	$^{133}\text{Cs}^{(o)}$	-195.3	0.34	0.79	-196.7	0.34	0.79

Table 6.3: A comparison of the solid state NMR data achieved for the group IA metals with their corresponding DFT-CASTEP data.  $^\square$  Chemical shift anisotropy present in the structure cannot be simulated with accuracy. (m) Monoclinic. (o) Orthorhombic.

quadrupolar asymmetry parameter  $\eta$ . The results for the alkali group IA metals may give some indication to the discrepancies observed amongst the  $^1\text{H}$ ,  $^{13}\text{C}$  and  $^{17}\text{O}$  results. Due to the very small quadrupole moments of lithium ( $^7\text{Li}$ ) and caesium ( $^{133}\text{Cs}$ ), both these spectra were fitted to their calculated DFT CASTEP results. The  $^7\text{Li}$  shows a single site which is predicted from the crystallographic data and the DFT parameters. The multiple field static  $^{39}\text{K}$  NMR data for the KHB sample has a small quadrupole coupling constant of 1.38 MHz and asymmetry parameter of 0.09; this is confirmed by the DFT ( $C_Q = 1.24$  MHz,  $\eta = 0.08$ ). The  $^{87}\text{Rb}$  static spectra of the RbHB system shows a single quadrupolar resonance with  $C_Q = 10.12$  MHz and  $\eta = 0.34$ , this gives good agreement with the calculated results of  $C_Q = 9.41$  MHz and  $\eta = 0.69$ ; the errors present here can be explained by the presence of chemical shift anisotropy interactions at the site. As these CSA interactions were small they could not be simulated with any accuracy. Due to caesium's large chemical shift range and small quadrupole moment it is possible to observe both the monoclinic and orthorhombic forms of the CsHB. The calculated spectra show that the isotropic shift of the monoclinic form (experimental  $\delta_{iso} = 188.2$  ppm, calculated  $\delta_{iso} = 184.5$  ppm) is higher than that of the orthorhombic (experimental  $\delta_{iso} = 195.3$  ppm, calculated  $\delta_{iso} = 196.7$  ppm). A final point to note are there is clear changes in the  $\eta$  parameter as you move from the LiHB down to the CsHB. This change can be directly correlated with the change in the hydrogen bonding as predicted by

the  $\delta_{22}$  parameter. It may be possible to use the asymmetry parameter as a direct measurement of the bond strength, however further analysis is required before this observation is confirmed.

## 6.4 Conclusions and Trends

A comparison of all parameters resolved by the multiple technique method is summarised in table 6.4. The  $^1\text{H}$  MAS NMR shows a stepwise change in the hydrogen bonding with the BZA and LiHB samples giving 'weak' bonding and the K/Rb/CsHB samples giving strong hydrogen bonding. This step in bonding strength is echoed in the  $^{13}\text{C}$  isotropic shifts, although the CsHB gives an anomalous result. The  $\delta_{22}$  tensor of the chemical shift anisotropy lies along the carboxyl group and is directly affected by the strength of the hydrogen bond. This shows a linear decrease as you move from the weakly bound BZA to the strong bonding of the CsHB sample. This would suggest a gradual change in the angle at the carboxyl, which can only be caused by a gradual change in the hydrogen bonding.

The IR stretching frequency at the carbonyl group is typically used to describe the hydrogen bonding interaction. The interaction usually gives a broad resonance caused by the variation in the hydrogen bonding. The resonances shown here have very limited correlation. Other literature methods include measuring the oxygen-oxygen distance across the hydrogen bond. These show a decrease in length from 2.608 Å for the BZA to 2.457 Å for the CsHB. This matches the results observed in the  $\delta_{22}$  anisotropic measurement giving a linear change on moving from the weakly hydrogen bonded systems to the strongly hydrogen bonded systems. A point to note is that the angle at the hydrogen, involved in the hydrogen bond, varies quite considerably as the alkali metal changes. Only the KHB case has a linear hydrogen bond, this reflects the ambiguity discovered during the multinuclear NMR results achieved on these samples. The final column shows the angle at the central carboxyl carbon (O–C–O), the angle shows the opposite trend to that found for the angle at the proton; this confirms that the hydrogen bonding in these systems does not change as linearly as expected.

I has been shown that characterising the hydrogen bonding by multiple techniques has variable degrees of success. As the diffraction studies fail in localising the proton positions then the hydrogen bonding interaction cannot be directly commented on, this is a common problem seen throughout the literature in organic samples. The oxygen-oxygen distance across the bond can be used to comment on the strength of the bond. However as the bond angle at the central proton varies this

Sample	$\delta_{\text{iso(MAS)}}^1\text{H}^{[a]}$	$\delta_{\text{iso(MAS)}}^{13}\text{C}^{[b]}$	$\delta_{22}^{13}\text{C}^{[b]}$	IR stretching frequency <sup>[d]</sup>	O-H-O distance <sup>[e]</sup>	O-H-O angle	O-C-O angle
	=O... <sup>1</sup> H-O	- <sup>13</sup> C-O-OH	- <sup>13</sup> C-O-OH	C=O			
	ppm/±0.25	ppm/±0.5	ppm/±2.0	cm <sup>-1</sup>	Å	°/degrees	°/degrees
BZA	13.2	172.2	187.08	1678.0	2.608 <sup>[g]</sup>	174.6	121.57
LiHB	13.0	173.5	189.2	1677.3	2.616	169.8	113.2
KHB	20.8	176.3	179.3	1689.9	2.452	180.0	110.8
RbHB	20.2	176.0	178.4	1675.6	2.455	158.7	113.6
CsHB	20.9	173.2	168.6	1633.7	2.457	167.7 <sup>[o]</sup> /170.1 <sup>[m]</sup>	114.8 <sup>[o]</sup> /114.3 <sup>[m]</sup>

Table 6.4: A comparison of commonly used parameters developed to study hydrogen bonding. [a] The isotropic shift <sup>1</sup>H Proton NMR chemical shift as determined by deconvolution of <sup>1</sup>H spectrum. [b] The isotropic shifts of the <sup>13</sup>C fast MAS NMR. [c] The  $\delta_{22}$  term of the tensorial components derived from slow MAS. [d] IR of the resonance of the carbonyl stretching frequency. [e] As achieved from the X-ray single crystal diffraction. [g] 20 K from the Wilson paper. [o] Orthorhombic. [m] Monoclinic

can cause discrepancies and give an illusion of the oxygen-oxygen distance changing. The IR results show no observed correlation.

Classically the chemical shift of the proton involved in the bond has been used to describe its nature. The samples show a step-wise change in the hydrogen bonding character with the BZA and LiHB samples being described as weak hydrogen bonds and the KHB, RbHB and CsHB samples being best described as very strong hydrogen bonds. The calculated proton shift positions agree unequivocally with these results. The <sup>13</sup>C chemical shift of the carboxyl carbon does not follow this description and so no observable correlation with the hydrogen bonding can be clarified. The anisotropic tensorial components of the chemical shift have been previously used to comment on the hydrogen bonding. Here the  $\delta_{22}$  terms is found to lie along the C=O bond. As the alkali metal gets larger (i.e. proton to caesium) the  $\delta_{22}$  decreases in shift. This follows a linear trend as also seen in the oxygen-oxygen distance case. Despite the isotropic shift positions being calculated to a high level of accuracy the  $\delta_{22}$  component show the opposite trend to those of the experimental.

Possible reasons for this could be that regardless of geometry optimisation being performed on the protons in the structure the position of the proton still has some ambiguity.

The  $^{17}\text{O}$  MAS, DOR and DFT results highlighted the uncertainty surrounding the hydrogen bonding in these systems. The MAS and DOR results confirm the number of oxygen environments in this series; two for BZA, KHB, RbHB and Cs, whilst LiHB has four. The spectral simulation of these lines shapes show the quadrupole coupling varies throughout the samples as well as the asymmetry parameters. It is shown that the hydroxyl tends to have a smaller isotropic shift and quadrupolar coupling parameter when compared to the carboxyl oxygen. The calculated spectra show the same developments, however as with the  $^{13}\text{C}$  anisotropies, no accuracy was once again present.

Finally the alkali metals showed a distinct change in quadrupole asymmetry parameters as the hydrogen bonding increased. This linear change could be directly compared to the  $^{13}\text{C}$   $\delta_{22}$  and oxygen-oxygen distances previously discussed. This could open up the opportunity to use the guest nuclei as a probe for its perpendicular proton hydrogen bonded neighbour. The ab initio computed results for these metals gave excellent agreement with the multiple field deconvoluted spectra.

# Chapter 7

## Summary

### 7.1 Characterisation of Platinum-based Fuel Cell Catalyst Materials using Wideline Solid State NMR

By using field sweep Fourier transform methods to reconstruct wideline  $^{195}\text{Pt}$  resonances from platinum nanoparticles It has been shown it is possible to gain information on the number of atoms present in the particle. It has been shown shown that this holds true when compared to theoretical nanoparticles and against the literature standard of TEM. In this thesis has also demonstrated that the current method of spin echo height spectroscopy (SEHS) is highly dependent on the number of sampling points used in the wideline reconstruction and generally particle size prediction is not possible.

A small 13 atom cluster was created, this sample was shown not to conduct and hence have no Knight shift. The isotropic shift of that line was shown to be nearly 10,000 ppm different from the IUPAC reference suggesting that the metals can also contain a large chemical shift component. As most Knight shifts are measured against the primary reference (including that of platinum) then these would contain appreciable errors. However, the exact shift of the cluster could not be determined as synthesising a sample without a distribution of particle sizes is currently not possible.

Platinum-tin intermetallics are heavily used in the fuel cell industry to prevent surface over-potential. The static field sweep  $\text{Pt}_3\text{Sn}$  solid state NMR results show an incredible amount of local order is present in the 3 : 1 and 1 : 1 platinum:tin complexes. The  $^{119}\text{Sn}$  NMR results confirm this order and show very sharp resonances in the 3 : 1 case. The shift of the line changes considerably with each complex and showing that assignment of impure phase mixtures is possible.

The alloyed platinum ( $\text{Pt}_3\text{X}$ ) systems show a variety of shifts which are dependent on the conduction electrons (i.e. electrons above the Fermi level) of the system and the number of  $d$ -electrons in the alloyed X-element. The shift becomes more positive in ppm with a greater number of  $d$ -electrons in the X alloyed atoms.

## 7.2 Apatite Oxide Ion Conductors

The use of  $^{17}\text{O}$  MAS solid state NMR and density functional theory calculations has shown that it is possible to follow the conduction pathway of a novel set of rare earth apatites. The presence of a  $\text{XO}_5$  resonance in the oxygen spectra and absence of any channel oxygens suggest the apatite is conducting via the labeling method. As the labeling was completed by allowing the sample to conduct then it can only be concluded that the sample transports the oxide by the framework tetrahedra present in all apatites.

Two dimensional 3QMAS and multiple field (7.05, 9.4, 11.7, 14.1 and 18.8 T) data was acquired to determine isotropic shift and quadrupole coupling parameters. It was shown that the  $\text{XO}_5$  interstitial formed during the conduction process had a bridging oxygen and its  $P_Q$  was surprisingly low; despite this result going against the entire literature on NMR of bridging oxygens the density functional theory results also confirmed this result. A comparison of the parameters achieved for both the silicon and germanium substituted apatites showed that the germanium apatites contained a larger amount of disorder; as they also gave better conduction then this disorder can only help the oxide transport process.

A molecular dynamics and density functional theory study was also completed to confirm the NMR results. This showed that the minimum energy pathway for conduction was by a helical  $S_N2$  method via the tetrahedra. Despite our best attempts to force the oxygen to conduct along the channel, during energy minimisation, the oxygen always moved by the hopping on and off the framework sites.

## 7.3 A Multi-Nuclear Solid State NMR, DFT and Diffraction study of Tight Hydrogen Bonds in Group IA Hemibenzoates

Hydrogen bonding is vital to high order biological and chemical structures and despite their importance analysis techniques used to describe their nature are inconsistent. In an attempt to find a trend between hydrogen bonding and the information given from three comparable solid state techniques (XRD, NMR and IR) a linear



series of hemibenzoates was synthesised. The synthesis involves taking benzoic acid and switching one of the protons for a group IA metal (Li, K, Rb and Cs).

To compare the hydrogen bonding by XRD one is able to get detailed information on the oxygen-proton-oxygen distance and its angle as well as the angle at the oxygen-carbon-oxygen carbonyl. These measurements have all be previously used in other literature studies as the proton position cannot be determined without detailed neutron diffraction studies and even then due to disorder and vibrations it is not always possible to locate. The results here show a large amount of ambuiguity as the angle at the hydrogen bonded proton tends to change.

The proton NMR study shows that the benzoic acid and lithium hemibenzoate have similar iostropic shifts which give evidence for weak hydrogen bonding, whilst the potassium, rubidium and cesium hemibenzoates have isotropic shifts in excess of 20 ppm which classically describes very strong hydrogen bonding. Density functional theory calculations of these shifts agree with this correlation. The  $a\delta_{22}$  component of the CSA tensor of the carbonyl  $^{13}\text{C}$  is also shown to be inversely proportional to the strength of the hydrogen bond. A linear change is observed as you move from benzoic acid through to the strong hydrogen interaction in the cesium hemibenzoate sample.

The  $^{17}\text{O}$  nuclei were analysed by density functional theory to confirm the multi-field MAS and DOR NMR to gain accurate information on the quadrupole interaction present in these samples. The errors within the results highlight the difficulties with studying hydrogen bonded systems caused by the quantum motion of protons in the sample. The alkali group IA metals give an excellent correlation with the calculated CASTEP results giving evidence that the motion is only present at the proton site. The project highlights the need to use multiple techniques to describe the strength of the hydrogen bond and the leading role  $^{17}\text{O}$  solid state NMR can play in this.

# Bibliography

- [1] P. M. Panchmatia, A. Orera, G. J. Rees, M. E. Smith, J. V. Hanna, P. R. Slater, and M. S. Islam. Oxygen defects and novel transport mechanisms in apatite ionic conductors: Combined (17) o nmr and modeling studies. *Angew Chem Int Ed Engl*, 50:9328–33, 2011.
- [2] N. Bohr. On the constitution of atoms and molecules, part i. *Philosophical Magazine*, 26:1–24, 1913.
- [3] N. Bohr. On the constitution of atoms and molecules, part ii systems containing only a single nucleus. *Philosophical Magazine*, 26(153):476–502, 1913.
- [4] N. Bohr. On the constitution of atoms and molecules, part iii systems containing several nuclei. *Philosophical Magazine*, 26(153):857–875, 1913.
- [5] S. Uhlenbeck, G. E. Goudsmit. Spinning electrons and the structure of spectra. *Nature*, 117:264–265, 1926.
- [6] W. Heisenberg. ber quantentheoretische umdeutung kinematischer und mechanischer beziehungen. *Zeitschrift fr Physik*, 33:879–893, 1925.
- [7] E. Schrodinger. Quantisierung als eigenwertproblem. *Annalen Der Physik*, 79:361–376, 1926.
- [8] *Nobel Lectures, Physics 1942–1962*. Elsevier, Amsterdam, 1964.
- [9] P. A. M. Dirac. *The Principles of Quantum Mechanics*. pp. x. 257. Clarendon Press: Oxford, 1930. [International Series of Monographs on Physics.].
- [10] D. M. Dennison. The rotation of molecules. *Phys. Rev.*, 28(2):318–333, 1926.
- [11] D. M. Dennison. Recollections of physics and of physicists during 1920s. *American Journal of Physics*, 42:1051–1056, 1974.
- [12] I. I. Rabi. Space quantization in a gyrating magnetic field. *Phys. Rev.*, 51(8):652, 1937.
- [13] Z. Gerlach, W. Stern. Das magnetische moment des silberatoms. *Zeitschrift fr Physik*, 9:353–355, 1922.

- [14] C. J. Gorter. Negative result of an attempt to detect nuclear magnetic spins. *Physica*, 3(9):995–998, 1936.
- [15] E. D. Becker, C. L. Fisk, and C. L. Khetrapal. *The Development of NMR*, volume 1 of *Encyclopedia of Magnetic Resonance*. Wiley, Chichester, 1996.
- [16] R. V. Pound. *Early Days in NMR*, volume 1 of *Encyclopedia of Magnetic Resonance*. Wiley, Chichester, 1996.
- [17] E. M. Purcell, H. C. Torrey, and R. V. Pound. Resonance absorption by nuclear magnetic moments in a solid. *Phys. Rev.*, 69(1-2):37, 1946.
- [18] F. Bloch. *The Principle of Nuclear Induction*, volume 1 of *Encyclopedia of Magnetic Resonance*. Wiley, Chichester, 1996.
- [19] W. W.; Packard M. E. Bloch, F.; Hansen. Nuclear induction. *Phys. Rev.*, 70:474, 1946.
- [20] H. S. Gutowsky and D. W. McCall. Nuclear magnetic resonance fine structure in liquids. *Phys. Rev.*, 82(5):748, 1951.
- [21] E. L. Hahn and D. E. Maxwell. Chemical shift and field independent frequency modulation of the spin echo envelope. *Phys. Rev.*, 84(6):1246, 1951.
- [22] C. P. Slichter. *Principles of magnetic resonance*. Springer, Berlin ; London, 3rd edition, 1990. C.P. Slichter. ill. ; 25 cm. Includes bibliography and indexes.
- [23] E. R. Andrew, A. Bradbury, and R. G. Eades. Removal of dipolar broadening of nuclear magnetic resonance spectra of solids by specimen rotation. *Nature*, 183:1802–1803, 1959.
- [24] E. R. Andrew, A. Bradbury, and R. G. Eades. Nuclear magnetic resonance spectra from a crystal rotated at high speed. *Nature*, 182:1659–1659, 1958.
- [25] A. Abragam. *The principles of nuclear magnetism*. Clarendon Press, Oxford, first paperback edition. edition, 1985.
- [26] W. D. Knight. Nuclear magnetic resonance shift in metals. *Physical Review Letters*, 76:1259–1260, 1949.
- [27] R. V. Pound. Nuclear electric quadrupole interactions in crystals. *Phys. Rev.*, 79(4):685, 1950.
- [28] E. D. Becker, C. L. Fisk, and C. L. Khetrapal. *The Development of NMR*, volume 1 of *Encyclopedia of Magnetic Resonance*. Wiley, Chichester, 1996.
- [29] S. R. Hartmann and E. L. Hahn. Nuclear double resonance in the rotating frame. *Phys. Rev.*, 128(5):2042, 1962.
- [30] A. Samoson, E. Lippmaa, and A. Pines. High-resolution solid-state nmr averaging of 2nd-order effects by means of a double-rotor. *Molecular Physics*, 65:1013–1018, 1988.

- [31] A. Llor and J. Virlet. Towards high-resolution nmr of more nuclei in solids: Sample spinning with time-dependent spinner axis angle. *Chem. Phys. Lett.*, 152(2-3):248–253, 1988.
- [32] F. Y. Alder. On the spin and magnetic moment of o17. *Phys. Rev.*, 81:1067–1068, 1951.
- [33] F Proctor, W.G. Yu. On the nuclear magnetic moments of several stable isotopes. *Phys. Rev.*, 81:20–30, 1951.
- [34] G. G. Mather, G. J. N. Rapsey, and A. Pidcock. Effect of anionic ligands on p-31 nmr parameters trialkylphosphine complexes of platinum(ii). *Inorganic & Nuclear Chemistry Letters*, 9:567–570, 1973.
- [35] P. S. Pregosin. The multi-nuclear nmr approach - contributions to the chemistry of platinum. *Chimia*, 35:43–49, 1981.
- [36] R. R. Ernst. *The Success Story of Fourier Transformation in NMR*, volume 1 of *Encyclopedia of Magnetic Resonance*. Wiley, Chicester, 1996.
- [37] R. R. Ernst and W. A. Anderson. Application of fourier transform spectroscopy to magnetic resonance. *Rev. Sci. Instrum.*, 37(1):93–102, 1966.
- [38] R. R. Ernst, G. Bodenhausen, and A. Wokaun. *Principles of Nuclear Magnetic Resonance in One and Two Dimensions*. Clarendon Press, Oxford, 1987.
- [39] A. Medek, J. S. Harwood, and L. Frydman. Multiple-quantum magic-angle spinning nmr: A new method for the study of quadrupolar nuclei in solids. *Journal of the American Chemical Society*, 117:12779–12787, 1995.
- [40] M. E. Rose. *Elementary theory of angular momentum*. Dover, New York, dover edition, 1995. 94041223 M.E. Rose. ill. ; 22 cm. Originally published: New York : Wiley, 1957, in series: Structure of matter series. Includes bibliographical references and indexes.
- [41] M. Eden. Computer simulations in solid-state nmr. i. spin dynamics theory. *Concepts in Magnetic Resonance Part A*, 17A:117–154, 2003.
- [42] M. Eden. Computer simulations in solid-state nmr. ii. implementations for static and rotating samples. *Concepts in Magnetic Resonance Part A*, 18A:1–23, 2003.
- [43] P. P. Man. *Quadrupolar Interactions*. John Wiley & Sons, Ltd, 2007.
- [44] N. S. Barrow. *Homonuclear Correlation in Solid-State NMR: Developing Experiments for Half-Integer Quadrupolar Nuclei*. PhD thesis, University of Warwick, 2009.
- [45] M. J. Duer. *Introduction to Solid-State NMR Spectroscopy*. Blackwell Publishing, Oxford, 2004.

- [46] M. H. Levitt. *Spin dynamics : basics of nuclear magnetic resonance*. John Wiley & Sons, 2nd edition, 2008.
- [47] M. Karplus. Contact electron-spin coupling of nuclear magnetic moments. *J. Chem. Phys.*, 30(1):11–15, 1959.
- [48] K.J.D. MacKenzie and M.E. Smith. *Multinuclear Solid State NMR of Inorganic Materials*, volume 1 of *Pergamon Materials Series*. Pergamon, Oxford, 1st edition, 2002.
- [49] R. K. Harris, R. E. Wasylshen, and M. J. Duer. *NMR crystallography*. Wiley-Blackwell, Oxford, 2009. GBA981047 bnb editors, Robin K. Harris, Roderick E. Wasylshen, Melinda J. Duer. ill. (some col.) ; 26 cm. EMR handbooks Formerly CIP. Uk Includes bibliographical references and index.
- [50] G. E. Pake. Nuclear resonance absorption in hydrated crystals: Fine structure of the proton line. *J. Chem. Phys.*, 16(4):327–336, 1948.
- [51] J. C. Facelli and A. M. Orendt. *Magnetic Shielding and Chemical Shifts: Basics*. John Wiley & Sons, Ltd, 2007.
- [52] R. K. Harris, E. D. Becker, S. M. C. de Menezes, R. Goodfellow, and P. Granger. Nmr nomenclature: Nuclear spin properties and conventions for chemical shifts - iupac recommendations 2001 (reprinted from pure appl. chem, vol 73, pg 1795-1818, 2001). *Solid State Nuclear Magnetic Resonance*, 22:458–483, 2002.
- [53] J. K. Harper. *Chemical Shift Anisotropy and Asymmetry: Relationships to Crystal Structure*. John Wiley & Sons, Ltd, 2007.
- [54] J. Herzfeld and A. E. Berger. Sideband intensities in nmr-spectra of samples spinning at the magic angle. *Journal of Chemical Physics*, 73:6021–6030, 1980.
- [55] U. Haeberlen. *Advances in Magnetic Resonance*. Academic Press, New York, 1976.
- [56] S. E. Ashbrook and M. E. Smith. Solid state o-17 nmr - an introduction to the background principles and applications to inorganic materials. *Chemical Society Reviews*, 35:718–735, 2006.
- [57] S. E. Ashbrook and S. Wimperis. *Quadrupolar Coupling: An Introduction and Crystallographic Aspects*. John Wiley & Sons, Ltd, 2007.
- [58] P. P. Man. *Quadrupolar Interactions*. John Wiley & Sons, Ltd, 2007.
- [59] R. Hajjar, Y. Millot, and P. P. Man. Phase cycling in mqmas sequences for half-integer quadrupole spins. *Progress in Nuclear Magnetic Resonance Spectroscopy*, 57:306–342, 2010.
- [60] M. Mehring. *Principles of high-resolution NMR in solids*. Springer-Verlag, Berlin, 2nd, rev. and enl. ed edition, 1983.

- [61] A. Jerschow. From nuclear structure to the quadrupolar nmr interaction and high-resolution spectroscopy. *Prog. Nucl. Magn. Reson. Spectrosc.*, 46(1):63–78, 2005.
- [62] F. Wolf, D. Kline, and H. S. Story. Nb-93 and na-23 nmr in polycrystalline sodium niobate. *Journal of Chemical Physics*, 53:3538–&, 1970.
- [63] J. J. van der Klink and H. B. Brom. Nmr in metals, metal particles and metal cluster compounds. *Progress in Nuclear Magnetic Resonance Spectroscopy*, 36:89–201, 2000.
- [64] R. Dupree, W. W. Warren, and F. J. Disalvo. Se-77 nmr-study of electronic instability in tise2. *Physical Review B*, 16:1001–1007, 1977.
- [65] J. Korringa. Nuclear magnetic relaxation and resonance line shift in metals. *Physica*, 16:601–610, 1950.
- [66] G. C. Carter, L. H. Bennett, and D. J. Kahan. *Metallic shifts in NMR : a review of the theory and comprehensive critical data compilation of metallic materials*. Progress in Materials Science. Pergamon Press, Oxford ; New York, 1st edition, 1977.
- [67] D. Carlier, M. Menetrier, C. P. Grey, C. Delmas, and G. Ceder. Understanding the nmr shifts in paramagnetic transition metal oxides using density functional theory calculations. *Physical Review B*, 67, 2003.
- [68] M. Matti Maricq and J. S. Waugh. Nmr in rotating solids. *J. Chem. Phys.*, 70(7):3300–3316, 1979.
- [69] R. E. Gang, 1969.
- [70] I. R. Dixon, W. D. Markiewicz, K. W. Pickard, and C. A. Swenson. Critical current and n-value of nb3sn conductors for the wide bore 900 mhz nmr magnet. *Ieee Transactions on Applied Superconductivity*, 9:2513–2516, 1999.
- [71] I. R. Dixon, W. D. Markiewicz, P. Murphy, T. A. Painter, and A. Powell. Quench detection and protection of the wide bore 900 mhz nmr magnet at the national high magnetic field laboratory. *Ieee Transactions on Applied Superconductivity*, 14:1260–1263, 2004.
- [72] L. R. Dixon, W. D. Markiewicz, W. W. Brey, and K. K. Shetty. Performance of the ultra wide bore 900 mhz nmr magnet at the national high magnetic field laboratory. *Ieee Transactions on Applied Superconductivity*, 15:1334–1337, 2005.
- [73] The world’s largest wide-bore nmr magnet comes to field. *Insight*, 44:610–610, 2002.
- [74] M. J. E. Golay. Field homogenizing coils for nuclear spin resonance instrumentation. *Rev. Sci. Instrum.*, 29:313–316, 1958.

- [75] A. A. Weston. Electrical current shims for correcting magnetic fields. *Rev. Sci. Instrum.*, 32:241–251, 1961.
- [76] F. D. Doty, R. R. Inners, and P. D. Ellis. A multi-nuclear double-tuned probe for applications with solids or liquids utilizing lumped tuning elements. *Journal of Magnetic Resonance*, 43:399–416, 1981.
- [77] F. D. Doty, G. Entzminger, and Y. A. Yang. Magnetism in high-resolution nmr probe design. ii: Hr mas. *Concepts in Magnetic Resonance*, 10:239–260, 1998.
- [78] F. D. Doty, G. Entzminger, and Y. A. Yang. Magnetism in high-resolution nmr probe design. i: General methods. *Concepts in Magnetic Resonance*, 10:133–156, 1998.
- [79] F. D. Doty, J. Kulkarni, C. Turner, G. Entzminger, and A. Bielecki. Using a cross-coil to reduce rf heating by an order of magnitude in triple-resonance multinuclear mas at high fields. *Journal of Magnetic Resonance*, 182:239–253, 2006.
- [80] F. D. Doty, G. Entzminger, and Y. A. Yang. Answers to review questions: Magnetism in high-resolution nmr probe design. ii: Hr mas. *Concepts in Magnetic Resonance*, 10:329–329, 1998.
- [81] F. D. Doty, G. Entzminger, and Y. A. Yang. Answers to review questions: Magnetism in high-resolution nmr probe design. i: General methods. *Concepts in Magnetic Resonance*, 10:327–328, 1998.
- [82] S. D’Arco, F. Ponci, F. D. Doty, and J. Staab. Velocity and pressure measurements for microturbine control in nmr application. *2007 Ieee Instrumentation & Measurement Technology Conference, Vols 1-5*, pages 1935–1939, 2007.
- [83] J. P. Bayle, J. Courtieu, J. Jullien, and S. K. Kan. High-resolution nmr in solids - a simple and improved magic angle probe design for conventional small gap c-13 ft spectrometers. *Organic Magnetic Resonance*, 16:85–89, 1981.
- [84] F. D. Doty and P. D. Ellis. Design of high-speed cylindrical nmr sample spinners. *Review of Scientific Instruments*, 52:1868–1875, 1981.
- [85] H. D.W. Hill and G. A. Gray. *Spectrometers: A General Overview*. John Wiley & Sons, Ltd, 2007.
- [86] D.I. Hoult. The origins and present status of the radio wave controversy in nmr. *Concepts Magn. Res. A*, 34A(4):193–216, 2009.
- [87] David I. Hoult and Balram Bhakar. Nmr signal reception: Virtual photons and coherent spontaneous emission. *Concepts Magn. Res.*, 9(5):277–297, 1997.
- [88] J. Van Kranendonk. Theory of quadrupolar nuclear spin-lattice relaxation. *Physica*, 20(7-12):781–800, 1954.

- [89] E. Matthias, B. Olsen, D. A. Shirley, J. E. Templeton, and R. M. Steffen. Theory of nuclear magnetic resonance detected by nuclear radiations. *Phys. Rev. A*, 4(4):1626, 1971.
- [90] I. P. Gerothanassis and C. G. Tsanaktsidis. Nuclear electric quadrupole relaxation. *Concepts Magn. Res.*, 8(1):63–74, 1996.
- [91] E. R. Andrew and D. P. Tunstall. Spin-lattice relaxation in imperfect cubic crystals and in non-cubic crystals. *Proc. Phys. Soc.*, 78:1–11, 1961.
- [92] M. Goldman. Formal theory of spin-lattice relaxation. *J. Magn. Reson.*, 149(2):160–187, 2001.
- [93] I. J. Lowe. Free induction decays of rotating solids. *Phys. Rev. Lett.*, 2(7):285, 1959.
- [94] I. J. Lowe and R. E. Norberg. Free-induction decays in solids. *Phys. Rev.*, 107(1):46, 1957.
- [95] M. Munowitz. *Coherence and NMR*. Wiley, Chicester, 1988.
- [96] J. J. Titman, A. L. Davis, E. D. Laue, and J. Keeler. Selection of coherence transfer pathways using inhomogeneous adiabatic pulses. removal of zero-quantum coherence. *J. Magn. Reson.*, 89(1):176–183, 1990.
- [97] Oxford english dictionary [electronic resource].
- [98] A. Pines and T. W. Shattuck. C-13 proton nmr cross-polarization times in solid adamantane. *Journal of Chemical Physics*, 61:1255–1256, 1974.
- [99] M. A. Eastman. Examples of hartmann-hahn match conditions for cp/mas between two half-integer quadrupolar nuclei. *J. Magn. Reson.*, 139(1):98–108, 1999.
- [100] D. Rovnyak. Tutorial on analytic theory for cross-polarization in solid state nmr. *Concepts in Magnetic Resonance Part A*, 32A:254–276, 2008.
- [101] G. Dybowski, C. Neue. *Wide Lines fo Nonquadrupolar Nuclei*, volume 1 of *Encyclopedia of Magnetic Resonance*. Wiley, Chicester, 2007.
- [102] T. Shimizu, H. Yasuoka, T. Imai, T. Tsuda, T. Takabatake, Y. Nakazawa, and M. Ishikawa. Site assignment for cu nqr lines in yba2cu3o7-delta superconductor. *Journal of the Physical Society of Japan*, 57:2494–2505, 1988.
- [103] R. Freeman, S. P. Kempell, and M. H. Levitt. Radiofrequency pulse sequences which compensate their own imperfections. *Journal of Magnetic Resonance*, 38:453–479, 1980.
- [104] W. G. Clark, M. E. Hanson, F. Lefloch, and P. Segransan. Magnetic-resonance spectral reconstruction using frequency-shifted and summed fourier-transform processing. *Review of Scientific Instruments*, 66:2453–2464, 1995.



- [105] L. A. O'Dell, K. Klimm, J. C. C. Freitas, S. C. Kohn, and M. E. Smith. (33)s mas nmr of a disordered sulfur-doped silicate: Signal enhancement via rapt, qcpmg and adiabatic pulses. *Applied Magnetic Resonance*, 35:247–259, 2009.
- [106] L. A. O'Dell, A. J. Rossini, and R. W. Schurko. Acquisition of ultra-wideline nmr spectra from quadrupolar nuclei by frequency stepped wurst-qcpmg. *Chemical Physics Letters*, 468:330–335, 2009.
- [107] L. A. O'Dell, S. L. P. Savin, A. V. Chadwick, and M. E. Smith. Structural characterization of sio<sub>2</sub> and al<sub>2</sub>o<sub>3</sub> zener-pinned nanocrystalline tio<sub>2</sub> by nmr, xrd and electron microscopy. *Journal of Physical Chemistry C*, 111:13740–13746, 2007.
- [108] L. A. O'Dell, S. L. P. Savin, A. V. Chadwick, and M. E. Smith. Multinuclear mas nmr investigation of sol-gel and ball-milled nanocrystalline ga<sub>2</sub>o<sub>3</sub>. *Applied Magnetic Resonance*, 32:527–546, 2007.
- [109] L. A. O'Dell and R. W. Schurko. Qcpmg using adiabatic pulses for faster acquisition of ultra-wideline nmr spectra. *Chemical Physics Letters*, 464:97–102, 2008.
- [110] L. A. O'Dell and R. W. Schurko. Fast and simple acquisition of solid-state (14)n nmr spectra with signal enhancement via population transfer. *Journal of the American Chemical Society*, 131:6658–+, 2009.
- [111] F. H. Larsen, H. J. Jakobsen, P. D. Ellis, and N. C. Nielsen. Qcpmg-mas nmr of half-integer quadrupolar nuclei. *Journal of Magnetic Resonance*, 131:144–147, 1998.
- [112] F. H. Larsen, J. Skibsted, H. J. Jakobsen, and N. C. Nielsen. Solid-state qcpmg nmr of low-gamma quadrupolar metal nuclei in natural abundance. *Journal of the American Chemical Society*, 122:7080–7086, 2000.
- [113] P. R. Bodart, J. P. Amoureux, Y. Dumazy, and R. Lefort. Theoretical and experimental study of quadrupolar echoes for half-integer spins in static solid-state nmr. *Molecular Physics*, 98:1545–1551, 2000.
- [114] R. Lefort, J. W. Wiench, M. Pruski, and J. P. Amoureux. Optimization of data acquisition and processing in carr-purcell-meiboom-gill multiple quantum magic angle spinning nuclear magnetic resonance. *Journal of Chemical Physics*, 116:2493–2501, 2002.
- [115] I. Hung and Z. H. Gan. On the practical aspects of recording wideline qcpmg nmr spectra. *Journal of Magnetic Resonance*, 204:256–265, 2010.
- [116] I. Hung, A. J. Rossini, and R. W. Schurko. Application of the carr-purcell meiboom-gill pulse sequence for the acquisition of solid-state nmr spectra of spin-(1)/(2) nuclei. *Journal of Physical Chemistry A*, 108:7112–7120, 2004.

- [117] I. J. F. Poplett and M. E. Smith. Field sweep broadband nmr spectroscopy. *Solid State Nuclear Magnetic Resonance*, 11:211–214, 1998.
- [118] D. Holland, S. A. Feller, T. F. Kemp, M. E. Smith, A. P. Howes, D. Winslow, and M. Kodama. Boron-10 nmr: what extra information can it give about borate glasses? *Physics and Chemistry of Glasses-European Journal of Glass Science and Technology Part B*, 48:1–8, 2007.
- [119] K. J. Pike, R. P. Malde, S. E. Ashbrook, J. McManus, and S. Wimperis. Multiple-quantum mas nmr of quadrupolar nuclei. do five-, seven- and nine-quantum experiments yield higher resolution than the three-quantum experiment? *Solid State Nucl. Magn. Reson.*, 16(3):203–215, 2000.
- [120] A. L. Davis, G. Estcourt, J. Keeler, E. D. Laue, and J. J. Titman. Improvement of z filters and purging pulses by the use of zero-quantum dephasing in inhomogeneous b1 or b0 fields. *J. Magn. Reson. Ser. A*, 105(2):167–183, 1993.
- [121] M. J. Duer. Determination of structural data from multiple-quantum magic-angle spinning nmr experiments. *Chem. Phys. Lett.*, 277(1-3):167–174, 1997.
- [122] M. J. Duer and A. J. Painter. Correlating quadrupolar nuclear spins: A multiple-quantum nmr approach. *Chem. Phys. Lett.*, 313(5-6):763–770, 1999.
- [123] L. Marinelli and L. Frydman. On the origin of spinning sidebands in mqmas nmr experiments. *Chem. Phys. Lett.*, 275(3-4):188–198, 1997.
- [124] D. Massiot. Sensitivity and lineshape improvements of mq-mas by rotor-synchronized data acquisition. *J. Magn. Reson. Ser. A*, 122(2):240–244, 1996.
- [125] S. P. Brown and S. Wimperis. Two-dimensional multiple-quantum mas nmr of quadrupolar nuclei: A comparison of methods. *Journal of Magnetic Resonance*, 128:42–61, 1997.
- [126] J. D. Gehman and J. L. Provis. Generalized biaxial shearing of mqmas nmr spectra. *Journal of Magnetic Resonance*, 200:167–172, 2009.
- [127] I. Hung, J. Trebosc, G. L. Hoatson, R. L. Vold, J. P. Amoureux, and Z. H. Gan. Q-shear transformation for mqmas and stmas nmr spectra. *Journal of Magnetic Resonance*, 201:81–86, 2009.
- [128] J. Amoureux and M. Pruski. *MQMAS Advances*. John Wiley & Sons, Ltd, 2007.
- [129] A. Samoson and E. Lippmaa. Synchronized double-rotation nmr-spectroscopy. *Journal of Magnetic Resonance*, 84:410–416, 1989.
- [130] R. Dupree. *Double Rotation NMR*. John Wiley & Sons, Ltd, 2007.
- [131] G. Wu, D. Rovnyak, P. C. Huang, and R. G. Griffin. High-resolution oxygen-17 nmr spectroscopy of solids by multiple-quantum magic-angle-spinning. *Chemical Physics Letters*, 277:79–83, 1997.

- [132] Y. Wu, B. Q. Sun, A. Pines, A. Samoson, and E. Lippmaa. Nmr experiments with a new double rotor. *Journal of Magnetic Resonance*, 89:297–309, 1990.
- [133] A. P. Howes, T. Anupold, V. Lemaitre, A. Kukol, A. Watts, A. Samoson, M. E. Smith, and R. Dupree. Enhancing resolution and sensitivity of o-17 solid-state nmr through combining double rotation, h-1 decoupling and satellite modulation for biomolecular applications. *Chemical Physics Letters*, 421:42–46, 2006.
- [134] W. Kohn. Nobel lecture: Electronic structure of matter-wave functions and density functionals. *Reviews of Modern Physics*, 71:1253–1266, 1999.
- [135] W. Kohn. Electronic structure of matter: Wave functions and density functionals. *Chimia*, 54:50–50, 2000.
- [136] S. A. Joyce, J. R. Yates, C. J. Pickard, and F. Mauri. A first principles theory of nuclear magnetic resonance j-coupling in solid-state systems. *J. Chem. Phys.*, 127(20):204107, 2007.
- [137] J. D. Jackson. *Classical electrodynamics*. Wiley, New York ; Chichester, 3rd ed. edition, 1999. GB9900319 bnb 2521 John David Jackson. ill. ; 26 cm. Previous ed.: 1975. Includes bibliographical references (p. 785-790) and index.
- [138] C. J. Pickard and F. Mauri. All-electron magnetic response with pseudopotentials: Nmr chemical shifts. *Physical Review B*, 63, 2001.
- [139] T. Gregor, F. Mauri, and R. Car. A comparison of methods for the calculation of nmr chemical shifts. *Journal of Chemical Physics*, 111:1815–1822, 1999.
- [140] M. Profeta, F. Mauri, and C. J. Pickard. Accurate first principles prediction of o-17 nmr parameters in sio2: Assignment of the zeolite ferrierite spectrum. *Journal of the American Chemical Society*, 125:541–548, 2003.
- [141] J. R. Yates, C. J. Pickard, M. C. Payne, and F. Mauri. Relativistic nuclear magnetic resonance chemical shifts of heavy nuclei with pseudopotentials and the zeroth-order regular approximation. *Journal of Chemical Physics*, 118:5746–5753, 2003.
- [142] R. Dillon, S. Srinivasan, A. S. Arico, and V. Antonucci. International activities in dmfc r&d: status of technologies and potential applications. *Journal of Power Sources*, 127:112–126, 2004.
- [143] A. Obuchi, A. Ohi, M. Nakamura, A. Ogata, K. Mizuno, and H. Ohuchi. Performance of platinum-group metal-catalysts for the selective reduction of nitrogen-oxides by hydrocarbons. *Applied Catalysis B-Environmental*, 2:71–80, 1993.
- [144] V. Mehta and J. S. Cooper. Review and analysis of pem fuel cell design and manufacturing. *Journal of Power Sources*, 114:32–53, 2003.

- [145] D. Astruc. *Nanoparticles and catalysis*. Wiley-VCH, Weinheim, 2008.
- [146] P. K. Babu, H. S. Kim, S. T. Kuk, J. H. Chung, E. Oldfield, A. Wieckowski, and E. S. Smotkin. Activation of nanoparticle pt-ru fuel cell catalysts by heat treatment: A pt-195 nmr and electrochemical study. *Journal of Physical Chemistry B*, 109:17192–17196, 2005.
- [147] P. K. Babu, H. S. Kim, E. Oldfield, and A. Wieckowski. Electronic alterations caused by ruthenium in pt-ru alloy nanoparticles as revealed by electrochemical nmr. *Journal of Physical Chemistry B*, 107:7595–7600, 2003.
- [148] P. K. Babu, H. S. Kim, A. Wieckowski, and E. Oldfield. Electrochemical nmr study of co adsorbed on pt nanoparticles decorated with pd. *Abstracts of Papers of the American Chemical Society*, 227:U835–U835, 2004.
- [149] T. Kobayashi, P. K. Babu, J. H. Chung, E. Oldfield, and A. Wieckowski. Coverage dependence of co surface diffusion on pt nanoparticles: An ec-nmr study. *Journal of Physical Chemistry C*, 111:7078–7083, 2007.
- [150] K. Franaszczuk, J. Wu, A. Wieckowski, B. Montez, and E. Oldfield. Solid-state nmr measurements of cyanides on powdered pt electrodes. *Abstracts of Papers of the American Chemical Society*, 206:44–Phys, 1993.
- [151] Y. Y. Tong, C. Belrose, A. Wieckowski, and E. Oldfield. First observation of platinum-195 nuclear magnetic resonance in commercial graphite-supported platinum electrodes in an electrochemical environment. *Journal of the American Chemical Society*, 119:11709–11710, 1997.
- [152] J. J. Wu, J. B. Day, K. Franaszczuk, B. Montez, E. Oldfield, A. Wieckowski, P. A. Vuissoz, and J. P. Ansermet. Recent progress in surface nmr-electrochemistry. *Journal of the Chemical Society-Faraday Transactions*, 93:1017–1026, 1997.
- [153] A. V. Ivanov, I. A. Lutsenko, M. A. Ivanov, A. V. Gerasimenko, and O. N. Antzutkin. Synthesis, structural and multinuclear natural abundance (c-13, p-31, pt-195) cp/mas nmr studies of crystalline o,o'-dialkyldithiophosphate platinum(ii) complexes. *Russian Journal of Coordination Chemistry*, 34:584–593, 2008.
- [154] A. V. Ivanov, V. I. Palazhchenko, V. E. Strikha, O. N. Antzutkin, and W. Forsling. Structural features and nmr pt-195 spectroscopy of cooperite monocrystals (natural pts). *Doklady Earth Sciences*, 410:1141–1144, 2006.
- [155] R. K. Brow, R. J. Kirkpatrick, and G. L. Turner. The short-range structure of sodium-phosphate glasses .1. mas nmr-studies. *Journal of Non-Crystalline Solids*, 116:39–45, 1990.
- [156] H. E. Rhodes, P. K. Wang, C. D. Makowka, S. L. Rudaz, H. T. Stokes, C. P. Slichter, and J. H. Sinfelt. Nmr of platinum catalysts .2. relaxation. *Physical Review B*, 26:3569–3574, 1982.

- [157] H. E. Rhodes, P. K. Wang, H. T. Stokes, C. P. Slichter, and J. H. Sinfelt. Nmr of platinum catalysts .1. line-shapes. *Physical Review B*, 26:3559–3568, 1982.
- [158] H. T. Stokes, H. E. Rhodes, P. K. Wang, C. P. Slichter, and J. H. Sinfelt. Nmr of platinum catalysts .3. microscopic variation of the knight-shifts. *Physical Review B*, 26:3575–3581, 1982.
- [159] Y. Y. Tong, A. Wieckowski, and E. Oldfield. Nmr of electrocatalysts. *Journal of Physical Chemistry B*, 106:2434–2446, 2002.
- [160] Y. Y. Tong, H. S. Kim, P. K. Babu, P. Waszczuk, A. Wieckowski, and E. Oldfield. An nmr investigation of co tolerance in a pt/ru fuel cell catalyst. *Journal of the American Chemical Society*, 124:468–473, 2002.
- [161] Y. Y. Tong, E. Oldfield, and A. Wieckowski. Diffusion on a nanoparticle surface as revealed by electrochemical nmr. *Faraday Discussions*, 121:323–330, 2002.
- [162] Y. Y. Tong, C. Rice, N. Godbout, A. Wieckowski, and E. Oldfield. Correlation between the knight shift of chemisorbed co and the fermi level local density of states at clean platinum catalyst surfaces. *Journal of the American Chemical Society*, 121:2996–3003, 1999.
- [163] M. M. P. Janssen and J. Moolhuysen. Platinum-tin catalysts for methanol fuel-cells prepared by a novel immersion technique, by electrocodeposition and by alloying. *Electrochimica Acta*, 21:861–868, 1976.
- [164] A. Marteel, J. A. Davies, M. R. Mason, T. Tack, S. Bektesevic, and M. A. Abraham. Supported platinum/tin complexes as catalysts for hydroformylation of 1-hexene in supercritical carbon dioxide. *Catalysis Communications*, 4:309–314, 2003.
- [165] D. E. Nikles, Z. Liu, D. Reed, G. Kwon, and M. Shamsuzzoha. Pt(3)sn nanoparticles with controlled size: High-temperature synthesis and room-temperature catalytic activation for electrochemical methanol oxidation. *Journal of Physical Chemistry C*, 111:14223–14229, 2007.
- [166] F. Caruso, C. Di Nicola, J. V. Hanna, F. Marchetti, C. Pettinari, R. Pettinari, M. Rossi, G. J. Rees, B. W. Skelton, and A. H. White. Novel bis(beta-diketonato)diorganotin(iv) derivatives containing bulky 4-acyl-5-pyrazolonato ligands: Influence of the steric hindrance of the acyl moiety on the solid state structures of tin complexes and their behaviour in solution. *Inorganica Chimica Acta*, 367:73–84, 2011.
- [167] T. H. Chang, C. P. Cheng, and C. T. Yeh. Sn-119 nmr-studies on alloying silica supported tin with nickel and palladium. *Materials Chemistry and Physics*, 22:503–510, 1989.

- [168] J. P. Bucher, J. Buttet, J. J. Vanderklink, M. Graetzel, E. Newson, and T. B. Truong. Pt-195 nmr-studies of supported catalysts. *Colloids and Surfaces*, 36:155–167, 1989.
- [169] J. P. Bucher, J. J. Vanderklink, J. Buttet, and M. Graetzel. Study and classification of platinum catalysts by nmr. *Helvetica Physica Acta*, 58:791–791, 1985.
- [170] Z. L. Wang. *Characterization of nanophase materials*. Wiley-VCH, Weinheim ; Chichester, 2000. GB 99-V7609 edited by Zhong Lin Wang. ill. ; 25 cm. Includes bibliographical references and index.
- [171] P. S. Pregosin. Platinum-195 nuclear magnetic resonance. *Coordination Chemistry Reviews*, 44:247 – 291, 1982.
- [172] T. J. Bastow, M. E. Smith, and S. N. Stuart. Observation of zr-91 nmr in zirconium-based metals and oxides. *Chemical Physics Letters*, 191:125–129, 1992.
- [173] R. P. Messmer, S. K. Knudson, K. H. Johnson, J. B. Diamond, and C. Y. Yang. Molecular-orbital studies of transition-metal and noble-metal clusters by self-consistent-field chialpha scattered-wave method. *Physical Review B*, 13:1396–1415, 1976.
- [174] B. J. Pronk, H. B. Brom, A. Ceriotti, and G. Longoni. Physical-properties of metal cluster compounds-iii - nmr-study of platinum carbonyl clusters. *Solid State Communications*, 64:7–10, 1987.
- [175] G. A. Cooper S. J. Buchanan, J. S. Hards. Catalyst material comprising platinum alloy supported on carbon, September 1991.
- [176] F. Wen, H. Bonnemann, R. J. Mynott, B. Spliethoff, C. Weidenthaler, N. Palina, S. Zinoveva, and H. Modrow. Preparation of pt-13 clusters in the presence of trialkylaluminium. *Applied Organometallic Chemistry*, 19:827–829, 2005.
- [177] William Hart Hayt and John A. Buck. *Engineering electromagnetics*. McGraw-Hill, New York, 8th int. ed. edition, 2012.
- [178] M. J. Woodman. The thermal conductivity and electrical resistivity of platinum. *Platinum Metals Rev.*, 10:132, 1966.
- [179] J. Kummerlen, A. Sebald, and H. Reuter. The structure of ((iso-bu)<sub>3</sub>n)<sub>2</sub>co<sub>3</sub> and (me<sub>3</sub>sn)<sub>2</sub>co<sub>3</sub> in solution and in the solid-state studied by c-13/sn-119 nmr-spectroscopy and x-ray-diffraction. *Journal of Organometallic Chemistry*, 427:309–323, 1992.
- [180] L. E. Barret. *Investigation into industrially viable catalytic materials using solid state nuclear magnetic resonance*. PhD thesis, University of Warwick, 2006.

- [181] S. T. Orr. *Multinuclear Solid-State NMR of Fuel Cell Materials*. PhD thesis, Univeristy of Warwick, 2010.
- [182] T. J. Bastow, M. A. Gibson, and C. T. Forwood. Ti-47,ti-49 nmr: hyperfine interactions in oxides and metals. *Solid State Nuclear Magnetic Resonance*, 12:201–209, 1998.
- [183] A. F. Lee, K. Wilson, and R. M. Lambert. Structure and stability of the platinum/aluminium interface: alloying and substrate vacancy formation on pt111/al. *Surface Science*, 446:145–152, 2000.
- [184] M. E. Smith, M. A. Gibson, C. T. Forwood, and T. J. Bastow. Detection of phase and antisite structure of ti-al alloys by al-27 solid state nuclear magnetic resonance. *Philosophical Magazine a-Physics of Condensed Matter Structure Defects and Mechanical Properties*, 74:791–809, 1996.
- [185] W. Bronger, P. Muller, and K. Wrzesien. The structure of platinum-rich aluminium/platinum alloys. *Zeitschrift Fur Anorganische Und Allgemeine Chemie*, 623:362–368, 1997.
- [186] E. Kendrick, D. Headspith, A. Orera, D. C. Apperley, R. I. Smith, M. G. Francesconi, and P. R. Slater. An investigation of the high temperature reaction between the apatite oxide ion conductor la<sub>9.33</sub>si<sub>6</sub>o<sub>26</sub> and nh<sub>3</sub>. *Journal of Materials Chemistry*, 19:749–754, 2009.
- [187] E. Kendrick, M. S. Islam, and P. R. Slater. Atomic-scale mechanistic features of oxide ion conduction in apatite-type germanates. *Chemical Communications*, pages 715–717, 2008.
- [188] E. Kendrick, M. S. Islam, and P. R. Slater. Investigation of the structural changes on zn doping in the apatite-type oxide ion conductor la<sub>9.33</sub>si<sub>6</sub>o<sub>26</sub>: A combined neutron diffraction and atomistic simulation study. *Solid State Ionics*, 177:3411–3416, 2007.
- [189] E. Kendrick, M. S. Islam, and P. R. Slater. Developing apatites for solid oxide fuel cells: insight into structural, transport and doping properties. *Journal of Materials Chemistry*, 17:3104–3111, 2007.
- [190] E. Kendrick, K. S. Knight, M. S. Islam, and P. R. Slater. Combined experimental and modelling studies of proton conducting la<sub>1-x</sub>ba<sub>1+x</sub>gao<sub>4-x/2</sub>: proton location and dopant site selectivity. *Journal of Materials Chemistry*, 20:10412–10416, 2010.
- [191] E. Kendrick, A. Orera, and P. R. Slater. Neutron diffraction structural study of the apatite-type oxide ion conductor, la<sub>8y2</sub>ge<sub>6</sub>o<sub>27</sub>: location of the interstitial oxide ion site. *Journal of Materials Chemistry*, 19:7955–7958, 2009.
- [192] E. Kendrick and P. R. Slater. Investigation of the influence of oxygen content on the conductivities of ba doped lanthanum germanate apatites. *Solid State Ionics*, 179:981–984, 2008.

- [193] L. Leon-Reina, E. R. Losilla, M. Martinez-Lara, S. Bruque, and M. A. G. Aranda. Interstitial oxygen conduction in lanthanum oxy-apatite electrolytes. *Journal of Materials Chemistry*, 14:1142–1149, 2004.
- [194] L. Leon-Reina, E. R. Losilla, M. Martinez-Lara, S. Bruque, A. Llobet, D. V. Sheptyakov, and M. A. G. Aranda. Interstitial oxygen in oxygen-stoichiometric apatites. *Journal of Materials Chemistry*, 15:2489–2498, 2005.
- [195] L. Leon-Reina, E. R. Losilla, M. Martinez-Lara, M. C. Martin-Sedeno, S. Bruque, P. Nunez, D. V. Sheptyakov, and M. A. G. Aranda. High oxide ion conductivity in al-doped germanium oxyapatite. *Chemistry of Materials*, 17:596–600, 2005.
- [196] L. Leon-Reina, J. M. Porras-Vazquez, E. R. Losilla, and M. A. G. Aranda. Phase transition and mixed oxide-proton conductivity in germanium oxy-apatites. *Journal of Solid State Chemistry*, 180:1250–1258, 2007.
- [197] A. Orera, E. Kendrick, D. C. Apperley, V. M. Orera, and P. R. Slater. Effect of oxygen content on the si-29 nmr, raman spectra and oxide ion conductivity of the apatite series,  $\text{la}_{8+x}\text{sr}_{2-x}(\text{si}_4)_6\text{o}_{2+x/2}$ . *Dalton Transactions*, pages 5296–5301, 2008.
- [198] A. Orera and P. R. Slater. Water incorporation studies in apatite-type rare earth silicates/germanates. *Solid State Ionics*, 181:110–114, 2010.
- [199] J. R. Tolchard, M. S. Islam, and P. R. Slater. Insight into doping effects in apatite silicate ionic conductors. *Advanced Functional Materials*, 17:2564–2571, 2007.
- [200] L. Malavasi, A. Orera, P. R. Slater, P. M. Panchmatia, M. S. Islam, and J. Siewenie. Local structure investigation of oxide ion and proton defects in ge-apatites by pair distribution function analysis. *Chemical Communications*, 47:250–252, 2010.
- [201] P. M. Panchmatia, A. Orera, E. Kendrick, J. V. Hanna, M. E. Smith, P. R. Slater, and M. S. Islam. Protonic defects and water incorporation in si and ge-based apatite ionic conductors. *Journal of Materials Chemistry*, 20:2766–2772, 2010.
- [202] S. S. Pramana, W. T. Klooster, and T. J. White. A taxonomy of apatite frameworks for the crystal chemical design of fuel cell electrolytes. *Journal of Solid State Chemistry*, 181:1717–1722, 2008.
- [203] S. S. Pramana, W. T. Klooster, and T. J. White. Framework ‘interstitial’ oxygen in  $\text{la}_{10}(\text{geo}_4)_5(\text{geo}_5)_2$  apatite electrolyte. *Acta Crystallographica Section B-Structural Science*, 63:597–602, 2007.
- [204] J. E. H. Sansom and P. R. Slater. Oxide ion conductivity in the mixed si/ge apatite-type phases  $\text{lag}_{9.33}\text{si}_{6-x}\text{ge}_x\text{o}_{26}$ . *Solid State Ionics*, 167:23–27, 2004.



- [205] J. E. H. Sansom, J. R. Tolchard, M. S. Islam, D. Apperley, and P. R. Slater. Solid state si-29 nmr studies of apatite-type oxide ion conductors. *Journal of Materials Chemistry*, 16:1410–1413, 2006.
- [206] I. Hung, A. C. Uldry, J. Becker-Baldus, A. L. Webber, A. Wong, M. E. Smith, S. A. Joyce, J. R. Yates, C. J. Pickard, R. Dupree, and S. P. Brown. Probing heteronuclear n-15-o-17 and c-13-o-17 connectivities and proximities by solid-state nmr spectroscopy. *Journal of the American Chemical Society*, 131:1820–1834, 2009.
- [207] A. Wong, A. P. Howes, B. Parkinson, T. Anupold, A. Samoson, D. Holland, and R. Dupree. High-resolution (17)o double-rotation nmr characterization of ring and non-ring oxygen in vitreous b(2)o(3). *Physical Chemistry Chemical Physics*, 11:7061–7068, 2009.
- [208] A. Wong, A. P. Howes, K. J. Pike, V. Lemaitre, A. Watts, T. Anupold, J. Past, A. Samoson, R. Dupree, and M. E. Smith. New limits for solid-state o-17 nmr spectroscopy: Complete resolution of multiple oxygen sites in a simple biomolecule. *Journal of the American Chemical Society*, 128:7744–7745, 2006.
- [209] A. Wong, I. Hung, A. P. Howes, T. Anupold, J. Past, A. Samoson, S. P. Brown, M. E. Smith, and R. Dupree. The determination of o-17 nmr parameters of hydroxyl oxygen: A combined deuteration and dor approach. *Magnetic Resonance in Chemistry*, 45:S68–S72, 2007.
- [210] A. Wong, K. J. Pike, R. Jenkins, G. J. Clarkson, T. Anupold, A. P. Howes, D. H. G. Crout, A. Samoson, R. Dupree, and M. E. Smith. Experimental and theoretical o-17 nmr study of the influence of hydrogen-bonding on c=o and o-h oxygens in carboxylic solids. *Journal of Physical Chemistry A*, 110:1824–1835, 2006.
- [211] T. Anupold, A. Reinhold, P. Sarv, and A. Samoson. A comparison of double rotation and multi-quantum magic angle spinning spectra. *Solid State Nuclear Magnetic Resonance*, 13:87–91, 1998.
- [212] W. Smith, C.W. Yong, and P.M. Rodger. Dl poly: Application to molecular simulation. *Molecular Simulation*, 28:385–471, 2002.
- [213] G. Kresse and J. Furthmüller. Efficient iterative schemes for *ab initio* total-energy calculations using a plane-wave basis set. *Phys. Rev. B*, 54:11169–11186, 1996.
- [214] S. J. Clark, M. D. Segall, C. J. Pickard, P. J. Hasnip, M. J. Probert, K. Refson, and M. C. Payne. First principles methods using castep. *Zeitschrift Fur Kristallographie*, 220:567–570, 2005.
- [215] K. Momma and F. Izumi. Vesta: a three-dimensional visualization system for electronic and structural analysis. *Journal of Applied Crystallography*, 41:653–658, 2008.

- [216] Alexey A. S. and Walsh A. and C. R. A. Catlow. Oxygen interstitial structures in close-packed metal oxides. *Chemical Physics Letters*, 492:44 – 48, 2010.
- [217] M. S. Islam, J. R. Tolchard, and P. R. Slater. An apatite for fast oxide ion conduction. *Chemical Communications*, pages 1486–1487, 2003.
- [218] A. Jones, P. R. Slater, and M. S. Islam. Local defect structures and ion transport mechanisms in the oxygen-excess apatite  $\text{La}_{9.67}(\text{SiO}_4)_6\text{O}_{2.5}$ . *Chemistry of Materials*, 20:5055–5060, 2008.
- [219] M. Magi, E. Lippmaa, A. Samoson, G. Engelhardt, and A. R. Grimmer. Solid-state high-resolution si-29 chemical-shifts in silicates. *Journal of Physical Chemistry*, 88:1518–1522, 1984.
- [220] P. Gillespie, G. Wu, M. Sayer, and M. J. Stott. Si complexes in calcium phosphate biomaterials. *Journal of Materials Science-Materials in Medicine*, 21:99–108, 2010.
- [221] M. L. Occelli, H. Eckert, A. Wolker, and A. Auroux. Crystalline galliosilicate molecular sieves with the beta structure. *Microporous and Mesoporous Materials*, 30:219–232, 1999.
- [222] T. J. Bastow and S. N. Stuart. O-17 nmr in simple oxides. *Chemical Physics*, 143:459–467, 1990.
- [223] R. Hussin, R. Dupree, and D. Holland. The ge-o-ge bond angle distribution in geo2 glass: a nmr determination. *Journal of Non-Crystalline Solids*, 246:159–168, 1999.
- [224] T. J. Bastow, P. J. Dirken, M. E. Smith, and H. J. Whitfield. Factors controlling the o-17 nmr chemical shift in ionic mixed metal oxides. *Journal of Physical Chemistry*, 100:18539–18545, 1996.
- [225] B. C. Bunker, C. H. F. Peden, R. J. Kirkpatrick, and G. L. Turner. O-17 nmr studies of titanate repolymerization in water. *Aqueous Chemistry and Geochemistry of Oxides, Oxyhydroxides, and Related Materials*, 432:39–43, 1997.
- [226] Y. Millot and P. P. Man. Procedures for labeling the high-resolution axis of two-dimensional mq-mas nmr spectra of half-integer quadrupole spins. *Solid State Nuclear Magnetic Resonance*, 21:21–43, 2002.
- [227] H. Eckert, J. P. Yesinowski, L. A. Silver, and E. M. Stolper. Water in silicate-glasses - quantitation and structural studies by h-1 solid echo and mas-nmr methods. *Journal of Physical Chemistry*, 92:2055–2064, 1988.
- [228] H. Eckert, J. P. Yesinowski, and E. M. Stolper. Quantitative nmr-studies of water in silicate-glasses. *Solid State Ionics*, 32-3:298–313, 1989.

- [229] J. P. Yesinowski and H. Eckert. Hydrogen environments in calcium phosphates - h-1 mas nmr at high spinning speeds. *Journal of the American Chemical Society*, 109:6274–6282, 1987.
- [230] J. P. Yesinowski, H. Eckert, and G. R. Rossman. Characterization of hydrous species in minerals by high-speed h-1 mas nmr. *Journal of the American Chemical Society*, 110:1367–1375, 1988.
- [231] I. Schnell, A. Watts, and H. W. Spiess. Double-quantum double-quantum mas exchange nmr spectroscopy: Dipolar-coupled spin pairs as probes for slow molecular dynamics. *Journal of Magnetic Resonance*, 149:90–102, 2001.
- [232] N. Asakawa, S. Kuroki, H. Kurosu, I. Ando, A. Shoji, and T. Ozaki. Hydrogen-bonding effect on c-13 nmr chemical-shifts of l-alanine residue carbonyl carbons of peptides in the solid-state. *Journal of the American Chemical Society*, 114:3261–3265, 1992.
- [233] C. M. Gowda, F. Vasconcelos, E. Schwartz, E. R. H. van Eck, M. Marsman, J. J. L. M. Cornelissen, A. E. Rowan, G. A. de Wijs, and A. P. M. Kentgens. Hydrogen bonding and chemical shift assignments in carbazole functionalized isocyanides from solid-state nmr and first-principles calculations. *Physical Chemistry Chemical Physics*, 13:13082–13095, 2011.
- [234] Z. T. Gu, C. F. Ridenour, C. E. Bronnimann, T. Iwashita, and A. McDermott. Hydrogen bonding and distance studies of amino acids and peptides using solid state 2d h-1-c-13 heteronuclear correlation spectra. *Journal of the American Chemical Society*, 118:822–829, 1996.
- [235] Z. T. Gu, R. Zambrano, and A. McDermott. Hydrogen-bonding of carboxyl groups in solid-state amino-acids and peptides - comparison of carbon chemical shielding, infrared frequencies, and structures. *Journal of the American Chemical Society*, 116:6368–6372, 1994.
- [236] S. Kuroki, S. Ando, I. Ando, A. Shoji, T. Ozaki, and G. A. Webb. Hydrogen-bonding effect on n-15 nmr chemical-shifts of the glycine residue of oligopeptides in the solid-state as studied by high-resolution solid-state nmr-spectroscopy. *Journal of Molecular Structure*, 240:19–29, 1990.
- [237] J. W. Traer, J. F. Britten, and G. R. Goward. A solid-state nmr study of hydrogen-bonding networks and ion dynamics in benzimidazole salts. *Journal of Physical Chemistry B*, 111:5602–5609, 2007.
- [238] G. A. Jeffrey. *An introduction to hydrogen bonding*. Oxford University Press, New York ; Oxford, 1997.
- [239] G. A. Jeffrey and W. Saenger. *Hydrogen bonding in biological structures*. Springer, Berlin, 1991.

- [240] J. Sponer, J. Leszczynski, and P. Hobza. Hydrogen bonding and stacking of dna bases: A review of quantum-chemical ab initio studies. *Journal of Biomolecular Structure & Dynamics*, 14:117–135, 1996.
- [241] J. M. Cole, G. J. McIntyre, M. S. Lehmann, D. A. A. Myles, C. Wilkinson, and J. A. K. Howard. Rapid neutron-diffraction data collection for hydrogen-bonding studies: application of the laue diffractometer (ladi) to the case study zinc (tris)thiourea sulfate. *Acta Crystallographica Section A*, 57:429–434, 2001.
- [242] G. Gemmecker. Direct detection of hydrogen bonds in biopolymers by nmr spectroscopy. *Angewandte Chemie-International Edition*, 39:1224–+, 2000.
- [243] B. Slootmaekers and H. O. Desseyn. Characterization of intermolecular and intramolecular hydrogen-bonding in the solid-state using variable-temperature ir spectroscopy. *Applied Spectroscopy*, 45:118–120, 1991.
- [244] A. K. Cheetham and A. P. Wilkinson. Synchrotron x-ray and neutron-diffraction studies in solid-state chemistry. *Angewandte Chemie-International Edition in English*, 31:1557–1570, 1992.
- [245] A. Wong, I. Hung, A. P. Howes, T. Anupold, J. Past, A. Samoson, S. P. Brown, M. E. Smith, and R. Dupree. The determination of o-17 nmr parameters of hydroxyl oxygen: A combined deuteration and dor approach. *Magnetic Resonance in Chemistry*, 45:S68–S72, 2007.
- [246] S. Schramm, R. J. Kirkpatrick, and E. Oldfield. Observation of high-resolution o-17 nmr-spectra of inorganic solids. *Journal of the American Chemical Society*, 105:2483–2485, 1983.
- [247] D. L. Pechkis, E. J. Walter, and H. Krakauer. High sensitivity of (17)o nmr to p-d hybridization in transition metal perovskites: First principles calculations of large anisotropic chemical shielding. *Journal of Chemical Physics*, 131, 2009.
- [248] E. Arunan, G. R. Desiraju, R. A. Klein, J. Sadlej, S. Scheiner, I. Alkorta, D. C. Clary, R. H. Crabtree, J. J. Dannenberg, P. Hobza, H. G. Kjaergaard, A. C. Legon, B. Mennucci, and D. J. Nesbitt. Definition of the hydrogen bond (iupac recommendations 2011). *Pure and Applied Chemistry*, 83:1637–1641, 2011.
- [249] G. R. Desiraju. Reflections on the hydrogen bond in crystal engineering. *Crystal Growth & Design*, 11:896–898, 2011.
- [250] G. R. Desiraju. A bond by any other name. *Angewandte Chemie-International Edition*, 50:52–59, 2011.
- [251] R. K. Harris, P. Jackson, L. H. Merwin, B. J. Say, and G. Hagele. Perspectives in high-resolution solid-state nuclear magnetic-resonance, with emphasis on combined rotation and multiple-pulse spectroscopy. *Journal of the Chemical Society-Faraday Transactions I*, 84:3649–3672, 1988.

- [252] R. Gobetto, C. Nervi, E. Valfre, M. R. Chierotti, D. Braga, L. Maini, F. Grepioni, R. K. Harris, and P. Y. Ghi. (1)h mas, (15)n cpmas, and dft investigation of hydrogen-bonded supramolecular adducts between the diamine 1,4-diazabicyclo-[2.2.2]octane and dicarboxylic acids of variable chain length. *Chemistry of Materials*, 17:1457–1466, 2005.
- [253] Z. T. Gu and A. McDermott. Chemical shielding anisotropy of protonated and deprotonated carboxylates in amino-acids. *Journal of the American Chemical Society*, 115:4282–4285, 1993.
- [254] A. Wong, K. J. Pike, R. Jenkins, G. J. Clarkson, T. Anupold, A. P. Howes, D. H. G. Crout, A. Samoson, R. Dupree, and M. E. Smith. Experimental and theoretical o-17 nmr study of the influence of hydrogen-bonding on c=o and o-h oxygens in carboxylic solids. *Journal of Physical Chemistry A*, 110:1824–1835, 2006.
- [255] G. Wu. Solid-state o-17 nmr studies of organic and biological molecules. *Progress in Nuclear Magnetic Resonance Spectroscopy*, 52:118–169, 2008.
- [256] G. Wu, D. Rovnyak, P. C. Huang, and R. G. Griffin. High-resolution oxygen-17 nmr spectroscopy of solids by multiple-quantum magic-angle-spinning. *Chemical Physics Letters*, 277:79–83, 1997.
- [257] G. Wu and K. Yamada. Determination of the o-17 nmr tensors in potassium hydrogen dibenzoate: a salt containing a short o center dot center dot center dot h center dot center dot center dot o hydrogen bond. *Solid State Nuclear Magnetic Resonance*, 24:196–208, 2003.
- [258] O. Neumuller, H. Rompp, and E. Uhlein. *Rompps Chemie-Lexicon*. Franckh, Stuttgart,, 1972.
- [259] G. A. Sim, J. M. Robertson, and T. H. Goodwin. The crystal and molecular structure of benzoic acid. *Acta Crystallographica*, 8:157–164, 1955.
- [260] A. J. Horsewill. Quantum tunnelling in the hydrogen bond. *Progress in Nuclear Magnetic Resonance Spectroscopy*, 52:170–196, 2008.
- [261] J. C. Speakman. *The hydrogen bond and other intermolecular forces*. Monographs for teachers. Chemical Society, London, 1975.
- [262] L. J. Barbour. X-seed a software tool for supramolecular crystallography. *Journal of Supramolecular Chemistry*, 1:189–191, 2001.
- [263] G. M. Sheldrick. A short history of shelx. *Acta Crystallographica Section A*, 64:112–122, 2008.
- [264] C. F. Macrae, P. R. Edgington, P. McCabe, E. Pidcock, G. P. Shields, R. Taylor, M. Towler, and J. van De Streek. Mercury: visualization and analysis of crystal structures. *Journal of Applied Crystallography*, 39:453–457, 2006.

- [265] R. K. Harris, E. D. Becker, S. M. C. de Menezes, R. Goodfellow, and P. Granger. Nmr nomenclature: Nuclear spin properties and conventions for chemical shifts - iupac recommendations 2001 (reprinted from pure appl. chem, vol 73, pg 1795-1818, 2001). *Solid State Nuclear Magnetic Resonance*, 22:458–483, 2002.
- [266] D. Massiot, F. Fayon, M. Capron, I. King, S. Le Calve, B. Alonso, J. O. Durand, B. Bujoli, Z. H. Gan, and G. Hoatson. Modelling one- and two-dimensional solid-state nmr spectra. *Magnetic Resonance in Chemistry*, 40:70–76, 2002.
- [267] J. P. Perdew, J. A. Chevary, S. H. Vosko, K. A. Jackson, M. R. Pederson, D. J. Singh, and C. Fiolhais. Atoms, molecules, solids, and surfaces - applications of the generalized gradient approximation for exchange and correlation. *Physical Review B*, 46:6671–6687, 1992.
- [268] C. J. Pickard and F. Mauri. All-electron magnetic response with pseudopotentials: Nmr chemical shifts. *Physical Review B*, 63, 2001.
- [269] J. R. Yates, C. J. Pickard, and F. Mauri. Calculation of nmr chemical shifts for extended systems using ultrasoft pseudopotentials. *Physical Review B*, 76, 2007.
- [270] R. Destro, R. Soave, and M. Barzaghi. Physicochemical properties of zwitterionic l- and dl-alanine crystals from their experimental and theoretical charge densities. *Journal of Physical Chemistry B*, 112:5163–5174, 2008.
- [271] D. A. Fletcher, R. F. McMeeking, and D. Parkin. The united kingdom chemical database service. *Journal of Chemical Information and Computer Sciences*, 36:746–749, 1996.
- [272] C. C. Wilson, N. Shankland, and A. J. Florence. A single-crystal neutron diffraction study of the temperature dependence of hydrogen-atom disorder in benzoic acid dimers. *Journal of the Chemical Society-Faraday Transactions*, 92:5051–5057, 1996.
- [273] H. J. Flammersheim. Physicochemical studies on systems of sodium benzoate and benzoic-acid .2. phase behavior of system sodium benzoate benzoic acid. *Journal of Thermal Analysis*, 7:571–585, 1975.
- [274] E. W. Hagaman, B. Chen, J. Jiao, and W. Parsons. Solid-state  $^{17}\text{O}$  nmr study of benzoic acid adsorption on metal oxide surfaces. *Solid State Nuclear Magnetic Resonance*.
- [275] G. Wu and K. Yamada. Determination of the  $^{17}\text{O}$  nmr tensors in potassium hydrogen dibenzoate: a salt containing a short o center dot center dot center dot h center dot center dot center dot o hydrogen bond. *Solid State Nuclear Magnetic Resonance*, 24:196–208, 2003.

- [276] C. J. Gorter. Bad luck in attempts. *Physics Today*, 20:76, 1967.
- [277] S. Dong, R. Ida, and G. Wu. A combined experimental and theoretical o-17 nmr study of crystalline urea: An example of large hydrogen-bonding effects. *Journal of Physical Chemistry A*, 104:11194–11202, 2000.

# Appendix A

## Appendix

### A.1 History

#### A.1.1 Endnotes

#### Notes

<sup>1</sup>Niels Bohr, Nobel laureate, Physics 1922

<sup>2</sup>George Uhlenbeck and Samuel Goudsmit

<sup>3</sup>Erwin Schrödinger, Nobel laureate, Physics 1933 (An interesting side note is that Schrödinger family came locally from Leamington Spa) and Werner Heisenberg, Nobel laureate, Physics 1932

<sup>4</sup>Wolfgang Pauli, Nobel laureate, Physics 1945 and Charles Darwin, grandson of the Charles Darwin

<sup>5</sup>Paul Dirac, shared the Nobel prize with Schrödinger in 1933

<sup>6</sup>David M. Dennison

<sup>7</sup>Otto Stern, Nobel laureate, Physics 1943 and Walter Gerlach

<sup>8</sup>Isidor Rabi, Nobel laureate, Physics 1944

<sup>9</sup>Cornelis Gorter, when he was awarded the Lorentz medal he gave a talk on the numerous discoveries his research failed to pick up on [276]

<sup>10</sup>Walter Kohn, Nobel Prize Chemistry, 1988

### A.2 Characterisation of Platinum-based Fuel Cell Catalyst Materials using Wideline Solid State NMR

The lattice parameters for the platinum alloy and intermetallic systems are shown in the table A.1. These are obtained from figure ?? and ??.



Sample	XRD		
	Crystallite size/nm	Lattice parameter/Å	Ordered
Pt <sub>3</sub> Sn	19.3 (Pt <sub>3</sub> Sn)	4.002 (cubic)	Yes
	7.7 (PtSn)	4.102, 5.457 (hex)	Yes
	5.9 (Pt)	3.930 (cubic)	No
PtSn	99	4.101, 5.441 (hex)	Yes
Pt <sub>3</sub> Ti	3.7	3.899	Yes
Pt <sub>3</sub> Zr	4.5	3.99	Yes, weak
Pt <sub>3</sub> Hf	5.7	3.97	No
Pt <sub>3</sub> Nb	?	?	?
Pt <sub>3</sub> Sc	7.3	3.949	Yes
Pt <sub>3</sub> Al	5.1	3.876	Yes

Table A.1: The lattice parameters for the PtSn, Pt<sub>3</sub>Sn and Pt<sub>3</sub>X alloys completed by X-ray diffraction studies.

## A.3 Apatite Oxide Ion Conductors

### A.3.1 DFT Simulation Input Files

The simulation shown in figure 5.2 was simulated using the pNMRsim which is discussed fully in the website <http://www.dur.ac.uk/solids.nmr/software/pnmrsim/>. An example input file is shown in figure A.1, for each of the 26 oxygen sites an individual file shown in this diagram was produced with their respected parameters and simulated. The resultant 26 FIDs were then summed and figure 5.2 was produced, the sample were internally referenced to the position of the major GeO<sub>4</sub> resonance.

## A.4 A Multi-Nuclear Solid State NMR, DFT and Diffraction study of Tight Hydrogen Bonds in Group IA Hemibenzozates

### A.4.1 Experimental

IR spectra were recorded on Perkin Elmer Spectrum 100 FT-IR Spectrometer using Attenuated Total Reflection sampling unless otherwise stated, and are reported in  $cm^{-1}$ . Mass spectra were recorded at the EPSRC Mass Spectrometry Centre at the University of Swansea. GCMS was carried out at NTU using Agilent Tech-

```

spinsys {
  nuclei 170
  proton_frequency 600e6
  shift 1 $4p
  quadrupole 1 2 $2 $3
}

par {
  spin_rate $1
  sw $1
  start_operator Inx
  detect_operator Inc
  crystal_file zcw2178308
  gamma_angles 0
  np 1024
}

proc {
  save $(name)_spin$1_cq$2_eta$3_Iso$4.fid -simpson
}

```

Isotropic Shift (ppm)  
 Quadrupole Coupling Constant (MHz),  $C_Q$   
 Quadrupole Asymmetry Parameter,  $\eta$   
 Spin rate (Hz)  
 Rotor Synchronised Sweep Width (Hz)  
 Number of Crystallites to calculate  
 Number of Time Domain points  
 File Name

Figure A.1: An example of a pNMRsim Input file for the simulation of the apatite system shown in figure 5.2.

nologies 6890N GC equipped with a 5975 mass detector. Chemical analysis data were obtained from Mr Stephen Boyer, London Metropolitan University. Microwave synthesis was performed using a CEM Discovery apparatus. All  $^{17}\text{O}$  labelled water was purchased from Cortecnet.

#### A.4.2 Synthesis and Characterisation

Below is a full synthetic pathway for generating labelled benzoic acid and then using this product to synthesise the hemibenzoates, the synthesis was mainly carried out by Dr. Alberth Lari and Prof. John Wallis in Nottingham Trent University.

#### A.4.3 $^{17}\text{O}$ -Enriched benzoic acid

$\alpha,\alpha,\alpha$ -Trichlorotoluene (660 mg, 3.38 mmol) and 70 %  $^{17}\text{O}$ -enriched water (193 mg, 10.1 mmol) were reacted together at 160 °C for 15 min in a 10 ml vial at a pressure of 16 bar in a microwave reactor. The vessel was allowed to cool to room temperature, and then excess pressure (HCl vapour) released. The mixture was again reacted at 160 °C for 45 min at 16 bar, and then cooled to room temperature and the pressure released. Depending on the degree of conversion to benzoic acid (as determined by GC-MS analysis), a further amount of  $^{17}\text{O}$ -labelled water added (typically 50 – 100  $\mu\text{L}$ ), and the mixture treated under the same microwave conditions (45 mins). This was repeated, if necessary, until GC-MS showed almost complete conversion to benzoic acid. Crude product was recrystallized from heptane, typical isolated yield 80 %. 70 %  $^{17}\text{O}$ -Enriched water gave benzoic acid containing 40.5 %  $\text{PhC}(^{17}\text{O})_2\text{H}$ ,

45.7 %  $\text{PhC}^{(17\text{O})}(\text{}^{16}\text{O})\text{H}$  and 13.8 %  $\text{PhCO}_2\text{H}$  by mass spectral analysis (64 % enrichment); elemental analysis calcd (%) for  $\text{C}_7\text{H}_6\text{O}_2$ : C 68.16, H 4.90; found: C 68.25, H 4.82; 90 %  $^{17}\text{O}$ -enriched water gave benzoic acid containing 74.2 %  $\text{PhC}^{(17\text{O})}_2\text{H}$ , 23.6 %  $\text{PhC}^{(17\text{O})}(\text{}^{16}\text{O})\text{H}$  and 2.2 %  $\text{PhCO}_2\text{H}$  by mass spectral analysis (86 % enrichment), m.p. 121–122 °C, IR (ATR):  $\nu = 3073, 2982, 2815, 2658, 2540, 1664$  (C=O), 1603, 1582, 1454, 1419, 1323, 1285 and 1276 (C–O), 1187, 1180, 1121, 1073, 1027, 931, 810, 798, 703, 684, 661  $\text{cm}^{-1}$  (cf. non-enriched benzoic acid, from heptane: IR (ATR):  $\nu = 3072, 2831, 2668, 2554, 1678, 1602, 1583, 1454, 1421, 1324, 1289$  (C–O), 1280 sh, 1187, 1180, 1128, 1073, 1027, 932, 805, 704, 684, 666  $\text{cm}^{-1}$ ).

#### A.4.4 Lithium hemibenzoate

Lithium hydroxide monohydrate (0.056 g) dissolved in water (0.5 ml) was added to a solution of the labelled benzoic acid (0.33 g, 2 equiv.) in warm methanol (1.5 ml). The mixture was heated for 5 min., methanol added dropwise until a solution was formed and the product left to crystallise out at room temperature. Colourless flat needles of the product were collected, washed with water and dried under vacuum. Yield 35 %. m.p. 119–121 °C; IR (ATR):  $\nu = 3072, 2829, 2667, 2552, 1678$  (C=O), 1601, 1583, 1453, 1420, 1324, 1288, 1179, 1128, 1073, 932, 805, 704, 684, 666  $\text{cm}^{-1}$ ; elemental analysis calcd (%) for  $\text{C}_{14}\text{H}_{11}\text{O}_4\text{Li}$ : C 67.21, H 4.43; found: C 67.19, H 4.54.  $^{17}\text{O}$ -Enriched lithium hemibenzoate was prepared from 4 %  $^{17}\text{O}$ -enriched benzoic acid: elemental analysis calcd (%) for  $\text{C}_{14}\text{H}_{11}\text{O}_4\text{Li}$ : C 66.53, H 4.39; found: C 66.21, H 4.42.

#### A.4.5 Sodium benzoate

Thick needle shaped crystals of this material were obtained by treatment of an ethanolic solution of benzoic acid with 0.5 equivalent of sodium hydroxide in water, and subsequent slow evaporation of the mixture, m.p.  $\geq 300$  °C; IR (ATR):  $\nu = 1698$  and 1673 (C=O), 1600, 1584, 1563, 1451, 1376, 1318, 1287, 1249, 1177, 1118, 1072, 1025, 1004, 934, 903, 800, 787, 704, 684, 663  $\text{cm}^{-1}$ . [273]

#### A.4.6 Potassium hemibenzoate

Method A: Potassium hydroxide (0.077 g) in water (1 ml) was added to a hot solution of  $^{17}\text{O}$ -labelled benzoic acid (0.33 g, 2 equiv.) in ethanol (2 ml) and a precipitate started form. The mixture was heated for 5 min., and then water was added dropwise with heating until a solution was just formed, and the product left to crystallise out at room temperature. Colourless flat needles of the product were

collected by filtration, washed with ethanol and ether, and dried in vacuo. Yield 45 %, m.p.  $\geq 300$  °C; IR (ATR):  $\nu = 3056, 1690$  br (C=O), 1580, 1448, 1070, 802, 702, 683, 660  $\text{cm}^{-1}$ ; elemental analysis calcd (%) for  $\text{C}_{14}\text{H}_{11}\text{O}_4\text{K}$ : C 59.55, H 3.93; found: C 59.44, H 3.83.  $^{17}\text{O}$ -Enriched potassium hemibenzoate was prepared from 64 %  $^{17}\text{O}$ -enriched benzoic acid: elemental analysis calcd (%) for  $\text{C}_{14}\text{H}_{11}\text{O}_4\text{K}$ : C 58.90, H 3.88; found: C 58.79, H 3.86. [277]

Method B: Potassium hydroxide (0.077 g) in methanol (1.5 ml) was added to a hot solution of benzoic acid (0.33 g, 2 equiv.) in THF (2.5 ml) and the immediately formed precipitate heated for 5 min. Methanol was added dropwise until a solution was just formed, and the product left to crystallise, to give the same polymorphic form of potassium hemibenzoate as obtained from ethanol/water.

#### A.4.7 Rubidium hemibenzoate

Method A above was employed but using a commercial 50 % solution of rubidium hydroxide to give the product as colourless flat needles. Yield 60 %. m.p.  $\geq 300$  °C; IR (ATR):  $\nu = 3059, 1690$  br (C=O), 1581, 1448, 1352, 1317, 1307, 1208, 1071, 804, 702, 683, 661  $\text{cm}^{-1}$ ; elemental analysis calcd (%) for  $\text{C}_{14}\text{H}_{11}\text{O}_4\text{Rb}$ : C 51.15, H 3.37; found: C 51.08, H 3.23.  $^{17}\text{O}$ -Enriched rubidium hemibenzoate was prepared from 64 % enriched  $^{17}\text{O}$ -enriched benzoic acid: elemental analysis calcd (%) for  $\text{C}_{14}\text{H}_{11}\text{O}_4\text{Rb}$ : C 50.76, H 3.35; found: C 50.37, H 3.34.

#### A.4.8 Caesium hemibenzoate - monoclinic polymorph

Following Method A above but using caesium hydroxide monohydrate gave colourless plates of the monoclinic polymorph of caesium hemibenzoate. Yield 76 %. m.p.  $\geq 300$  °C; IR (ATR):  $\nu = 3055, 1671$  sh and 1634 (C=O), 1600, 1577, 1448, 1343, 1314, 1281, 1067, 803, 688, 669  $\text{cm}^{-1}$ ; elemental analysis calcd (%) for  $\text{C}_{14}\text{H}_{11}\text{O}_4\text{Cs}$ : C 44.70, H 2.95; found: C 44.75, H 2.87.  $^{17}\text{O}$ -Enriched caesium hemibenzoate was prepared from 64 %  $^{17}\text{O}$ -enriched benzoic acid: elemental analysis calcd (%) for  $\text{C}_{14}\text{H}_{11}\text{O}_4\text{Cs}$ : C 44.40, H 2.93; found: C 44.20, H 3.00.

#### A.4.9 Caesium hemibenzoate - orthorhombic polymorph

Caesium hydroxide monhydrate (0.23 g) in methanol (1.5 ml) was added to a solution of benzoic acid in THF (2.5 ml) and the immediately formed precipitate was heated to reflux for 5 min. Methanol was added dropwise until a solution was almost formed, the solution filtered, and the filtrate left to crystallise at 0 °C. Plate-like crystals of the orthorhombic polymorph of caesium hemibenzoate were collected

and washed with THF and dried under vacuum. Yield 36 %, m.p.  $\geq 300$  °C; IR (ATR):  $\nu = 3055, 1671$  sh and  $1634$  (C=O),  $1600, 1577, 1448, 1343, 1314, 1281, 1067, 804, 688, 669$   $\text{cm}^{-1}$ ; elemental analysis calcd (%) for  $\text{C}_{14}\text{H}_{11}\text{O}_4\text{Cs}$ : C 44.70, H 2.95; found: C 44.75, H 2.87.  $^{17}\text{O}$ -Enriched caesium hemibenzoate was prepared from 64 %  $^{17}\text{O}$ -enriched benzoic acid.

#### A.4.10 X-ray Crystallography

All this data was achieved by Prof. John Wallis in Nottingham Trent University. X-ray diffraction datasets were measured on a Bruker-Nonius FR591 diffractometer equipped with a rotating anode and a Bruker-Nonius Roper CCD camera (National Crystallography Service, Southampton University, UK). The orthorhombic polymorph of caesium hemibenzoate was measured on a Oxford Diffraction Xcalibur diffractometer equipped with a Sapphire CCD detector at Nottingham Trent University. Crystal cooling was provided by an Oxford Cryosystems Cryostream low temperature system. Crystal structure solution and refinement were carried out with SHELXS and SHELXL programs using the XSEED interface. Non-hydrogen atoms were assigned anisotropic displacement parameters. All hydrogen atom positions were determined geometrically and refined with a riding model, except as follows: lithium hemibenzoate and sodium benzoate: benzoic acid: coordinates of the (O)H atoms refined; potassium hemibenzoate: two (O)H positions, related by a centre of symmetry in the middle of the O—O vector, refined with half occupancies; rubidium hemibenzoate and both polymorphs of caesium hemibenzoate: electron density corresponding to the (O)H atom located on a two-fold axis and equidistant from two O atoms (O—O: (Rb)  $2.455$  Å, (Cs monoclinic)  $2.457$  Å, (Cs orthorhombic)  $2.457$  Å) and only the y coordinate refined in each case. In the rubidium and caesium cases, these (O)H positions may be misleading, and may be rather an average of a disorder between two positions in which the H atom lies closer to one O atom or the other. Molecular illustrations were made with Mercury and POV-Ray. [262, 263, 272]

#### A.4.11 Crystal data

Lithium hemibenzoate:  $\text{C}_{14}\text{H}_{11}\text{O}_4\text{Li}$ , Mr = 250.17, triclinic,  $a = 5.3600(3)$ ,  $b = 8.5693(7)$ ,  $c = 13.4999(11)$  Å,  $\alpha = 98.830(4)$ ,  $\beta = 93.800(5)$ ,  $\gamma = 95.524(5)^\circ$   $V = 607.80(8)$  Å<sup>3</sup>,  $Z = 2$ ,  $P-1$ ,  $D_c = 1.37$   $\text{gcm}^{-3}$ ,  $\mu = 0.099$   $\text{mm}^{-1}$ , T = 120 K, 2763 unique reflections, 1833 with  $F^2 \geq 2\sigma$ ,  $R(F, F^2 \geq 2\sigma) = 0.054$ ,  $Rw(F^2, \text{all data}) = 0.13$ .

Sodium benzoate. 2benzoic acid:  $C_{21}H_{17}O_6Na$ , Mr = 388.34, monoclinic,  $a = 5.80770(10)$ ,  $b = 14.4331(4)$ ,  $c = 22.0139(6)$  Å,  $\alpha, \beta = 97.047(2)^\circ$ ,  $V = 1831.33(8)$  Å<sup>3</sup>,  $Z = 4$ ,  $P2_1/c$ ,  $Dc = 1.41$  gcm<sup>-3</sup>,  $\mu = 0.123$  mm<sup>-1</sup>, T = 120 K, 3434 unique reflections, with  $F^2 \geq 2\sigma$ ,  $R(F, F^2 \geq 2\sigma) = 0.041$ ,  $Rw(F^2, \text{all data}) = 0.10$ .

Potassium hemibenzoate:  $C_{14}H_{11}O_4K$ , Mr = 282.33, monoclinic,  $a = 29.586(2)$ ,  $b = 3.7964(3)$ ,  $c = 11.1214(8)$  Å,  $\alpha, \beta = 97.096(9)^\circ$ ,  $V = 1239.59(16)$  Å<sup>3</sup>,  $Z = 4$ ,  $C2/c$ ,  $Dc = 1.51$  gcm<sup>-3</sup>,  $\mu = 0.435$  mm<sup>-1</sup>, T = 120 K, 1428 unique reflections, 1203 with  $F^2 \geq 2\sigma$ ,  $R(F, F^2 \geq 2\sigma) = 0.043$ ,  $Rw(F^2, \text{all data}) = 0.11$ ; original measurement.

Rubidium hemibenzoate:  $C_{14}H_{11}O_4Rb$ , Mr = 328.70, monoclinic,  $a = 29.0315(9)$ ,  $b = 6.9630(2)$ ,  $c = 6.6156(2)$  Å,  $\alpha, \beta = 99.297(2)^\circ$ ,  $V = 1319.75(7)$  Å<sup>3</sup>,  $Z = 4$ ,  $C2/c$ ,  $Dc = 1.65$  gcm<sup>-3</sup>,  $\mu = 3.76$  mm<sup>-1</sup>, T = 120 K, 1510 unique reflections, 1439 with  $F^2 \geq 2\sigma$ ,  $R(F, F^2 \geq 2\sigma) = 0.28$ ,  $Rw(F^2, \text{all data}) = 0.070$ .

Caesium hemibenzoate, monoclinic polymorph:  $C_{14}H_{11}O_4Cs$ , Mr = 376.14, monoclinic,  $a = 28.9095(8)$ ,  $b = 7.0509(2)$ ,  $c = 6.7779(2)$  Å,  $\alpha, \beta = 99.970(2)^\circ$ ,  $V = 1360.73(7)$  Å<sup>3</sup>,  $Z = 4$ ,  $C2/c$ ,  $Dc = 1.84$  gcm<sup>-3</sup>,  $\mu = 2.73$  mm<sup>-1</sup>, T = 120 K, 1565 unique reflections, 1529 with  $F^2 \geq 2\sigma$ ,  $R(F, F^2 \geq 2\sigma) = 0.019$ ,  $Rw(F^2, \text{all data}) = 0.046$ .

Caesium hemibenzoate, orthorhombic polymorph:  $C_{14}H_{11}O_4Cs$ , Mr = 376.14, orthorhombic,  $a = 28.3393(19)$ ,  $b = 7.0215(3)$ ,  $c = 6.9066(4)$  Å,  $V = 1374.31(14)$  Å<sup>3</sup>,  $Z = 4$ ,  $Pbcn$ ,  $Dc = 1.82$  gcm<sup>-3</sup>,  $\mu = 2.70$  mm<sup>-1</sup>, T = 150 K, 1664 unique reflections, 1389 with  $F^2 \geq 2\sigma$ ,  $R(F, F^2 \geq 2\sigma) = 0.031$ ,  $Rw(F^2, \text{all data}) = 0.050$ .

#### A.4.12 CASTEP Output of Hemibenzoate CIFs by different Optimisation Methods

In the chapter 6 the following tables 6.4, 6.2 and 6.1 contain the simulated geometry optimised CASTEP results for the various hemibenzoates. The geometry optimisation method used involves allowing all the atoms present in the cell to be able to move to their local energy minima (within specific constraints). This method is quite controversial amongst crystallographers as the XRD experiment is known to give highly accurate information for all atoms except for protons. In the two tables (A.2 and A.3) the CASTEP results for the CIFs and proton only optimised CIFs are compared. These both highlight the inaccuracies with these methods when compared to the all atom optimisation in chapter 6. Examples are present in reference [49].

Sample	$\delta_{\text{iso}}$ $^1\text{H}^{[a]}$	$\delta_{\text{iso}}$ $^{13}\text{C}^{[c]}$	$\delta_{11}$ $^{13}\text{C}$	$\delta_{22}$ $^{13}\text{C}$	$\delta_{33}$ $^{13}\text{C}$	$\delta_{\text{iso}}(\text{MAS})$ $^{17}\text{O}$	$\text{C}_Q$ $^{17}\text{O}$	$\eta$ $^{17}\text{O}$
	$= \text{O} \cdots ^1\text{HO}$	$-^{13}\text{COOH}$	$-^{13}\text{COOH}$	$-^{13}\text{COOH}$	$-^{13}\text{COOH}$			
	ppm	ppm	ppm	ppm	ppm	ppm	MHz	
BZA	7.9	169.4	240.9	188.4	78.9	395.1/ 194.4	8.28/ 9.06	0.23/ 0.30
LiHB	13.2	169.1	236.5	180.0	90.9	334.6/ 232.8/ 276.9/ 263.6	7.73/ 8.55/ 7.82/ 7.93	0.16/ 0.25/ 0.65/ 0.50
KHB	21.42	176.7	249.5	165.0	115.5	289.5/ 226.9	6.28/ 8.59	0.58/ 0.26
RbHB	20.68	174.8	247.0	171.5	105.8	228.7/ 222.8	7.98/ 8.02	0.93/ 0.26
CsHB	21.21	172.5	232.7	192.0	92.8	278.2/ 192.5	6.92/ 8.75	0.43/ 0.14

Table A.2: The NMR parameters achieved from the CASTEP calculations on the XRD produced CIFs, the proton poisitons are given as average proton-carbon distances.

Sample	$\delta_{\text{iso}}$ $^1\text{H}^{[a]}$	$\delta_{\text{iso}}$ $^{13}\text{C}^{[c]}$	$\delta_{11}$ $^{13}\text{C}$	$\delta_{22}$ $^{13}\text{C}$	$\delta_{33}$ $^{13}\text{C}$	$\delta_{\text{iso}}(\text{MAS})$ $^{17}\text{O}$	$\text{C}_Q$ $^{17}\text{O}$	$\eta$ $^{17}\text{O}$
	$= \text{O} \cdots ^1\text{HO}$	$-^{13}\text{COOH}$	$-^{13}\text{COOH}$	$-^{13}\text{COOH}$	$-^{13}\text{COOH}$			
	ppm	ppm	ppm	ppm	ppm	ppm	MHz	
BZA	14.9	172.2	259.6	174.0	82.9	347.6/ 231.6	7.24/ 7.46	0.16/ 0.55
LiHB	12.9	169.3	247.5	188.1	102.2	336.3/ 234.4/ 277.2/ 266.7	7.50/ 8.82/ 7.71/ 7.90	0.21/ 0.26/ 0.66/ 0.51
KHB	21.33	173.45	243.2	176.4	100.8	291.5/ 229.8	6.29/ 8.56	0.58/ 0.27
RbHB	21.40	174.35	241.1	183.1	96.2	289.9/ 209.6	6.40/ 8.86	0.55/ 0.22
CsHB	21.08	172.3	233.1	191.0	92.8	277.7/ 195.2	6.86/ 8.72	0.42/ 0.14

Table A.3: he NMR parameters achieved from the proton optimised CASTEP calculations on the XRD produced CIFs.